

DISSERTATION

PERFORMANCE-BASED SEISMIC RETROFIT (PBSR) METHODOLOGY FOR MULTI-
STORY BUILDINGS WITH FULL-SCALE EXPERIMENTAL VALIDATION

Submitted by

Pouria Bahmani

Department of Civil and Environmental Engineering

In partial fulfillment of the requirements

For the Degree of Doctor of Philosophy

Colorado State University

Fort Collins, Colorado

Spring 2015

Doctoral Committee:

Advisor: John W. van de Lindt

Paul R. Heyliger
Hussam N. Mahmoud
Donald W. Radford

Copyright by Pouria Bahmani 2015

All Rights Reserved

ABSTRACT

PERFORMANCE-BASED SEISMIC RETROFIT (PBSR) METHODOLOGY FOR MULTI-STORY BUILDINGS WITH FULL-SCALE EXPERIMENTAL VALIDATION

Recent earthquakes such as Loma Prieta (1989) and Northridge (1994) in California have highlighted the poor performance of one class of existing buildings. Many older buildings were designed prior to the implementation of modern seismic design codes. Although building codes have clearly evolved, the problem is still unresolved for older buildings that are code-deficient such as soft-story wood-frame buildings. Many retrofit procedures have been proposed by the research and structural engineering communities including force-based and performance-based retrofit methodologies. A performance-based seismic retrofit (PBSR) methodology is developed and validated in this dissertation and is a method that seeks to meet or exceed minimum performance criteria specified by building stakeholders when the building is subjected to a predefined seismic intensity level. Unlike traditional force-based design methods, the PBSR method enables engineers to design and retrofit buildings based on the performance level expected by the stakeholders; and eventually, results in a more comprehensive method of retrofitting multi-story buildings.

The objective of this study was twofold. The first objective was to develop a new displacement-based design (DBD) method with the ability to account for torsion (DBDT), thereby, generalizing the displacement-based design to be applied to linear and non-linear structures with vertical and torsional (horizontal) irregularities without the need for time-history analysis. This first objective involves the decoupling of translational and torsional mode shapes of the structure,

standardizing the global stiffness and mass matrices, and finally combining the decoupled translational and torsional mode shapes to meet the designated performance criteria. The second objective was to develop a new performance-based seismic retrofit (PBSR) methodology for retrofitting existing multi-story buildings with torsional (horizontal) and vertical irregularities. The PBSR method was developed using the proposed DBDT method and was validated numerically to retrofit a three-story soft-story building with excessive torsion at all stories. The PBSR method was then modified to eliminate the torsion in the building and satisfy the designated performance criteria. This enables the design to use only the dominant translational mode shape (i.e., first mode shape) for the retrofit. This also eliminates the need for modal analysis and the decoupling of translational and torsional mode shapes makes it more straightforward for practice. The new simplified PBSR method for retrofitting multi-story buildings was then applied to a four-story soft-story wood-frame building with torsional irregularities at all stories and assessed numerically using non-linear time-history (NLTH) analysis.

The method developed in this dissertation was validated experimentally by conducting a series of full-scale tests on a four-story 370 m^2 ($4,000 \text{ ft}^2$) soft-story wood-frame building at the outdoor uni-axial shake table at the University of California - San Diego's Network for Earthquake Engineering Simulation (NEES) laboratory. The test provided the first-of-its-kind (landmark) dataset for use by researchers and practitioners for retrofitting soft-story wood-frame buildings. The experimental test results showed that the retrofitted building met the designated performance criteria and essentially validated the PBSR method developed in this dissertation. It should be noted that although the PBSR method was only validated experimentally for the asymmetric soft-story wood-frame building, the method can be used for any type of structure provided the

necessary details of design and material properties are addressed. Finally, in order to investigate the collapse mechanism of soft-story wood-frame buildings the un-retrofitted building was subjected to series of ground motion with increasing intensities until it collapsed. These series of tests are the first full-scale collapse tests of a full-size building.

ACKNOWLEDGMENTS

This material is based upon work supported by the National Science Foundation under Grant No. CMMI-1041631 and 1314957 (NEES Research) and NEES Operations. Any opinions, findings, and conclusions or recommendations expressed in this material are those of the author and do not necessarily reflect the views of the National Science Foundation. A sincere thank you to Simpson Strong-Tie for their financial, personnel, and product support throughout the project.

I would like to express my deepest gratitude to my advisor, Dr. John van de Lindt, who has supported me kindly and patiently throughout my PhD studies. His vast knowledge and encouragement gave me motivation to work hard and made even the most difficult minutes pleasant to me. His help and support is greatly appreciated.

My special thanks would be for Dr. Bijan Boroomand at Isfahan University of Technology and Dr. Nadim Wehbe at South Dakota State University to whom I owe a vast amount of my knowledge in the field of structural engineering. I would like to recognize Dr. Paul Heyliger, Dr. Hussam Mahmoud, and Dr. Marvin Criswell at Colorado State University who taught me advanced courses in structural engineering, and on top of that, guided me throughout my academic career. I would also like to thank structural engineers, Mr. Steven Pryor, Mr. Gary Mochizuki, and Mr. Mikhail Gershfeld who supported me throughout this project with their great knowledge and experience in design and retrofit of buildings. My sincere thanks to fellow graduate student, Ms. Jingjing Tian, and undergraduate students, Ms. Sandra Gutierrez, Ms. Faith Silva, Mr. Gabriel Banuelos, Mr. Rocky Chen, Ms. Connie Tsui, and Mr. Vaishak Gopi, who helped me in data analysis and instrumentation during this project.

Finally, I would like to extend my special thanks to my father, mother, and two lovely sisters who have unconditionally supported me throughout my life. Their encouragement and continued support helped me to discover my talents and motivated me to accomplish my goals.

DEDICATION

To the people of Bam, Iran, who lost their lives and loved ones in 2003 Bam earthquake

And,

To all the people who suffered from earthquake in the world.

TABLE OF CONTENTS

ABSTRACT	ii
ACKNOWLEDGMENTS	v
DEDICATION.....	vi
LIST OF TABLES	xi
LIST OF FIGURES	xiii
Chapter 1. Introduction	1
1.1 Motivation for Development of Performance-Based Seismic Retrofit (PBSR).....	1
1.2 Classification of Structurally Deficient Irregular Buildings	4
1.2.1 Vertical Irregularity.....	6
1.2.2 Horizontal (Torsional) Irregularity	7
1.3 Major Retrofit Methodologies	8
1.3.1 FEMA P-807 and PBSR Retrofit Methods	11
1.4 Objectives of this Dissertation.....	14
1.5 Organization of This Dissertation.....	15
Chapter 2. Performance-Based Seismic Design (PBSD) Development for Torsionally	
Irregular Buildings.....	18
2.1 Performance-Based Design (PBD)	18
2.2 Displacement-Based Design of Buildings with Torsion (DBDT)	22
2.2.1 Direct Displacement Design (DDD).....	22
2.2.2 Displacement-Based Design Procedure with Torsion (DBDT)	23
2.2.3 Summary of Displacement-Based Design Procedure with Torsion (DBDT).....	45
2.2.4 Numerical Verification and Illustrative Examples	49
Chapter 3. Performance-Based Seismic Retrofit (PBSR) Development.....	60
3.1 PBSR Procedure by Including Torsion	64
3.1.1 Retrofitting a 3-story torsionally irregular soft-story building using PBSR with torsion	67

3.2	Simplified PBSR Procedure by Eliminating Torsion'	71
Chapter 4. Isolated Wood-Frame Wall Tests		83
4.1	Experimental Test Setup and Test Specimens	86
4.1.1	<i>Single-layer Sheathing Tests</i>	92
4.1.2	<i>Two- and Three-layer Sheathing Tests</i>	100
4.2	Comparison of backbones from the experimental tests and P-807 data set	102
4.3	Understanding Sheathing Combinations	104
4.3.1	<i>Backbone Curves – Strength Approach</i>	104
4.3.2	<i>Non-linear Time-History Analysis – Statistical Approach</i>	108
4.4	Evaluation of FEMA P-807 Sheathing Combination Rule	111
Chapter 5. Numerical Validation and Retrofit Design of a Four-Story Soft-Story Wood-Frame Building Using Simplified PBSR Method		115
5.1	Building Specifications	115
5.2	Retrofit Design with Simplified PBSR Procedure	117
5.3	Practical Consideration for Experimental Validation	127
5.3.1	<i>Steel Moment Frame (SMF)</i>	128
5.3.2	<i>Wood Structural Panel (WSP)</i>	132
5.4	Numerical Validation	139
5.4.1	<i>Bi-axial Analysis: Cumulative Distribution of ISD Ratios at $S_a = 1.8g$</i>	140
5.4.2	<i>Uni-axial Analysis: Cumulative Distribution of ISD Ratios at $S_a = 1.8g$</i>	142
5.4.3	<i>Uni-axial Analysis: Multi-record Incremental Dynamic Analysis (MIDA)</i>	144
Chapter 6. Full-Scale Shake Table Validation of the PBSR Methodology		147
6.1	Background on Full-Scale Testing of Wood-Frame Buildings	147
6.1.1	<i>Brief Overview of the NEES-Soft Project</i>	149
6.2	Shake Table Test Setup and Construction of the Test Building	151
6.2.1	<i>Building Details</i>	151
6.2.2	<i>Construction</i>	156
6.3	Installation of Retrofits	160

6.4	Shake Table Test Planning and Preparation	166
6.4.1	<i>Instrumentation</i>	166
6.4.2	<i>Testing Plan and Ground Motion Records</i>	169
6.5	Shake Table Test Results	171
6.5.1	<i>Data Sampling and Analysis</i>	171
6.5.2	<i>White Noise Analysis: Fundamental Period and Intrinsic Damping</i>	172
6.5.3	<i>Global Responses</i>	177
6.5.4	<i>Response of the Retrofit Components</i>	187
6.5.5	<i>Rigidity Level of Diaphragm</i>	193
6.5.6	<i>Energy Distribution</i>	197
6.5.7	<i>Damage Inspection</i>	200
6.6	Comparison of Multi-story and Single-story Retrofit Methods	204
6.6.1	<i>Displacement Profile</i>	204
6.6.2	<i>Energy Distribution</i>	206
Chapter 7.	Collapse Mechanism and Deformation Capacity	209
7.1	Background and Motivation for Full-Scale Collapse Test	209
7.2	Experimental Test Setup, Test Planning, and Feasibility of the Collapse Test	210
7.3	Instrumentation	214
7.4	Ground motions	215
7.5	Numerical Analysis	219
7.6	Experimental Test Results	222
7.7	Comparison of Retrofitted and Un-retrofitted Building	229
Chapter 8.	Summary, Conclusions, Contributions, and Recommendations	232
8.1	Summary	232
8.2	Conclusions	233
8.3	Contributions to Research and Practice in Structural and Earthquake Engineering	235
8.4	Recommendations for Future Research	236
8.4.1	<i>Recommendations for the PBSR Method</i>	236
8.4.2	<i>Recommendations for the Full-scale Shake Table Testing</i>	237
8.4.3	<i>Recommendations for the Isolated Wall Testing</i>	237

References	238
Appendices	250
List of Abbreviations and Acronyms	287

LIST OF TABLES

Table 1-1: Classifications of irregular buildings	6
Table 1-2: Sources of torsional irregularities in buildings due to distribution of SFRS elements ..	8
Table 2-1: Set of scaled 22 earthquake records with corresponding ISD drift ratios for each story	55
Table 2-2: Set of scaled 22 earthquake records with corresponding ISD ratios for each story.....	58
Table 3-1: Stiffness and ISD ratios before and after applying PBSR	70
Table 4-1: Sheathing materials included in the experimental study	89
Table 4-2: Experimental test matrix for 2.44×2.44 m (8×8 ft) wall specimens	92
Table 4-3: CUREE 10-hysteresis parameters for specimens with single sheathing	98
Table 4-4: EPHM 16-hysteresis parameters for specimens with single sheathing	99
Table 4-5: EPHM 16-hysteresis parameters for specimens with combined sheathing	101
Table 4-6: Comparison between backbones from experimental tests and P-807 data	103
Table 5-1: Lateral stiffness and in-plane eccentricities of the 4-story building	116
Table 5-2: PBSR design parameters for the four-story wood-frame building	118
Table 5-3: Distribution of lateral stiffness at each story using PBSR method	121
Table 5-4: Eccentricity and distribution of stiffness at each story in x – direction.....	126
Table 5-5: Eccentricity and distribution of stiffness at each story in y – direction.....	127
Table 5-6: Lateral stiffness and displacement for steel frames – (after Silvia and Badie, 2008) ..	129
Table 5-7: Design parameters and steel sections of the steel special moment frames.....	132
Table 5-8: Hysteretic parameters [*]	135
Table 5-9: PBSR retrofit design details and descriptions.....	137
Table 5-10: PBSR retrofit design details and descriptions of WSP's and ATS rods	139
Table 6-1: Retrofit techniques and design criteria for the four-story building.....	151

Table 6-2: comparison between construction material in archaic building and the test building	155
Table 6-3: Summary of instrumentation of the four-story wood-frame building.....	167
Table 6-4: Test sequences and ground motions used in shake table tests.....	171
Table 6-5: Global response of retrofitted four-story building subjected to ground motion excitations.....	178
Table 6-6: Maximum uplift forces in ATS rods during ground motions at MCE intensity.....	191
Table 6-7: Third story's diaphragm rigidity level for ground motions at MCE intensity.....	195
Table 7-1: Ground motions used in collapse test.....	216

LIST OF FIGURES

Figure 1-1: Damaged and near collapse soft-story wood-frame buildings during the 1989 Loma Prieta earthquake (photos: USGS).	3
Figure 1-2: Soft-story wood-frame buildings in California, USA; (a) Photo by Mikhail Gershfeld, (b) Photo by Steven Pryor.	4
Figure 1-3: Soft (or weak) story classifications: (a) vertical irregularity, (b) torsional irregularity.	5
Figure 1-4: Retrofit methodologies and design approaches.	10
Figure 1-5: Generic multi record incremental dynamic analysis (IDA) plots of a retrofitted building in accordance with: (a) FEMA P-807 guidelines, (b) PBSR methodology.	13
Figure 2-1: N -story building with static eccentricity between centers of mass and centers of rigidity (after Kan and Chopra, 1977).....	27
Figure 2-2: Stiffness matrix for buildings (a) with no symmetry; (b) symmetrical about one axis; (c) symmetrical about both axes (after Shepherd and Donald, 1967).....	28
Figure 2-3: (a) Torsionally coupled N – story building; (b) Plan view of the i^{th} floor.....	35
Figure 2-4: Explanation of period determination based on the target displacement using the displacement response spectrum.....	42
Figure 2-5: Flow diagram of the DBDT (Bahmani et al., 2013)	48
Figure 2-6: A 3-story building with excessive torsion: (a) plan view; (b) elevation view.	51
Figure 2-7: Probability of non-exceedance vs. ISD ratio for a regular 3-story building with linear system.....	52
Figure 2-8: Building with excessive torsion: (a) plan view; (b) elevation view.	53
Figure 2-9: Probability of non-exceedance vs. ISD ratio for a 3-story soft-story building with linear system	54
Figure 2-10: (a) Plan view; (b) distribution of lateral stiffness over height; (c) optimum design.	56
Figure 2-11: Probability of non-exceedance vs. ISD ratio for a 10-story building with non-linear EPP system	57
Figure 2-12: Probability of non-exceedance vs. ISD ratio for a 10-story building with non-linear EPP system (design optimization)	59

Figure 3-1: Flow diagram for PBSR procedure by including torsion.....	67
Figure 3-2: Three-story building retrofitted using PBSR with torsion method: (a) plan view; (b) distribution of lateral stiffness for un-retrofitted building; (c) distribution of lateral stiffness for retrofitted building.	68
Figure 3-3: Probability of non-exceedance vs. ISD ratio: (a) original un-retrofitted building, (b) retrofitted building (elimination of soft-story behavior)	69
Figure 3-4: Translational and torsional displacements in a torsionally unbalanced building: (a) N – story building, and (b) plan view of the j^{th} story.....	72
Figure 3-5: Equivalent SDOF model of multi-story building (Bahmani et al., 2014).....	73
Figure 3-6: Steps for producing inelastic displacement response spectra: (a) seismic hazard map (ASCE 7-10, 2010); (b) elastic acceleration response spectra; (c) elastic displacement response spectra; (d) inelastic displacement response spectra.....	77
Figure 3-7: Flow diagram for PBSR procedure by eliminating torsion.....	81
Figure 4-1: Test setup of the cyclic testing of isolated shear walls at Colorado State University	87
Figure 4-2: Experimental test setup for wall testing at Colorado State University: (a) side view, (b) front view, (c) bottom boundary condition, (d) top boundary condition.	88
Figure 4-3: Displacement-based test protocol used for wall tested at CSU with 0.1 Hz loading rate.....	88
Figure 4-4: Wood framing used for sheathing combination tests: (a) front view elevation, (b) side view elevation.	90
Figure 4-5: Schematic showing the wall sheathing designation for layering.....	91
Figure 4-6: Construction sequence of stucco sheathing: (a) weather barrier layer, (b) wire lath, (c) scratch coat, (d) brown coat, (e) finish coat.	93
Figure 4-7: CUREE ten-parameter hysteretic model (data from Pei and van de Lindt, 2008).	94
Figure 4-8: EPHM sixteen-parameter hysteretic model (data from Pei and van de Lindt, 2008).	95
Figure 4-9: Hysteresis curves of single-layer sheathing specimens for the first set of tests: a) Experimental; and b) EPHM 16-parameter hysteresis fitted to experimental backbone.	96
Figure 4-10: Hysteresis curves of single-layer sheathing specimens for the second set of tests: a) Experimental; and b) EPHM 16-parameter hysteresis fitted to experimental backbone.	97
Figure 4-11: Hysteresis curves of two- and three-layer sheathing specimens: a) experimental; and, b) EPHM 16-parameter hysteresis fitted to experimental backbones.	102

Figure 4-12: Comparison of backbones from the experimental tests and P-807 data: a) gypsum wallboard; b) horizontal wood siding; c) stucco; d) wood structural panel.	104
Figure 4-13: Comparison of average backbones of experimental data for two-layer and three-layer sheathing tests	107
Figure 4-14: Comparison of probability of non-exceedance versus lateral displacement for two-layer and three-layer sheathing tests	110
Figure 4-15: Evaluating the FEMA P-807 combination rules and comparing with combined experimental test data.....	113
Figure 5-1: Floor plans of the four-story wood-frame building: (a) first story, and (b) upper stories.	116
Figure 5-2: Elastic and inelastic displacement response spectra.	120
Figure 5-3: Elastic and inelastic displacement response spectra.	124
Figure 5-4: Elastic and inelastic displacement response spectra.	125
Figure 5-5: Bilinear spring model of steel frames.	129
Figure 5-6: Backbones of steel special moment frames at the first story.	132
Figure 5-7: The ten-parameter hysteretic spring element used in numerical model of WSP and existing wall sheathings.....	133
Figure 5-8: Backbones of HWS and GWB used in the PBSR procedure.	136
Figure 5-9: Backbones of wood structural panels with different nail schedules.	136
Figure 5-10: Detail of PBSR retrofit elements: (a) Plan view of first story, (b) Plan view of upper stories, (c) Steel SMF along longitudinal direction, (d) Steel SMF along transverse direction. .	138
Figure 5-11: Existing wall sheathing in un-retrofitted building: (a) first story, (b) upper stories.	140
Figure 5-12: Numerical validation of the retrofitted building subjected to 22 bi-axial records: Probability of non-exceedance vs. ISD ratio at $S_a = 1.8g$ along: (a) X-direction, (b) Y-direction.	142
Figure 5-13: Numerical validation of the retrofitted building subjected to 44 uni-axial records: Probability of non-exceedance vs. ISD ratio at $S_a = 1.8g$	144
Figure 5-14: Numerical validation of the retrofitted building subjected to 44 uni-axial records: Median multi-record incremental dynamic analysis (IDA).....	146

Figure 6-1: Floor plan views of the four-story test building: (a) first story, and (b) upper stories	152
Figure 6-2: Elevation views of the test building: (a) East view, (b) South view, (c) West view, (d) North view.	153
Figure 6-3: Isometric views of the test building	154
Figure 6-4: Comparison of the architecture for a soft-story wood building (a) in the San Francisco Bay Area, and (b) the test building designed as part of the NEES-Soft project.....	156
Figure 6-5: Construction sequence of the four-story wood-frame building on top of the shake table.	158
Figure 6-6: Position of the four-story building on top of the shake table: (a) plan view, (b) south elevation view (Section A-A), (c) west elevation view (Section B-B).....	159
Figure 6-7: Location of retrofits: (a) first story, (b) upper stories.	160
Figure 6-8: SMF retrofits at the first floor: (a) installation of west span of SMF in Line D, (b) installation of east span of SMF in Line D, (c) West span of SMF in Line D, (d) East span of SMF in Line D, (e) North span of SMF in Line 5; (f) South span of SMF in Line 5; (g) view of SMF installed in Line D from outside of the building.	162
Figure 6-9: Details of steel SMF in Line D along the X-direction	163
Figure 6-10: WSP's at the 2 nd story: (a) Line D, (b) Line 3, (c) intersection of Lines D and 3. .	164
Figure 6-11: Installation of ATS rods: (a) first story A-8, (b) first story A-7, (c) third story A-6 and A-7, (d) close up view of A-6 at 3 rd story, (e) close up view of A-7 at 3 rd story	165
Figure 6-12: First story diaphragm retrofitted with WSP, steel connectors, and metal straps: (a) left side of Line 3, (b) right side of Line 3, (c) Line 3R, (d) steel connectors at left side of Line 3, (e) steel connectors and metal straps at Line 3R	166
Figure 6-13: Location of sensors installed in the first story: (a) accelerometers, (b) string potentiometers.....	168
Figure 6-14: Instrumentations: (a) accelerometers in X- and Y-directions, (b) cameras, (c) linear potentiometer mounted on SMF in Line D, (d) string potentiometer and linear potentiometers at a wall corner; (e) strain gauges mounted on SMF, (f) strain gauges mounted on ATS rod.	168
Figure 6-15: Ground motions and spectral accelerations: (a) spectral acceleration scaled to 1.2g, (b) spectral acceleration scaled to 1.8g, (c) Loma Prieta record scaled to $S_a = 1.8g$, (d) Cape Mendocino record scaled to $S_a = 1.8g$	170
Figure 6-16: Fundamental period of the building and effect of repair.....	174
Figure 6-17: Fundamental period of the building and effect of repair.....	175

Figure 6-18: Intrinsic Damping – White noise test No. 1	176
Figure 6-19: Maximum building displacement profile in X-direction.	179
Figure 6-20: Normalized story shear ($V_{\text{story}}/W_{\text{Total}}$) for the building retrofitted in accordance with PBSR method ($C_{\text{Story}} = V_{\text{Story}}/W_{\text{Total}}$).	181
Figure 6-21: Base shear v.s. roof displacement subjected to: (a) Loma Prieta at DBE, (b) Cape Mendocino-Rio at DBE, (c) Cape Mendocino-Rio at MCE, (d) Loma Prieta at MCE.	181
Figure 6-22: Translational response of the retrofitted building subjected to Cape Mendocino-Rio ground motion at MCE intensity (Seismic Test 3): (a) X-direction, (b) Y-Direction.	183
Figure 6-23: Translational response of the retrofitted building subjected to Loma Prieta-Gilroy ground motion at MCE intensity (Seismic Test 4): (a) X-direction, (b) Y-Direction.	184
Figure 6-24: In-plane translational and torsional displacements of a rectangular-shape diaphragm	185
Figure 6-25: Inter-story rotational response of the building subjected to ground motions scaled to MCE intensity: (a) Cape Mendocino (Test 3), (b) Loma Prieta (Test 4).	187
Figure 6-26: Hysteresis time-history response of the steel SMF along X-direction subjected to the ground motion records at MCE intensity: (a) Cape Mendocino, (b) Loma Prieta.	189
Figure 6-27: Maximum ATS tensile forces when the building is subjected to ground motions at MCE intensity: (a) Cape Mendocino, (b) Loma Prieta.	192
Figure 6-28: Illustration of flexible diaphragm (Figure from ASCE7-10, 2010 – Figure 12.3-1)	194
Figure 6-29: Maximum diaphragm deflection during Cape Mendocino ground motion at MCE (Seismic Test 3)	196
Figure 6-30: Maximum diaphragm deflection during Loma Prieta ground motion at MCE (Seismic Test 4)	197
Figure 6-31: Distribution of energy dissipated at each story subjected to ground motions at MCE intensity: (a) Cape Mendocino, (b) Loma Prieta.	200
Figure 6-32: Typical damage observed in different locations of the building retrofitted with PBSR method.	203
Figure 6-33: Maximum displacement profile the retrofitted building: (a) FEMA P-807 guidelines; (b) PBSR methodology.	205
Figure 6-34: Distribution of energy dissipated at each story subjected to Loma Prieta ground motion: (a) Normalized dissipated energy for FEMA P-807 retrofit, (b) Time-history of absorbed	

cumulative energy for FEMA P-807 retrofit, (c) Normalized dissipated energy for PBSR method, and (d) Time-history of absorbed cumulative energy for PBSR method.....	208
Figure 7-1: Position of the four-story building with its potential collapse area on top of the shake table: (a) plan view, and (b) elevation view (section A-A).	213
Figure 7-2: Instrumentation plan: (a) first story, and (b) fourth story.	215
Figure 7-3: Response spectral accelerations of ground motions scaled to (a) $S_a = 0.4g$; (b) $S_a = 0.9g$; (c) $S_a = 1.2g$; (d) $S_a = 1.8g$; ground acceleration records at MCE intensity for (e) Loma Prieta; (f) Cape Mendocino; (g) Superstition Hills.	217
Figure 7-4: Response spectral displacements of ground motions scaled to (a) $S_a = 0.4g$; (b) $S_a = 0.9g$; (c) $S_a = 1.2g$; (d) $S_a = 1.8g$; ground acceleration records at MCE intensity for (e) Loma Prieta; (f) Cape Mendocino; (g) Superstition Hills.	219
Figure 7-5: Probability of non-exceedance versus inter-story drift ratio of the four-story building subjected to ground motions scaled to different spectral accelerations: (a) $S_a = 0.4g$, (b) $S_a = 0.9g$, (c) $S_a = 1.2g$, and (d) $S_a = 1.8g$	222
Figure 7-6: Time-history of ground motions and corresponding responses of the building during consecutive seismic tests: (a) time-histories of the ground motions, (b) time-history responses of the first story.	224
Figure 7-7: Displacement time-history record of the first story subjected to Superstition Hills earthquake record: (a) Test No. 6, and (b) Test No. 8.	227
Figure 7-8: Collapse sequence of the four-story building (from its east view) subjected to Superstition Hills record at $S_a = 1.8g$ (Test No. 8) – Photo courtesy of Reuters.....	228
Figure 7-9: Photos of the collapsed building: (a) east view, (b) west view, (c) south-west view, and (d) north-east view.	229
Figure 7-10: Comparison of Retrofitted and Un-retrofitted building subjected to ground motions at MCE intensity.	231

Chapter 1. INTRODUCTION

1.1 Motivation for Development of Performance-Based Seismic Retrofit (PBSR)

One of the natural hazards that still threaten human life worldwide is earthquakes because of their unpredictable occurrence and magnitude. In addition, the poor performance of buildings with structural deficiencies during earthquakes leads to economic loss and even fatalities around the world. Although building codes have been modified to improve the performance of buildings and structures when they are subjected to ground motions, earthquakes are still hazardous for older (code-deficient) buildings that were not designed in accordance with modern seismic provisions. These buildings are prone to damage or collapse due to insufficient strength and stiffness of their seismic force resisting system. Furthermore, vertical and torsional (horizontal) irregularities in buildings can lead to excessive deformation and accelerate the collapse of the buildings during a moderate to high intensity earthquake.

U.S. earthquakes such as the 1989 Loma Prieta and 1994 Northridge in California have highlighted the poor performance of a specific class of existing buildings known as soft-story (or weak-story) buildings. These buildings were designed prior to the implementation of modern seismic design codes and are code-deficient. In a soft- or weak-story building, one story (typically the bottom story) has relatively less stiffness or strength compared to other stories. One prevalent types of soft-story building are wood-frame buildings which are typically large multi-family buildings with parking located at the ground level. The existence of thousands of these types of buildings in California has been recognized as a disaster preparedness problem with concerted mitigation efforts underway in many cities throughout the state.

During a moderate to intense earthquake, a soft- or weak-story building can go through large inter-story drifts (ISD) at the level of the soft story with the upper stories almost behaving as a rigid body. The rigid body behavior of the upper stories results in most of the input energy from the ground motion being absorbed by the soft story which can result in significant structural damage. This, in fact, is what leads to collapse of the building in what has been referred to as a soft-story collapse mechanism. Furthermore, in many cases, poor performance of the seismic force resisting system (SFRS) intensifies the irregularity of the building. For example, the strength and stiffness of the SFRS at each story can change due strength and stiffness degradation of the material used in the design and construction of the SFRS. This degradation in stiffness and strength can be addressed by using appropriate structural elements in modeling and analyzing the building. In the case of a lack of information regarding the behavior of the SFRS's elements, experimental testing is an option to obtain the parameters to describe the behavior of the SFRS.

Figure 1-1 presents soft-story buildings that were severely damaged during the 1989 Loma Prieta earthquake. A significant residual inter-story drift (ISD) experienced by the first story (i.e., soft story) during the earthquake can be observed in these photos. Rigid body behavior of upper stories can be seen with relatively less structural damage compared to the first story. This highlights the fact that most of the input energy of the earthquake was dissipated by the softer part of the building (i.e., soft story). In some cases, the building may have significant torsional irregularity (i.e., in-plane eccentricity) in addition to vertical irregularity. This results in an in-plane torsional moment in addition to the lateral seismic force and hence, the building may experience even larger deformations.

Figure 1-2 shows photos of typical existing soft-story wood-frame buildings in the Bay Area, California. It can be seen that both buildings are very similar to the buildings in Figure 1-1 in the way that both have large openings at the first story. It is estimated that approximately 4000 of these buildings exist in San Francisco (CAPSS report, 2010) alone. As will be discussed later in this dissertation, these buildings are prone to severe damage or even collapse during moderate to large earthquakes; therefore, retrofitting these types of buildings is critical to decrease economic losses, prevent fatalities, and ensure resilience.



Figure 1-1: Damaged and near collapse soft-story wood-frame buildings during the 1989 Loma Prieta earthquake (photos: USGS).



Figure 1-2: Soft-story wood-frame buildings in California, USA; (a) Photo by Mikhail Gershfeld, (b) Photo by Steven Pryor.

1.2 Classification of Structurally Deficient Irregular Buildings

The first step in retrofitting structurally deficient irregular buildings is to identify the source of deficiency and categorize the buildings based on the nature and intensity of the deficiencies. The *“Minimum Design Loads for Buildings and Other Structures - ASCE 7-10”* (ASCE, 2010) classifies soft (or weak) story buildings into four major categories with regard to vertical irregularity and two major categories with regard to in-plane horizontal irregularities (i.e., torsional irregularity). Figure 1-3a presents a schematic illustration of a vertically irregular four-story building with a soft (or weak) story at the ground level. Figure 1-3b presents a plan view of story of a torsionally (horizontally) irregular building that lacks enough in-plane torsional stiffness (or strength). Table 1-1 presents soft (or weak) story building classifications based on the ASCE7-10 definition. A building may not only lack stiffness (or strength) in translation in one or more of its stories, but may also lack torsional stiffness (i.e., in-plane eccentricities). Therefore, in order to retrofit this type of building, both lateral stiffness and strength (vertical irregularities) and torsional stiffness and strength (in-plane horizontal irregularities) should be

addressed appropriately. It should be noted that in order to identify a torsionally irregular building according to ASCE7-10, the response of the building is needed. However, the response of an existing building is typically unknown before designing a building or may be difficult to evaluate (i.e., required non-linear time-history analysis). Therefore, in this dissertation in order to define a criterion to identify torsionally irregular buildings without conducting time-history analysis, the in-plane torsional irregularity is defined by obtained the in-plane eccentricities of the building. To do this, the in-plane eccentricities (e_x or e_y) of each story along the two principal axes of the building should be obtained based on the secant stiffness at the pre-defined target inter-story drift (ISD). Then, the ratio of the in-plane eccentricities along the principal axes of the building to the dimension of the building along the same axis (i.e., e_x / L_x or e_y / L_y) can be calculated. If the eccentricity ratios are more than the accidental eccentricity (i.e., 5%) defined by ASCE7-10 (ASCE, 2010), then the building is identified as a torsionally irregular building.

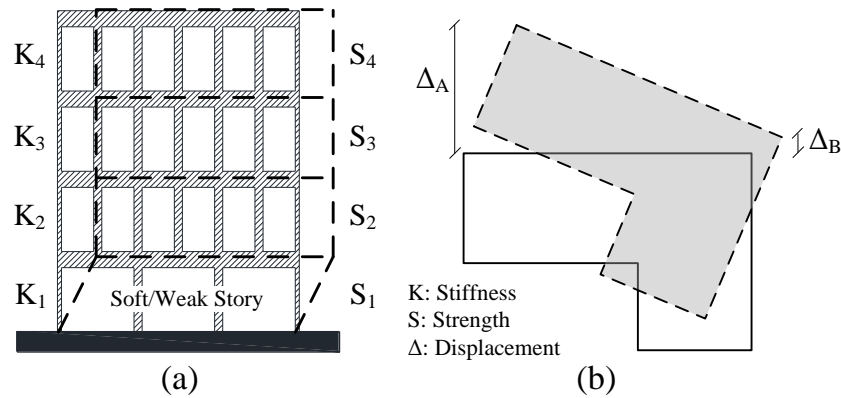


Figure 1-3: Soft (or weak) story classifications: (a) vertical irregularity, (b) torsional irregularity.

Table 1-1: Classifications of irregular buildings

Type of irregularity	Criteria	Structural Description ^(a)
Vertical	Stiffness	Stiffness soft-story
		$K_1 < 0.7 K_2$ OR
		$K_1 < 0.8 \text{ Avg } (K_2, K_3, K_4)$
		Stiffness-extreme soft-story
Vertical	Strength	$K_1 < 0.6 K_2$ OR
		$K_1 < 0.7 \text{ Avg } (K_2, K_3, K_4)$
		Strength weak-story
		$S_1 < 0.8 S_2$
Horizontal	Displacement	Strength-extreme weak-story
		$S_1 < 0.65 S_2$
		Torsional Irregularity
		$\Delta_A > 1.2 \text{ Avg } (\Delta_A, \Delta_B)$
Horizontal	Displacement	Extreme Torsional Irregularity
		$\Delta_A > 1.4 \text{ Avg } (\Delta_A, \Delta_B)$

^(a) See Figure 1-3 for definitions of K, S, and Δ .

1.2.1 Vertical Irregularity

According to ASCE7-10, irregular buildings can be classified into stiffness-soft story and stiffness-extreme soft story buildings. Based on ASCE7-10's definition, the stiffness-soft story is a story in which the lateral stiffness is less than 70% of that in the above story or less than 80% of the average stiffness of the three stories above. Stiffness-extreme soft story is a story whose lateral stiffness is less than 60% of that in the above story or less than 70% of the average

stiffness of the three stories above (Table 1-1). It should be noted that many soft-story wood-frame buildings in the United States fall into the latter category.

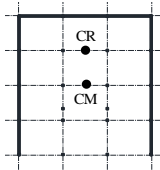

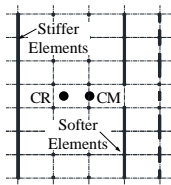
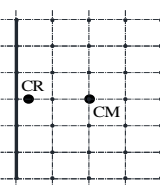
1.2.2 Horizontal (Torsional) Irregularity

In-plane torsional irregularity can occur when the center-of-mass (CM) and center-of-rigidity (CR) of a story do not coincide with one another. This can be caused by any or a combination of the following three factors: (1) irregular distribution of mass in the plane of a story; or, (2) irregular geometry of the floor plan of the story; or, (3) irregular distribution of lateral force resisting elements in the plane of the story. In the majority of buildings, in-plane torsional irregularity is due to the last two factors (i.e., irregular geometry or irregular distribution of lateral force resisting elements). However, in many multi-story residential buildings, the irregular distribution of lateral force resisting elements is the dominant factor causing in-plane irregularity in the buildings since many buildings are geometrically symmetric.

Irregularity in the lateral force resisting system (LFRS) of a story, which is called the seismic force resisting system (SFRS) in earthquake engineering, can be due to either (1) location of the SFRS elements with respect to other elements; or, (2) different relative stiffness (or strength) ratios of the SFRS elements of the story; or, both factors. In a torsionally irregular building due to irregular distribution of lateral force resisting elements, the center of rigidity (CR) of a story moves toward the stiffer part of the story which eventually increases the distance between the CR and center of mass (CM) of the story (i.e., in-plane eccentricity). This in-plane eccentricity causes in-plane torsional moments in addition to lateral loads from seismic excitation and, in some case, increases the lateral displacement of the building at the level of irregularity. Table 1-2

presents buildings with different types of in-plane torsional irregularities due to the location of lateral load resisting elements.

Table 1-2: Sources of torsional irregularities in buildings due to distribution of SFRS elements

Deficient in one direction		Deficient in both directions	
Structural description	Floor plan configuration	Structural description	Floor plan configuration
Soft in translation in one direction and in torsion		Soft in both translational directions and in torsion	
Extremely soft in translation in one direction and in torsion		Extremely soft in both translational directions and in torsion	

1.3 Major Retrofit Methodologies

In order to improve the performance of structurally deficient buildings, several retrofit methodologies have been proposed within U.S. building codes or introduced as guidelines for adoption by governing jurisdictions (International Code Council (2012), ASCE-41 (2014), and FEMA P-807 Guidelines (2012)). The retrofit methodologies differ from one another but all have the objective of improving the building's performance in all earthquakes and reducing the probability of collapse in an extreme earthquake. This can be achieved by increasing the stiffness and strength of the building either by modifying SFRS (e.g., increasing the moment of inertia of columns and beams); or, in some cases, integrating additional elements into the building's SFRS (e.g., steel moment frames), or both. The retrofit methodologies discussed can be categorized into two major groups regardless of the specifics of the technique itself: (1) Single-story retrofit:

this methodology focuses on retrofitting only the structurally deficient story (i.e., soft story) and is typically used if logistical and/or cost constraints are present; and, (2) multi-story retrofit: this methodology intends to improve the overall performance of the building by distributing the seismic demand over the stories.

In the single-story retrofit method, the objective is limiting the retrofit to the deficient story (i.e., soft or weak story) which reduces the cost and time for the retrofit and attempts to eliminate the need for temporary relocation of building occupants. This method is cost effective and improves the performance of the building by increasing the margin against collapse but, in general, the building design may still result in a structure that is below currently acceptable code level and still susceptible to significant damage or even collapse during large earthquakes. In the multi-story retrofit method, the objective is to distribute the seismic demand to the entire building thereby maximizing the margin against collapse. In this method, the cost and time of implementing the retrofits are more than that of the single-story retrofit method and temporary relocation of tenants would typically be needed. However, the building can be shown to perform much better during a large earthquake and the damage and ground motion input energy will be shown to be distributed to all stories thereby reducing the chance of local and global failure in a specific story.

It should be noted that each of these two retrofitting methodologies can be implemented by using either force-based or displacement-based retrofit design approaches. The force-based retrofit design seeks to improve the strength and stiffness of the building so that it can resist the lateral seismic forces defined by current building codes. In other words, the building after applying the retrofit is expected to have enough strength and stiffness to resist seismic forces defined by the building codes. Although this retrofitting method is acceptable, it does not guarantee the

performance of the building subjected to a specific seismic intensity. However, in displacement-based retrofit design, the building should be retrofitted such that the ISD of all the stories does not exceed a specified displacement under a specific seismic intensity in a certain percentage of the time, i.e. probabilistic. This retrofitting method targets the displacement (i.e., lateral or torsional displacements) of the building rather than only its strength and stiffness. Figure 1-4 presents the major categories of retrofit methodologies and retrofit design approaches.

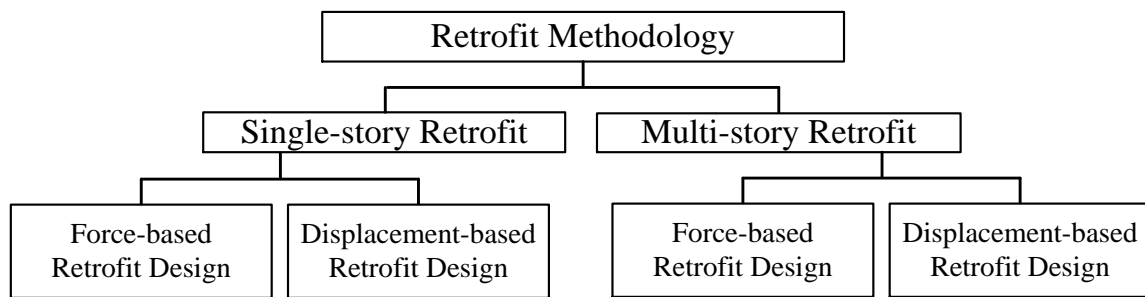


Figure 1-4: Retrofit methodologies and design approaches.

This dissertation focuses on development of a new performance-based seismic retrofit (PBSR) method by limiting the ISD ratios at all stories of a multi-story building to a pre-defined target displacement (Chapter 2 and Chapter 3). However, in order to investigate the difference between the two major retrofit methodologies (i.e., single-story and multi-story retrofit methodologies), the overall performance of a four-story building retrofitted in accordance with the FEMA P-807 guidelines and the PBSR method will be evaluated in Chapter 6 using the data from the experimental shake table tests conducted as part of this study. The first retrofit, which falls into the single-story retrofit category, is the retrofit guideline introduced by the United States Federal Emergency Management Agency (FEMA) through the document entitled “*Seismic Evaluation and Retrofit of Multi-Unit Wood-Frame Buildings With Weak First Stories*” (FEMA P-807,

2012) and the second retrofit is the new PBSR method developed in this dissertation. Both retrofits have advantages and disadvantages which are discussed herein.

1.3.1 FEMA P-807 and PBSR Retrofit Methods

In order to improve the performance of soft-story wood-frame buildings and make retrofitting more affordable and cost effective, the FEMA P-807 guideline has the following advantages: (1) It focuses on placing structural elements for the retrofit in the first story (i.e., soft story) only; (2) it reduces the chance that tenants will be required to relocate during the retrofit; and (3) it focuses on improving the first story performance just enough to prevent collapse while at the same time not over strengthening the bottom story and risk moving the soft-story failure mechanism into the upper stories. There are, however, some disadvantages associated with retrofits designed in accordance with the FEMA P-807 guideline such as: (1) the retrofitted soft-story still experiences the largest inter-story drift compared to other stories and therefore still exhibits soft-story behavior if the seismic intensity increases, which may be problematic if there is a large earthquake with much higher intensity than for which the retrofit was designed; (2) almost all the input energy of the ground motion is absorbed and dissipated by the bottom story. This fact leads to a concentration of damage at the bottom story. This is fine provided the demand does not exceed the capacity, otherwise it may still be dangerous; and (3) the full lateral load resisting capacity of the building is not activated to withstand high intensity earthquakes (i.e., the upper stories do not contribute to dissipate the input energy from the earthquakes).

The second approach is the PBSR methodology which has several advantages: (1) in PBSR, the stiffness and strength of the structure is distributed along its height and in the plane of each story which leads to more homogenous performance during an earthquake; (2) the PBSR method

enables engineers to retrofit buildings based on the performance level expected by the stakeholders, either at code level or with even better performance; (3) all stories can be retrofitted such that they experience approximately the same level of inter-story drift which leads to a homogeneous distribution of force and energy demand over the height of the building and reduces the concentration of damage in any one story. The major disadvantage of PBSR is the cost and time for the retrofit whose benefits will not be realized in small earthquakes but only larger, typically more damaging, earthquakes. It should be noted that PBSR during remodeling or between tenants may be a logical approach.

In order to illustrate the different levels of performance of a retrofitted building with a soft first story, a multi-record incremental dynamic analysis (IDA) can be applied (Vamvatsikos and Cornell, 2002). In IDA, a suite of earthquake records were scaled to a range of ascending spectral accelerations and then is applied to the numerical model of the structure. The response of the structure is then recorded and plotted against the spectral acceleration. The type of the response can be force- or displacement-based; however, in performance-based design the displacement response of the structure is often shown as an inter-story drift (ISD) ratio in IDA plots, since displacement is a key engineering demand parameter in that approach.

Figure 1-5a and Figure 1-5b present conceptual multi-record IDA's for a four-story building retrofitted using FEMA P-807 and the PBSR approach, respectively, based on observation of previous analyses results. It can be seen from Figure 1-5a that the building retrofitted using FEMA P-807 still demonstrates a soft-story behavior (since it is still code deficient) but with an acceptable range of inter-story drift at an intensity of 50% MCE. The upper stories behave almost like a rigid body with small ISD ratios compared to the first story. Furthermore, it can be seen that the first story can experience a large ISD ratio at MCE level increasing the probability

of collapse of the retrofitted building at this level of seismic intensity. However, Figure 1-5b presents a generic multi-record IDA of the same building retrofitted using PBSR method. It can be seen that the maximum ISD ratio at MCE intensity is in the acceptable range and close to the target performance criteria. All the stories experience almost the same ISD ratio confirming the distribution of force and energy all over the building. It can also be seen that the IDA plots are very close to straight lines. This shows that all the stories not only experience approximately the same inter-story drift ratios, but also they go through approximately the same ISD ratio over a range of spectral accelerations which leads to consistent performance for the suite of earthquakes with different spectral accelerations. Furthermore, this feature emphasizes the distribution of seismic demand over the entire building which results in avoiding concentration of damage in anyone story.

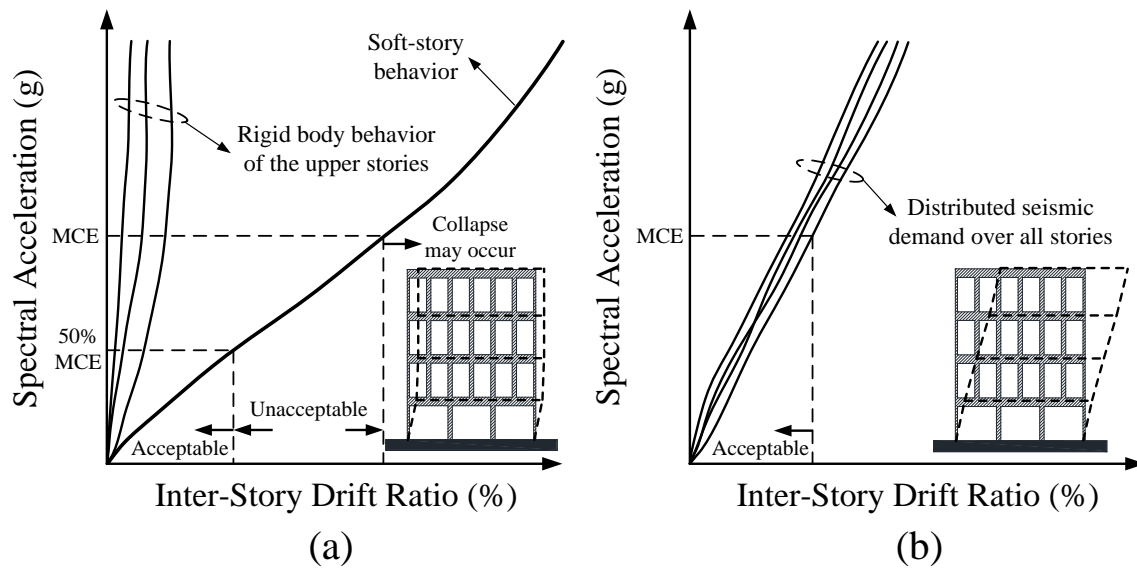


Figure 1-5: Generic multi record incremental dynamic analysis (IDA) plots of a retrofitted building in accordance with: (a) FEMA P-807 guidelines, (b) PBSR methodology.

1.4 Objectives of this Dissertation

The basic concept and research method of the doctoral dissertation entitled: “*Performance-Based Seismic Retrofit (PBSR) Methodology for Multi-Story Buildings with Full-Scale Experimental Validation*” is presented herein. In this dissertation the state-of-the-art methods in displacement-based design (DBD) and direct displacement design (DDD) methodologies are presented; the deficiencies in the current DBD and DDD methods for irregular buildings are addressed, and the new PBSR method for retrofitting multi-story buildings is proposed and validated numerically and then experimentally by testing a full-scale four-story soft-story wood-frame building on a large outdoor uni-axial shake table at the Network for Earthquake Engineering Simulation (NEES) at the University of California - San Diego laboratory.

The main goal of this study was to develop and validate a new performance-based seismic retrofit (PBSR) methodology to retrofit vertically and horizontally irregular buildings thereby providing a mechanism by which to reduce the seismic risk of at-risk wood-frame buildings in the United States. In order to achieve this goal the following objectives are defined in this dissertation and achieved during the course of this study:

- 1) Generalization of displacement-based design method for buildings with some level of in-plane torsional irregularities (DBDT).
- 2) Apply the DBDT concept in the development of the new PBSR method for retrofitting irregular buildings and simplifying the PBSR method to make it easier to be used by practitioners.

- 3) Identifying the hysteretic parameters of seismic force resisting elements in existing wood-frame buildings suitable for use in the PBSR (and other design) methods.
- 4) Examine practical retrofitting techniques for applying the PBSR methodology to buildings with strength and stiffness deficiencies (e.g., soft-story buildings).
- 5) Validate the proposed PBSR methodology numerically using non-linear time history analysis (NLTHA) and experimentally by conducting a series of full-scale shake table tests on a four-story wood-frame building with vertical and horizontal irregularities.
- 6) Develop a better understanding of the collapse mechanism and deformation capacity of soft-story wood-frame buildings during earthquakes.
- 7) Produce a landmark dataset for use by researchers and practitioners in soft-story wood-frame research.

1.5 Organization of This Dissertation

This dissertation is organized into eight chapters in order to address the objectives and goals of this study. This chapter states the structural deficiencies that many existing buildings have due to translational and torsional stiffness (or strength) deficiencies, introduces the performance-based seismic retrofit methodology as a new method of retrofitting these types of buildings, and addresses the main objectives of this study.

In Chapter 2 entitled “*Performance-Based Seismic Design (PBSD) Development for torsionally irregular buildings*” a background of performance-based design (PBD) and direct displacement design (DDD) is presented and their advantages are discussed. It is shown that the displacement-

based design (DBD) and DDD methodologies, in its current status, do not address the design of buildings with torsional irregularities. Then, the full details of the displacement-based design of buildings with in-plane torsional irregularities (i.e., DBDT) methodology is presented in this chapter. Several illustrative examples are presented to numerically validate the DBDT. This chapter addresses the first objective of this dissertation.

In Chapter 3 entitled “*Performance-Based Seismic Retrofit (PBSR) Development*” the PBSR method is developed based on the DBDT method to include the torsional response of an existing building that has torsional irregularity even after applying the retrofit. The PBSR method is then simplified to eliminate the torsional response of retrofitted building by using the first translational mode shape and distributing the retrofit elements over the plane of each story. This chapter addresses the second objective of this dissertation.

In Chapter 4 entitled “*Isolated Wood-Frame Wall Tests*” an experimental and numerical assessment of wood-frame sheathing layer combinations for use in performance-based design and performance-based seismic retrofit is presented. The results of the study presented in this chapter was used in the design of retrofit and numerical modeling of a four-story wood-frame building retrofitted using simplified PBSR method which eventually was built and tested at NEES at University of California-San Diego. The third objective of this dissertation is addressed in this chapter.

Chapter 5 entitled “*Numerical Validation and Retrofit Design of a four-Story Soft-Story Wood-Frame Building using simplified PBSR Method*” focuses on the retrofit design of a four-story wood-frame building with extreme soft-story at its first floor and high level of torsional irregularities by applying the simplified PBSR method proposed in Chapter 3. Furthermore,

practical techniques for retrofitting wood-frame buildings are presented in this chapter. This chapter addresses the fourth and fifth objectives of this study.

Chapter 6 entitled “*Full-Scale Shake Table Validation of the PBSR Methodology*” presents the test planning and setup, building detailing, and the results of the full-scale shake table test of a four-story wood-frame building retrofitted with steel special moment frames and wood structural panels by applying the PBSR method. The fifth and seventh objectives of this dissertation are addressed in this chapter.

Chapter 7 entitled “*Collapse Mechanism and Deformation Capacity*” presents the result of a series of shake table tests conducted on the un-retrofitted soft-story four-story building to obtain the deformation capacity and collapse mechanism of these types of building during large earthquakes. These series of tests was conducted and the performance of the building was evaluated to achieve the sixth and seventh objectives of this dissertation.

Chapter 8 entitled “*Summary, Conclusions, Contributions, and Recommendations*” summarizes the research work completed in this study, mentions the contributions to the structural engineering research and practice, and finally suggests recommendations for future research in improving the PBSR method.

Chapter 2. PERFORMANCE-BASED SEISMIC DESIGN (PBSD) DEVELOPMENT FOR TORSIONALLY IRREGULAR BUILDINGS

2.1 Performance-Based Design (PBD)

Within the structural engineering community there is some consensus that future engineering design methodologies will be based on multiple performance levels. In current design methodologies, the design criteria are either based on limiting stress or forces in structural members and connectors to prevent their failure or limiting deformation for serviceability, or both. Traditional design criteria limit the flexibility and efficiency of a structural seismic design since they cannot explicitly account for performance, making damage and loss analysis, and applying financial constraints difficult when designing new structures. These deficiencies in traditional design methods led to a new design philosophy known as performance-based design (PBD). This new design philosophy seeks to incorporate multiple and comprehensive performance levels explicitly into the design procedure and allows structures to be designed according to stakeholder expectations.

The first effort in standardizing a performance-based approach was led by the Federal Emergency Management Agency (FEMA) through the Applied Technology Council in the ATC-33 (1992) project entitled “*Development of national consensus guidelines for the seismic retrofit of buildings*”, with the objective of quantifying performance levels that can be related to specific design parameters. In 1995, the Structural Engineers Association of California (SEAOC) initiated the Vision 2000 project with the objective of applying performance-based seismic design to the design of new buildings. That project sets a framework for seismic design of buildings with multiple performance levels. About the same time, FEMA published a new

document entitled “*NEHRP Recommended Provisions for the Development of Regulations for New Buildings and NEHRP Maps*” (FEMA 222A, 1995).

Performance-based seismic design (PBSD) was developed with the objective of designing buildings that can satisfy specified performance criteria during different levels of seismic intensity. Whittaker et al. (1998) performed non-linear dynamic analyses for a single-degree-of-freedom (SDOF) system that was designed using performance-based design methodologies and subjected to different levels of earthquake intensities. They applied the non-linear static procedure proposed by FEMA 273 (1997) to design a bi-linear building with the assumption that inelastic displacements of a building can be estimated using the results of linear analysis. They have found that the FEMA 273 assumption is conservative for bi-linear structures with strength ratio greater than 0.20 and elastic periods greater than the characteristic site period, but unconservative for other structures.

A performance-based plastic design procedure for steel moment frames was presented later by Leelataviwat et al. (1999). In their research, the role of plastic analysis in seismic design of structures was investigated. They concluded their new design method eliminates the drift check after designing the building and also eliminates the use of response modification factor in design since it is inherently used in the design procedure. Priestley (2000) investigated and compared three methods that have been used in traditional force-based and the performance-based seismic design of structures. He showed that in the force-based design procedures additional check on displacement limits and damage was required; however, the performance-based design approach eliminates this requirement. In addition, it was shown that performance-based design can be used for structures with non-standard hysteretic characteristics and for variation of seismic intensity for a specific design.

By 2002, numerous papers began to appear proposing the use of PBSD in the design of different types of structures. Grierson et al. (2002) conducted pushover analysis to design steel structures using a PBSD approach and Filiatrault et al. (2002) applied PBSD to wood-frame structures by employing non-linear time history analysis using hysteretic parameters of wood shear walls developed as part of CUREE-Caltech project (Folz and Filiatrault, 2001). Foschi et al. (2003) conducted reliability analysis in the performance-based design of wood shear walls using a neural network approach. A neural network approach was applied to identify the optimal nail spacing for a given wall configuration in order to achieve a desired reliability index for a single transient drift requirement.

Furthermore, statistical and probabilistic approaches were also used to investigate the performance-based seismic design concept. Rosowsky and Ellingwood (2002) utilized a fragility analysis methodology for wood-frame structures. Their method is applicable to all types of loading and was later presented for wind loading (Ellingwood et al., 2004). Van de Lindt et al. (2008) integrated a system identification concept to the performance-based seismic design for wood-frame buildings. Their approach was found to work well for wood-frame structures and showed promise for extension to more complicated structures with different performance measures.

Performance-based seismic design has also been applied to reinforced concrete and bridges. Tayebi et al. (2003) discovered high correlation between the drift and spectral acceleration at the fundamental period of reinforced concrete and steel moment frame structures. The Pacific Earthquake Engineering Research Center (PEER) implemented a performance-based design concept in bridge engineering through the PEER 312 Project (Mackie and Stojadinovic, 2003). In that project, highway bridges in California were examined in order to find a relationship

between earthquake intensity and structural demand. Furthermore, the PEER investigated the resiliency of communities by evaluating existing structures using performance-based engineering concept (Mieler et al., 2013). Although just a sample of PBSO studies is presented herein, the larger body of literature, including practice-based ideas for development and integration (Hamburger, 2002 and Hamburger et al., 2002), led to development of Performance-based Seismic Design Guidelines through the ATC-58 (2006) project sponsored by FEMA.

The concept of performance-based seismic design is somewhat established, however, a simple and practical procedure for designing a new structure or retrofitting an existing one with specific performance criteria under seismic load had not been agreed upon as of 2003. In order to address this issue, direct displacement design (DDD) and performance-based seismic retrofit (PBSR) emerged in the engineering practice and research communities. These two methods branched out from the performance-based design (PBD) methodology with the objective of proposing practical design and retrofit procedures for buildings to meet specific performance criteria during earthquakes. The rest of this chapter is dedicated to introduce the state-of-the-art development on these two methods. Section 2.2 presents a brief introduction to the existing DDD method which has been developed for torsionally symmetric buildings; then, it introduces the displacement-based design for torsionally unbalanced buildings (i.e., DBDT) which is developed as part of this doctoral dissertation. This method has been validated numerically through non-linear time history analysis. Chapter 3 presents a summary of the performance-based seismic retrofit methodology; then, outlines a simple but effective and practical procedure for retrofitting buildings in order to meet the pre-defined performance criteria. This method was validated numerically using non-linear time-history analysis and then verified experimentally through a full-scale shake table testing of a four-story wood-frame building (see Chapter 5 and 6).

2.2 Displacement-Based Design of Buildings with Torsion (DBDT)¹

2.2.1 *Direct Displacement Design (DDD)*

There have been numerous proposals for performance-based seismic design (PBSD) approaches with one that received more attention than others, namely the direct displacement design (DDD) procedure. DDD is a procedure that allows one to distribute the forces induced by an earthquake to the levels of a multi-story building to ensure the desired level of inter-story drift is not exceeded. DDD was first proposed for designing reinforced concrete structures by Priestley (1998). The methodology was developed for application to precast/prestressed concrete buildings (Priestley 2002) and was later modified and applied to multi-story light-frame wood buildings by Filiatrault and Folz (2002). Pang and Rosowsky (2007) built on the work of Priestley (1998) and Filiatrault and Folz (2002) to eliminate the need for iteration which was originally needed to accurately determine the correct level of total damping in the system. Finally, Wang et al. (2010) extended the work of Pang et al. to allow correction as a function of building height. The approach was validated based on a six-story wood-frame shake table test program (van de Lindt et al., 2010) by Pang et al. (2010).

Direct displacement design in its present form provides a simple and effective procedure to ensure a multi-story building meets the desired inter-story drift requirements when subjected to a specified seismic intensity. This procedure allows one to consider the stiffness and strength degradation during non-linear response at the designated inter-story drift level. However, to date, DDD has only been able to be applied to buildings that do not exhibit significant torsional response which has been perhaps the only drawback. In buildings with no in-plane irregularities,

¹ Bahmani, P., van de Lindt, J., and Dao, T. (2013). "Displacement-Based Design of Buildings with Torsion: Theory and Verification." *ASCE J. Struct. Eng.*, Jun. 17, 2013. DOI 10.1061/(ASCE)ST.1943-541X.0000896 , 04014020.

the displacement at each story is caused by lateral forces applied at the level of the story; however, in buildings with in-plane irregularities, the displacements are not only due to lateral forces but also due to torsional moments at each story. In the aforementioned DDD approach, the displacements are considered to be pure translation which may lead to an unconservative design in certain cases.

In this chapter, DBD is generalized for buildings with in-plane asymmetry by applying an approach to decouple the torsional and translational modal contributions to the total deformation that was originally formulated by Kan and Chopra (1977) for linear systems. In that approach vibration periods and mode shapes of a torsionally coupled building were approximated as a linear combination of uncoupled mode shapes resulting from modal analysis of the corresponding torsionally uncoupled system (i.e., the same building with coincident center of mass and center of rigidity). Kan and Chopra showed that decoupling torsional mode shapes from translational mode shapes leads to a simpler procedure for analyzing the response of torsionally coupled buildings with what they felt was an acceptable level of accuracy.

The new displacement-based design with torsion (DBDT) proposed in this study is validated using detailed finite element models of asymmetric buildings and found to accurately reproduce the desired dynamic structural properties. Both linear and non-linear systems are demonstrated and the accuracy verified. The method is shown to be very accurate for linear systems and slightly conservative for non-linear systems.

2.2.2 Displacement-Based Design Procedure with Torsion (DBDT)

The method proposed herein can be employed to design buildings with in-plane irregularity and discontinuity in lateral strength (i.e., soft or weak story) in order to meet the desired performance

criteria and will be verified for linear and non-linear building systems using a 3-D finite element model. The performance criterion in this study is defined by a limiting inter-story drift ratio calculated at the center of mass of each story. The approach presented is a basic, yet accurate, method to determine the required distribution of lateral and torsional stiffness at each story based on the location and relative stiffness ratio of lateral load resisting elements (i.e. shear walls, moment-resisting frames, etc.), such that the building meets the desired performance level at the specified seismic intensity. In this study, the in-plane irregularity that is due to an unsymmetrical distribution of lateral load resisting elements in the plane of each story is investigated but irregularity in the distribution of mass is not covered in the proposed approach.

The relative stiffness ratio over the height of building can be estimated by distributing the lateral stiffness of each story in proportion to the sum of the forces acting at each story and the stories above if only the first translational mode of vibration is considered (i.e., the same procedure that is used in the equivalent lateral force procedure with the exception of using a ratio rather than actual values). The relative stiffness ratios within the plane of each story of the building can be approximately determined by computing the relative length ratio of shear wall elements or member size that may be obtained from architectural drawings, in reinforced concrete and wood-frame buildings. In steel braced frame buildings, the relative stiffness ratio can be found by calculating the length of bracing. One limitation of the approach is that the member sizes in steel and reinforced concrete moment frames cannot be obtained by employing this method of distributing stiffness ratios. It should be mentioned that one can change the relative stiffness ratios over the height of the building and in-plane of each floor to achieve the optimum design. For reinforced concrete (RC) structures, once the dimensional design has been achieved by this

method, the detailing for each member can be specified by traditional RC design using the internal forces carried by that member.

In direct displacement design (DDD), the stiffness of each lateral load resisting element has to be defined such that the desired performance level can be achieved at a certain seismic intensity level (e.g., design basis earthquake (DBE) or maximum considered earthquake (MCE) level). The method presented herein differs from previous work in that it is the first time that the distribution of the stiffness of lateral load resisting system of a torsionally unbalanced building can be computed and designed with DDD, thereby ensuring the maximum inter-story drift experienced by the structure is less than the pre-defined target inter-story drift. For a symmetrical building (i.e., no torsion), only the distribution of the lateral stiffness over the height of the building has to be determined; whereas, in an unsymmetrical building (i.e. torsionally coupled building) the lateral stiffness must be defined both in the plane of each story (i.e., the location of walls in the plan view) and over the height of the building.

2.2.2.1 Modal Analysis for Torsionally Coupled Buildings

One way to analyze the response of buildings under earthquake excitation is to conduct modal analysis which is a very simple yet accurate and reliable method. If the response of the building is dominated by the first few modes, the results from modal analysis based on the first few modes will be accurate enough and the contribution of the higher modes in overall response of the structure can be eliminated. Modal analysis can be employed in order to calculate the displacements of a building due to lateral forces and torsional moments under ground motion excitation. The advantage of modal analysis over time-history analysis is that it can be conducted simply by determining the global mass and stiffness matrices of the structure. The maximum

responses, then, can be obtained by means of the pseudo-acceleration response spectra for the region where the building is located. However, for a torsionally coupled system, calculating the global stiffness matrix is cumbersome which leads to the need to solve a high order eigenvalue problem. A method was proposed by Kan and Chopra (1977) in order to decouple the torsional and translational mode shapes and combine the uncoupled modal displacements to obtain the total displacements. This method of decoupling the torsional and translational mode shapes is applied herein with DDD.

By decoupling torsional modes from translational modes, the size of stiffness matrices reduces from $3N \times 3N$ to $N \times N$ for an N – story building. In addition, there is then no need to define the coupled stiffness terms in the global stiffness matrix and the order of eigenvalue problem reduces which make it more feasible to perform modal analysis. The response of the building due to each mode shape can be determined by using the displacement response spectra. The final response is then, of course, determined using the well-known Square-Root-of-Sum-of-Squares (SRSS) or Complete Quadratic Combination (CQC) methods.

In the DDD method, the stiffness matrices must be determined such that the desired target inter-story drift is not exceeded after combining the inter-story drifts due to all modal responses. However, the individual stiffness of the lateral load resisting elements are unknown which leads to a trial-and-error process in performing modal analysis for DDD. Furthermore, as will be shown later, the global stiffness matrix for a torsionally unbalanced building consists of coupled and uncoupled stiffness terms which make the analysis and therefore the design procedure significantly more complex. The method proposed herein, overcomes these problems by decoupling the translational and torsional mode shapes and then, conducting modal analysis assuming fixed mass-to-stiffness ratios at each story and fixed relative stiffness ratios of lateral

2.2.2.2 Equation of Motion

27

The global stiffness matrices for several different types of buildings are presented in Figure 2-2. Specifically, Figure 2-2a shows a typical stiffness matrix shape for an unsymmetrical (or torsionally unbalanced) building. Figure 2-2b and Figure 2-2c present the stiffness matrices of buildings which are symmetrical about one or both principal axis of the building. As mentioned earlier, the stiffness matrix for an unsymmetrical building is $3N \times 3N$ (three degrees of freedom at each story) which consists of pure translational and torsional stiffness terms as well as coupled stiffness terms (off-diagonal terms).

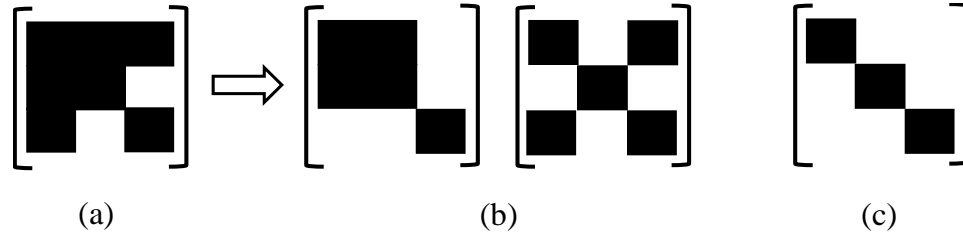


Figure 2-2: Stiffness matrix for buildings (a) with no symmetry; (b) symmetrical about one axis; (c) symmetrical about both axes (after Shepherd and Donald, 1967)

2.2.2.3 Decoupling torsional and translational mode shapes

In general, the equation of motion for an undamped coupled system can be expressed as (Kan and Chopra, 1977):

$$\begin{bmatrix} M & & \\ & M & \\ & & M \end{bmatrix} \begin{bmatrix} \ddot{U}_x \\ \ddot{\tilde{U}}_\theta \\ \ddot{U}_y \end{bmatrix} + \begin{bmatrix} K_{xx} & K_{x\theta} & 0 \\ K_{x\theta}^T & K_{\theta\theta} & K_{y\theta}^T \\ 0 & K_{y\theta} & K_{yy} \end{bmatrix} \begin{bmatrix} U_x \\ \tilde{U}_\theta \\ U_y \end{bmatrix} = \begin{bmatrix} -M \bar{1} \ddot{U}_{gx} \\ 0 \\ -M \bar{1} \ddot{U}_{gy} \end{bmatrix} \quad (2-1)$$

where, U_x , \tilde{U}_θ , and U_y are the displacement sub-vectors. \ddot{U}_{gx} and \ddot{U}_{gy} are ground acceleration sub-vectors in x - and y -directions, respectively. M and K are mass and stiffness sub-matrices, respectively. The sub-matrices and sub-vectors are presented in detail in Appendix A.

The mode shapes and their corresponding vibration frequencies of the N – story building shown in Figure 2-1 can be obtained by solving the following eigenvalue problem of order $3N$:

$$([K]_{3N \times 3N} - \omega^2 [M]_{3N \times 3N}) [\Phi]_{3N \times 1} = [0]_{3N \times 1} \quad (2-2)$$

$$\begin{bmatrix} K_{xx} - \omega^2 M & K_{x\theta} & 0 \\ K_{x\theta}^T & K_{\theta\theta} - \omega^2 M & K_{y\theta}^T \\ 0 & K_{y\theta} & K_{yy} - \omega^2 M \end{bmatrix} \begin{bmatrix} \Phi_x \\ \Phi_\theta \\ \Phi_y \end{bmatrix} = \begin{bmatrix} 0 \\ 0 \\ 0 \end{bmatrix} \quad (2-3)$$

where Φ_x , Φ_θ , and Φ_y are the mode shape vectors ($N \times 1$ vectors) and ω represents the vibration frequencies. It can be seen that the global stiffness matrix, $[K]_{3N \times 3N}$, can be divided into two sub-matrices: K_{UC} which only consists of uncoupled stiffness terms (diagonal terms); and, K_C which only includes coupled stiffness terms (off-diagonal terms); therefore, the eigenvalue problem can be expressed as

$$([K_{UC}]_{3N \times 3N} + [K_C]_{3N \times 3N} - \omega^2 [M]_{3N \times 3N}) [\Phi]_{3N \times 1} = [0]_{3N \times 1} \quad (2-4)$$

where,

$$[K_{UC}]_{3N \times 3N} = \begin{bmatrix} K_{xx} & 0 & 0 \\ 0 & K_{\theta\theta} & 0 \\ 0 & 0 & K_{yy} \end{bmatrix}; [K_C]_{3N \times 3N} = \begin{bmatrix} 0 & K_{x\theta} & 0 \\ K_{x\theta}^T & 0 & K_{y\theta}^T \\ 0 & K_{y\theta} & 0 \end{bmatrix}$$

For a torsionally uncoupled system (i.e., $e_y = e_x = 0$), the equation of motion can be divided into three sub-equations since three displacement components (x, y, θ) are independent from each

other (i.e., uncoupled system). The global eigenvalue problem can then be expressed as three sets of eigenvalue problems of order N .

$$\left([K_{xx}]_{N \times N} - \omega_x^2 [M]_{N \times N} \right) [\psi_x]_{N \times 1} = [0]_{N \times 1} \quad (2-5)$$

$$\left([K_{\theta\theta}]_{N \times N} - \omega_\theta^2 [M]_{N \times N} \right) [\psi_\theta]_{N \times 1} = [0]_{N \times 1} \quad (2-6)$$

$$\left([K_{yy}]_{N \times N} - \omega_y^2 [M]_{N \times N} \right) [\psi_y]_{N \times 1} = [0]_{N \times 1} \quad (2-7)$$

Kan and Chopra (1977) showed that mode shapes and vibration frequencies of torsionally coupled systems can be presented in terms of mode shapes and vibration frequencies of the corresponding torsionally uncoupled system (i.e. the same building but with $e_y = e_x = 0$) with the help of perturbation theory (Wilkinson, 1965), where the modes shapes and vibration frequencies of the corresponding torsionally uncoupled system can be obtain by solving Equations 2-5, 2-6, and 2-7. It was shown that the proposed method by Kan and Chopra results in an exact solution for a particular class of buildings which satisfy the following conditions:

- a) The principal lines of resistance for all the stories are oriented along the x - and y -axes;
- b) The center of mass of all floors are located at one vertical axis;
- c) The center of rigidity of all stories lies on one vertical axis, i.e. in-plane eccentricities (e_x and e_y) are the same for all the stories;
- d) All the floors have the same radius of gyration about the vertical axis through the center of mass of the floors;

e) The ratio of the following three stiffness quantities are the same for all the stories:

$$\rho_y = \frac{K_{y,i}}{K_{x,i}}, \rho_\theta = \frac{K_{\theta,i}}{r^2 K_{x,i}}$$

where r is the radius of gyration of the floor about a vertical axis through the center of mass of the floor.

However, they also showed that if the building does not satisfy the last three restrictions, the method is still valid and the error of the approximate solution is in the range of acceptable error for design of buildings. The error becomes larger for higher vibration frequencies which are known to have a smaller effect on the response of the building. It should be noted that the proposed method results in larger error if the first two restrictions are not satisfied. Therefore, the approach is folded into DBD since the first two requirements above are satisfied for the vast majority of realistic building designs.

According to the method proposed by Kan and Chopra, the vibration modes of a torsionally coupled building can be approximated by the following form:

$$[\Phi]_{3N \times 1} \cong \begin{bmatrix} \alpha_x \psi_x \\ \alpha_\theta \psi_\theta \\ \alpha_y \psi_y \end{bmatrix} \quad (2-8)$$

where α_x , α_θ , and α_y are modal coupling parameters and ψ_x , ψ_θ , and ψ_y are mode shapes of the corresponding torsionally uncoupled building which have been normalized such that $\psi_l^T M \psi_l = 1$ where l corresponds to x -, θ -, or y -direction. The modal coupling parameters

can be found by determining the mode shapes and corresponding vibration frequencies of an associated one-story system.

In the associated one-story building method, an N –story building should be divided into N groups of three uncoupled vibration mode shapes along the x –, θ –, and y –directions. Therefore, the j^{th} story can be presented by the j^{th} group of three uncoupled vibration modes that are $\psi_{x,j}$, $\psi_{\theta,j}$, and $\psi_{y,j}$. The modal coupling parameters for the j^{th} group of the three uncoupled vibration mode shapes are the mode shapes of the j^{th} associated one-story building that can be obtained by solving the following eigenvalue problem:

$$\begin{bmatrix} K_x - \omega^2 m & -\frac{e_y}{r} K_x & 0 \\ -\frac{e_y}{r} K_x & K_\theta - \omega^2 m & \frac{e_x}{r} K_y \\ 0 & \frac{e_x}{r} K_y & K_y - \omega^2 m \end{bmatrix}_j \begin{bmatrix} \alpha_x \\ \alpha_\theta \\ \alpha_y \end{bmatrix}_j = \begin{bmatrix} 0 \\ 0 \\ 0 \end{bmatrix} \quad (2-9)$$

where, m is the mass of the j^{th} floor; r is the radius of gyration of the j^{th} floor about a vertical axis through the center of mass; K_x and K_y are the translational stiffness of the j^{th} story along the x – and y –directions, respectively; K_θ is the torsional stiffness of the j^{th} story divided by r^2 ; e_x and e_y are the eccentricities in x – and y –directions between the center of rigidity and the center of mass of the j^{th} story, respectively. The stiffness terms in Equation 2-9 can be calculated as follows,

$$K_x = \omega_{x,j}^2 m; K_\theta = \omega_{\theta,j}^2 m; K_y = \omega_{y,j}^2 m$$

where, $\omega_{x,j}$, $\omega_{\theta,j}$, $\omega_{y,j}$ are the j^{th} vibration frequencies in x -, θ -, and y -directions, respectively, that can be found by solving the eigenvalue problems presented in Equations 2-5, 2-6 and 2-7.

Once the vibration modes and the corresponding modal coupling parameters (i.e. α_x , α_θ , and α_y) are found, the absolute displacements, relative to the ground, due to earthquake ground motion along the principal axes of resistance of the building can be calculated using a standard procedure (Clough and Penzien, 1975),

$$u_{l,nj} = \alpha_{l,nj} L_j \frac{S_a(\omega_{nj}, \xi)}{\omega_{nj}^2} \Phi_{nj} \quad (2-10)$$

where, the eigenvectors $\alpha_{l,nj}$ and Φ_{nj} have been normalized such that $\alpha_{l,nj}^T \alpha_{l,nj} = 1$ and $\Phi_{nj}^T M \Phi_{nj} = 1$. The modal participation factor for the j^{th} associated one-story building, L_j , can be obtained using Equation 2-11,

$$L_j = \psi_{l,j}^T m \bar{1} \quad (2-11)$$

where l is the direction of the ground motion excitation that can be either along the x - or y -direction; and, $\psi_{l,j}$ is the j^{th} mode of vibration in l -direction of the corresponding torsionally uncoupled system, and $\bar{1}$ is a $N \times 1$ identity vector.

2.2.2.4 Standard mode shapes

Modal analysis cannot be performed without knowing the global stiffness matrix. In the DBD procedure the stiffnesses of the lateral load resisting system are being sought which eventually

leads to an iteration process for the stiffness matrix during the design. In order to eliminate the iteration process in conducting modal analysis, the vibrational mode shapes of the building should be standardized in such a way that their shape (but not their amplitude) are independent of the stiffness matrix of the building. In other words, the ratios of the modal values at each mode remain constant but the values themselves depend on the actual stiffness and mass of the building. This can be achieved by assuming that the mass-to-stiffness ratio over the height of the building and relative stiffness ratios of lateral load resisting elements at each floor remain constant during the analysis. In this case, according to Equations 2-5 to 2-7, the eigenvalue problems results in only one set of mode shapes since the stiffness ratio and mass ratio matrices assume to be constant during the analysis. The optimal design of the building can be achieved by selecting appropriate mass-to-stiffness ratios (over the height and in-plane) such that all stories experience almost the same inter-story drifts. This method will be discussed in Section 2.2.4.3.1.

One may consider a torsionally coupled N –story building shown in Figure 2-3. The circular vibration frequencies (i.e., ω) and mode shapes (i.e., ϕ) of the building can be determined by solving the following eigenvalue problem:

$$([K] - \omega^2 [M]) [\Phi] = [0] \quad (2-12)$$

where, $[K]$ and $[M]$ are global stiffness and mass matrices of the building, respectively. After decoupling translational and torsional mode shapes following the method described earlier in Section 2.2.2.3, the eigenvalue problem can be expressed as

$$([K]_t - \omega^2 [M]_t) [\Phi]_t = [0] \quad (2-13)$$

where, $[K]_l$ and $[M]_l$ are stiffness and mass matrices in l direction which can be substituted by x , y or θ .

In order to simplify the modal analysis and eliminate the iteration process during modal analysis, the mass and stiffness matrices in Equation 2-13 should be determined such that the vibrational mode shapes of the building become independent of the actual value of stiffness and mass of each story. To overcome this problem, standard mass and stiffness matrices must be defined as described herein.

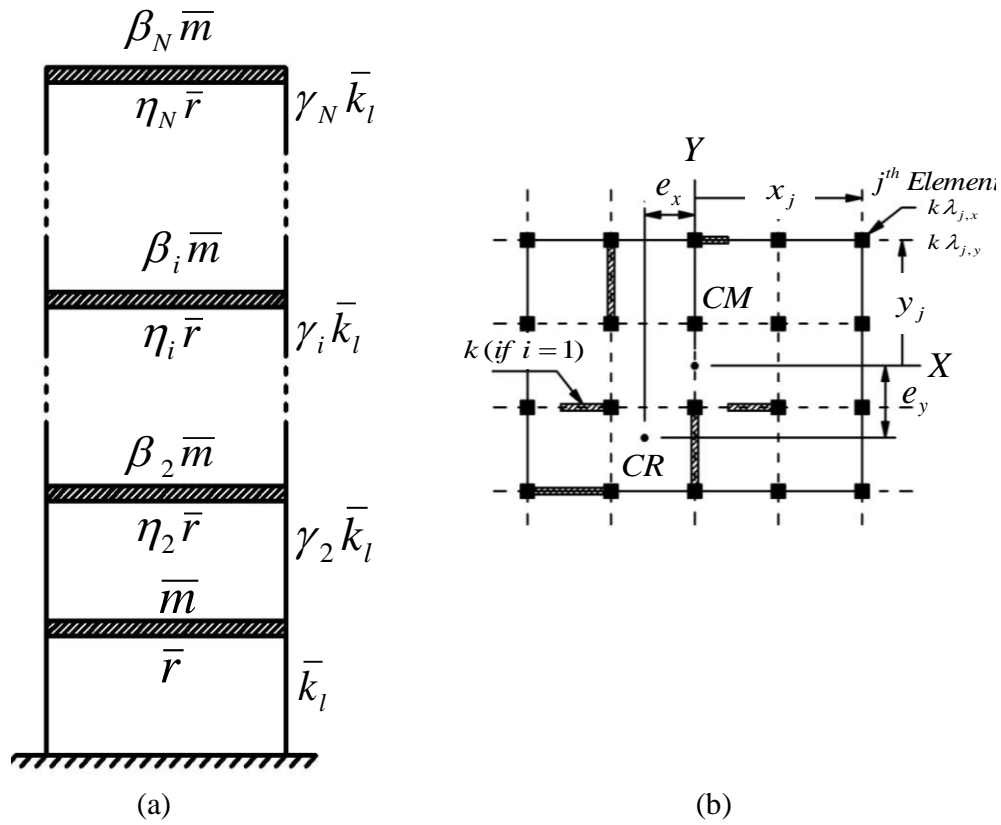


Figure 2-3: (a) Torsionally coupled N – story building; (b) Plan view of the i^{th} floor

2.2.2.4.1 Mass matrices

Assume that the total lumped mass of the i^{th} story of the building shown in Figure 2-3a can be expressed as

$$m_i = \beta_i \bar{m} \quad (2-14)$$

where, \bar{m} is the total lumped mass of the first floor and β_i is the ratio of the mass of i^{th} floor to the first floor. Therefore, the global translational mass matrix can be presented as:

$$[M] = \bar{m} \begin{bmatrix} 1 & 0 & \dots & & 0 \\ 0 & \beta_2 & & & \vdots \\ \vdots & & \ddots & & 0 \\ 0 & & & \beta_i & \\ \vdots & & & & \ddots \\ 0 & \dots & 0 & \dots & \beta_n \end{bmatrix}$$

or, in a simplified form,

$$[M] = \bar{m} [\tilde{\beta}] \quad (2-15)$$

where, $[\tilde{\beta}]$ is the mass ratio matrix of the building and can be calculated by determining the area and unit mass of each floor. Since the unit mass and area of each floor is (assumed) constant during the analysis, $[\tilde{\beta}]$ remains unchanged. Accordingly, the radius of gyration of the i^{th} story about a vertical axis through the center of mass of the floor can be expressed as

$$r_i = \eta_i \bar{r} \quad (2-16)$$

where, \bar{r} is the radius of gyration of the first floor and η_i is the ratio of the radius of gyration of the i^{th} floor to the first floor. Therefore, the radius of gyration matrix can be expressed as

$$[R] = \bar{r} \begin{bmatrix} 1 & 0 & \dots & & 0 \\ 0 & \eta_2 & & & \vdots \\ \vdots & & \ddots & & 0 \\ 0 & & & \eta_i & \\ \vdots & & & & \ddots & \vdots \\ 0 & \dots & 0 & & \dots & \eta_n \end{bmatrix}$$

or, in a simplified form,

$$[R] = \bar{r} [\tilde{\eta}] \quad (2-17)$$

where, $[\tilde{\eta}]$ is the radius of gyration ratio matrix of the building. Since the geometric properties of the floors do not change, $[R]$ and $[\tilde{\eta}]$ remain constant during the analysis. The mass matrix in Equation 2-13 for determining torsional mode shapes can be calculated as

$$[M]_{\theta} = \bar{m} \bar{r}^2 [\tilde{\beta}] [\tilde{\eta}]^2 \quad (2-18)$$

2.2.2.4.2 Stiffness matrices

Consider the i^{th} story of the building shown in Figure 2-3b and assume that the location and type of each lateral load resisting system are known (reasonable assumptions if the floor plans and the types of resisting elements are provided). The uncoupled lateral stiffness matrices of the i^{th} story along the principal axes of resistance x and y can be expressed as

$$K_{i,x} = \sum_{j=1}^{p_x} k \lambda_{j,x} \quad ; \quad K_{i,y} = \sum_{j=1}^{p_y} k \lambda_{j,y} \quad (2-19)$$

where, $K_{i,x}$ and $K_{i,y}$ are the total lateral stiffness of the i^{th} story in the x – and y – directions, respectively; p_x and p_y are the total number of lateral load resisting elements acting in the x – and y –directions, respectively; $\lambda_{j,x}$ and $\lambda_{j,y}$ are the stiffness ratios of the j^{th} lateral load

resisting element in the x – and y –directions, respectively, to the stiffness of the weakest resisting element of the first story (i.e., k).

The uncoupled torsional stiffness matrix defined at the center of mass of the i^{th} floor can then be expressed as

$$K_{i,\theta} = \sum_{j=1}^{P_x} (k \lambda_{j,x}) y_j^2 + \sum_{j=1}^{P_y} (k \lambda_{j,y}) x_j^2 \quad (2-20)$$

where, $K_{i,\theta}$ is the torsional stiffness about the center of mass of the i^{th} floor; and, x_j and y_j are the distances between the center of mass of the floor to the centroid of the resisting element in x – and y –directions, respectively. Then, the uncoupled translational and torsional stiffness matrices of the building can be expressed as:

$$[K]_l = \begin{bmatrix} K_1 + K_2 & -K_2 & 0 & \dots & 0 \\ -K_2 & -K_2 + K_3 & & & \\ 0 & & \ddots & & \vdots \\ \vdots & & & K_i + K_{i+1} & -K_{i+1} \\ & & & -K_{i+1} & K_{i+1} + K_{i+2} \\ & & & & \ddots & 0 \\ 0 & \dots & & 0 & K_{n-1} + K_n & -K_n \\ & & & & -K_n & K_n \end{bmatrix} \quad (l = x, y, \theta)$$

By defining $\gamma_{i,l}$ as the stiffness ratio of the i^{th} story to the first story in the l direction ($l = x$ or y or θ), the translational stiffness ratio, $\gamma_{i,l}$, can be expressed as

$$\gamma_{i,l} = \frac{\left(\sum_j^{p_l} \lambda_j \right)_{i,l}}{\left(\sum_j^{p_l} \lambda_j \right)_{1,l}} \quad (l = x \text{ or } y) \quad (2-21)$$

and the torsional stiffness ratio can be expressed as

$$\gamma_{i,\theta} = \frac{\left(\sum_j^{p_x} (\lambda_{j,x}) y_j^2 + \sum_j^{p_y} (\lambda_{j,y}) x_j^2 \right)_{i,\theta}}{\left(\sum_j^{p_x} (\lambda_{j,x}) y_j^2 + \sum_j^{p_y} (\lambda_{j,y}) x_j^2 \right)_{1,\theta}} \quad (2-22)$$

Thus, the uncoupled stiffness matrices can be reformulated as

$$[K]_l = \bar{k}_l \begin{bmatrix} 1 + \gamma_2 & -\gamma_2 & 0 & \dots & 0 \\ -\gamma_2 & -\gamma_2 + \gamma_3 & & & \\ 0 & & \ddots & & \vdots \\ \vdots & & & \gamma_i + \gamma_{i+1} & -\gamma_{i+1} \\ & & & -\gamma_{i+1} & \gamma_{i+1} + \gamma_{i+2} \\ & & & & \ddots & 0 \\ 0 & \dots & & 0 & \gamma_{n-1} + \gamma_n & -\gamma_n \\ & & & & -\gamma_n & \gamma_n \end{bmatrix}_l$$

or, in a simplified form,

$$[K]_l = \bar{k}_l [\tilde{\gamma}]_l \quad (2-23)$$

where, $[\tilde{\gamma}]_l$ is the stiffness ratio matrix of the building along the l direction. \bar{k}_l is the sum of the stiffness of resisting elements in l direction at the first story and can be calculated as

$$\bar{k}_l = K_{1,l} = k \left(\sum_j^{p_l} \lambda_{j,l} \right)_{1,l} \quad (\text{for translational stiffness}) \quad (2-24)$$

$$\bar{k}_\theta = K_{1,\theta} = k \left(\sum_j^{p_x} (\lambda_{j,x}) y_j^2 + \sum_j^{p_y} (\lambda_{j,y}) x_j^2 \right)_{1,\theta} \quad (\text{for torsional stiffness}) \quad (2-25)$$

By substituting the mass ratio matrix (i.e., $[\tilde{\beta}]$), the radius of gyration ratio matrix (i.e., $[\tilde{\eta}]$), and stiffness ratio matrix (i.e., $[\tilde{\gamma}]$) into Equation 2-13 the eigenvalue problem for a torsionally uncoupled system can be reformulated as

$$\left(k \left(\sum_j \lambda_j \right)_1 [\tilde{\gamma}] - \omega^2 \bar{m} [\tilde{\beta}] \right)_x [\Phi]_x = [0] \quad (2-26)$$

$$\left(k \left(\sum_j \lambda_j \right)_1 [\tilde{\gamma}] - \omega^2 \bar{m} [\tilde{\beta}] \right)_y [\Phi]_y = [0] \quad (2-27)$$

$$\left(k \left(\sum_j^{p_x} (\lambda_{j,x}) y_j^2 + \sum_j^{p_y} (\lambda_{j,y}) x_j^2 \right)_1 [\tilde{\gamma}] - \omega^2 \bar{m} \bar{r}^2 [\tilde{\beta}] [\tilde{\eta}]^2 \right)_\theta [\Phi]_\theta = [0] \quad (2-28)$$

As one can see from inspection of Equations 2-26 to 2-28, the only variables are k and \bar{m} and all other terms are assumed to be constant during the analysis. Therefore, it can be concluded that the mode shapes and their corresponding frequencies only depend on the value of k and \bar{m} . The mass of each story can be estimated with reasonable accuracy before the design, thus the response of the structure depends only on the stiffness of the weakest element in the first floor (i.e., k).

The standard mode shapes of the building can be determined by solving the eigenvalue problems presented in Equations 2-26, 2-27, and 2-28 where k and \bar{m} are both equal to unity. Therefore, the actual vibrational frequencies and mode shapes of the building are only a function of the lateral stiffness of the weakest resisting element at the first story (i.e., k) and the lumped mass of the first floor (i.e., \bar{m}). Since the total response of the building is the combination of modal responses, the target performance level can be achieved only by varying k assuming that \bar{m} is known. It should be noted that changing the value of k implies iteration. However, the iteration will only be on the value of k provided that the relative mass and stiffness ratio matrices remain the same during the iteration process. By changing the value of k , the period of each mode changes and consequently the spectral displacement associated with the mode will be different which gives a unique response under a specific spectral acceleration at the level of each story.

Figure 2-4 presents a generic displacement response spectrum for the governing story in a building that is designed by displacement-based design with torsion (DBDT) procedure. T_1 and T_2 are the periods of the first story corresponding to the first and second trials, respectively. The relationship between the period of the first story (i.e., T_{1st}) in the l direction and the stiffness of the weakest element in the first story (i.e., k) can be obtained by using:

$$T_{1st,l} = \frac{2\pi}{\sqrt{k \left(\sum_j^{p_l} \lambda_{j,l} \right)_{1,l} / \bar{m}}} \quad (2-29)$$

Most of the time, the spectral displacements fall into the linear portion of the displacement response spectrum as shown in Figure 2-4. This gives a linear relationship between the period of

the first story and the corresponding spectral displacement. Therefore, one can find the exact value of “ k ” by using linear interpolation to obtain the period corresponding to the target displacement. This means that the design converges very fast by, at most, three iterations which only carry over k .

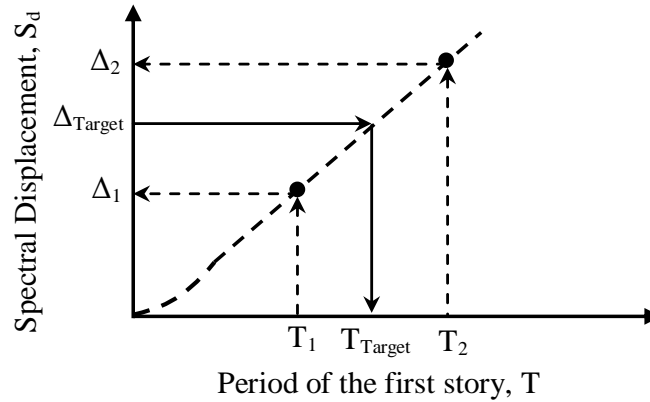


Figure 2-4: Explanation of period determination based on the target displacement using the displacement response spectrum

It is assumed that the DBD is performed with the motivation to enable a building to perform in a superior manner to conventional design, i.e. limited or very limited damage, and thus none of the lateral load resisting elements fail during the earthquake and the change in the stiffness ratio matrix can be assumed to be negligible. One can check the extra drift ratios caused by rotation of floor at the location of each lateral load resisting element after the design is completed. If it exceeds the ultimate deformation of the element, then either a stronger element should be used or the element should be eliminated from the stiffness ratio matrix.

2.2.2.5 *Non-linear systems and inelastic response*

The DBDT procedure presented herein can also be employed for non-linear systems by using inelastic displacement spectra. Studies that have been performed including one by Chopra and Goel (1999) that presented a method to modify an elastic design spectrum by using the ductility factor and the total damping ratio. Borzi et. al (2001) performed another method to develop inelastic response spectra from elastic response spectra using two characteristics that play the most important role in the response of a structure: (1) the period of the vibration in the inelastic system and (2) energy that is dissipated due to the inelastic behavior of the structure. Borzi et al (2001) showed that the maximum inelastic displacement response can be obtained by conducting linear elastic analysis using an equivalent structure (i.e., substitute structure) that has the same period of vibration and energy dissipation capacity as the inelastic system. Therefore, an equivalent period, T_E , and equivalent damping value, ζ_E , have to be defined for the structure with inelastic lateral load resisting elements in order to modify the elastic response spectrum. Gulkan and Sozen (1974) showed that the period of the structure that corresponds to the secant stiffness at the maximum displacement (i.e., target displacement in DBDT procedure) can be used as the most representative period of vibration of the structure. Therefore, in the DBDT procedure, the period of the building at the secant stiffness at the target drift has been used to construct the inelastic response spectra.

The equivalent elastic period of a bilinear system can be calculated using the elastic period of the structure as:

$$T_{1st,l} = T_l \sqrt{\frac{\mu}{1 + a\mu - a}} \quad (2-30)$$

where, T_l is the elastic period of the structure, μ is the ductility factor for the structure, and a is defined as the ratio of the secondary stiffness to the initial stiffness in a bilinear spring. In order to account for the energy that dissipates in inelastic systems, Borzi et al (2001) defined a reduction factor R that is defined using:

$$R = \frac{S_d^{Elastic}(T_E)}{S_d^{Inelastic}(T_E)} \quad (2-31)$$

The reduction factor R only depends on the total damping of the system. The reduction factor can be calculated based on the type of inelastic spring used to model the lateral load resisting elements in the structure and is defined by Borzi et al (2001) for an elastic perfectly plastic (EPP) spring as well as bilinear and tri-linear springs with ductility factors of $\mu = 2, 3, 4, 6$. In order to apply the DBDT method proposed in this study to an inelastic structure, the displacement response spectrum should be modified by appropriately calculating the reduction factor which depends on the damping and equivalent period of the structure at the secant stiffness corresponding to the target displacement of the structure. A 10-story steel braced frame modeled as an elastic perfectly plastic system was designed based on the DBDT approach for inelastic systems and will be presented later in Section 2.2.4.3.

2.2.2.6 *P-Delta effect*

The P-Delta effect has not been explicitly included in the proposed DBDT method. However, one can investigate the P-Delta effect on the structure by using the ASCE7-10 (2010) approach. Per ASCE 7-10, the P-Delta effect should be considered if the stability coefficient, χ , is greater than 0.1. For a building that is designed based on the proposed DBDT method and has the stability coefficient greater than 0.1, two future options can be pursued:

- 1) One can increase the calculated stiffness value (i.e., k) to decrease the stability coefficient to less than 0.1. In this case, the P-Delta effect can be neglected; or,
- 2) One can decrease the target inter-story drift by a factor of $(1 - \chi)$ in order to compromise the P-Delta effect. In this case, one iteration process will be added to the proposed DBDT method in order to examine the P-Delta effect.

2.2.3 Summary of Displacement-Based Design Procedure with Torsion (DBDT)

The following steps, which are shown in a flow diagram in Figure 2-5, should be followed in order to perform DBDT of buildings when torsion is present and is to be included in the design:

- Step 1. Define the desired performance level (i.e., Δ_{Target}) at a specific earthquake intensity (i.e., MCE or DBE level).
- Step 2. Select the lateral load resisting system based on architectural drawings, including constraints, and performance expectations. Find the relative stiffness ratio for each line of resistant. This can be done by finding the relative length ratios of shear walls in a reinforced concrete building (assuming that the thickness of wall and reinforcement ratios are the same for all walls), or by finding the length of bracing in steel braced frame buildings (assuming that the cross section of the bracing are the same at each story), or by finding the relative length of wood shear walls in each story that can be modified based on nail schedule for each wall.

Then, assign stiffness ratios for each story over the height of the building. This can be done by finding the relative ratios of the sum of the forces acting at each story and the stories above if only the first translational mode of vibration is considered

(i.e., the same procedure that is used in the equivalent lateral load procedure with the exception of using ratio than actual values).

- Step 3. Calculate the translational and torsional stiffness ratio matrices. Determine the mass and moment of inertia ratio matrices for each floor.
- Step 4. Conduct modal analysis by decoupling translational and torsional mode shapes and determining the modal coupling parameters by solving Equation 2-9. Then, find the normalized mode shapes by solving Equations 2-26 to 2-28.
- Step 5. Determine if the structure falls into the linear or non-linear category; then, find the maximum displacement response at the level of each story. Combine displacement responses using SRSS or CQC method for the assumed earthquake intensity.
- Step 6. Develop displacement response spectrum for each story for the specific earthquake intensity.
- Step 7. Determine the period of the structure associated with the target displacement from the response spectrum of the weakest story. Then, find the required lateral stiffness for the weakest element in the structure (i.e., k) and consequently for the entire building using the stiffness ratio matrices.
- Step 8. Check jurisdictional design requirements to ensure the building meets the strength criteria as well as performance (displacement) criteria.

It is important to point out that conventional design such as the application of the equivalent lateral force procedure has three major differences compared to the DBDT proposed in this

study: (1) In conventional design, one is only able to consider one design level such as the Design Earthquake level which is $2/3$ of MCE, but in the proposed DBDT multiple demand levels can be considered; (2) the shear demand is only based on one R-factor for the lowest corresponding R-factor, essentially penalizing mixed systems. In the DBDT structure, there is no use of an R-factor and therefore no penalty, essentially forming a composite response; and (3) in conventional design, the system and its components are designed for resistance at nominal, but in DBDT this level is selected depending on the performance requirements including ultimate capacity.

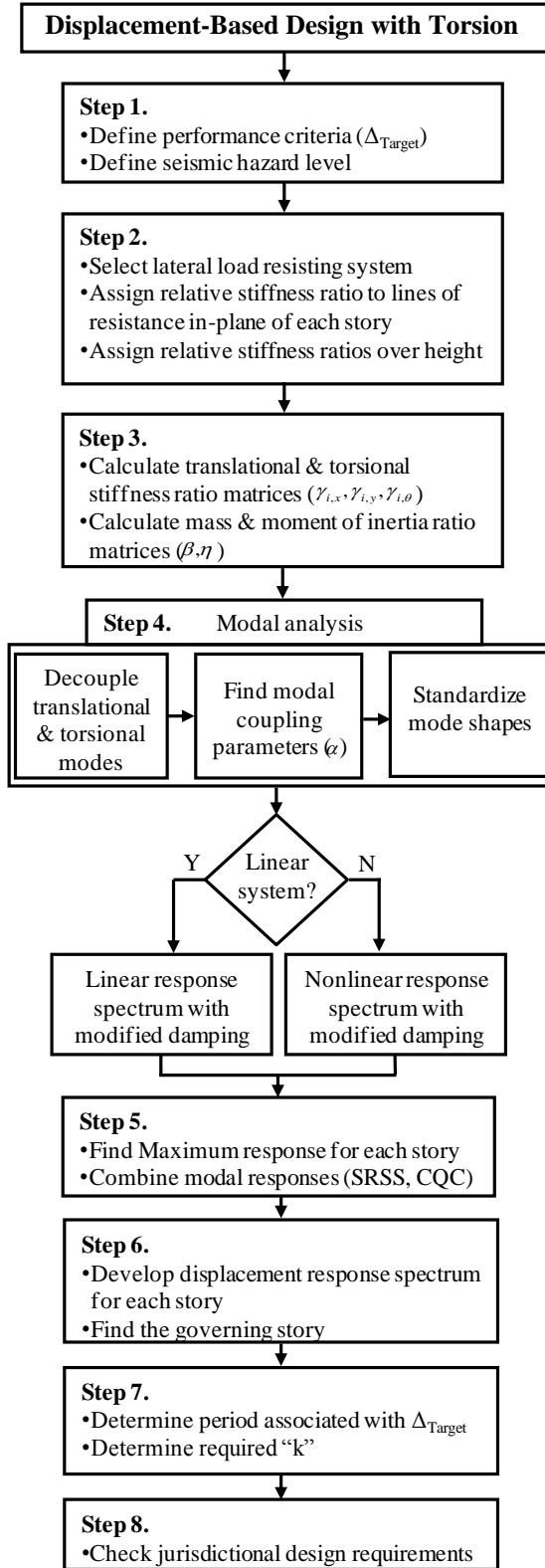


Figure 2-5: Flow diagram of the DBDT (Bahmani et al., 2013)

2.2.4 Numerical Verification and Illustrative Examples

In order to verify the proposed DBDT procedure, four examples are provided in this section. The buildings are selected such that they have large eccentricities in both directions; therefore, the effect of torsional moments on inter-story drifts must be considered in their design. The first building is a three-story regular building with excessive in-plane torsional irregularities. The second building is a three-story building with a weak-story at the first level and 12.5% eccentricity ratio in the x -direction (i.e. e_x / L_x) and 16.7% eccentricity ratio in the y -direction (i.e., e_y / L_y) at all stories. These buildings were designed assuming that all lateral load resisting elements behave linearly during an earthquake (i.e., verification for linear systems). The third and fourth buildings are designed based on non-linear behavior of structural elements. The third building is a four-story wood-frame building with 10.6% and 15.6% eccentricity ratios in the x - and y -direction, respectively. This building is designed by modeling wood shear walls using the ten-parameter hysteretic spring (Filiatrault and Folz, 2001). And finally, the fourth building is a 10-story steel braced frame building with 14.5% eccentricity ratio in the x -direction and 18.8% eccentricity ratio in the y -direction. This building is designed assuming that the steel bracing behaves nonlinearly during an earthquake. Furthermore, it is shown that the DBDT procedure can be optimized and the optimum design for the 10-story building is presented and validated numerically. Non-linear time-history analysis was conducted using a detailed finite element model of the designed buildings to verify the performance of the buildings that were designed based on the proposed DBDT method. A well-known suite of 22 far field earthquake records (FEMA P-695, 2009) scaled to the seismic intensity corresponding to spectral acceleration for MCE level in San Francisco, California were used in the verification examples.

2.2.4.1 Design of a regular 3-story building with excessive torsion (linear system)

A three-story building with severe torsion at all stories was designed using the proposed DBDT with torsion procedure under MCE level earthquakes in San Francisco area to satisfy the desired performance criteria (i.e., 2% ISD ratio for the softest story). A detailed finite element model of the building was used in order to verify the performance of the building subjected to 22 far-field earthquakes. The in-plane eccentricity ratio (i.e. e_x / L_x and e_y / L_y) in the x - and y -direction for all stories was 16.1% and 21.5%, respectively. Figure 2-6 presents the floor plan and elevation view of the building. The stiffness ratios of lateral load resisting elements within each story are constant for all stories (i.e., $\lambda_{j,m} / \gamma_m = \lambda_{j,n} / \gamma_n$, where j represents the element number in the m and n stories). Thus, the centers of rigidity for the entire building are located at one vertical axis (i.e., satisfying the second limitation of Kan and Chopra's method). The bold lines show the elements with higher lateral stiffness per unit length. The ratio of stiffness over the height of the building are shown Figure 2-6b. It can be seen that the building does not have a soft-story level ($K_1 / K_2 = 1.11$ and $K_2 / K_3 = 1.29$). It should be noted that the stiffness ratios can be changed in order to optimize the design.

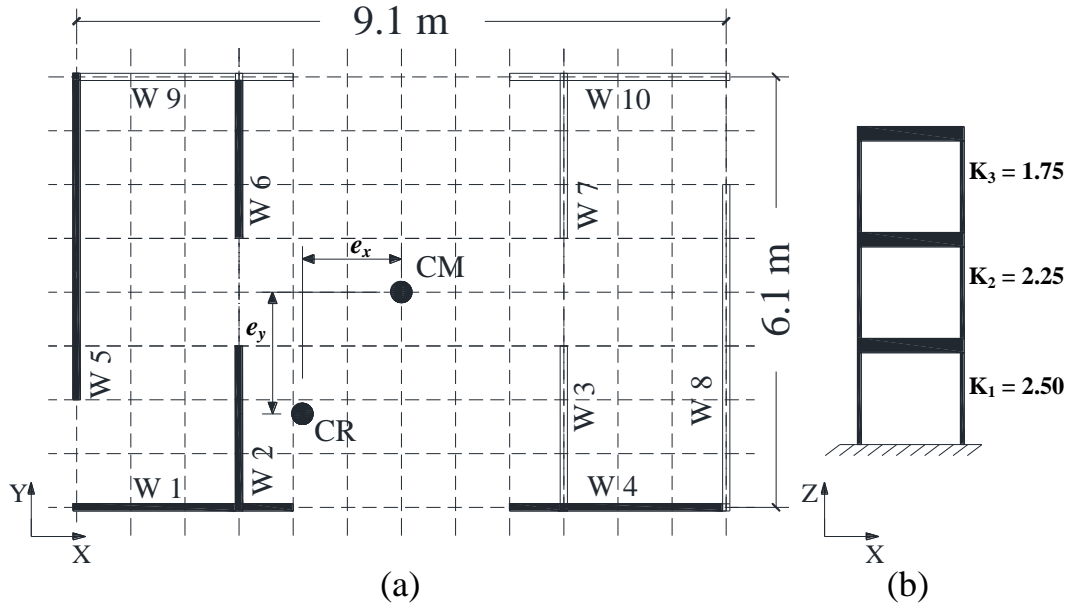


Figure 2-6: A 3-story building with excessive torsion: (a) plan view; (b) elevation view.

A time-history analysis was conducted using a detailed finite element model of the building to verify the performance of the building subjected to 22 far field ground motions (FEMA P-695, 2009) applied in x -direction. The fundamental natural period of the building and the corresponding spectral acceleration were $T_n = 0.577$ s and $S_a = 1.5g$ (5% damped) at MCE level, respectively. The probability of non-exceedance (PNE) of 50% means that the building should meet the performance criteria (i.e. 2% inter-story drift ratio) 50 percent of the time when subjected to MCE level earthquakes. It should be noted that while 50% PNE at 2% ISD ratio is targeted in these examples at MCE level, any ISD ratio could be targeted and the PNE can be adjusted based on the approach proposed by Pang et al (2010). Figure 2-7 presents the rank ordered peak inter-story drifts from time history analysis, providing the probability of non-exceedance versus inter-story drift of the building subjected to the 22 earthquakes. It can be seen that the inter-story drift ratio corresponding to PNE of 50% at the first story is 2.04% which is very close to the target drift of 2.00%. The error for the DBDT method in this example, assuming

the time history analysis is perfect, is 2.0%. The inter-story drift (ISD) ratios at the 2nd and 3rd stories are both less than 2.00% which meets the desired performance criteria.

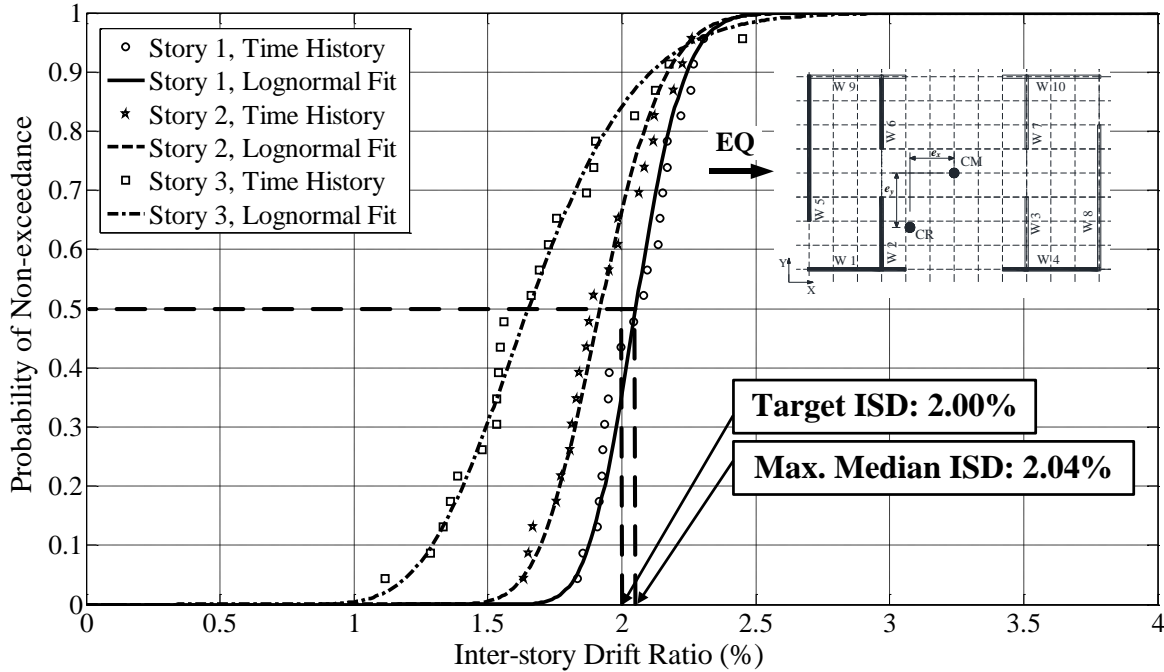


Figure 2-7: Probability of non-exceedance vs. ISD ratio for a regular 3-story building with linear system

2.2.4.2 Design of a 3-story building with torsional irregularity and a weak-story (linear system)

A three-story soft-story building with severe torsion at all stories was designed using the proposed DBDT procedure under MCE level earthquake spectral acceleration for the San Francisco area. The performance objective is to satisfy a 2% inter-story drift ratio limit for the softest story (i.e., the desired performance criteria) for half the earthquake suite. The in-plane eccentricity ratios (i.e. e_x / L_x and e_y / L_y) in the x - and y -direction for all stories were 12.5% and 16.7%, respectively. Figure 2-8 presents the floor plan and elevation of the building. The stiffness ratios of lateral load resisting elements within each story are constant for all stories (i.e.,

$\lambda_{j,m} / \gamma_m = \lambda_{j,n} / \gamma_n$, where j represents the element number in the m and n stories). The bold lines show the elements with higher lateral stiffness per unit length. Thus, the centers of rigidity of stories are located at one vertical axis (i.e., satisfying the second limitation of the Kan and Chopra's method). The ratios of lateral stiffness over the height of the building are shown in Figure 2-8b. The lateral stiffness of the first story is 77% of the lateral stiffness of the second story which results in a weak story condition for the first story as defined by ASCE7-10 (2010) (i.e., $K_1 / K_2 = 0.77$). However, the proposed DBDT method is still valid to design the building with a weak-story (or soft-story) level such that it meets the performance criteria at all stories (i.e. 50% non-exceedance probability for 2% inter-story drift ratio).

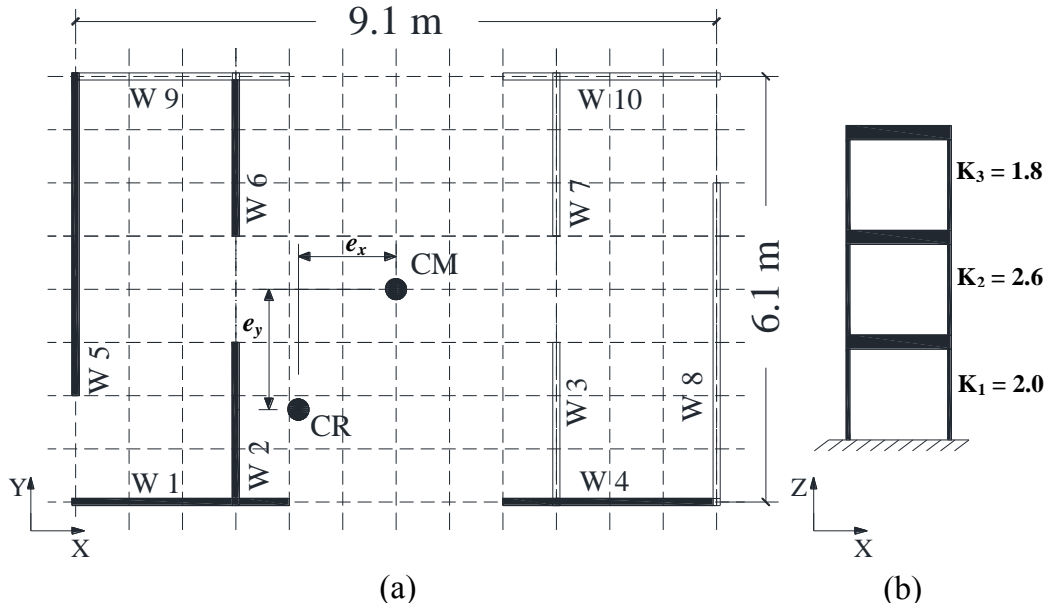


Figure 2-8: Building with excessive torsion: (a) plan view; (b) elevation view.

A time-history analysis was conducted using a detailed finite element model of the building to verify the performance of the building subjected to 22 far field ground motions applied in x -direction. The fundamental natural period of the building and the corresponding spectral

acceleration were $T_n = 0.489$ s and $S_a = 1.5g$ (5% damped) at MCE level, respectively. The target inter-story drift ratio for all stories was set to 2% with the probability of non-exceedance (PNE) of 50%. Table 2-1 presents the maximum ISD ratios measured at the center of mass of each story under the 22 far-field earthquake records.

Figure 2-9 presents the rank ordered peak inter-story drift ratio in the form of probability of non-exceedance versus inter-story drift ratios when subjected to the 22 far-field earthquakes. It can be seen that the inter-story drift ratio corresponding to 50% probability of non-exceedance at the first story is 1.93% which is close to the target drift of 2.00%, providing a design with an error of only 3.5%. The inter-story drift ratios at the 2nd and 3rd story were less than 2.00% which meet the desired performance criteria.

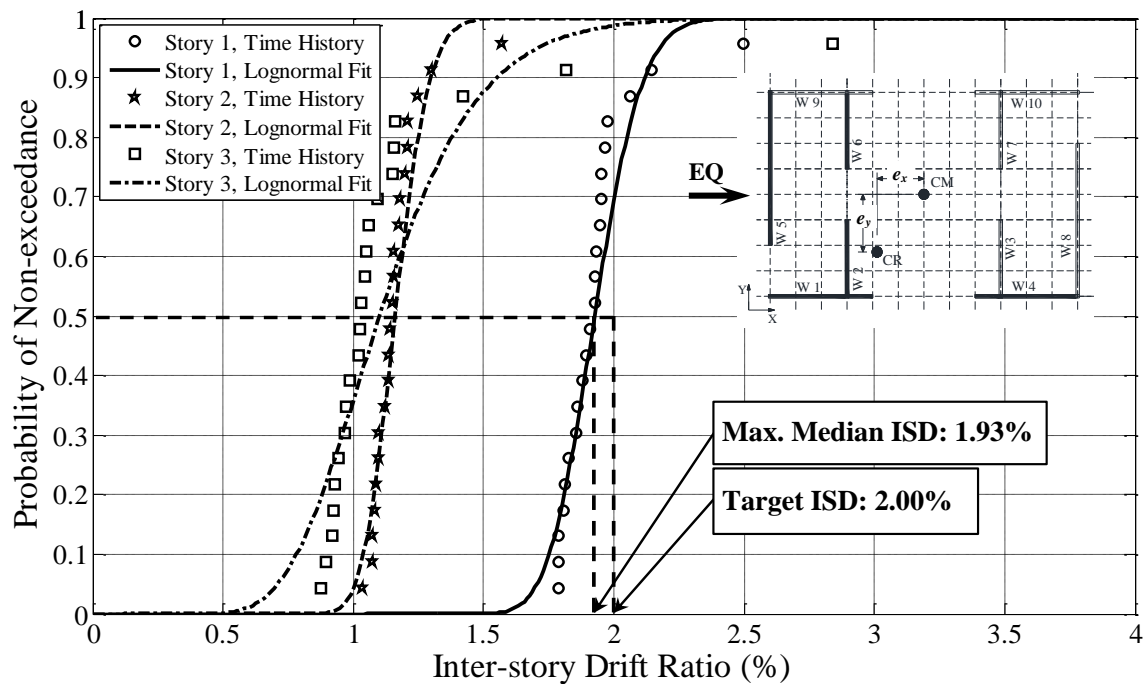


Figure 2-9: Probability of non-exceedance vs. ISD ratio for a 3-story soft-story building with linear system

Table 2-1: Set of scaled 22 earthquake records with corresponding ISD drift ratios for each story

Earthquake number	Earthquake event	Inter-story drift ratio (%)		
		Story number		
		1	2	3
1	Northridge	1.880	1.082	0.874
2	Northridge	1.787	1.178	1.155
3	Duzce, Turkey	1.978	1.207	1.047
4	Hector Mine	1.788	1.086	0.893
5	Imperial Valley	1.813	1.153	1.025
6	Imperial Valley	1.908	1.176	1.093
7	Kobe, Japan	1.788	1.100	0.918
8	Kobe, Japan	1.967	1.137	0.925
9	Kocaeli, Turkey	1.951	1.153	0.966
10	Kocaeli, Turkey	1.809	1.301	1.817
11	Landers	1.930	1.137	0.971
12	Landers	1.945	1.200	1.020
13	Loma Prieta	2.495	1.572	2.838
14	Loma Prieta	1.854	1.034	1.163
15	Manjil, Iran	2.062	1.096	1.421
16	Superstition Hills	2.146	1.143	1.031
17	Superstition Hills	1.827	1.120	0.944
18	Cape Mendocino	1.892	1.210	1.058
19	Chi-Chi, Taiwan	1.861	1.072	0.930
20	Chi-Chi, Taiwan	1.950	1.247	1.051
21	San Fernando	1.932	1.155	1.153
22	Friuli, Italy	1.928	1.075	0.986

2.2.4.3 Design of a 10-story steel braced frame building with torsion (non-linear system)

A 10-story steel braced frame building with severe torsion at all stories was designed under MCE level earthquake in San Francisco area in order to meet the desired performance criteria (i.e., 2% ISD ratio for all stories). The floor plan dimensions of the building were 21.3×30.5 m (70×100 ft) with a height of 30.5 m (100 ft). The in-plane eccentricity ratios (i.e. e_x / L_x and e_y / L_y) in x - and y -direction for all stories were 14.5% and 18.8%, respectively. As shown in Figure

2-10a the building has 22 steel braced frames in both x - and y -direction. The steel braced frames are shown in bold lines in Figure 2-10a. The relative stiffness ratios within each story were calculated by counting the number of steel frames in each line of resistance (e.g., the lateral stiffness ratio of Line 4 to Line 2 is 5.0). The stiffness ratios over the height of the building are shown in Figure 2-10b.

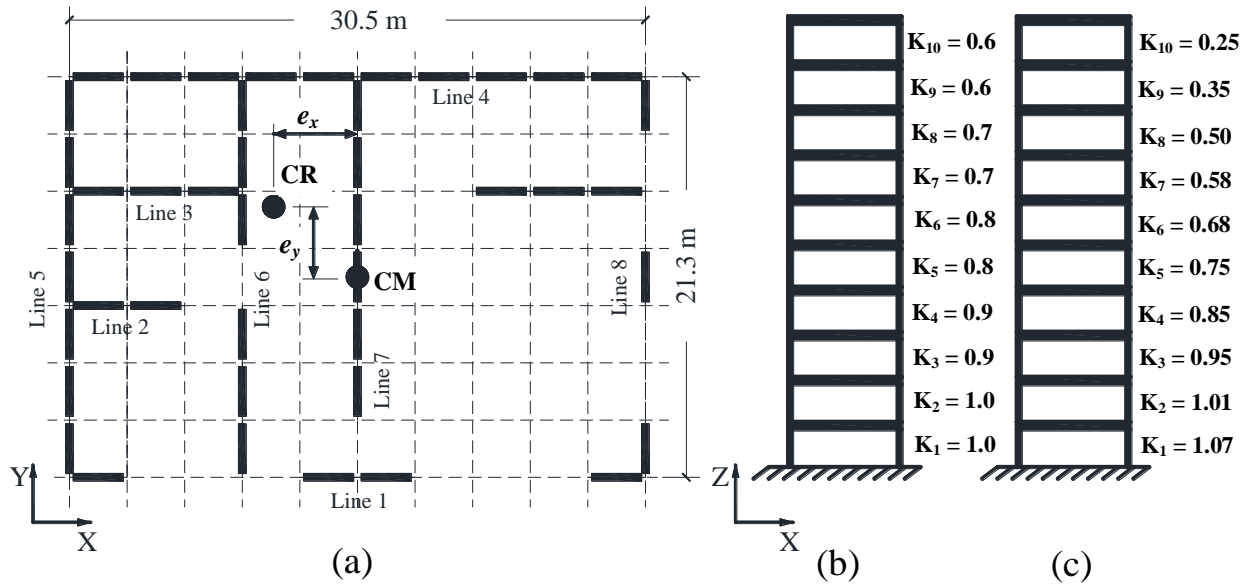


Figure 2-10: (a) Plan view; (b) distribution of lateral stiffness over height; (c) optimum design.

The steel braced frame was modeled as a non-linear elastic-perfectly plastic (EPP) spring with a ductility of $\mu = 2.0$. Since the steel braced frames acted as non-linear springs, the displacement response spectrum was modified in order to consider the ductility of 2.0 based on the aforementioned procedure in Section 2.2.2.5. The elastic fundamental natural period of the building and the corresponding spectral acceleration were calculated as $T_n = 1.71$ s and $S_a = 0.485g$ (5% damped) for MCE level in San Francisco, respectively. The equivalent fundamental natural period of the building at the target inter-story drift was $T_{Eq} = 2.42$ s. A non-

linear time history analysis was conducted for the designed building subjected to 22 scaled earthquake records shown.

Table 2-2 presents the maximum inter-story drift ratio measured at the center of mass of each story under each earthquake ground motion. Figure 2-11 presents the rank ordered peak inter-story drift ratios for all the stories. It can be seen that the maximum inter-story drift ratio at the first story (i.e., governing story for this building) corresponding to 50% probability of non-exceedance is 1.91% which is close to the 2% target inter-story drift ratio. The error for the proposed designed compared to the results of non-linear time-history analysis is 4.5%. It should be noted that the inter-story drift in all other stories are less than 2%, but not all close to the 2% target, which can typically be refined.

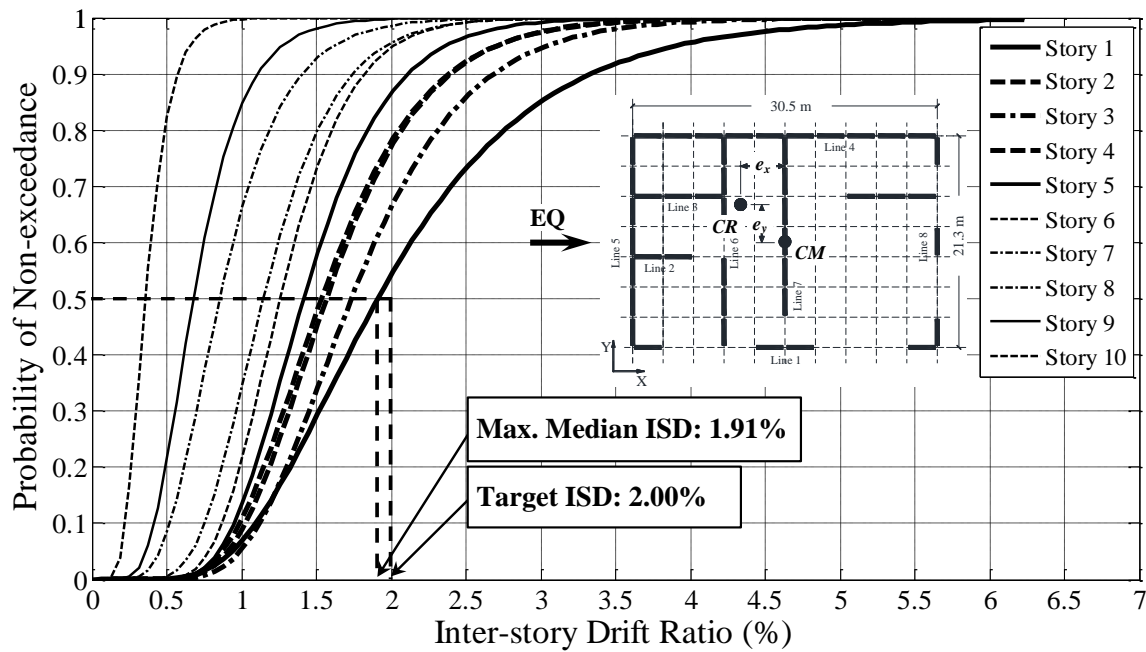


Figure 2-11: Probability of non-exceedance vs. ISD ratio for a 10-story building with non-linear EPP system

Table 2-2: Set of scaled 22 earthquake records with corresponding ISD ratios for each story

Earthquake number	Earthquake event	Inter-story drift ratio (%)									
		Story number									
		1	2	3	4	5	6	7	8	9	10
1	Northridge	1.27	1.30	1.52	1.45	1.45	1.22	1.07	0.82	0.70	0.36
2	Northridge	1.35	1.14	0.99	1.08	1.12	1.72	1.94	1.62	1.32	0.66
3	Duzce, Turkey	1.90	1.44	1.70	1.58	1.76	1.57	1.40	1.46	1.25	0.66
4	Hector Mine	1.66	1.33	1.43	1.27	1.19	0.97	0.87	0.66	0.55	0.30
5	Imperial Valley	0.56	0.51	0.50	0.43	0.43	0.38	0.37	0.39	0.35	0.19
6	Imperial Valley	1.61	1.22	1.27	1.14	1.19	1.34	1.57	1.27	1.06	0.57
7	Kobe, Japan	1.61	1.66	1.77	1.46	1.28	1.25	1.17	0.88	0.72	0.39
8	Kobe, Japan	4.50	2.45	2.44	1.84	1.30	1.17	0.92	0.60	0.51	0.43
9	Kocaeli, Turkey	1.66	1.49	1.71	1.57	1.51	1.24	1.10	0.85	0.71	0.36
10	Kocaeli, Turkey	2.16	1.61	1.60	1.53	1.50	1.24	1.10	0.85	0.63	0.29
11	Landers	1.63	1.67	2.08	1.88	1.75	1.34	1.22	0.86	0.61	0.29
12	Landers	1.85	1.49	1.88	2.37	2.75	2.53	2.39	1.68	1.10	0.45
13	Loma Prieta	1.79	1.06	0.83	0.79	0.81	0.72	0.81	0.64	0.52	0.27
14	Loma Prieta	3.39	2.16	2.38	1.96	1.51	1.60	1.76	1.45	1.15	0.56
15	Manjil, Iran	6.23	3.18	3.09	2.42	1.91	1.29	1.21	1.03	0.89	0.47
16	Superstition Hills	1.80	1.78	2.31	2.25	2.04	1.48	1.37	1.07	0.68	0.39
17	Superstition Hills	2.48	1.89	2.02	1.58	1.54	1.33	1.13	0.79	0.83	0.48
18	Cape Mendocino	4.86	2.45	2.40	2.23	2.29	2.01	1.83	1.29	0.87	0.37
19	Chi-Chi, Taiwan	2.13	1.68	1.80	1.51	1.33	1.04	0.90	0.66	0.52	0.27
20	Chi-Chi, Taiwan	0.35	0.31	0.30	0.26	0.31	0.29	0.29	0.22	0.18	0.09
21	San Fernando	3.16	2.58	3.44	3.20	2.80	1.97	1.43	0.76	0.50	0.25
22	Friuli, Italy	2.96	1.98	1.86	1.43	1.22	0.96	0.97	0.79	0.67	0.35

2.2.4.3.1 Design Optimization

As mentioned in the DBDT procedure, the design can start with an assumption for lateral stiffness ratios and can be optimized by changing the relative lateral stiffness ratio of the stories over the height of the building. The design is optimum when all the stories experience approximately the same inter-story drift as the defined target inter-story drift (i.e., 2% in this example). The lateral stiffness ratios over the height of the 10-story building have been changed in order to optimize the design. The optimum stiffness ratios are shown in Figure 2-10c. The

rank ordered peak inter-story drift ratios for all the stories are shown in Figure 2-12. It should be mentioned that since all the floors had the same mass, radius of gyration, and in-plane eccentricity ratios, the modal coupling parameters (i.e., α) were the same for all stories which simplified the design procedure in this illustrative example.

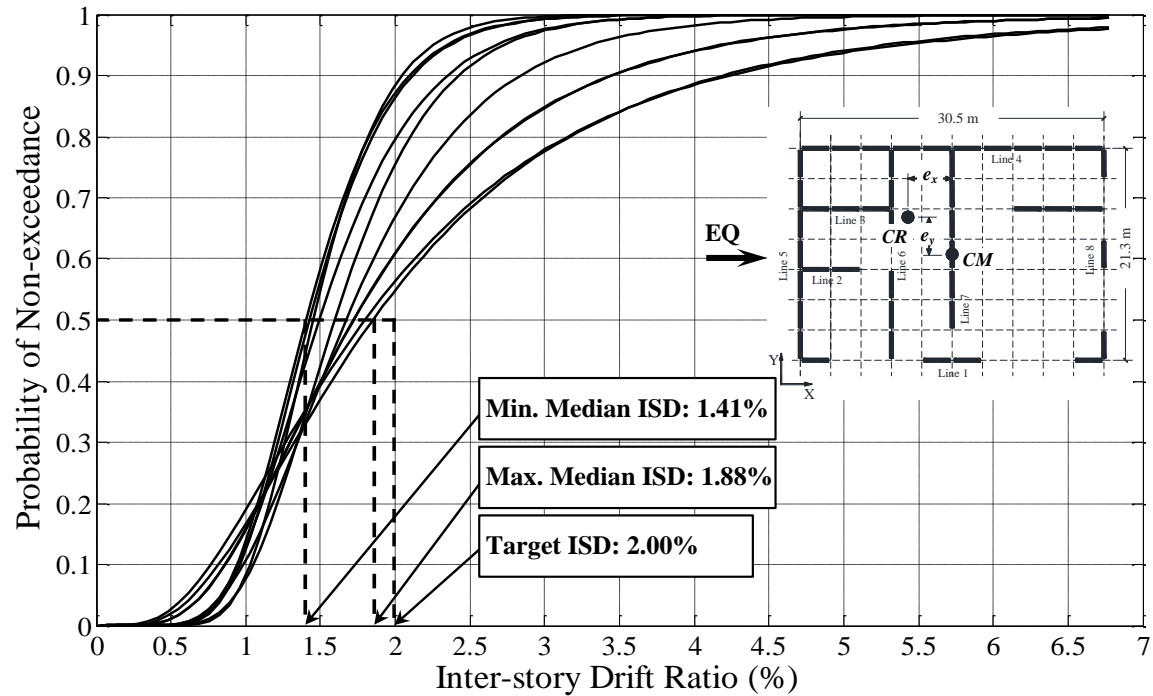


Figure 2-12: Probability of non-exceedance vs. ISD ratio for a 10-story building with non-linear EPP system (design optimization)

Chapter 3. PERFORMANCE-BASED SEISMIC RETROFIT (PBSR) DEVELOPMENT

In Chapter 2, the new displacement-based design with torsion (DBDT) method was developed and validated to incorporate torsional responses in the design of new buildings. However, there has been an increasing demand for approaches to retrofit existing buildings that were not designed in accordance with seismic provisions of current codes. Recent earthquakes have highlighted the fact that these buildings can experience severe damage and even collapse during an earthquake which will lead to property loss and fatalities. In this chapter a new performance-based seismic retrofit (PBSR) procedure for retrofitting structurally deficient existing buildings is proposed and numerically validated. The new PBSR procedure enables structural engineers to include or eliminate the torsional response of the structure in the retrofit design; hence, provides retrofit options.

Over the past several decades several key efforts to identify at-risk buildings and to propose effective and efficient retrofit techniques were undertaken. In 1992, FEMA published FEMA 178 (1992) document entitled “*NEHRP Handbook for Seismic Evaluation of Existing Buildings*” in order to evaluate the vulnerability of existing buildings to earthquakes. About the same time, studies on incorporating performance-based design (PBD) into retrofitting existing buildings was beginning to receive more attention among structural engineers. However, it was not until 1997 that the American Society of Civil Engineers (ASCE) worked with FEMA in publishing a guideline for the seismic rehabilitation of buildings (FEMA 273, 1997). In this guideline the performance level was defined based on lateral displacement of stories (i.e., inter-story drift) for a number of different seismic force resisting systems. Furthermore, the ground motions for designing and analyzing buildings were probabilistically specified and associated with

performance objectives of different structures. Several seminars were organized by the Applied Technology Council (ATC) in 1997 and 1998 to explain the new provisions in the FEMA 273 and its commentary, FEMA 274 (1997). These seminars enhanced the familiarity of structural engineering practitioners with these new documents.

In 1998, a joint effort between FEMA and ASCE led to publishing the FEMA 310 guideline entitled “*Handbook for the Seismic Evaluation of Buildings: A Prestandard*” which was an update on the FEMA 178 (1992) guideline. In 2003, ASCE published ASCE 31-03 (2003) standard entitled “*Seismic Evaluation of Existing Buildings*” in order to systematically codify the seismic evaluation of existing buildings subjected to ground motion excitation. In 2006, ASCE published the ASCE 41-06 standard entitled “*Seismic Rehabilitation of Existing Buildings*” with the objective of retrofitting structurally deficient buildings; and, most recently published ASCE 41-13 (2014) entitled “*Seismic Evaluation and Retrofit of Existing Buildings*” which is a combination of ASCE 31-03 and ASCE 41-06 standards. A new project, funded by NIST and led by the Applied Technology Council, is underway to update the pushover curves in ASCE 41-13 to non-linear time history analysis models; ATC 114.

Although a number of studies have been completed to evaluate and retrofit existing buildings, none of them specifically has proposed a retrofit procedure that enables engineers to explicitly meet the pre-defined performance criteria for different level of earthquake intensity. This need in the structural engineering community led to emergence of performance-based seismic retrofit (PBSR) concepts. PBSR, which is essentially a subset of performance-based seismic design (PBSD), is a method that seeks to meet or exceed a minimum performance criteria specified by the owner or stakeholders under a specified seismic intensity level. This method can offer an efficient and effective way to retrofit buildings by distributing the stiffness and strength of

retrofits over the height of the building and in the plane of each story while keeping inter-story drifts below the pre-defined values assumed during the design process. In addition, the PBSR method prevents over- and under-strengthening floor levels by limiting the relative stiffness and strength ratio of stories to pre-defined ranges; hence, eliminating irregularities (i.e., soft- or weak- story behavior) in the retrofitted building.

A structural engineer can face many structural and architectural challenges in retrofitting an existing building depending on the type of the building, its location, availability of retrofit material, accessibility to different parts of the building, and the cost and time of implementation of the retrofits. These challenges make retrofitting an existing building more challenging than designing a new building and highlight the key difference between the PBSR and PBSR methodologies. In PBSR, the structural engineer can choose the design specifications such as location and type of seismic force resisting members. He or she also has the authority to revise the architectural plan if needed to accommodate the structural design of the building. However, in the PBSR methodology, the structural engineer has to deal with an existing building in which defining the location, size, and type of seismic force resisting members are mostly dictated by the architectural constraints, availability of retrofit material, and cost and time of the retrofit. Aesthetic and architectural aspects of the building such as openings (e.g., doors and windows), load bearing walls, and living areas further complicate retrofit scenarios and can rule out many structurally effective options for the retrofit. In addition, as mentioned earlier, it is imperative that the disruption to tenants and cost of retrofits be minimized whenever possible; therefore, time and cost of implementing retrofits play a very critical role in any retrofit procedure including PBSR. This has motivated structural engineers to seek new retrofitting techniques that are structurally effective, easy to install, and contractor friendly with less disruption to tenants.

As mentioned in Chapter 2, the existing direct displacement design (DDD) method (Priestley 1998, Filiatrault and Folz 2002, and Pang et al. 2010) and new DBDT method (Bahmani et al., 2013) determine the required lateral stiffness over the height of the structure and in the plane of each story such that the building meets the pre-defined displacement under a specified seismic intensity. These design methodologies can be modified to be applicable to retrofit at-risk existing buildings. The retrofit procedure should address vertical and horizontal irregularities of the existing buildings in addition to aforementioned challenges in retrofitting existing buildings.

Many of existing buildings are identified as code-deficient with respect to vertical and horizontal irregularities. Vertical irregularities can lead to soft- or weak-story behavior which results in higher displacements due to uneven distribution of lateral force over the height of the building. Vertical irregularity also causes uneven distribution of dissipated energy by the building which leads to concentration of damage at the deficient story. Likewise, horizontal irregularities can lead to higher displacements due to the effect of in-plane torsional moments in addition to lateral forces. The new PBSR procedure proposed herein can eliminate the vertical irregularities by distributing the lateral stiffness and strength of retrofit members over the height of the building. It also addresses the horizontal (i.e., torsional) irregularities by either including the torsional responses into the total displacements of the retrofitted building or by eliminating the torsion. In some cases it is not feasible to eliminate the torsion due to existing building constraints. In these cases, the PBSR approach can be applied by using the DBDT concept developed in Chapter 2 to include the extra displacements caused by the in-plane torsional moments. In fact, there may be cases where allowing some level of torsion to remain in the retrofitted building is much less expensive and, as such, enables the owner to retrofit. An example of retrofitting a three-story

weak-story torsionally unbalanced building retrofitted using this method is presented in Section 3.1.1 of this chapter.

It should be noted that, whenever practical, the torsional response of the structure should be eliminated by distributing the retrofit properly in the plane of each story. The same logic and methodology that was used in the simplified DDD method (Pang et al, 2010) was employed to develop a simplified PBSR method with three major differences: (1) The stiffness and strength of the existing SFRS should be calculated in addition to the stiffness and strength of the retrofit elements at the pre-defined (i.e., target) inter-story drift; (2) the displacement response spectrum should be modified based on total damping of both the existing SFRS and retrofit members; and, (3) the retrofits should be distributed in the plane of each story such that in-plane eccentricities are minimized (or ideally eliminated) when the story approaches the pre-defined (i.e., target) inter-story drift. The simplified method of retrofitting multi-story torsionally unbalanced buildings is also explained in this chapter and described in detail in Section 3.2. A full-scale four-story soft-story wood-frame building was retrofitted using this approach and is validated along with the numerical analysis and full-scale experimental shake table tests. The retrofit design and specifics with numerical verification are presented in Chapter 5 and the experimental shake table test validation is presented in Chapter 6 of this dissertation.

3.1 PBSR Procedure by Including Torsion

The same logic that has been used in developing the DBDT methodology can be employed to retrofit buildings with vertical and in-plane horizontal irregularities (i.e., torsionally unbalanced buildings). As mentioned earlier, the only major difference between retrofitting an existing building and designing a new building is that in the case of retrofit a structural engineer must

deal with existing vertical and lateral load resisting systems which may be made of archaic materials and even have unknown properties.

The DBDT developed in Chapter 2 can be modified with the following steps in order to retrofit a torsionally irregular building in which the in-plane eccentricities cannot be eliminated:

Step 1. Calculate the lateral stiffness of the existing seismic force resisting systems (SFRS) at the specified target displacement (i.e., Δ_{Target}) at each story using DBDT described in Sections 2.2.2 and 2.2.3.

Step 2. Obtain the secant stiffness of retrofit elements (i.e., $K_{Retrofit}$) by subtracting the secant stiffness of the existing SFRS (i.e., $K_{Available}$) from the required secant stiffness calculated based on the DBDT procedure (i.e., $K_{Required}$) at each story at the specified target displacement.

Step 3. Strengthen and stiffen the existing SFRS elements of the building by modifying the existing SFRS or by installing retrofit elements.

Case 1. Steel structures: This can be done by increasing the moment of inertia of columns and beams of steel moment frames or increasing the cross-sectional area of bracing in steel braced frames.

Case 2. Reinforced concrete structures: This can be done by adding materials such as fiber-reinforced polymer (FRP) layers to the beams and columns. Also, increasing the cross sectional area of columns and beams can be an

alternative option to strengthening and stiffening the existing reinforced concrete SFRS.

Case 3. Wood-frame structures: This can be done by adding additional wood shear wall to the existing walls or decreasing nail spacing by adding additional nails to the existing wood shear walls.

Step 4. Calculate the eccentricities in both principal directions of the building after applying retrofits.

Case 1. If the retrofits are added such that the relative stiffness ratio of the retrofitted SFRS elements are the same as the relative stiffness ratio of the existing SFRS elements at each story, the location of the CR and eventually the in-plane eccentricities at each story will not change. Therefore, the eccentricities before and after applying the retrofits remain the same no further check is required for the retrofit design.

Case 2. If the in-plane eccentricities after applying the retrofit are less than the eccentricities before installing the retrofits, no further check in design is needed since the torsional responses were calculated based on higher values of eccentricities (i.e., conservative retrofit design);

Case 3. If the in-plane eccentricities after applying the retrofit are greater than the eccentricities before installing the retrofits, one more iteration in designing retrofits with the new values of eccentricities are required.

Figure 3-1 presents a flow diagram of the steps for PBSR procedure with torsion. In order to verify this method, a three-story building with excessive in-plane eccentricities and a soft and weak story at its first level is retrofitted with this method.

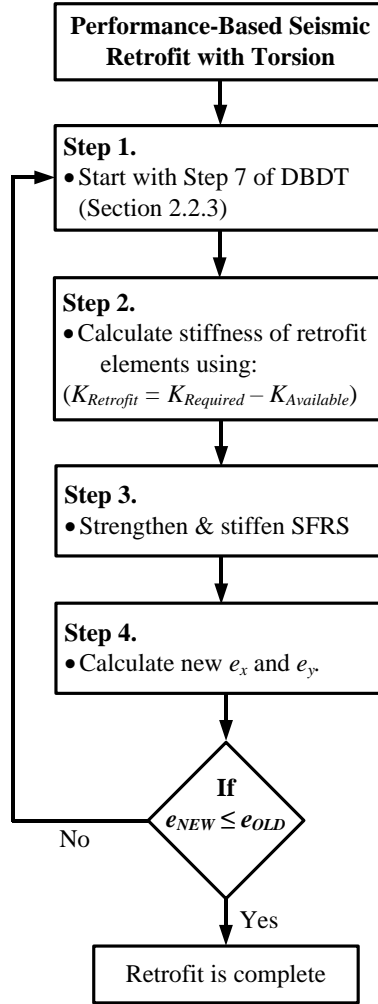


Figure 3-1: Flow diagram for PBSR procedure by including torsion

3.1.1 Retrofitting a 3-story torsionally irregular soft-story building using PBSR with torsion

In order to verify the proposed method for PBSR with torsion a three-story building with excessive vertical and horizontal irregularities is retrofitted and its responses to a suite of ground motions are evaluated. The building is selected such that it has large eccentricities in both

principal directions (i.e., the x – and y –direction); therefore, the effect of torsional moments on inter-story drifts is significant. The building has 12.5% and 16.7% eccentricities in the x – and y –direction, respectively, at all stories with an extreme soft-story at its first level (i.e., $K_1 / K_2 = 0.50$). Figure 3-2 presents the plan view and distribution of lateral stiffness over the height of the building. This building is retrofitted to satisfy the performance criteria (i.e., 2% ISD ratio at 50% probability of non-exceedance) by including the torsional response but eliminating the soft-story behavior. Time-history analyses were conducted using a detailed finite element model of the building to verify the performance of the building that was retrofitted using the proposed PBSR with torsion procedure.

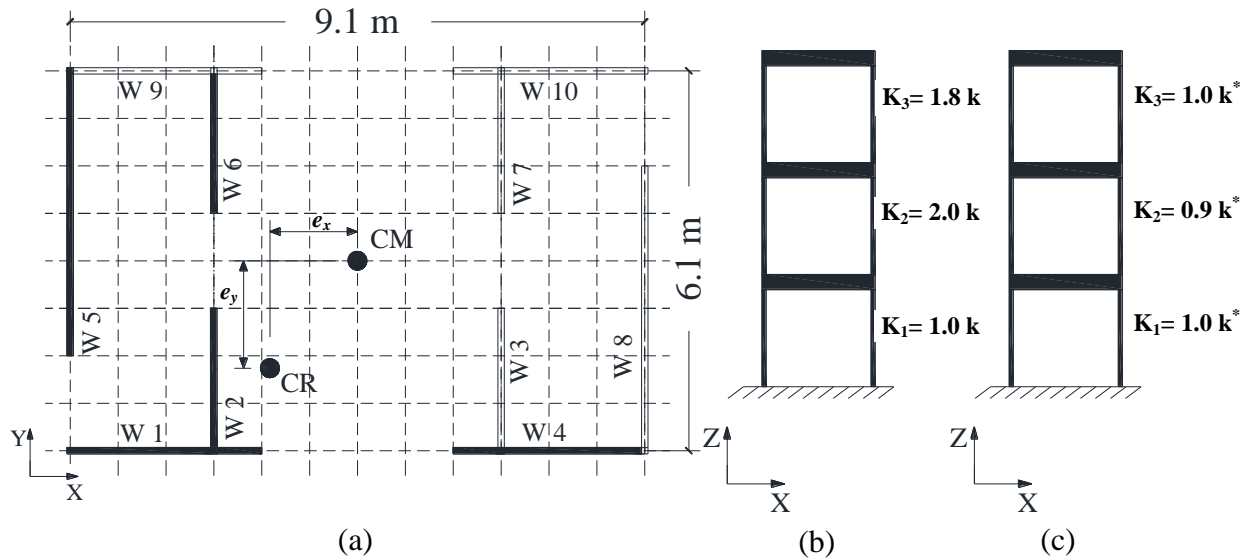


Figure 3-2: Three-story building retrofitted using PBSR with torsion method: (a) plan view; (b) distribution of lateral stiffness for un-retrofitted building; (c) distribution of lateral stiffness for retrofitted building.

In order to illustrate the effectiveness of the retrofit procedure, the building is subjected to a suite of ground motions before and after applying the retrofit. The cumulative distributions of the peak inter-story drift (ISD) ratios are calculated for the un-retrofitted and retrofitted building subjected to twenty-two far-field earthquake records (FEMA P-695, 2009) scaled to the seismic intensity corresponding to a spectral acceleration of $S_a = 1.5g$ at the natural period of the building. Figure 3-3a and Figure 3-3b present the cumulative distribution function (CDF) of the ISD ratios before and after applying the retrofit, respectively. Each point in the CDF plot of a story represents the maximum absolute ISD ratio experienced by the story when the building is subjected to a specific ground motion. It should be noted that lognormal functions are used to interpolate between the points for each story.

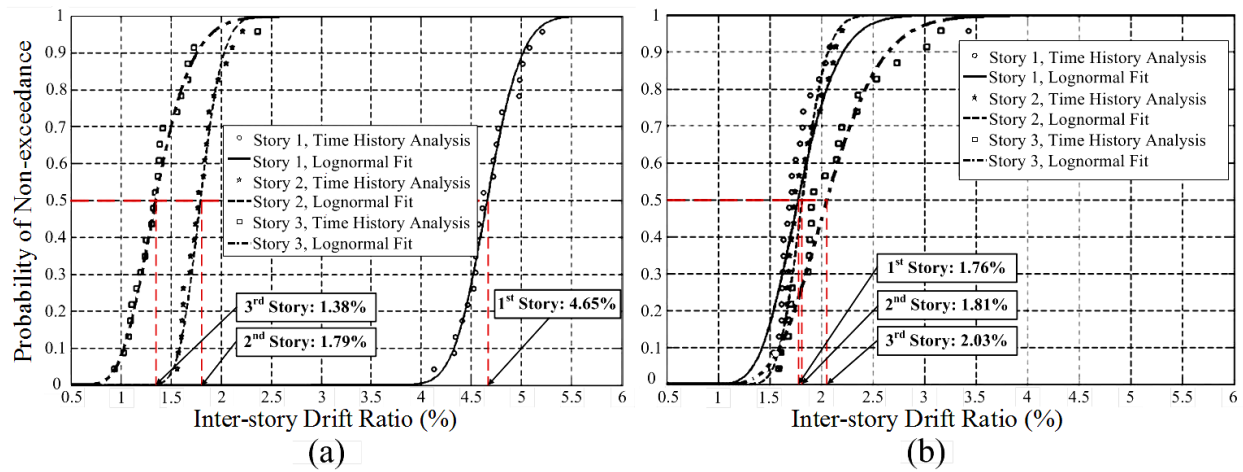


Figure 3-3: Probability of non-exceedance vs. ISD ratio: (a) original un-retrofitted building, (b) retrofitted building (elimination of soft-story behavior)

It can be seen from Figure 3-3a that the original un-retrofitted building has a soft first story since the first story experiences inter-story drifts approximately 2.5 times the upper stories (i.e., median ISD ratios of 4.5% at the 1st story compared to 1.79% and 1.38% at the 2nd and 3rd stories, respectively). Therefore, it can be concluded that the building is vertically irregular in

addition to its horizontal irregularity; hence, the proposed PBSR procedure should be used to retrofit the building by including the torsional response but eliminating the soft-story behavior. Figure 3-3b presents the probability of non-exceedance versus ISD ratios of the retrofitted building. It can be observed that the retrofitted building meets the performance criteria for all stories (i.e., 2% ISD ratio at 50% PNE at MCE level).

Table 3-1 presents the median ISD ratios and stiffness ratios of the stories over the height of the building before and after applying the retrofits. By evaluating the lateral stiffness ratios, it can be seen that the building is extremely soft at its first story before applying the retrofit; however, the distribution of the lateral stiffness ratios over the height of the building has changed after applying the retrofit which brings the building to the current design code regulations (i.e., ASCE 7-10, 2010).

Table 3-1: Stiffness and ISD ratios before and after applying PBSR

Story number	Original (un-retrofitted) Building		Retrofitted Building	
	Stiffness ^(a)	Median ISD Ratio (%)	Stiffness ^(b)	Median ISD Ratio (%)
1	1.00 k	4.65	1.00 k [*]	1.76
2	2.00 k	1.79	0.90 k [*]	1.81
3	1.80 k	1.38	0.70 k [*]	2.03

^(a) k: Translational stiffness of the 1st story in the original building

^(b) k^{*}: Translational stiffness of the 1st story in the retrofitted building

The proposed PBSR limits the maximum median ISD ratios to 2% (i.e., pre-defined target ISD ratio). Furthermore, no indication of soft-story behavior can be observed from the CDF graphs (Figure 3-3b). It should be noted that since the relative stiffness ratios of SFRS elements in the plane of each story is remained the same before and after applying the retrofit, the locations of

the CR's have not changed from the original positions and, therefore, no iteration in design is needed.

3.2 Simplified PBSR Procedure by Eliminating Torsion^{2,3}

It was shown in Chapter 2 that in a vertically irregular and torsionally unbalanced building, the total inter-story drift at each story consists of displacements due to lateral forces and additional torsional moments caused by in-plane eccentricities. During an earthquake, the resultant of the lateral forces induced by the ground motion excitation applies to the center of mass (CM) of each story and the resultant internal force of SFRS applies at the center of rigidity (CR) of the story. If the CM of the story does not coincide with its CR, additional torsional moment will be induced by a torsional couple due to the two equal and opposite forces, one applies to the CM and one applies to the CR of the story. This additional in-plane torsional moment can lead to additional displacement in the story (except at the CR). Figure 3-4a presents a torsionally irregular N -story building with lumped weights of W_j 's (j : story number). It can be seen that the total displacement at the center of mass of the j^{th} story have two major components: (1) the displacement due to lateral force, Δ_j^{Tns} , and, (2) the displacement due to torsional moment, Δ_j^{Tor} . However, if the retrofits are placed in such a pattern that the new location of the CR of the story moves toward its CM when the story approaches a specific target inter-story drift, the in-plane eccentricity will become small enough such that the in-plane torsional moment and the rotational

² Bahmani, P., van de Lindt, J.W., Gershfeld, M., Mochizuki, G.L., Pryor, S.E., Rammer, D. (2014). "Experimental Seismic Behavior of a Full-Scale Four-Story Soft-Story Woodframe Building with Retrofits I: Building Design, Retrofit Methodology, and Numerical Validation", ASCE J. Struct. Eng., DOI: 10.1061/(ASCE)ST.1943-541X.0001207.

³ Bahmani, P., van de Lindt, J.W., Pryor, S.E., Mochizuki, G. L. (2014). "Performance-based Seismic Retrofit of Soft-Story Wood-frame Buildings Using Steel Special Moment Frames: Methodology and Full-Scale Experimental Validation", Submitted to *Engineering Structures*, January 2015.

response can be neglected (i.e., $e_x = e_y \approx 0 \rightarrow T_j \approx 0 \rightarrow \Delta_j^{Tor} \approx 0$ in Figure 3-4b). In this case, the building after the retrofit is close to a torsionally symmetric building; therefore, the simplified DDD concept can be used and modified to develop the new simplified PBSR procedure.

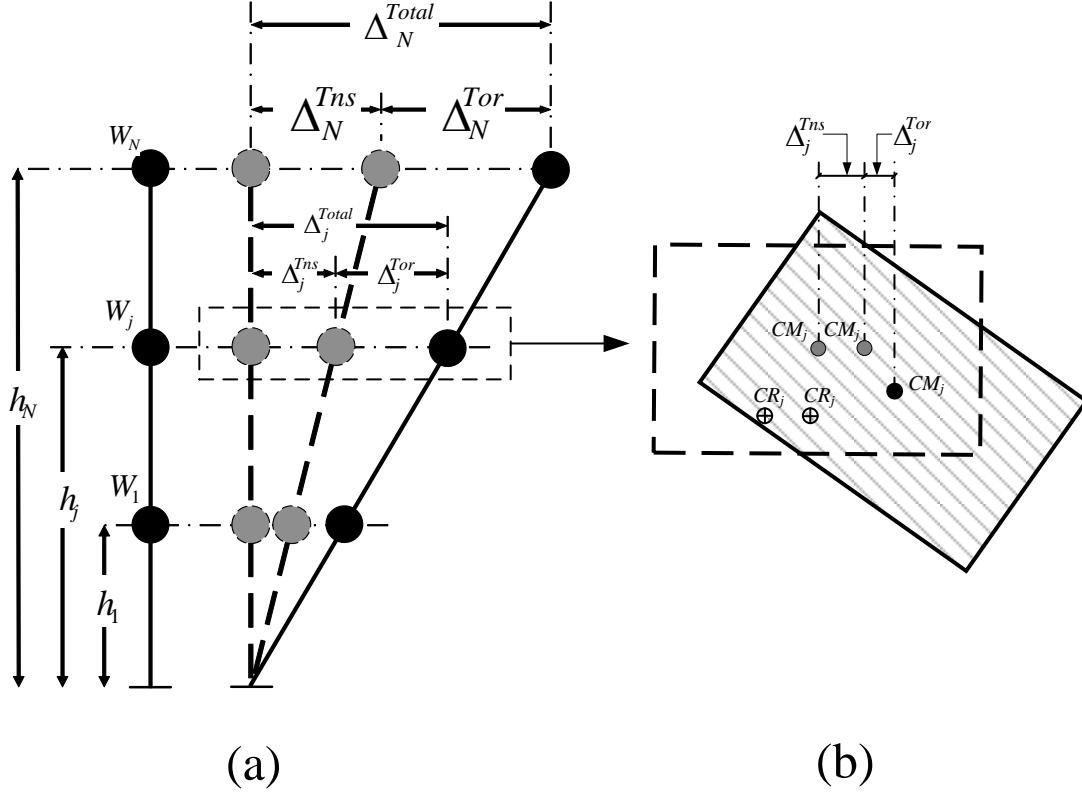


Figure 3-4: Translational and torsional displacements in a torsionally unbalanced building: (a) N – story building, and (b) plan view of the j^{th} story.

In order to develop the simplified PBSR approach, the multi-story building in Figure 3-4a can be simplified to an equivalent single degree of freedom (SDOF) system presented in Figure 3-5. This can be done by calculating the effective weight (W_{Eff}), the effective height (h_{Eff}), and the lateral load distribution factors ($C_{v,j}$) based on the approach outlined by Pang et al. (2010) and Wang et al. (2010):

$$W_{Eff} = \frac{\left(\sum_j^N W_j \Delta_j \right)^2}{\sum_j^N W_j \Delta_j^2} \quad , \quad j = 1, 2, \dots, N \quad (3-1)$$

$$h_{Eff} = \sum_j^N C_{v,j} h_j \quad , \quad j = 1, 2, \dots, N \quad (3-2)$$

$$C_{v,j} = \frac{W_j \Delta_j}{\sum_i^N W_i \Delta_i} \quad , \quad j = 1, 2, \dots, N \quad (3-3)$$

where, j is the story number, h_j is the height of the j^{th} story from the ground, W_j is the weight of the j^{th} story, and Δ_j is the absolute lateral displacement of the center of mass of the j^{th} story.

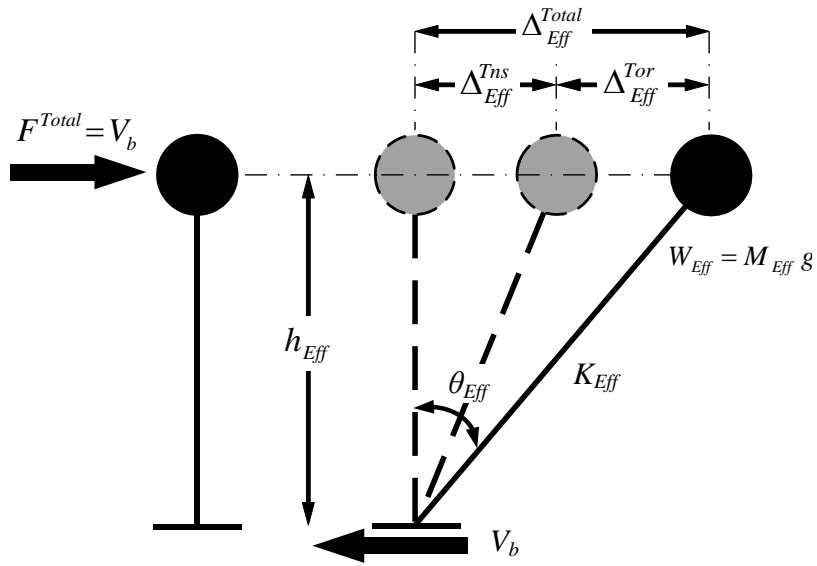


Figure 3-5: Equivalent SDOF model of multi-story building (Bahmani et al., 2014).

The next step in the PBSR procedure is finding the displacement of the equivalent SDOF system that ultimately leads to finding the distribution of the lateral forces and stiffness over the height

of the building. Non-linear time history (NLTH) analysis can be conducted to find the displacement of any structural system using the basic principle of structural dynamics; however, this method has three shortcomings from a design (or retrofit) standpoint. First, conducting NLTH analysis takes a significant amount of time; second, it needs a structure with known stiffness and mass matrices which is not the case in designing a structure; and third, it requires iterations to obtain the best design. Earthquake engineers have overcome these problems by introducing a new method of analyzing a structure subjected to a ground motion which is called “Response Spectrum Analysis”. In this method, a SDOF system with different fundamental period, T_n , (i.e., different stiffness-to-mass ratio) is subjected to an earthquake and its maximum absolute displacement (i.e., response) is recorded for each T_n . This procedure can be done for a suite of earthquakes and the median displacement for each T_n can be obtained. In this way, one does not need to run NLTH analysis to find the maximum displacement and can use the pre-calculated values if T_n of the structure is known. Conversely, the period of the equivalent SDOF of the to-be-designed structure can be found by knowing the maximum displacement (that can be set to the target displacement in DDD or PBSR procedures). Once the period is known, the lateral stiffness of the equivalent SDOF can be found by using the following relationship between the mass (or weight), the lateral stiffness, and the period of the equivalent SDOF:

$$T_n = \frac{2\pi}{\sqrt{K_{eff} / M_{eff}}} = \frac{2\pi}{\sqrt{K_{eff} g / W_{eff}}} \quad (3-4)$$

This, of course, is based on the assumption that the mass (or weight) of each story is known from architectural plans of the structure and types of material that will be used in the structure.

This concept can be used to obtain the period of the building that needs to be retrofitted (or designed using the response spectrum determined from seismic hazard maps provided in ASCE7-10 (2010) for different locations in the United States. In this case, the response spectrum analysis for the equivalent SDOF system can be calculated by modifying the design response spectrum obtained from seismic hazard maps (ASCE7-10, 2010). The following equation can be used to produce the displacement response spectrum from the design response spectrum for the equivalent SDOF system.

$$S_d^{Elastic} = \frac{1}{\omega_{Eff}^2} S_a^{Elastic} \quad (3-5)$$

where, $S_a^{Elastic}$ and $S_d^{Elastic}$ are the values of the elastic acceleration response spectra and displacement response spectra for the SDOF with $T_n = T_{Eff}$, respectively. The ω_{Eff} is the effective circular frequency that can be expressed as:

$$\omega_{Eff}^2 = \frac{K_{Eff} g}{W_{Eff}} = \left(\frac{2\pi}{T_{Eff}} \right)^2$$

(3-6)

where, g is the gravitational acceleration and K_{Eff} is the effective lateral stiffness of the equivalent SDOF system and is to be determined.

It should be noted that the design response spectrum obtained from seismic hazard maps are constructed based on an elastic SDOF system with 5% intrinsic damping; however, since most structures behave nonlinearly during an earthquake, an inelastic response spectrum should be produced considering the energy dissipated in the structure by the nonlinear behavior of the

SFRS elements. To account for the energy that dissipates in inelastic systems the response spectrum can be modified. Borzi et al (2001) and Filiatrault et al. (2002) suggested using a reduction factor, R , (also defined in Equation 2-31) that can be obtained by dividing response spectra of an elastic system by that of an inelastic system. The reduction factor, R , can be obtained by estimating the total damping of the system that includes both intrinsic and hysteretic damping ($\xi_{Total} = \xi_{Intrinsic} + \xi_{Hysteretic}$) and can be expressed as:

$$R = \frac{S_d^{Elastic}}{S_d^{Inelastic}} = \sqrt{\frac{2 + \xi_{Total}}{7}} \quad (3-7)$$

Therefore, the inelastic displacement response spectrum can be obtained by substituting Equations 3-6 and 3-7 into Equation 3-5:

$$S_d^{Inelastic} = \frac{W_{Eff}}{K_{Eff} g R} S_a^{Elastic} \quad (3-8)$$

Figure 3-6 presents the steps of producing the inelastic displacement response spectrum for a specific hazard level. Each point in the $S_d^{Inelastic}$ versus T_n curve represents the median of the maximum displacements of a SDOF system with fundamental period of T_n .

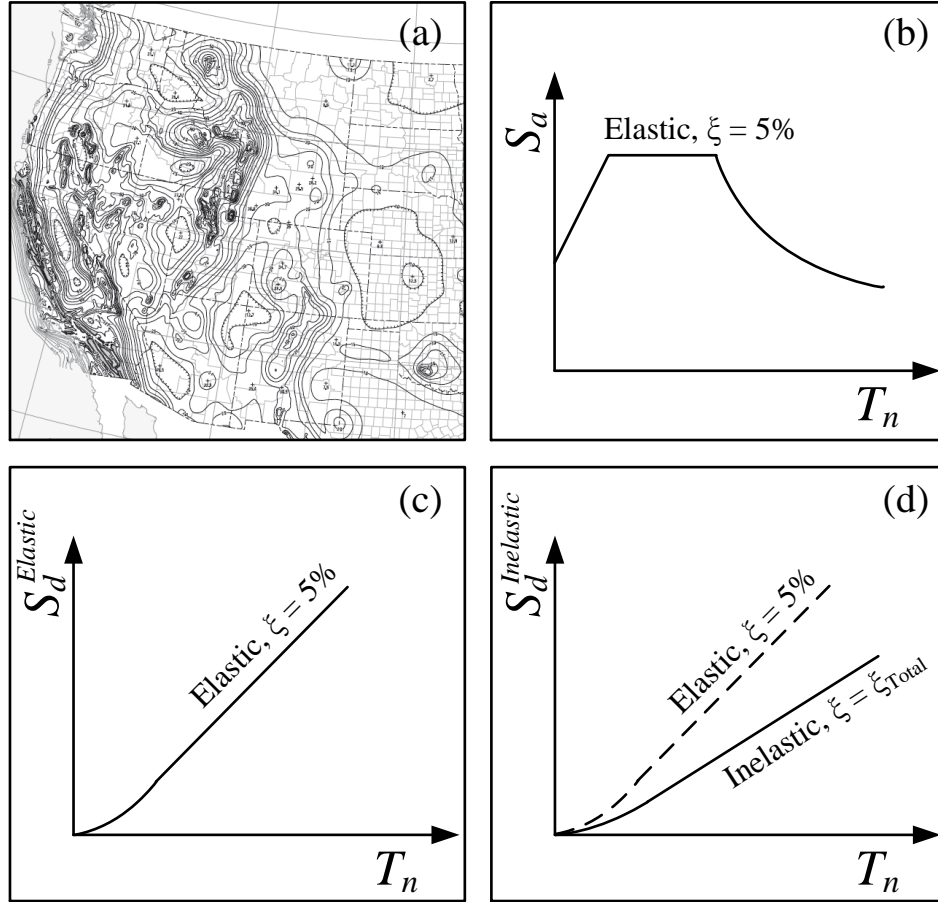


Figure 3-6: Steps for producing inelastic displacement response spectra: (a) seismic hazard map (ASCE 7-10, 2010); (b) elastic acceleration response spectra; (c) elastic displacement response spectra; (d) inelastic displacement response spectra.

The $S_d^{Inelastic}$ curves play a critical role in developing the DDD and simplified PBSR procedures in a way that it relates the maximum displacement of the SDOF to its fundamental period. As mentioned earlier, in the PBSR procedure the displacement is a known parameter (i.e., defined by the owner or building code), therefore, by setting the value of inelastic displacement response spectra equal to the specified target lateral displacement in Equation 3-8 (i.e.,

$S_d^{Inelastic} = \Delta_{Target} = \theta_{Target} \times h_{Eff} = \theta_{Eff @ Target} \times h_{Eff}$), the equivalent lateral stiffness (K_{Eff}) of the equivalent SDOF system can be calculated:

$$K_{Eff} = \frac{W_{Eff}}{h_{Eff} \theta_{Target} g R} S_a^{Elastic} \quad (3-9)$$

$$K_{Eff} = \frac{W_{Eff}}{h_{Eff} \theta_{Target} g R} \left\{ \begin{array}{ll} \left(\frac{3}{2} \right) S_{DS} \left(0.4 + 0.6 \frac{2\pi \sqrt{\frac{W_{Eff}}{K_{Eff} g}}}{T_0} \right) & , K_{Eff} > \frac{4\pi^2 W_{Eff}}{T_0^2 g} \\ \left(\frac{3}{2} \right) S_{DS} & , \frac{4\pi^2 W_{Eff}}{T_0^2 g} \geq K_{Eff} \geq \frac{4\pi^2 W_{Eff}}{T_s^2 g} \\ \left(\frac{3}{2} \right) \frac{S_{D1}}{2\pi \sqrt{\frac{W_{Eff}}{K_{Eff} g}}} & , \frac{4\pi^2 W_{Eff}}{T_s^2 g} > K_{Eff} \geq \frac{4\pi^2 W_{Eff}}{T_L^2 g} \\ \left(\frac{3}{2} \right) \frac{S_{D1} T_L}{\left(2\pi \sqrt{\frac{W_{Eff}}{K_{Eff} g}} \right)^2} & , K_{Eff} < \frac{4\pi^2 W_{Eff}}{T_L^2 g} \end{array} \right. \quad (3-10)$$

where, θ_{Eff} is the drift ratio of the equivalent SDOF (i.e., $\theta_{Eff} = \Delta_{Eff} / h_{Eff}$). It can be seen that all the parameters in the right side of Equation 3-10 are known; hence, K_{Eff} can be obtained by considering the ranges that step function is valid. It should be noted that K_{Eff} can be found by plotting the $S_d^{Inelastic}$ versus T_{Eff} .

The next step is finding the base shear, V_b which is also equal to the total lateral force applied to the structure (Figure 3-5). The base shear can be determined by multiplying the effective stiffness by the target lateral displacement of the SDOF system:

$$V_b = K_{Eff} \theta_{Target} h_{Eff} = K_{Eff} \Delta_{Target} \quad (3-11)$$

The distribution of lateral forces, F_j , can then be determined by multiplying $C_{v,j}$ of each story by V_b (Equation 3-12). The secant lateral stiffness at each story, $K_{s,j}$, can be calculated by dividing the shear force at the level of the story, V_j , by the pre-defined target inter-story drift at each story (Equation 3-13):

$$F_j = C_{v,j} V_b \quad , \quad j = 1, 2, \dots, N \quad (3-12)$$

$$K_{s,j} = \frac{V_1 = V_b}{(h_1) \theta_{1,Target}} \quad \text{for } j = 1 \quad \text{and} \quad K_{s,j} = \frac{V_j = \sum_{i=j}^N F_i}{(h_j - h_{j-1}) \theta_{j,Target}} \quad \text{for } j = 2, 3, \dots, N \quad (3-13)$$

The secant stiffness of the retrofits (i.e., $K_{Ret.}$) can then be calculated by subtracting the available secant stiffness of the existing SFRS (i.e., $K_{Avail.}$) from the required secant stiffness obtained from Equation 3-13 (i.e., $K_{Req.}$):

$$K_{Ret.} = K_{Req.} - K_{Avail.} \quad (3-14)$$

The last step in the simplified PBSR procedure is distributing the lateral force resisting elements such that the in-plane eccentricities (i.e., $e_x = |CR_x - CM_x|$ and $e_y = |CR_y - CM_y|$) in both principle directions at each story are minimized. From the basic principle of mechanics, the location of CR in the x – and y – direction can be calculated using the following equations:

$$CR_{x,j} = \frac{\left(\sum_{i=1}^{p_{y,Avail.}} k_{i,y}^{Avail.} x_i + \sum_{i=1}^{p_{y,Ret.}} k_{i,y}^{Ret.} x_i \right)_j}{\left(\sum_{i=1}^{p_{y,Avail.}} k_{i,y}^{Avail.} + \sum_{i=1}^{p_{y,Ret.}} k_{i,y}^{Ret.} \right)_j}, \quad j = 1, 2, \dots, N \quad (3-15)$$

$$CR_{y,j} = \frac{\left(\sum_{i=1}^{p_{x,Avail.}} k_{i,x}^{Avail.} y_i + \sum_{i=1}^{p_{x,Ret.}} k_{i,x}^{Ret.} y_i \right)_j}{\left(\sum_{i=1}^{p_{x,Avail.}} k_{i,x}^{Avail.} + \sum_{i=1}^{p_{x,Ret.}} k_{i,x}^{Ret.} \right)_j}, \quad j = 1, 2, \dots, N \quad (3-16)$$

where, $p_{x,Avail.}$ and $p_{y,Avail.}$ are the number of existing seismic force resisting members in the j^{th} story in the x - and y -direction, respectively; $p_{x,Ret.}$ and $p_{y,Ret.}$ are the number of retrofit elements in the j^{th} story in the x - and y -direction, respectively; $k_{i,x}^{Avail.}$ and $k_{i,y}^{Avail.}$ are the i^{th} elements of the existing SFRS in the x - and y -direction, respectively; $k_{i,x}^{Ret.}$ and $k_{i,y}^{Ret.}$ are the i^{th} elements of the retrofit system in the x - and y -direction, respectively; and, x_i and y_i are the distance of the SFRS elements from a specified coordinate system in the x - and y -direction, respectively. Figure 3-7 presents the steps for retrofitting existing buildings using the simplified PBSR procedure.

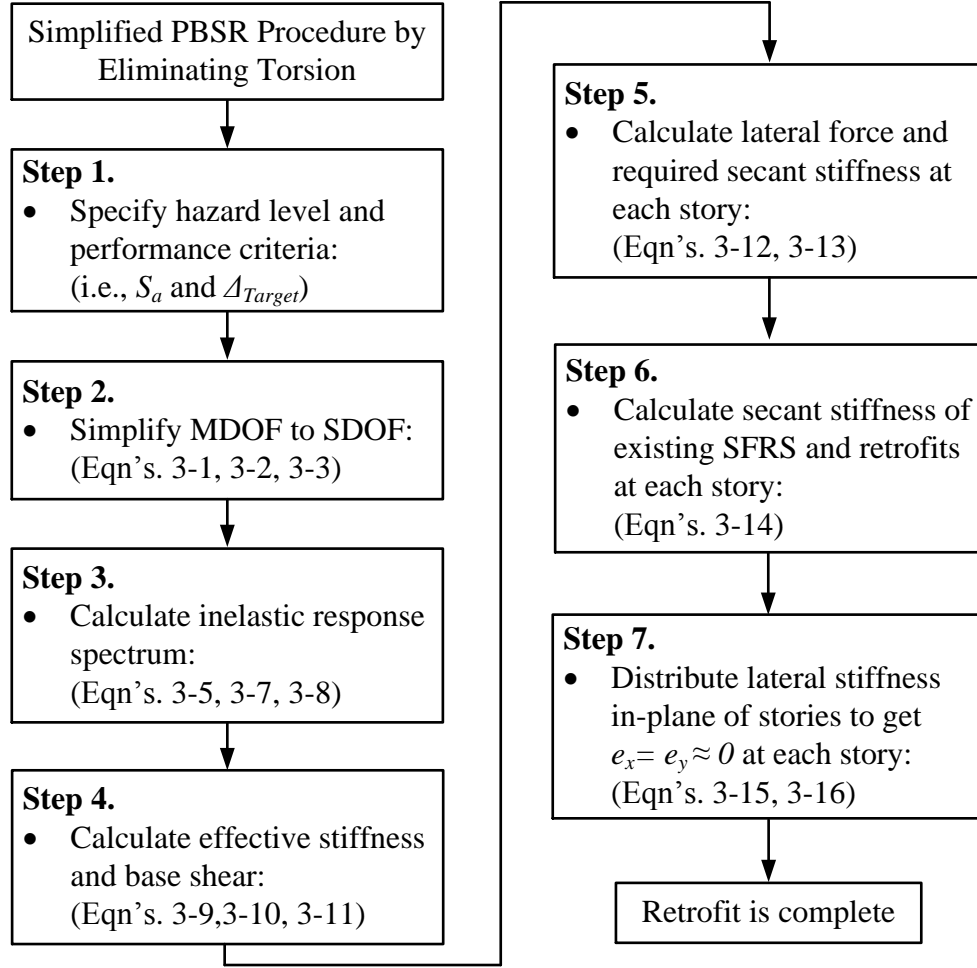


Figure 3-7: Flow diagram for PBSR procedure by eliminating torsion

The simplified PBSR method described in this section was applied to retrofit a four-story soft-story wood-frame building with in-plane horizontal (i.e., torsional) irregularity and its effectiveness was validated numerically using NLTH analysis and experimentally validated through full-scale shake table testing.

It should be noted that in order to retrofit any building, it is necessary to know the stiffness and strength of the existing SFRS of the building. The application and validation study in this dissertation is of a building constructed between 1920 and 1950 in San Francisco Bay Area. Since these buildings were constructed with archaic materials and many had not been adequately

tested for strength or stiffness, thus, the need for conducting tests on these materials was felt to be necessary during the course of this study. The next chapter presents a series of cyclic tests on isolated wood-frame walls with different sheathing materials in order to determine the relationship between strength (or stiffness) and displacement of these types of walls. The results of many of these tests were eventually used in retrofit design of the four-story soft-story wood-frame building (Chapter 5).

Chapter 4. ISOLATED WOOD-FRAME WALL TESTS⁴

As mentioned in the previous chapter, the strength and stiffness of the existing seismic force resisting system (SFRS) elements plays a very important role in retrofitting an existing structure. Existing buildings have walls and floor systems that consist of archaic material with unknown stiffness and strength. This becomes more of an issue when retrofitting existing wood-frame buildings. Wood-frame buildings are unique in that the non-structural finishes such as gypsum wall board and stucco have been shown to provide significant stiffness and strength relative to the designated seismic force resisting system, e.g. wood shear walls (Filiatrault et al, 2010). Wall finishes, or components within a wood-frame wall sub-assembly, can consist of multiple layered modern and/or archaic elements such as wood planks, drywall, plaster on lathe, stucco, and plywood. There exist significant differences in ductility amongst these materials raising questions on how best to superimpose single-degree-of-freedom hysteretic models or backbone curves during non-linear time-history (NLTH) analysis or when combining backbone curves for design and retrofit.

Hysteretic modeling of light-frame wood (wood-frame) buildings typically consists of modeling each wood shear (or other) wall or wall segment as a single-degree-of-freedom (SDOF) hysteretic oscillator and then combining them into a more complex system. This method has been used for decades but gained significant popularity within the research community as a result of the development of the Seismic Analysis of Wood-frame Structure (SAWS) model (Folz and Filiatrault, 2004a; 2004b). The SAWS model allowed three degrees of freedom at each story,

⁴ Bahmani, P. and van de Lindt, J. (2014). "Experimental and Numerical Assessment of Woodframe Sheathing Layer Combinations for Use in Strength-Based and Performance-Based Design." *J. Struct. Eng.*, 10.1061/(ASCE)ST.1943-541X.0001134 , E4014001.

assuming a rigid plate for each floor/roof diaphragm. Later, this seminal model was improved upon to allow six DOF's at each diaphragm but the rigid plate assumption remained (Pei and van de Lindt, 2008). More advanced models that allow the combination of hysteretic wall elements and other conventional finite elements have been developed (see e.g. Pang and Hassanzadeh Shirazi, 2013; Dao and van de Lindt, 2013). One common thread that runs throughout all of those models is the need to accurately superimpose the effect of layering sheathing materials, which provides impetus for this study.

Layering of wall materials in non-linear numerical models has been utilized within several projects. Rosowsky (2002) modeled wood-frame shear walls using SAWS and later added the effect of gypsum wall board (GWB) (Kim and Rosowsky, 2005). van de Lindt et al. (2010) modeled the two-story building tested by Filiatrault et al. (2010) at different stages of building finish, specifically wood-only, GWB added, and the completed building with stucco on the outside. They superimposed the hysteretic shear wall representation directly with no reduction factor for less ductile sheathing materials. The accuracy of the numerical predictions compared with test results was deemed to be good, but discrepancies with the stucco model persisted. A recent report published by the Federal Emergency Management Agency (FEMA) on seismic evaluation and retrofit of weak-story wood-frame buildings provided a detailed approach to superimpose hysteric backbones for wall sheathing materials with high and low displacement capacity (FEMA P-807, 2012). In the FEMA P-807 document, it is stated that when wood structural panels are combined with other sheathing materials in a wall assembly, the total strength is less than the sum of the parts. It is then proposed in FEMA P-807 document to construct two load-drift curves and select the curve with the larger peak strength. A backbone curve, designated as *composite curve* one is then constructed using 50 percent of the strength of

the wood structural panel and 100 percent of other sheathing material, and *composite curve two* is constructed using 100 percent of the strength of the wood structural panel and 50 percent of the other sheathing material. This was reasoned out through extensive discussion during the project but a dearth of experimental data on walls tested with more than one layer of sheathing (other than wood structural panels + gypsum wall board) remains. It is duly noted that during the development of the values used to represent various combination of wall sheathing in FEMA P-807, archaic, primarily monotonic data, was used. Therefore, one purpose of this test program beyond numerical combination in non-linear time-history (NLTH) analysis, is to provide additional information for consideration when retrofitting soft-story wood-frame buildings.

This chapter presents the method and results of an experimental study of 18 wood-frame walls with one, two, or three of the finishes described is presented. Testing was performed to determine the best approach to add the sheathing layers numerically when combining the backbone curves for analysis and design. Non-linear time-history (NLTH) analyses were then conducted to quantify the difference between the behavior of the combined sheathing test and the superimposed single layer sheathings. The hysteric backbones are constructed for each combination of sheathing materials using the CUREE ten-parameter hysteretic model (Folz and Filiatrault, 2001) and Evolutionary Parameter Hysteretic Model (EPHM) (Pang et. al, 2007) and compared to the FEMA P-807 proposed approach. Relevant test results were used to calibrate models for the the retrofit design of a four-story building tested at the NEES@UC-San Diego shake table facility. Furthermore, these results can be used to retrofit a wide range of wood-frame building made of walls sheathed with different sheathing material thereby serving as a first of its kind data set for retrofitting wood-frame buildings.

4.1 Experimental Test Setup and Test Specimens

Figure 4-1 shows the test setup in the Structural Engineering Laboratory at Colorado State University. A single actuator with pin-pin end conditions was attached to a steel loading bar. Six 16 mm (5/8 in.) diameter anchor bolts and standard commercially-available hold downs were used to connect the sill plate to the base steel (i.e., foundation). The anchor bolts were used to transfer the shear force to the base steel and the hold downs were used to ensure that it was the sheathing being tested, i.e. essentially eliminate the risk of an end-post failure prior to reaching peak capacity. The test setup was designed such that the exterior sheathing(s) can rotate freely at the top and bottom edges of the wall. Figure 4-2 presents the details of the experimental test setup and the boundary conditions at the top and bottom connections. It should be noted that the loading bar was free to rotate in the plane of applied force by the actuator and did not add any constraint to the vertical displacement. The CUREE-Caltech loading protocol was used as a guide, but no monotonic testing was performed as typically required to identify the so-called reference displacement (Krawinkler et al., 2000); instead a reference displacement was assumed based on information from other tests and remained consistent for all tests regardless of sheathing type. The test protocol is shown in Figure 4-3 and was used throughout the test program. The loading rate was 0.2 Hz and then was reduced to 0.1 Hz which led to smoother hysteresis curves and better captured the peak points for the backbone curve development. This loading rate modification was not felt to result in any substantial change in the magnitude or shape of the test results, but as mentioned was simply modified to allow easier data processing, and was therefore neglected. It should be noted that the test was stopped prior to completing the full test protocol for many of the specimens due to failure of the specimen (i.e., observing a flat load-displacement curve) or instability, or both.

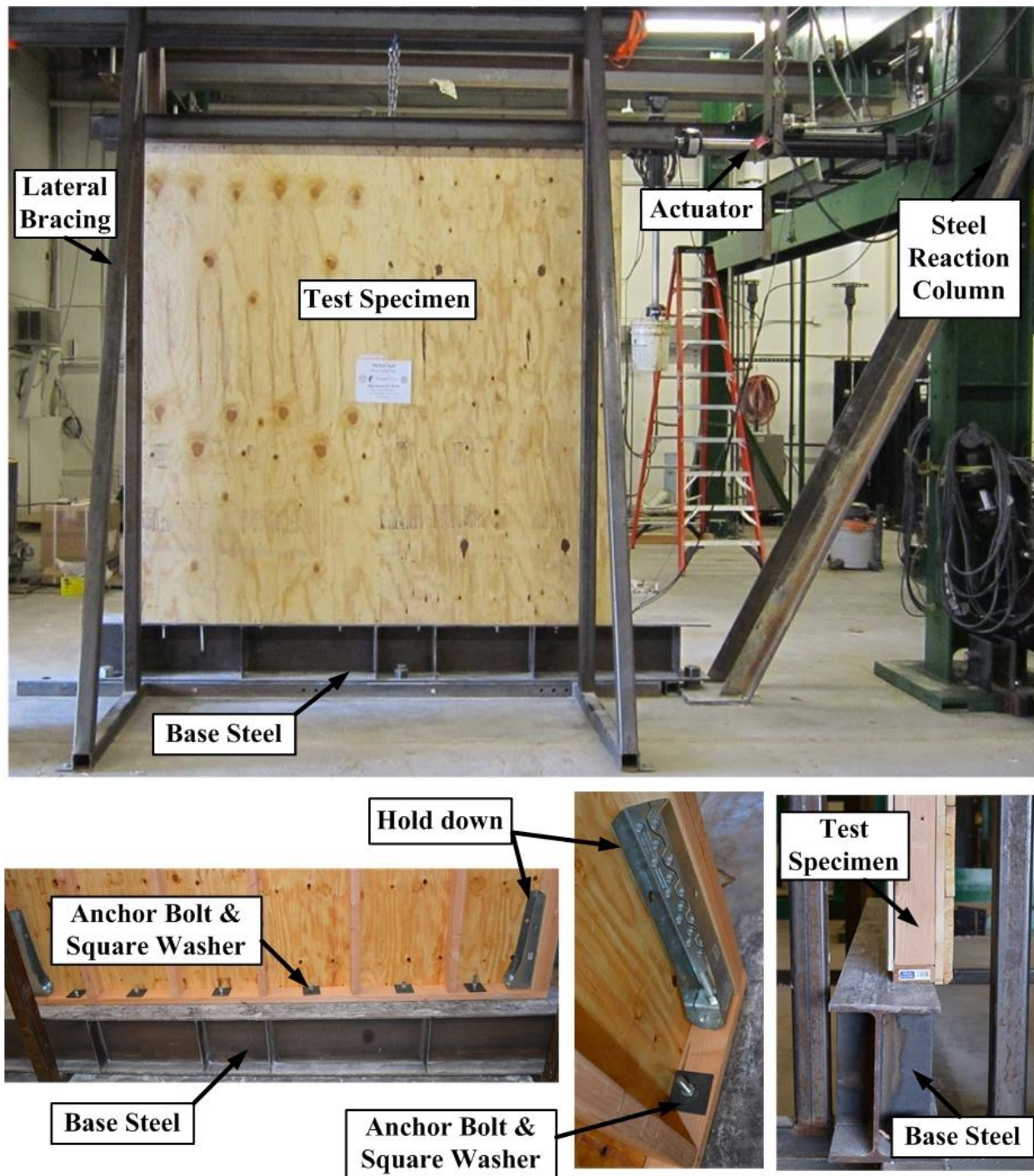


Figure 4-1: Test setup of the cyclic testing of isolated shear walls at Colorado State University

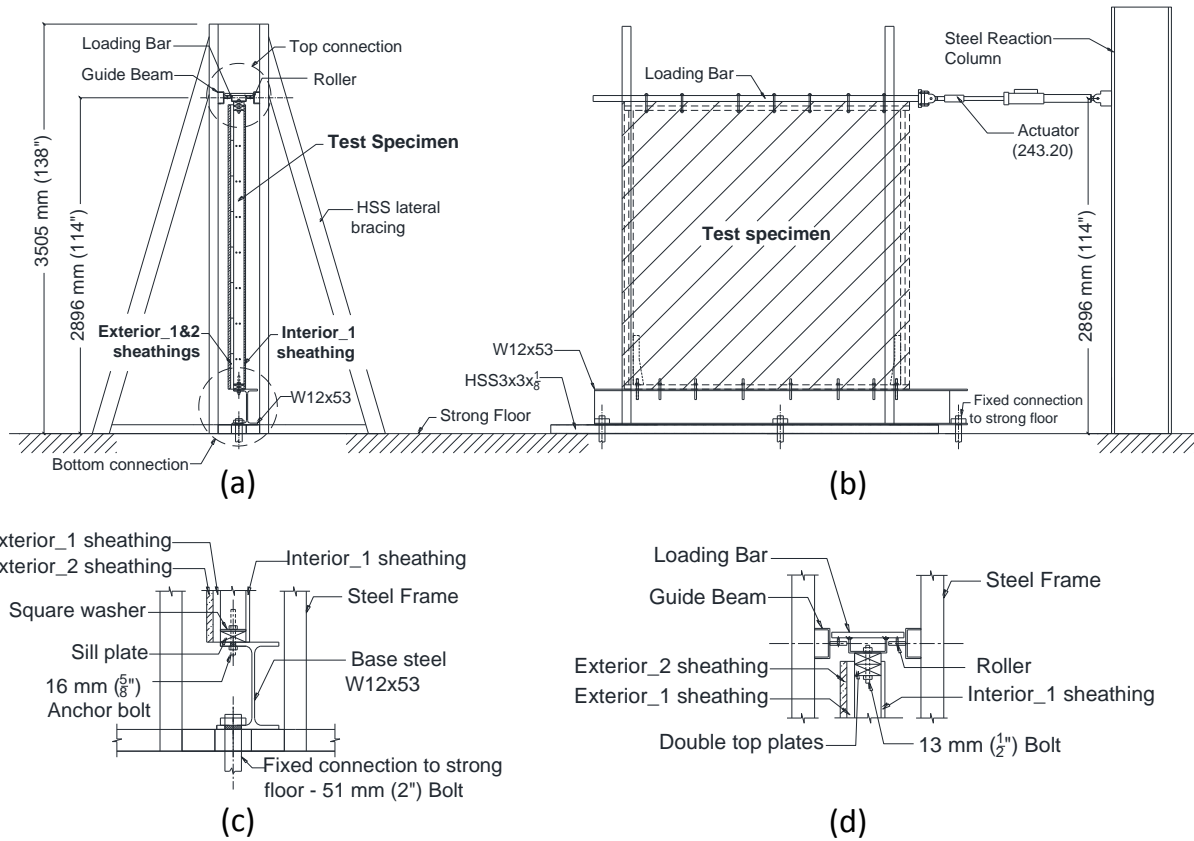


Figure 4-2: Experimental test setup for wall testing at Colorado State University: (a) side view, (b) front view, (c) bottom boundary condition, (d) top boundary condition.

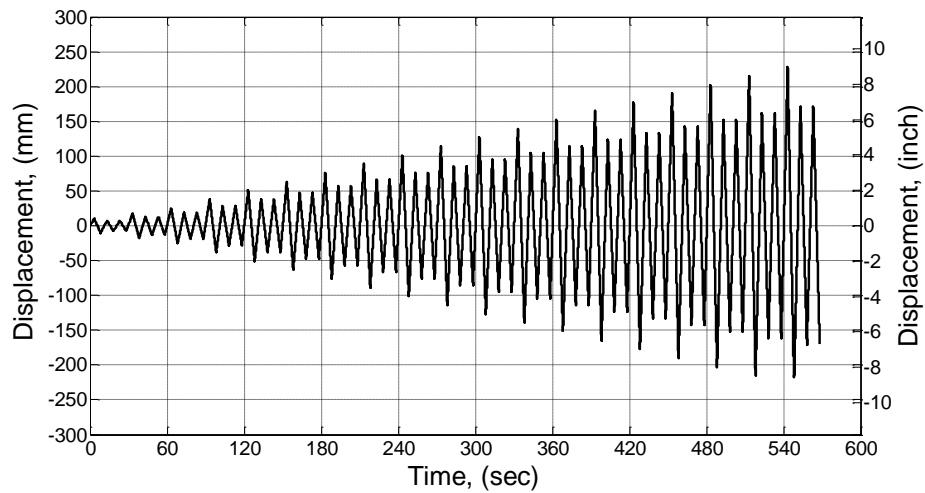


Figure 4-3: Displacement-based test protocol used for wall tested at CSU with 0.1 Hz loading rate.

Although FEMA P-807 includes eight different types of sheathing materials in its load-drift (backbone) curve discussion, only four were investigated in this experimental study. Table 4-1 presents a comparison of the most common sheathing materials (FEMA P-807, 2012) with an indication as to whether they were included in the present experimental study.

Table 4-1: Sheathing materials included in the experimental study

Sheathing Material	Included
Stucco	Yes
Horizontal wood sheathing or wood siding	Yes
Diagonal wood sheathing	Yes
Plaster on wood lath	No
Plywood panel siding	No
Gypsum wallboard	Yes
Plaster on gypsum lath	No
WSP, 8d@102 mm (4") o.c. ^(a)	Yes

^(a) WSP is wood structural panel; Spacing of 8d and 10d nails at 51 mm, 76 mm, 102 mm and 152 mm (2, 3, 4 and 6 in.) o.c. was also considered in Table 4-1 of FEMA P-807.

Each of these sheathing materials was tested individually by being attached to 2×4 Douglas-Fir-Larch (DFL) framing with studs at 406 mm (16 in.) o.c., a double top plate and double end posts where hold downs were installed. Hold downs were included to ensure that the test was focused on the sheathing materials and their combinations and not failure of the framing, such as end post failure or sill plate splitting. A typical test specimen with three layers of sheathing is shown in Figure 4-4. 16d common nail with shank diameter of 4.1 mm (0.162 in.) and shank length of 88.9 mm (3.5 in.) nails were used for framing of the wall specimens.

to the 2×4 wood framing on the interior of the building. Figure 4-5 shows a schematic for clarity. The same logic was used for the exterior sheathing layer.

Eighteen 2.44×2.44 m (8×8 ft) shear wall test specimen were constructed. Table 4-2 shows the specimens with one, two, and three layers of sheathing material. Eight specimens with single layer sheathing were tested in order to obtain the hysteresis and backbone curve for one layer of sheathing material. The results of these single sheathing tests were combined using several different approaches and compared to the strength of the walls tested with the same two- or three-layered sheathing combination. For example, the backbone curves for S-01 and W-01 are combined and compared with the backbone curve of SW-01. In reality the same test types were averaged and then the comparison conducted. Three specimens with two layers of sheathing material and seven specimens with three-layer sheathings were tested.

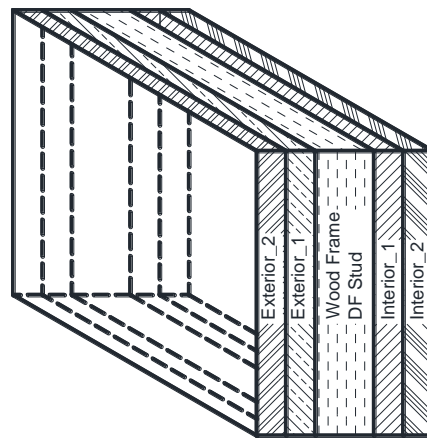


Figure 4-5: Schematic showing the wall sheathing designation for layering

Table 4-2: Experimental test matrix for 2.44×2.44 m (8×8 ft) wall specimens

Test No.	Specimen	Sheathing Material		
		Exterior_2	Exterior_1	Interior_1
1	G-01	-		Gypsum Wallboard
2	G-02	-		Gypsum Wallboard
3	H-01*	-	Horizontal Wood Siding	-
4	H-02*	-	Horizontal Wood Siding	-
5	S-01*	-	Stucco	-
6	S-02*	-	Stucco	-
7	W-01	-	Wood Structural Panel	-
8	W-02	-	Wood Structural Panel	-
9	SDG-01	Stucco	Diagonal Wood Sheathing	Gypsum Wallboard
10	SDG-02	Stucco	Diagonal Wood Sheathing	Gypsum Wallboard
11	SW-01*	Stucco	Wood Structural Panel	-
12	SW-02	Stucco	Wood Structural Panel	-
13	HG-01	-	Horizontal Wood Siding	Gypsum Wallboard
14	HDG-01	Horizontal Wood Siding	Diagonal Wood Sheathing	Gypsum Wallboard
15	HWG-01	Horizontal Wood Siding	Wood Structural Panel	Gypsum Wallboard
16	HWG-02	Horizontal Wood Siding	Wood Structural Panel	Gypsum Wallboard
17	SWG-01	Stucco	Wood Structural Panel	Gypsum Wallboard
18	SWG-02	Stucco	Wood Structural Panel	Gypsum Wallboard

* Loading rate= 0.2 Hz.

4.1.1 Single-layer Sheathing Tests

Eight specimens with single layers of sheathing were tested using the cyclic load protocol shown earlier in order to obtain the hysteresis and backbone curve for each sheathing material. The gypsum wallboard specimens had one layer of 12.7 mm (0.5 in.) thick regular gypsum wallboard fastened to framing studs with #6 coarse thread bugle head drywall screws at 406 mm (16 in.) spacing. The gypsum wallboard panels were installed vertically and the edge at the middle was sealed with mud and mesh tape. Two specimens were tested under cyclic loading up to about 130 mm (~ 5 in.) of lateral displacement. The specimens with horizontal wood siding were made of single layer of 1×8 (25×203 mm) Spruce-Pine-Fir (SPF) wood siding attached to the framing stud by means of 8d common nails with shank diameter of 3.4 mm (0.134 in.), shank length of

63.5 mm (2.5 in.), and head diameter of 7.1 mm (9/32 in.). The distance from the nail to the edge of the wood siding (i.e., edge distance) was 38 mm (1.5 in.). Two specimens with one layer of 22.2 mm (7/8 in.) thick stucco were constructed to be as close as possible to the construction method of the 1920's to 1950's. This consisted of five sub layers: a weather barrier layer, wire lath, a scratch coat, a brown coat, and a finish coat. Figure 4-6 presents the construction sequence for the stucco sheathing process. The stucco specimens were fully cured before testing and had 28 day compressive strength from 17.2 to 20.7 Mpa (2.5 to 3.0 ksi) and a unit weight of 478 N/m² (10 psf) but were tested approximately six months after construction of the specimens with stucco. The specimens with wood structural panels were constructed using 11.9 mm (15/32 in.) thick plywood (sheathing rated) attached with 8d common nails to the framing studs with edge and field nail spacing of 102 mm (4 in.) o.c. and 305 mm (12 in.) o.c., respectively.

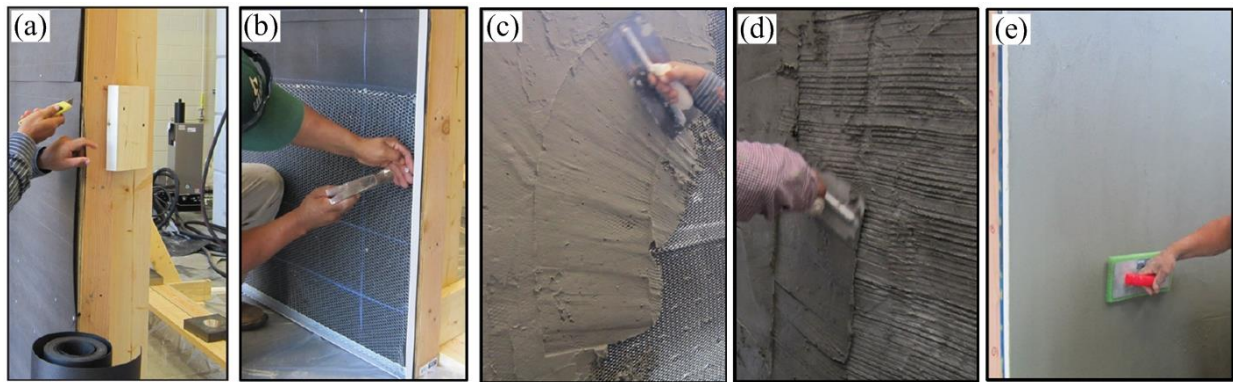


Figure 4-6: Construction sequence of stucco sheathing: (a) weather barrier layer, (b) wire lath, (c) scratch coat, (d) brown coat, (e) finish coat.

All the single-layer sheathing specimens were tested using a cyclic displacement protocol, as mentioned, and the force recorded resulting in a hysteresis curve. The CUREE ten-parameter hysteretic model (Folz and Filiatrault, 2001) and EPHM hysteretic model (Pang et al., 2007) were then fit to the experimental data to obtain the hysteretic parameters. Figure 4-7 and Figure

4-8 provide the CUREE ten-parameter and EPHM hysteretic models, respectively (Pei and van de Lindt, 2008 and also Pang et al, 2007). Both experimental hysteresis and numerical hysteresis curves for all eight single sheathing test specimens (Tests 1 to 8) are presented in Figure 4-9 and Figure 4-10. The experimental hysteresis curves with experimental backbones are presented in column (a) of the figures; whereas, the EPHM sixteen-parameter numerical hysteresis fit to the experimental backbones are presented in column (b) of the figures. The hysteretic parameters of CUREE and EPHM hysteretic models are presented in Table 4-3 and

Table 4-4, respectively.

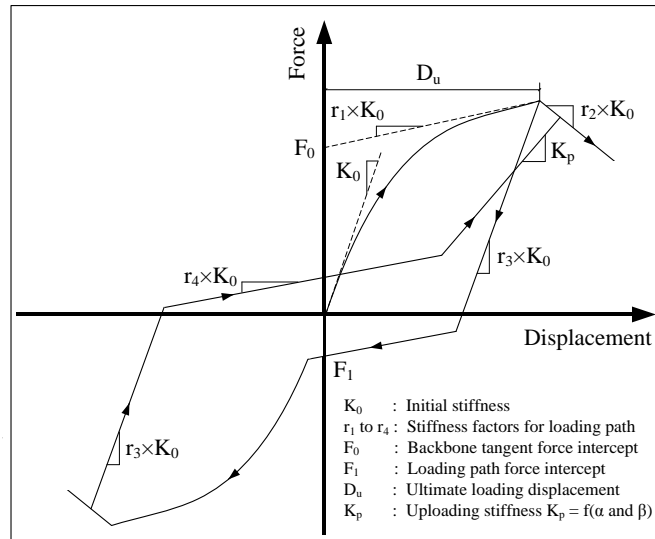


Figure 4-7: CUREE ten-parameter hysteretic model (data from Pei and van de Lindt, 2008).

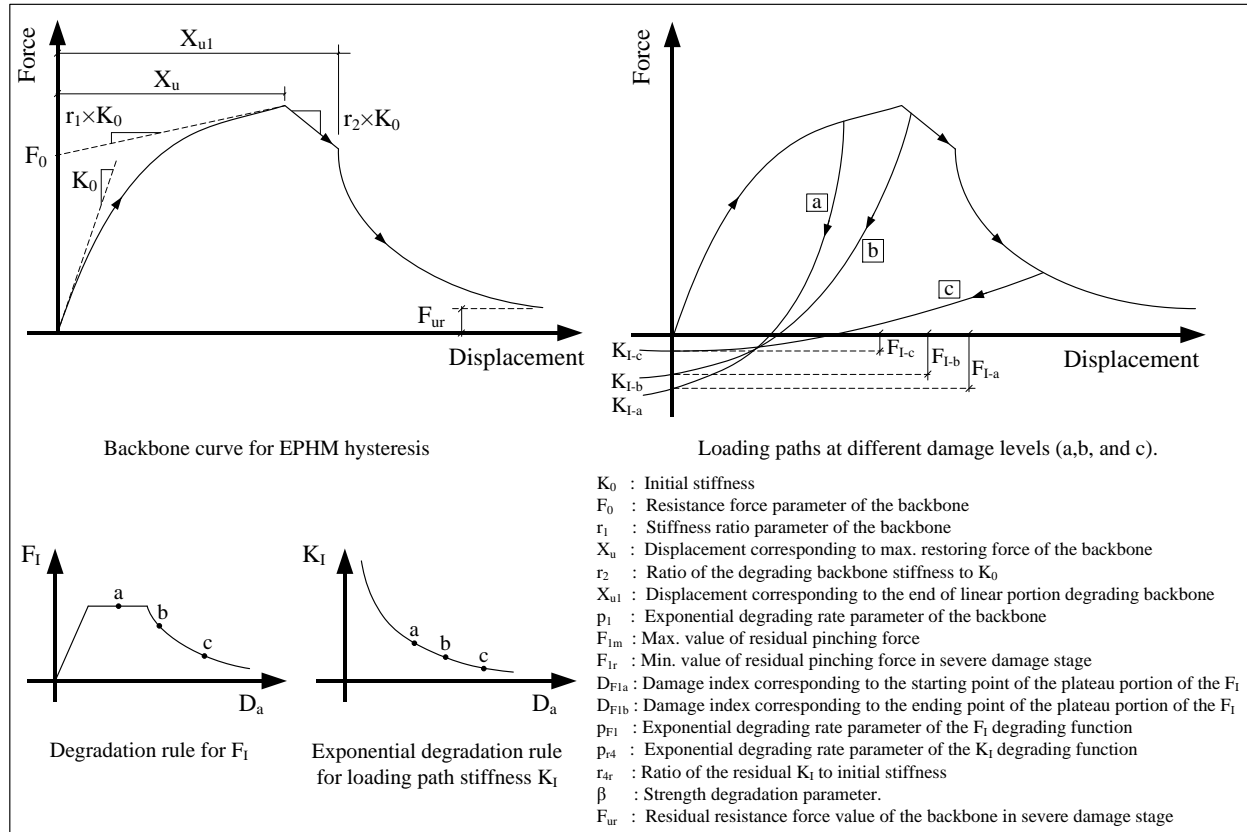


Figure 4-8: EPHM sixteen-parameter hysteretic model (data from Pei and van de Lindt, 2008).

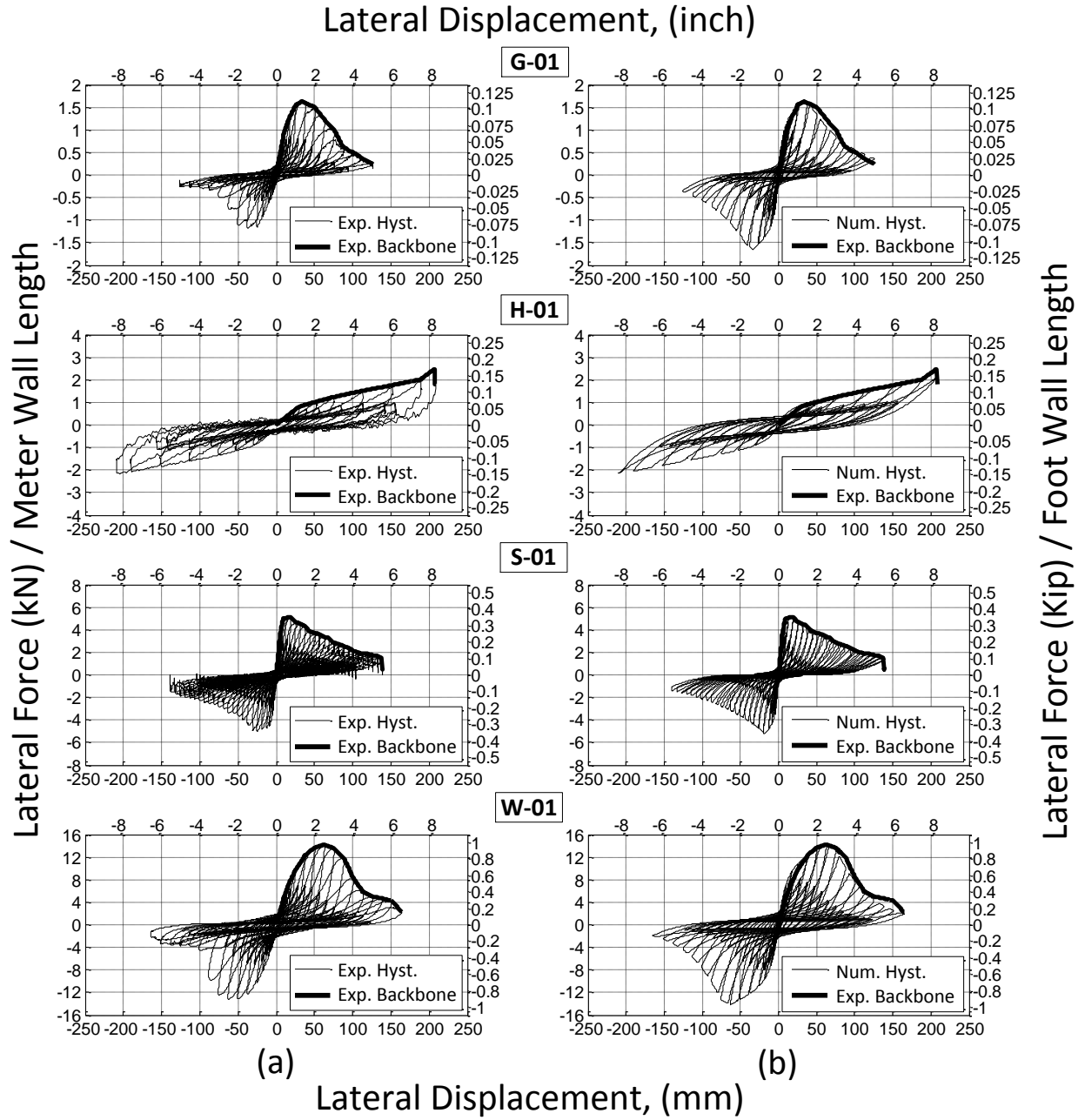


Figure 4-9: Hysteresis curves of single-layer sheathing specimens for the first set of tests: a) Experimental; and b) EPHM 16-parameter hysteresis fitted to experimental backbone.

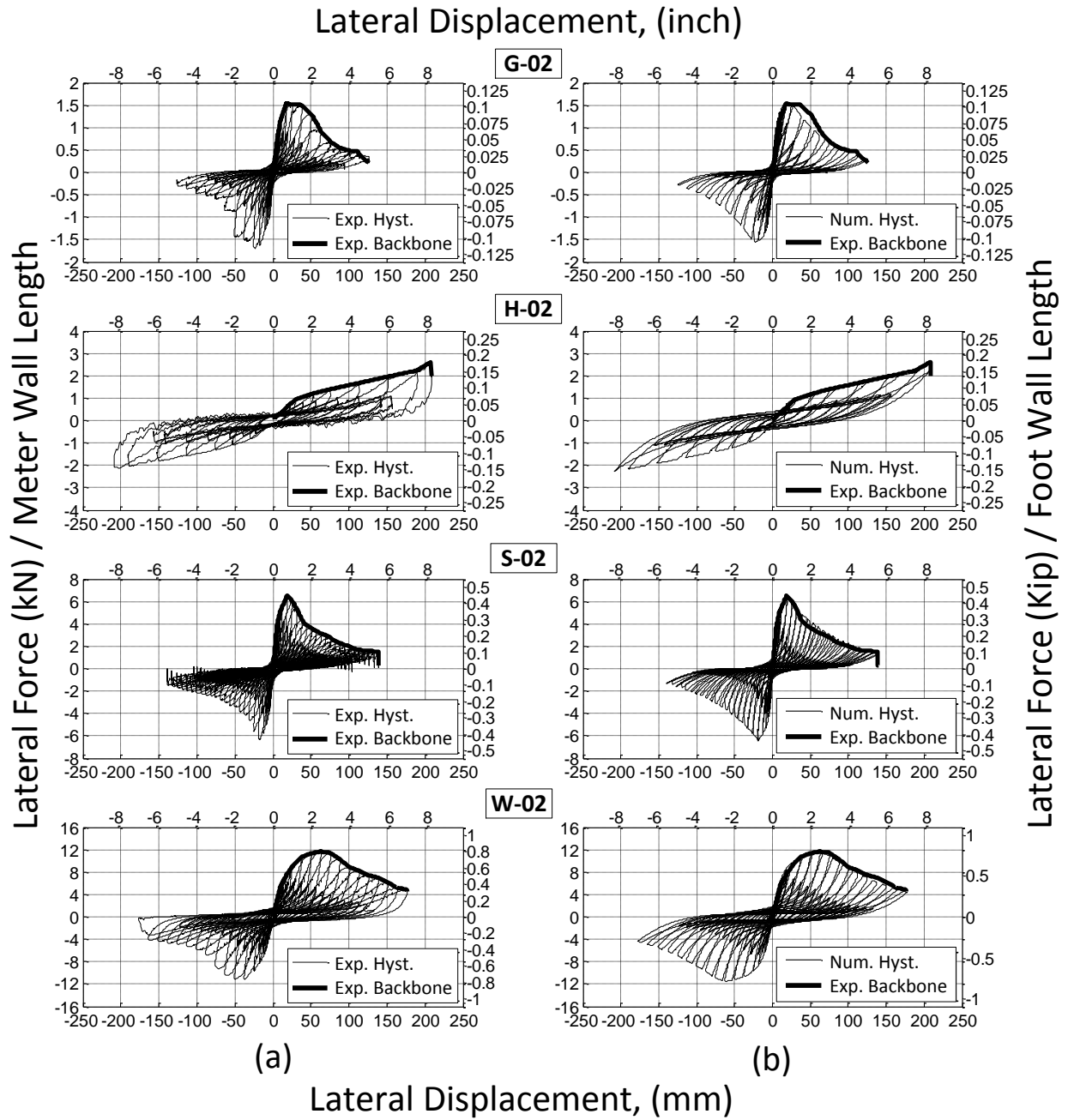


Figure 4-10: Hysteresis curves of single-layer sheathing specimens for the second set of tests: a) Experimental; and b) EPHM 16-parameter hysteresis fitted to experimental backbone.

Table 4-3: CUREE 10-hysteresis parameters for specimens with single sheathing

Specimen	K_0 , kN/mm/m (Kip/in./ft)	F_0 , kN/m (Kip/ft)	F_1 , kN/m (Kip/ft)	r_1	r_2	r_3	r_4	D_u , mm (in.)	α	β
G-01	0.24 (0.42)	1.17 (0.08)	0.15 (0.01)	0.070	-0.078	1.070	0.007	34.1 (1.34)	0.75	1.05
G-02	0.36 (0.62)	1.46 (0.10)	0.15 (0.01)	0.020	-0.040	1.000	0.006	23.6 (0.93)	0.75	1.05
H-01	0.06 (0.11)	0.58 (0.04)	0.29 (0.02)	0.140	-0.050	1.000	0.070	208 (8.19)	0.44	1.10
H-02	0.06 (0.11)	0.88 (0.06)	0.29 (0.02)	0.115	-0.050	1.050	0.070	208 (8.19)	0.35	1.05
S-01	1.36 (2.37)	4.09 (0.28)	0.44 (0.03)	0.040	-0.030	1.000	0.005	18.8 (0.74)	0.85	1.05
S-02	1.74 (3.02)	4.52 (0.31)	0.73 (0.05)	0.050	-0.045	1.000	0.005	19.1 (0.75)	0.70	1.05
W-01	1.13 (1.97)	9.19 (0.63)	1.61 (0.11)	0.061	-0.115	1.000	0.016	63.0 (2.48)	0.70	1.10
W-02	0.93 (1.61)	9.49 (0.65)	1.61 (0.11)	0.035	-0.080	1.000	0.015	63.0 (2.48)	0.73	1.10

Table 4-4: EPHM 16-hysteresis parameters for specimens with single sheathing

EPHM Parameters	Units per wall length	Specimen							
		G-01	G-02	H-01	H-02	S-01	S-02	W-01	W-02
K_0	kN/mm/m	0.24	0.36	0.06	0.06	1.36	1.74	1.13	0.93
	Kip/in/ft	0.42	0.62	0.11	0.11	2.38	3.02	1.97	1.61
F_0	kN/m	1.17	1.46	0.73	0.88	4.09	4.67	9.49	10.07
	Kip/ft	0.08	0.10	0.05	0.06	0.28	0.32	0.65	0.69
r_1	-	0.07	0.02	0.11	0.11	0.04	0.05	0.07	0.03
X_u	mm	34.0	23.6	208	208	19.1	19.1	63.0	63.0
	in.	1.34	0.93	8.19	8.19	0.75	0.75	2.48	2.48
r_2	-	-0.05	-0.05	-0.05	-0.05	-0.05	-0.05	-0.05	-0.05
X_{u1}	mm	40.9	28.4	249	249	22.6	22.6	75.4	75.4
	in.	1.61	1.12	9.82	9.83	0.89	0.89	2.97	2.98
p_1	-	-0.44	-0.43	-0.20	-0.20	-0.28	-0.34	-0.57	-0.23
F_{1m}	kN/m	0.29	0.29	0.44	0.44	0.73	1.02	2.19	1.75
	Kip/ft	0.02	0.02	0.03	0.03	0.05	0.07	0.15	0.12
F_{1r}	kN/m	0.012	0.013	0.019	0.020	0.039	0.049	0.107	0.088
	Kip/ft	0.0008	0.0009	0.0013	0.0014	0.0027	0.0034	0.0073	0.0060
D_{F1a}	mm	17.0	11.9	103.9	104.1	9.40	9.40	31.5	31.5
	in.	0.67	0.47	4.09	4.10	0.37	0.37	1.24	1.24
D_{F1b}	mm	40.9	28.4	249.4	249.7	22.6	22.6	75.4	75.7
	in.	1.61	1.12	9.82	9.83	0.89	0.89	2.97	2.98
p_{F1}	-	-0.62	-0.89	-0.10	-0.10	-1.12	-1.12	-0.34	-0.34
p_{r4}	-	-1.95	-2.07	-0.82	-1.32	-3.14	-3.44	-1.20	-1.20
r_{4r}	-	0.0001	0.0001	0.0450	0.0610	0.0001	0.0001	0.0001	0.0001
β	-	1.08	1.10	1.10	1.10	1.05	1.05	1.05	1.05
F_{ur}	kN/m	0.015	0.015	0.029	0.029	0.058	0.073	0.146	0.117
	Kip/ft	0.001	0.001	0.002	0.002	0.004	0.005	0.010	0.008

4.1.2 Two- and Three-layer Sheathing Tests

In order to model the behavior of the specimens with combined sheathings, the EPHM hysteretic model was used since this model has more flexibility to fit into the backbone of the two- and three-layer sheathing specimens. The EPHM hysteretic curve was fit to the averaged backbone curve of the two identical specimens. Table 4-5 presents the sixteen parameters per unit length of the wall for the EPHM models of each combined sheathing test. The experimental test results with the corresponding numerical hysteresis fits of six different sheathing combinations are presented in Figure 4-11. It should be noted that the test regarding the second specimen with stucco and WSP sheathings was stopped due out-of-plane movement of the specimen and thus, the hysteretic parameters are not presented in Table 4-5. The test setup was modified for the remainder of the tests and out of plane movement was no longer an issue.

Table 4-5: EPHM 16-hysteresis parameters for specimens with combined sheathing

EPHM Parameters	Units per wall length	Specimen								
		SDG 01	SDG 02	SW 01	HG 01	HDG 01	HWG 01	HWG 02	SWG 01	SWG 02
K_0	kN/mm/m	0.80	0.81	2.07	0.34	1.11	1.04	1.04	1.92	2.14
	Kip/in/ft	1.40	1.41	3.61	0.60	1.94	1.81	1.81	3.35	3.73
F_0	kN/m	9.92	11.68	6.42	1.61	7.44	9.05	9.05	6.57	7.59
	Kip/ft	0.68	0.80	0.44	0.11	0.51	0.62	0.62	0.45	0.52
r_1	-	0.05	0.04	0.14	0.08	0.10	0.18	0.23	0.13	0.14
X_u	mm	48.5	63.0	50.0	37.6	63.0	53.3	53.3	50.3	50.3
	in.	1.91	2.48	1.97	1.48	2.48	2.10	2.10	1.98	1.98
r_2	-	-0.05	-0.07	-0.05	-0.05	-0.05	-0.05	-0.05	-0.08	-0.08
X_{u1}	mm	58.2	75.7	59.9	45.2	75.7	60.5	60.5	60.5	60.5
	in.	2.29	2.98	2.36	1.78	2.98	2.38	2.38	2.38	2.38
p_1	-	-0.77	-1.27	-1.85	-0.40	-1.07	-1.04	-1.04	-1.04	-1.84
F_{1m}	kN/m	1.77	1.55	3.11	0.39	2.10	3.25	3.25	2.90	3.23
	Kip/ft	0.1213	0.1062	0.2131	0.0267	0.1439	0.2227	0.2227	0.1987	0.2213
F_{1r}	kN/m	0.09	0.10	0.16	0.02	0.11	0.16	0.16	0.15	0.16
	Kip/ft	0.0062	0.0069	0.0110	0.0014	0.0075	0.0110	0.0110	0.0103	0.0110
D_{F1a}	mm	24.1	6.1	24.9	18.8	31.5	25.1	25.1	25.1	25.1
	in.	0.95	0.24	0.98	0.74	1.24	0.99	0.99	0.99	0.99
D_{F1b}	mm	58.2	75.7	59.9	45.2	75.7	60.5	60.5	60.5	60.5
	in.	2.29	2.98	2.36	1.78	2.98	2.38	2.38	2.38	2.38
p_{F1}	-	-0.44	-0.34	-0.42	-0.56	-0.34	-0.42	-0.42	-0.62	-0.42
p_{r4}	-	-1.52	-1.50	-1.51	-1.37	-1.15	-1.30	-1.30	-2.20	-2.50
r_{4r}	-	0.01	0.02	0.02	0.00	0.00	0.02	0.02	0.02	0.02
β	-	1.06	1.06	1.10	1.10	1.10	1.10	1.10	1.10	1.10
F_{ur}	kN/m	0.12	0.13	0.21	0.03	0.14	0.22	0.22	0.19	0.22
	Kip/ft	0.0082	0.0089	0.0144	0.0021	0.0096	0.0151	0.0151	0.0130	0.0151

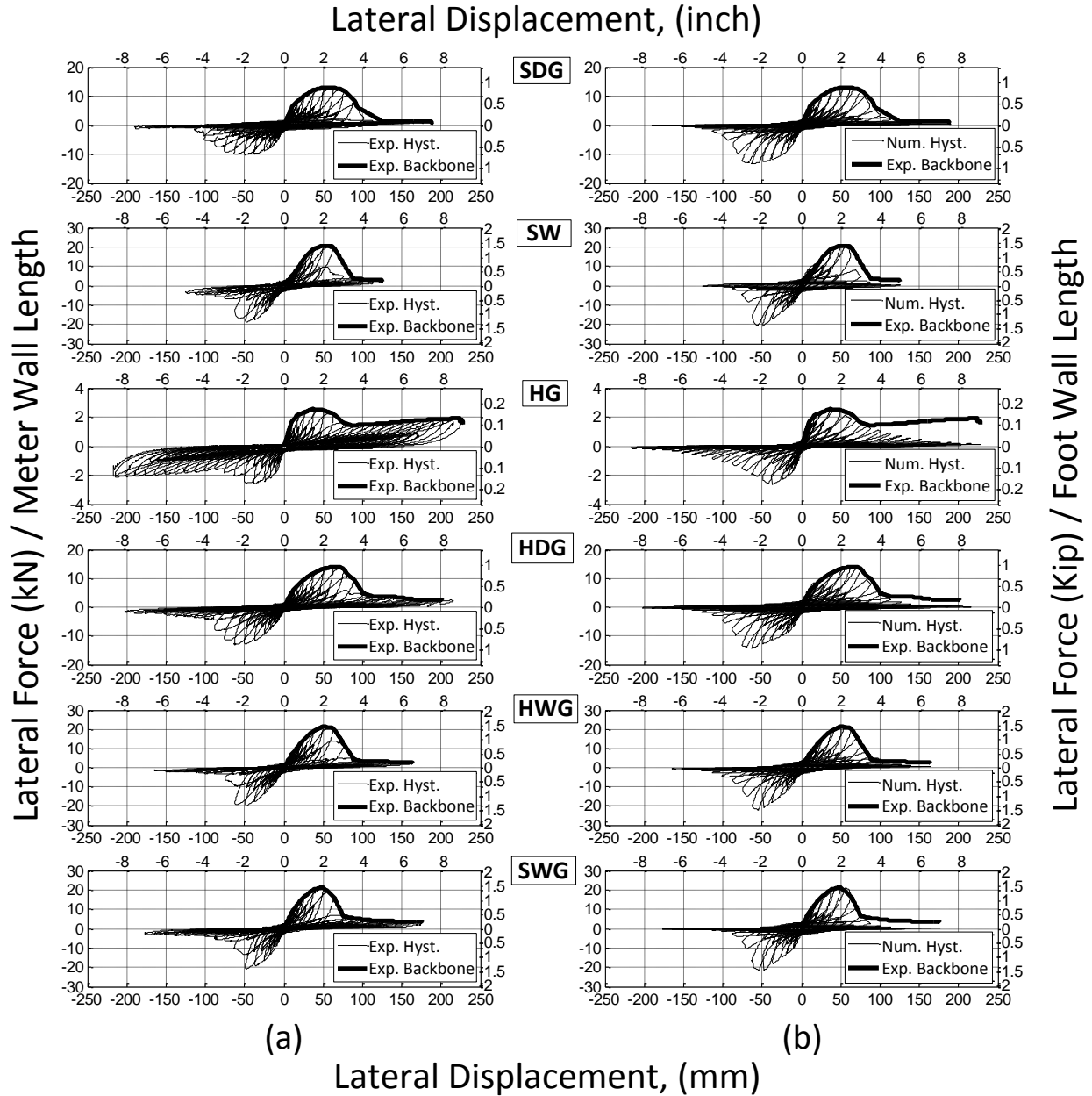


Figure 4-11: Hysteresis curves of two- and three-layer sheathing specimens: a) experimental; and, b) EPHM 16-parameter hysteresis fitted to experimental backbones.

4.2 Comparison of backbones from the experimental tests and P-807 data set

In order to make a direct comparison between the backbones used in FEMA P-807 (2012) and the hysteretic backbones obtained from the experimental tests, the backbones for each single

sheathing wall specimen are shown in Figure 4-12 along with the force-displacement backbones provided by FEMA P-807. From inspection of Figure 4-12, one can see that the backbones from the experimental data are close for the specimens with stucco and wood structural panel, but there is a significant difference between the backbone of the specimens with horizontal wood siding (HWS). The GWB had a different connector spacing as noted in Figure 4-12a, so a direct comparison cannot be made. Recent full-scale building testing of a soft-story wood-frame structure showed that the horizontal wood siding is capable of very significant deformation, suggesting that the HWS backbones suggested by the P-807 document may be quite conservative. Table 4-6 presents a full comparison of the ultimate load and displacement of backbones obtained from the current test program and those extracted from FEMA P-807.

Table 4-6: Comparison between backbones from experimental tests and P-807 data

Sheathing material	Specimen 1		Specimen 2		Avg. Experimental Data		FEMA P-807 Data		% Difference	
	F _{ult} kN/m (Kip/ft)	Δ _{ult} mm (in.)	F _{ult} kN/m (Kip/ft)	Δ _{ult} mm (in.)	F _{ult} kN/m (Kip/ft)	Δ _{ult} mm (in.)	F _{ult} kN/m (Kip/ft)	Δ _{ult} mm (in.)	F _{ult}	Δ _{ult}
Gypsum wallboard ^(a)	13.1 (0.9)	33.0 (1.3)	11.7 (0.8)	30.5 (1.2)	12.4 (0.85)	31.8 (1.25)	24.8 (1.7)	17.8 (0.7)	-97.7	43.8
Horizontal wood siding	20.4 (1.4)	208 (8.2)	20.4 (1.4)	208 (8.2)	20.4 (1.4)	208 (8.2)	20.4 (1.4)	73.7 (2.9)	1.85	64.8
Stucco	40.9 (2.8)	17.8 (0.7)	52.5 (3.6)	20.3 (0.8)	46.7 (3.2)	19.1 (0.75)	39.4 (2.7)	12.7 (0.5)	17.0	35.6
WSP 8d@ 102 mm (4") o.c.	113.8 (7.8)	63.5 (2.5)	93.4 (6.4)	63.5 (2.5)	103.6 (7.1)	63.5 (2.5)	175.1 (12.0)	73.7 (2.9)	-68.7	-16.1

^(a) Fastener spacing in FEMA P-807 data was 178 mm (7") whereas, it was 406 mm (16") o.c. in this study to be consistent with what was used in the NEES-Soft Project and in-situ site visits.

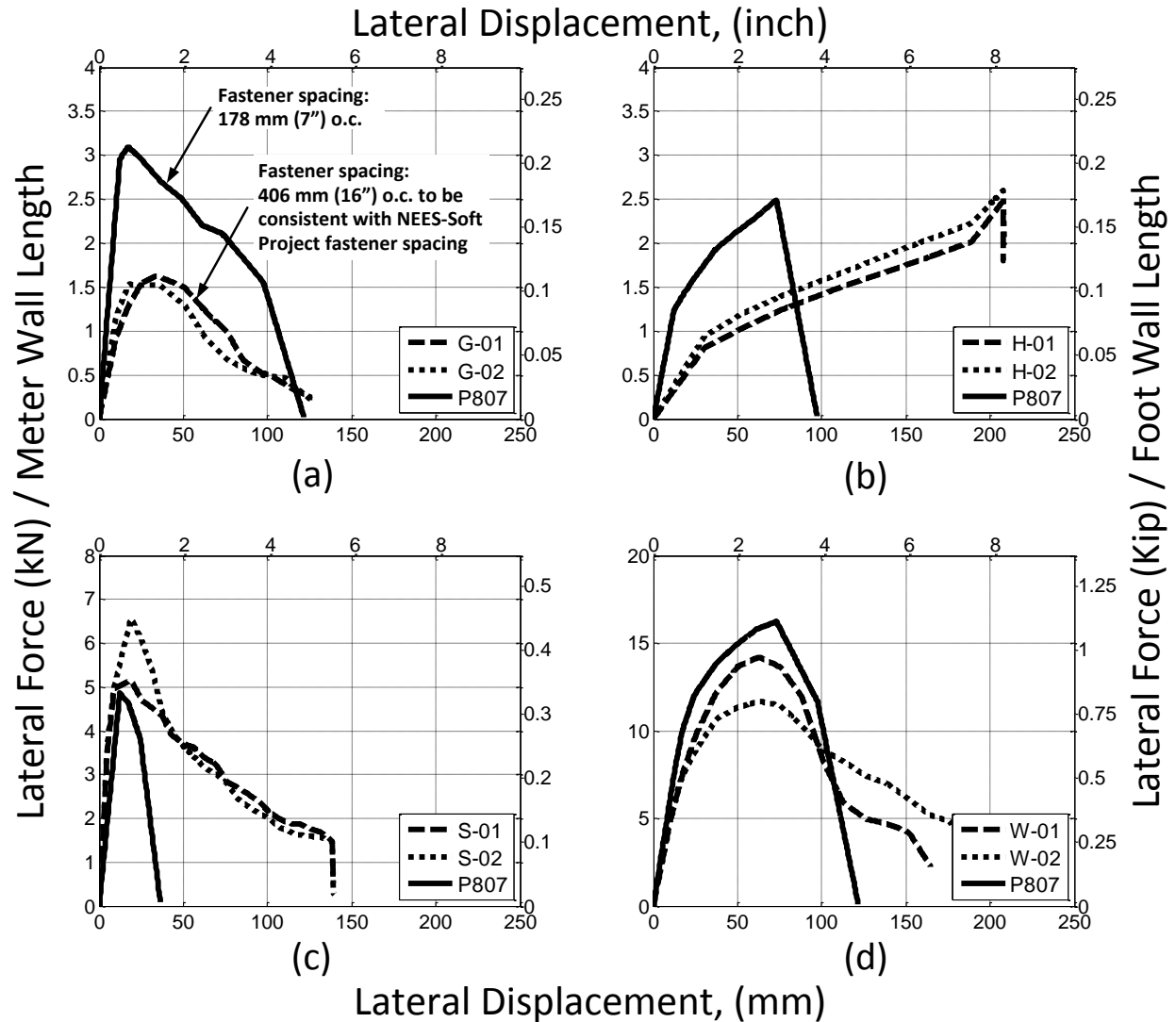


Figure 4-12: Comparison of backbones from the experimental tests and P-807 data: a) gypsum wallboard; b) horizontal wood siding; c) stucco; d) wood structural panel.

4.3 Understanding Sheathing Combinations

4.3.1 Backbone Curves – Strength Approach

Recall that one of the objectives of this study was to investigate the behavior of wood walls when multiple sheathing materials are combined together. One key consideration is whether they can be directly added (i.e., superimposing backbones) or whether a different combination rule, as

suggested by the FEMA P-807 guideline and other studies, should be utilized by designers. In order to evaluate the effect of multiple sheathing layers on the overall strength of wood walls, three specimens with two-layers of sheathing and seven specimens with three-layers of sheathing were tested using the same displacement control test protocol described earlier. Then, the backbones of the combined tests were compared to the backbone of superimposed individual sheathing layers that were used in constructing the two- or three-layer sheathing specimen. It should be noted that the backbones of the single-layer sheathing specimens were superimposed at 100 percent of their values.

Two sets of two-layer sheathing specimens (HWS+GWB and Stucco+WSP) and two sets of three-layer sheathing specimens (HWS+WSP+GWB and Stucco+WSP+GWB) were selected to evaluate the superimposing rule. The average of the two identical tests were used as the final backbone for both single-layer and two-layer (i.e., combined) sheathing specimens. Figure 4-13 presents the averaged backbone of the two- and three-layers sheathing specimen accompanied with the backbone of the corresponding combined test specimen.

In Figure 4-13a shows the specimens with HWS and GWB sheathing. There seems to be a reasonable match between the combined backbone curves and superimposed backbone curve up to about 60 mm (about 2.4 in.) of lateral displacement; however, the capacity of the combined test dropped for higher displacement. In Figure 4-13b which shows the specimens with Stucco and WSP sheathings, it can be observed that the combined backbone has a lower stiffness than the superimposed single sheathings. The peak in both backbones occurs at the same displacement but the combined test reaches a higher lateral force (about 25% higher than the superimposed backbone curve); however, the strength capacity of the combined test dropped below the strength

of the superimposed single layer sheathings for larger displacements. The combination of gypsum wallboard and horizontal siding (Figure 4-13a) behaved quite differently in that it was additive until the deformation capacity of the gypsum wall board was reached and then appeared to return to the strength and overall behavior of the horizontal wood siding. The combined test, in Figure 4-13b and Figure 4-13d, drop below the capacity of the combined individual test by itself indicating some type of effect caused by the stucco layer.

Figure 4-13c and Figure 4-13d present the comparison between combined and superimposed backbones for three-layer sheathing specimens. In Figure 4-13c, it can be seen that the two backbones are very close up to about 20 mm (0.79 in.) of lateral displacement; however, the superimposed backbones shows lower strength as the forces in both backbones reach to their peak values. Both backbones reach their peak almost at the same lateral displacement, then at about 75 mm (2.95 in.) both backbones meet and the combined backbone dropped below the superimposed backbone of the individual tests. In Figure 4-13d, the backbone of the combined test shows lower stiffness than the superimposed individual backbones. Both backbones reach their peak at about the same lateral displacement (about 50 mm / 2 in.); however, the combined backbone reaches a higher force. As was observed in all previous graphs, the strength of combined backbone dropped very quickly after reaching the peak force and its value is lower than the superimposed backbones after about 60 mm (about 2.4 in.) of lateral displacements.

In general, it seems that the peak occurs at about the same lateral displacement for both the combined test and combined individual backbones; however, the backbone of the combined test has a larger peak force than the combined individual test. The stiffness of the combined test was lower than the stiffness of the combined individual tests over the elastic region for each

combination. Finally, it can be observed that the rate of stiffness decrease of the combined test was faster than the combined individual test which leads to a lower strength at higher deformation levels (i.e., displacement after reaching the peak force).

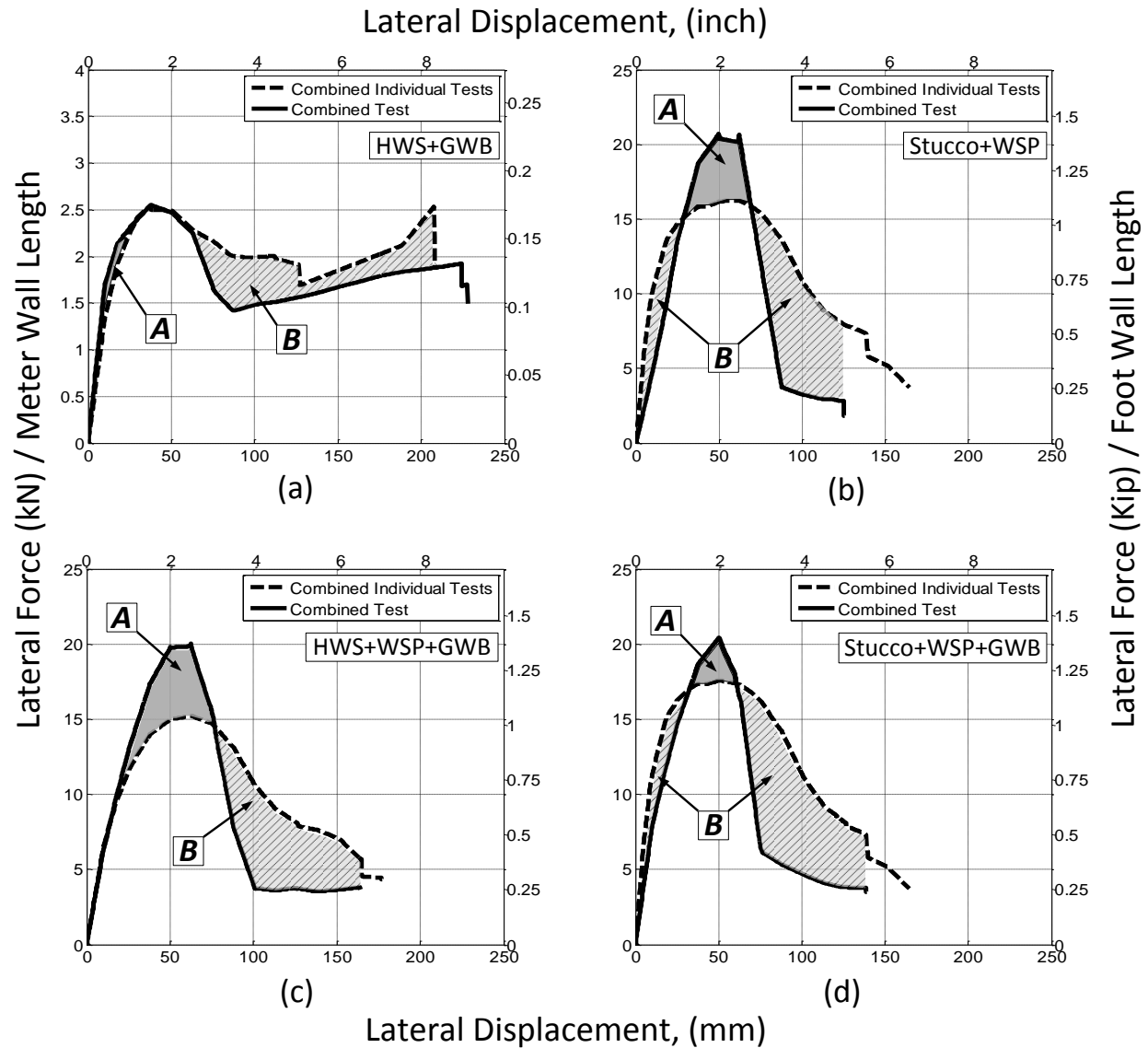


Figure 4-13: Comparison of average backbones of experimental data for two-layer and three-layer sheathing tests

4.3.2 Non-linear Time-History Analysis – Statistical Approach

In order to evaluate the dynamic behavior of the combined sheathings under seismic excitation, a suite of non-linear time-history (NLTH) analysis was conducted by modeling each specimen as a single-degree-of-freedom (SDOF) system. Both individual test specimens with one-, two- and three-layer sheathing were modeled as an EPHM spring. The EPHM model was used in the numerical analysis since it gives more accurate numerical analysis at larger deformations and also eliminates the discrepancies and error due to using two different models (i.e., CUREE ten-parameter and EPHM springs) for single- and combined- layer sheathing specimens. The EPHM hysteresis parameters were obtained from

Table 4-4 and Table 4-5.

The same sheathing combinations that were investigated in the previous section were used in the NLTH analysis. The lumped weight for each set of combination was selected such that the specimens with combined individual tests has a fundamental period of $T_n = 0.3 s$. It should be noted that the weight for the combined individual test and combined test specimens were kept the same for each set of combination but varied from one combination to another. A suite of 44 uniaxial far field earthquake records (FEMA P695, 2009) scaled to the seismic intensity corresponding to a spectral acceleration of $S_a = 1.0g$ at $T_n = 0.3 s$ were used to statistically evaluate the behavior of combined sheathings under seismic excitation.

Figure 4-14 presents the probability of non-exceedance (PNE) versus drift for all four sets of combinations based on rank ordering the peak drifts from each of the NLTH analyses. It can be seen that the combined test specimens experienced slightly higher drift ratios than the combined

individual test specimens (i.e., by superimposing 100% strength of two- or three- layers) except for the specimen with HWS, WSP, and GWB (Figure 4-14c). Although the combined test specimens seem to have higher peak capacity than the superimposed individual sheathing layers, they have higher drift ratio under dynamic analysis. Upon further inspection of the backbones in Figure 4-13a, Figure 4-13b, Figure 4-13d, it can be seen that combined individual test specimens have higher stiffness over the elastic region of the backbone and provide higher restoring forces slightly after reaching the peak force than the specimens with combined sheathing. Also, the strength of the specimens with combined sheathing dropped faster after reaching the peak force.

Furthermore, it can be seen that the areas under the backbones of the specimens with combined sheathing in Figure 4-13a, Figure 4-13b, and Figure 4-13d are less than the areas under the backbones of the combined individual tests. Areas that are named “A” and “B” in Figure 4-13 show the differences between areas underneath combined test and individual combined tests backbones in each region. Since the area under the force-displacement curve represents the internal work and amount of dissipated energy, it can be concluded that the energy dissipated by the combined sheathing specimen is less than summation of energy dissipated by each individual sheathing layer (i.e., area A is less than area B in Figure 4-13a, Figure 4-13b, Figure 4-13d); hence, higher displacement is anticipated (as shown in Figure 4-14a, Figure 4-14b, Figure 4-14d). However, in Figure 4-13c the area underneath the backbone for the combined test is about the same as the area under the backbone of the combined individual tests (i.e., area $A \approx B$). Moreover, the stiffness over the elastic region is about the same for both combinations but the combined test provides a higher peak force. These all lead to lower drifts ratio for the combined test as shown in Figure 4-14c. The lateral displacements corresponding to 50% and 90% non-exceedance for each set of combinations are also presented in the tables in Figure 4-14. It should

be noted that the displacements greater than 203 mm (8 in.) were not shown in Figure 4-14 since these types of phenomenological models lose accuracy of such large displacements (i.e., failure of specimen before reaching larger numerical displacement), hence, those were truncated at 203 mm (8 in.).

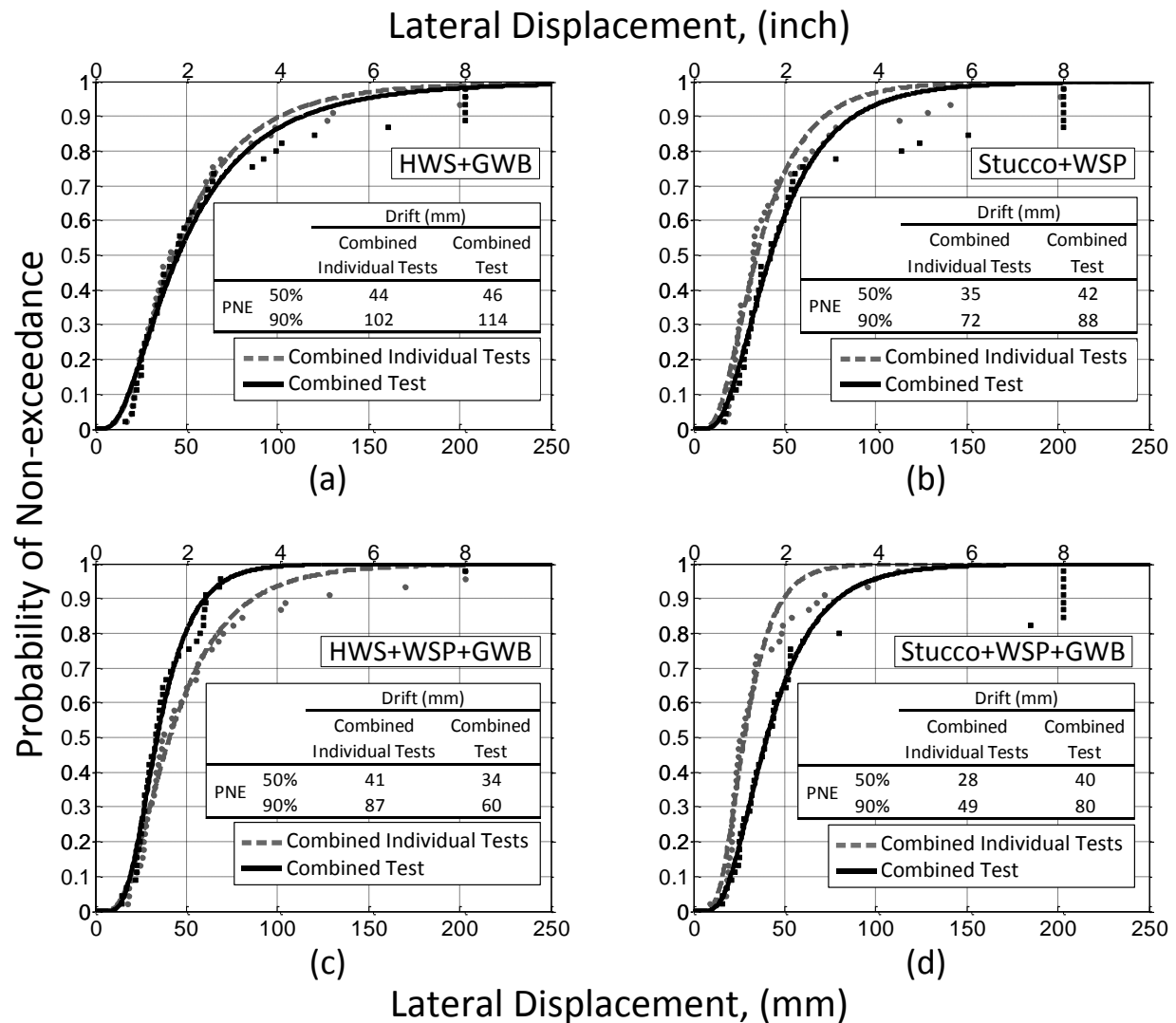


Figure 4-14: Comparison of probability of non-exceedance versus lateral displacement for two-layer and three-layer sheathing tests

4.4 Evaluation of FEMA P-807 Sheathing Combination Rule

In order to evaluate the combination rules suggested by FEMA P-807, the backbones obtained from the experimental tests were combined by applying the FEMA P-807 combination rule, which was described earlier, and the resultant backbone was compared to the backbone of the combined sheathing test. Since the FEMA P-807 suggested combination rule only applies to the specimens with WSP sheathing, only the specimens with WSP were examined in this section. Figure 4-15 presents the backbones resulting from application of the FEMA P-807 combination rule to single-layer sheathing and the corresponding combined test. The average of two identical tests for each single-layer and combined-layer sheathing test was taken and then the FEMA P-807 combination rule was applied to combine the backbones. Then, the backbones obtained by the combined sheathing tests were compared with the backbones obtained by applying the FEMA P-807 combination rule.

Figure 4-15a presents the combination of backbones for specimens with stucco and WSP sheathings. Two backbones were constructed using the FEMA P-807 combination rule: 1) 100% strength of the WSP and 50% strength of the stucco sheathing, and 2) 50% of strength of the WSP and 100% strength of the stucco sheathing. It can be seen that the first combination results in greater forces and should be chosen for use per the P-807 rule. Figure 4-15b and Figure 4-15c present the backbones of specimens with three-layer sheathing. In Figure 4-15b, the combination of HWS, WSP and GWB sheathing were evaluated and in Figure 4-15c the combination of Stucco, WSP and GWB sheathing were investigated based on FEMA P-807 combination rules. It

can be seen in both plots that the combinations which consists of 100% strength of WSP have greater forces and should be selected as the backbone for use per FEMA P-807 combination rule.

From the comparison of the backbones with different combination rules, it can be seen that the combined backbones produced from the FEMA P-807 combination rule provides less strength, up to about 70 mm (2.76 in.), than the backbone obtained from the combined sheathing test. The difference in peak forces is about 31% for the specimens with two-layer sheathing test (Figure 4-15a) and 23% and 20% for the three-layer sheathing tests (Figure 4-15b and Figure 4-15c). However, as mentioned earlier, the combination of single-layer sheathings provide higher strength slightly after reaching the peak force in the backbones. Furthermore, the areas under the backbone curves of combined individual tests are, in general, slightly greater than the areas under the combined tests after 70 mm (2.76 in.) of lateral displacement. This leads to concluding that higher amount of energy can be dissipated by the combination of individual tests than the combined test at larger lateral displacements.

In order to compare the behavior of the combined test specimens with the FEMA P-807 combination rule, a NLTH analysis was conducted by applying the same ground motions used in the previous section. The EPHM spring was used to model the combined test and produce the spring models that represent the combination of the layers by using the FEMA P-807 combination rule. The probability of non-exceedance versus lateral displacement for each set of combinations is presented in Figure 4-15d-f. It can be seen that the FEMA P-807 selected combinations result in larger lateral displacement. This is due to a decrease in stiffness and strength of sheathing (except WSP) by 50% which also decreases the amount of energy that can be dissipated. Unlike the superimposing of sheathing layers which leads to unconservative

design, it can be seen that the FEMA P-807 combination rule results in conservative design within a reasonable range.

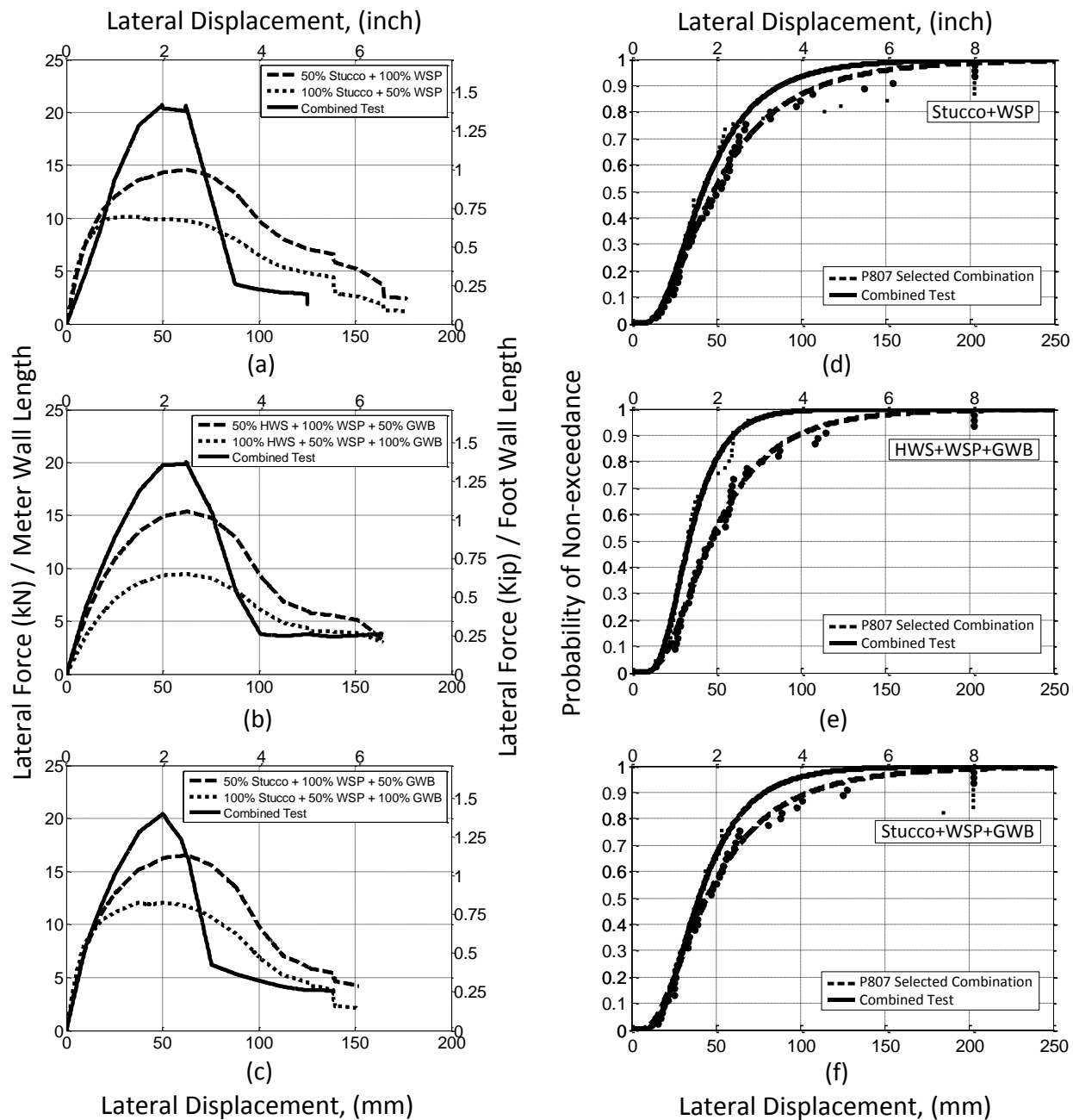


Figure 4-15: Evaluating the FEMA P-807 combination rules and comparing with combined experimental test data

It was shown that superimposing sheathing with 100% of strength leads to a slightly unconservative design; whereas, using the FEMA P-807 (2012) rule leads to conservative design that is in acceptable range. It should be noted that the comparison and subsequent conclusions presented in this chapter are limited to the boundary conditions used herein. An extensive experimental study for all sheathing combinations with varying boundary conditions is recommended to make a more comprehensive conclusion.

The wall parameters obtained from the isolated wall tests presented in this chapter were used in numerical modeling and retrofit design of a four-story wood-frame building that was tested at NEES at the UC-San Diego shake table facility. The next three chapters of this dissertation are dedicated to numerical modeling, retrofit design, and full-scale experimental shake table testing of the four-story wood-frame building.

Chapter 5. NUMERICAL VALIDATION AND RETROFIT DESIGN OF A FOUR-STORY SOFT-STORY WOOD-FRAME BUILDING USING SIMPLIFIED PBSR METHOD^{5,6}

Two different PBSR approaches are presented in Chapter 3. The first method, which is based on the DBDT concept, enables one to allow some level of torsional response in a building if eliminating torsion is not feasible. This method was explained and numerically validated in Chapter 3. The second method, which was developed based on DDD, simplifies the retrofit procedure by eliminating torsional responses for cases where this is feasible. The retrofit procedure for the simplified PBSR was also presented in Chapter 3. In this chapter, the simplified method of retrofitting irregular code-deficient buildings is applied to retrofit a four-story soft-story wood-frame building. The retrofit procedure, design details, and numerical validation are presented along with practical retrofit considerations for wood-frame buildings.

5.1 Building Specifications

In order to investigate the effectiveness and feasibility of the proposed simplified PBSR procedure, a four-story wood-frame building with a soft- and weak-story at the ground level was retrofitted using this method. The first story (ground level) has several openings for garage parking spaces, storage, and laundry room. As mentioned earlier, these openings result in low shear wall density at the first floor compared to the upper stories which in turn leads to soft-story behavior at this level. The floor plans of the first story and upper stories of the building are

⁵ Bahmani, P., van de Lindt, J.W., Gershfeld, M., Mochizuki, G.L., Pryor, S.E., Rammer, D. (2014). “Experimental Seismic Behavior of a Full-Scale Four-Story Soft-Story Woodframe Building with Retrofits I: Building Design, Retrofit Methodology, and Numerical Validation”, *ASCE J. Struct. Eng.*, DOI: 10.1061/(ASCE)ST.1943-541X.0001207.

⁶ Bahmani, P., van de Lindt, J.W., Pryor, S.E., Mochizuki, G. L. (2014). “Performance-based Seismic Retrofit of Soft-Story Wood-frame Buildings Using Steel Special Moment Frames: Methodology and Full-Scale Experimental Validation”, *Engineering Structures*, January 2015.

presented in Figure 5-1. The four-story wood-frame building is sheathed with horizontal wood siding (HWS) in the outside face of exterior walls and gypsum wallboard (GWB) in the interior walls. Based on the test data provided by the cyclic tests in Chapter 4, the initial lateral stiffness of each wall segment can be calculated and then, the lateral stiffness and in-plane eccentricities can be determined in order to decide whether the building is code-deficient with respect to vertical and horizontal irregularities. Table 5-1 presents the distribution of initial lateral stiffness and in-plane eccentricity ratios for this building.

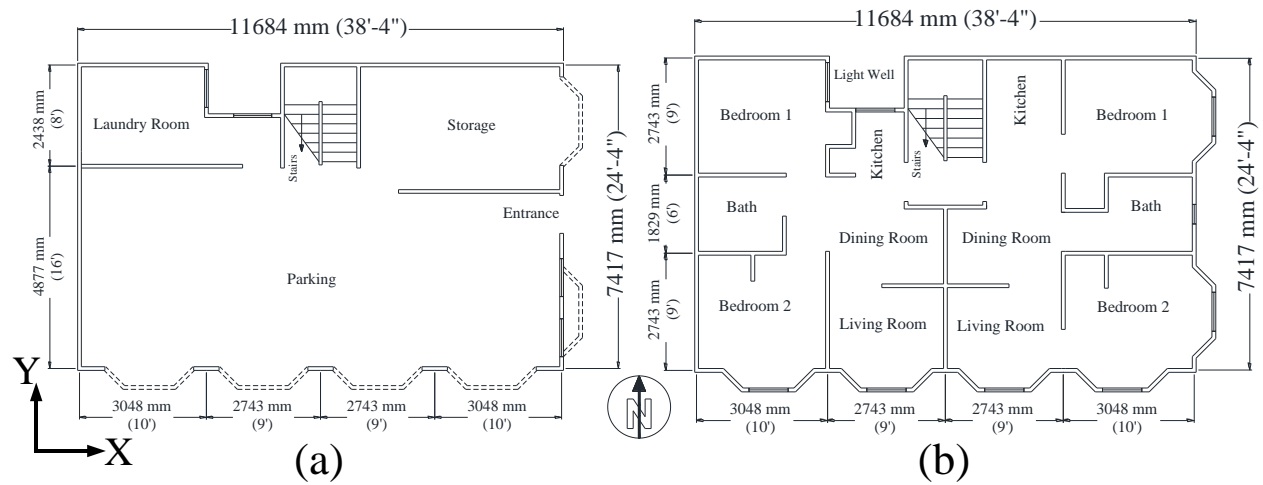


Figure 5-1: Floor plans of the four-story wood-frame building: (a) first story, and (b) upper stories.

Table 5-1: Lateral stiffness and in-plane eccentricities of the 4-story building

Story	Initial lateral stiffness, kN/mm (kip/in.)		Eccentricity ratios ^(a) (%)	
	x – direction	y – direction	e_x / L_x	e_y / L_y
4 th	8.27 (47.2)	12.8 (73.1)	8.65	13.8
3 rd	8.27 (47.2)	12.8 (73.1)	8.65	13.8
2 nd	8.27 (47.2)	12.8 (73.1)	8.65	13.8
1 st	5.15 (29.4)	4.06 (23.2)	9.83	31.4

^(a) $L_x = 11684 \text{ mm} (460 \text{ in.})$ and $L_y = 7417 \text{ mm} (292 \text{ in.})$

From Table 5-1 it can be seen that the ratios of the initial lateral stiffness of the first story to the average initial lateral stiffness of the upper stories were 62% and 32% in the x - and y -direction, respectively. This places the building in the “stiffness-extreme soft story” category per the ASCE7-10 (2010) definition (Table 1-1). Furthermore, The in-plane eccentricities (i.e., e_x / L_x and e_y / L_y) calculated based on initial stiffness values are 9.8% and 31.4% at the first floor the x - and y -direction, respectively. The in-plane eccentricities are 8.65% and 13.8% at the upper stories in the x - and y -direction, respectively. These high eccentricity ratios in all stories indicate that the building is also torsionally irregular and susceptible to damage or collapse during an earthquake; hence, retrofitting it is necessary.

5.2 Retrofit Design with Simplified PBSR Procedure

The four-story building is retrofitted using the simplified PBSR method explained in Section 3.2 of Chapter 3. The objective of the retrofit design is to find the distribution of retrofit stiffness over the height of the building and in the plane of each story so that the torsional responses are eliminated and all story ISD do not exceed the 2% performance criteria associated with a 50% probability non-exceedance for the maximum considered earthquake (MCE). It should be noted that for the generic site used in this design, the MCE seismic intensity was assumed to be equal to a spectral acceleration of $S_a = 1.8g$. The simplified PBSR design procedure for this particular building to meet the per-defined performance objective is as follows:

Step 1. Specifying the hazard level and performance criteria

As mentioned earlier, the building is retrofitted such that the ISD ratio in all stories does not exceed the pre-defined 2% ISD ratio (i.e., $\theta_{Story} \leq \theta_{Target} = \Delta_{Target} / h_{Story} = 2\%$) at MCE intensity with spectral acceleration of $S_a = 1.8g$.

Step 2. Simplifying the building to an equivalent SDOF system

The four-story building is simplified to an equivalent SDOF system by calculating the effective weight (W_{Eff}), the effective height (h_{Eff}), and the lateral load distribution factors ($C_{v,j}$). The weights, absolute heights, displacements, and lateral load distribution factors are presented in Table 5-2. The calculated W_{Eff} and h_{Eff} for this building are 391.0 kN (87.91 kips) and 7819 mm (307.85 in.), respectively.

Table 5-2: PBSR design parameters for the four-story wood-frame building

Story	h_j mm (in)	θ_{Target} (%)	Δ_j mm (in)	W_j kN (kip)	$W_j \times \Delta_j$ kN-mm (kip-in)	$W_j \times \Delta_j^2$ kN-mm ² (kip-in ²)	$C_{v,j}$	$C_v \times h_j$ mm (in)	F_j kN (kip)	$V_{s,j}$ kN (kip)	$K_{s,j}$ kN/mm (kip/in)
4 th	10884 (428.500)	2	218 (8.570)	91.28 (20.52)	19870 (175.86)	4325069 (1507.09)	0.325	3536 (139.22)	134.6 (30.26)	134.6 (30.26)	2.47 (14.10)
3 rd	8163 (321.375)	2	163 (6.428)	126.3 (28.39)	20617 (182.48)	3365920 (1172.87)	0.337	2752 (108.35)	139.6 (31.38)	274.2 (61.64)	5.04 (28.78)
2 nd	5442 (214.250)	2	109 (4.285)	126.3 (28.39)	13745 (121.65)	1495977 (521.28)	0.225	1223 (48.15)	93.2 (20.95)	367.4 (82.59)	6.75 (38.54)
1 st	2721 (107.125)	2	54 (2.143)	127.2 (28.60)	6924 (61.28)	376749 (131.28)	0.113	308.1 (12.13)	46.8 (10.52)	414.2 (93.12)	7.61 (43.45)
Total	-	-	-	471.1 (105.9)	61155 (541.27)	9563715 (3332.52)	1.000	7819 (307.85)	-	-	-

Step 3. Producing inelastic displacement response spectra for the specified seismic hazard

In order to produce inelastic displacement response spectra, the design response spectra for a generic site with S_a of $1.8g$ for MCE intensity is needed. Furthermore, both intrinsic and hysteretic damping ratios are required to construct the inelastic displacement response spectra from the elastic one. It should be noted that the intrinsic damping for the wood-frame buildings and the hysteretic damping for the equivalent SDOF system are assumed to be 1% and 17%, respectively (i.e., $\xi_{Intrinsic} = 1\%$ and $\xi_{Hysteretic} = 17\%$) based on the empirical values proposed by Filiatrault et al., 2003. Therefore, the total damping must set to 18% in Equation 3-7; hence, the reduction factor can be calculated as follows:

$$R = \frac{S_d^{Elastic}}{S_d^{Inelastic}} = \sqrt{\frac{2 + \xi_{Total}}{7}} = \sqrt{\frac{2 + (1 + 17)}{7}} = 1.690$$

Therefore, the values of the elastic displacement response spectrum (i.e., $S_d^{Elastic}$) should be divide by $R = 1.690$ in order to obtain the inelastic displacement response spectrum (i.e., $S_d^{Inelastic}$) corresponding to the total damping of 18% (i.e., $\xi_{Total} = 18\%$). Figure 5-2 presents the modified inelastic displacement response spectra.

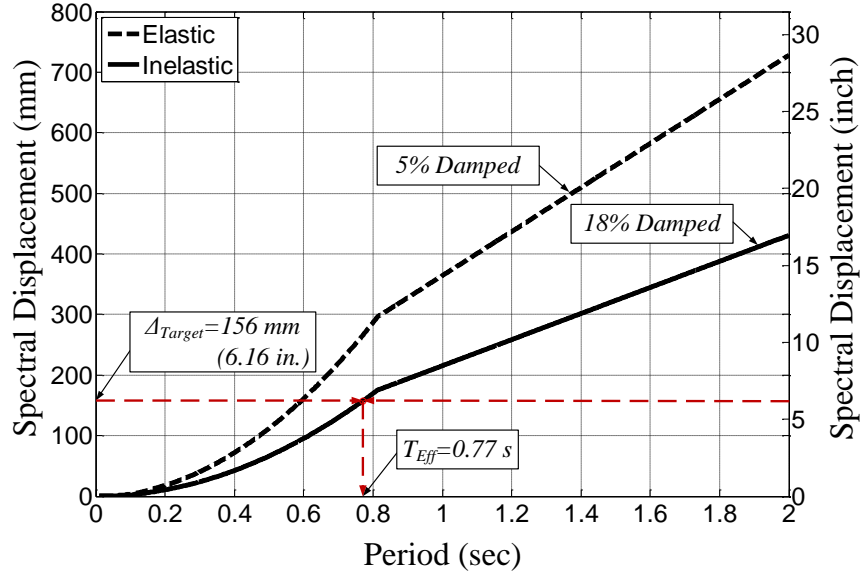


Figure 5-2: Elastic and inelastic displacement response spectra.

Step 4. Calculating the effective lateral stiffness and base shear of the equivalent SDOF system

The next step in the simplified PBSR procedure is finding the period of the equivalent SDOF system that corresponds to the target displacement ($\Delta_{\text{Target}} = \theta_{\text{Target}} \times h_{\text{Eff}} = 2\% \times 7819 = 156 \text{ mm}$).

By setting the $S_d^{\text{Inelastic}}$ equal to 156 mm (6.16 in.), the period of the equivalent SDOF system, T_{Eff} , can be found and is equal to 0.77 s (Figure 5-2). The lateral stiffness of the equivalent SDOF is then can be calculated by modifying Equation 3-6:

$$K_{\text{Eff}} = \left(\frac{2\pi}{T_{\text{Eff}}} \right)^2 \frac{W_{\text{Eff}}}{g} = \left(\frac{2\pi}{0.77 \text{ s}} \right)^2 \frac{391.0 \text{ kN}}{9807 \text{ mm/s}^2} = 2.655 \text{ kN/mm} (15.16 \text{ kip/in})$$

Having the equivalent lateral stiffness, the base shear of the equivalent SDOF system, V_b , can be found by multiplying the Δ_{Target} by the K_{Eff} :

$$V_b = K_{\text{Eff}} \times \Delta_{\text{Eff}} = (2.655 \text{ kN/mm}) \times (156 \text{ mm}) = 414.2 \text{ kN} (93.1 \text{ kip})$$

Step 5. Calculating lateral forces and required secant stiffness at each story

From static equilibrium equation, it can be seen that the base shear should be equal to the total lateral forces applied to the building (see Figure 3-5). The lateral forces at the level of stories can be obtained by multiplying the lateral load distribution factors, $C_{v,j}$, by the calculated base shear (Equation 3-12). For each story, the story shear force can be obtained by summing the force applied at the story and the stories above it. Finally, the secant stiffness of each story (i.e., $K_{\text{Req.}}$) can be calculated using Equation 3-13. The story lateral forces, story shear forces, and secant stiffness of the stories are presented in Table 5-2.

Step 6. Calculating secant stiffness of retrofit at each story

In order to find the stiffness of the retrofit elements (i.e., $K_{\text{Ret.}}$), the available secant stiffness of the existing SFRS elements at the θ_{Target} of 2% (i.e., $K_{\text{Avail.}}$) should be subtracted from the required lateral stiffness calculated in the previous step for each story. Table 5-3 presents the distribution of $K_{\text{Req.}}$, $K_{\text{Avail.}}$, and $K_{\text{Ret.}}$ over the height of the building.

Table 5-3: Distribution of lateral stiffness at each story using PBSR method

Story	θ_{Target} (%)	Secant Stiffness at Δ_{Target} , kN/mm (kip/in.)					
		x – direction			y – direction		
		$K_{\text{Req.}}$	$K_{\text{Avail.}}$	$K_{\text{Ret.}}$	$K_{\text{Req.}}$	$K_{\text{Avail.}}$	$K_{\text{Ret.}}$
4 th	2	2.47 (14.10)	1.01 (5.79)	1.46 (8.34)	2.47 (14.10)	1.47 (8.39)	1.00 (5.71)
3 rd	2	5.04 (28.78)	1.01 (5.79)	4.03 (23.01)	5.04 (28.78)	1.47 (8.39)	3.57 (20.39)
2 nd	2	6.75 (38.54)	1.01 (5.79)	5.74 (32.78)	6.75 (38.54)	1.47 (8.39)	5.28 (30.15)
1 st	2	7.61 (43.45)	0.69 (3.96)	6.92 (39.51)	7.61 (43.45)	0.58 (3.31)	7.03 (40.14)

Step 7. Distributing the lateral stiffness in the plane of each story.

The last step in the simplified PBSR procedure is distributing the retrofits in the plane of each story such that the values of the in-plane eccentricities approach to zero. This leads to elimination of contribution of the rotational response of each story in the overall behavior of the building. In order to reduce the in-plane eccentricities, the retrofits should be located such that the *CR* of each story moves toward the *CM* of the story when the story reaches the pre-defined inter-story drift (i.e., Δ_{Target}). It should be noted that the locations of the *CM*'s remains unchanged since the distribution of mass (or weights) do not changed during an earthquake. However, the locations of *CR*'s changes over time during an earthquake due to non-linear behavior of the SFRS elements. Therefore, in order to examine the in-plane eccentricities in both directions for all stories the location of *CR*'s should be calculated the secant stiffness of SFRS elements when the building reaches the target inter-story drift (i.e., Δ_{Target}). The locations of the *CR*'s calculated based on the initial stiffness and secant stiffness of the existing SFRS are shown in Figure 5-3 and Figure 5-4 for the first and upper stories, respectively. The $e_{x,s}$ and $e_{y,s}$ are the in-plane eccentricities calculated based on the secant stiffness of SFRS elements at the Δ_{Target} .

According to Equations 3-15 and 3-16, both the location and stiffness of retrofit elements can be altered to move the location of *CR*'s which eventually reduce the eccentricities at the target inter-story drift (i.e., $e_{x,s}$ and $e_{y,s}$). There are infinite numbers of solutions for these two equations since each equation has two variables (i.e., retrofit stiffness and its location). However, the architectural constraints, and practical and engineering considerations rule out many of the mathematically possible solutions.

The possible locations for retrofit elements at the first floor are marked with the dashed lines in Figure 5-3. Since the CR_{Secant} is located in the north side of the CM , it can be concluded that in order to reduce the eccentricity in y -direction (i.e., e_y) at the first story, the greater portion of the retrofit stiffness should be added at the south side of the building (i.e., below the CM in the floor plan view). Therefore, the retrofit elements should be located either in the parking space (i.e., Pos. 5) or right behind the south wall of the building (i.e., Pos. 6). These two positions remain as possible options for the locations of retrofits at this point. With the same analogy, it can be concluded that less retrofit should be added to the north side of the story. Therefore, at first glance, only one of the four positions (Pos. 1 to Pos. 4) may be used for adding retrofits. Since, Pos. 1 and Pos. 2 have higher moment arms from the CM , these two positions will be the best candidates at this point and Pos. 3 and Pos. 4 are left as reserve positions.

In order to reduce the eccentricity in the x -direction (i.e., e_x), three possible locations for retrofits can be considered (i.e., Pos. 7 to 9). Since the CR_{Secant} is located in the west side of the CM , it can be concluded that higher portion of lateral stiffness of retrofits in the y -direction should be assigned to Pos. 8 and Pos. 9 with the priority of Pos. 9 due its higher moment arm from the CM . It should be noted that Pos. 7 remains as a reserve position at this point which may be used later to balance the distribution of retrofits.

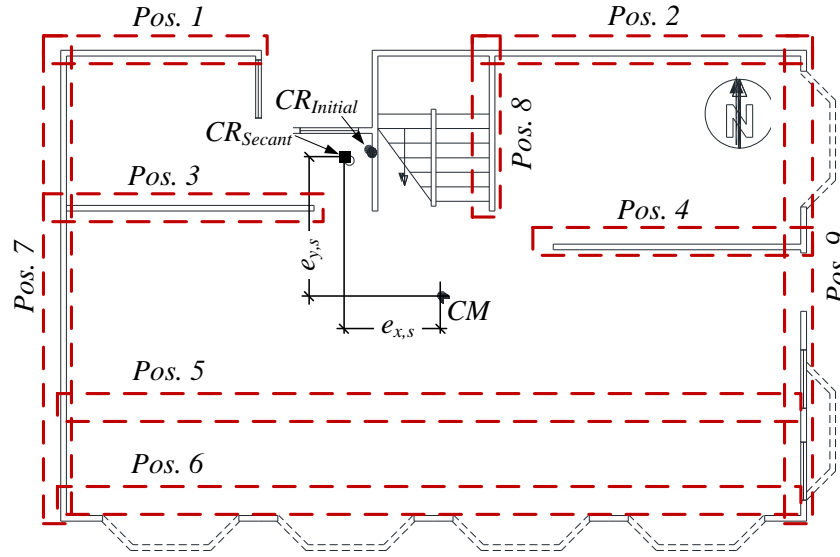


Figure 5-3: Elastic and inelastic displacement response spectra.

The same analogy that was used to select possible locations of retrofits at the first floor can be used in order to find the possible locations of retrofits in the upper stories. The possible locations of retrofit elements for the upper stories are shown with dashed lines in Figure 5-4. In order to reduce the in-plane eccentricity in the y -direction (i.e., e_y), the greater portion of retrofit stiffness should be assigned to the positions in the south of the CM of the upper stories. This makes Pos. 5 and Pos. 6 good candidates with the priority of Pos. 6 due to its greater moment arm from the CM . With the same reasoning, the lesser portion of retrofit stiffness should be assigned to Pos. 1 to Pos. 4 with the priority of Pos. 1 and Pos. 2. These positions remain as reserve positions in order to balance the design.

Likewise, the in-plane eccentricity in the x -direction (i.e., e_x), at the upper stories can be reduced by distributing the lateral stiffness of the retrofits between Pos. 7 to Pos. 12. A greater portion of lateral stiffness should be assigned to the positions in the east side of the CM (i.e., Pos. 10 to Pos. 12). The positions in the west side of CM can be used later if balancing the

design is required. It should be noted that the retrofits in Pos. 9 have a special characteristic in retrofitting the building. Since the line of resistance of the retrofits located at Pos. 9 go through the CM , the moment arm from the CM will be close to zero; therefore, these retrofits will contribute almost solely to the lateral stiffness of the story without contributing to its torsional stiffness. It can be seen that many mathematical solutions for the location of retrofits have been ruled out only by using a good combination of engineering judgment and Equations 3-15 and 3-16.

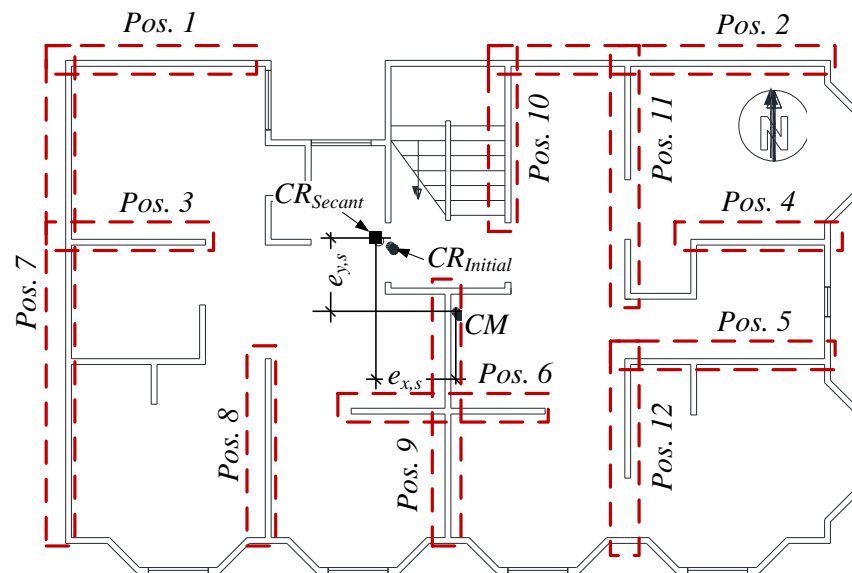


Figure 5-4: Elastic and inelastic displacement response spectra.

Another issue that should be considered is the vertical elements of SFRS that are needed to transfer the upward or downward forces induced in the building. This imposes another structural constraint in choosing the location of retrofits in transferring the vertical forces produced in the retrofit elements in addition to the lateral forces. Upward (or downward) forces are produced in all the SFRS elements including the retrofit elements to counteract the moments developed in the element due to the lateral forces. These vertical forces must transfer to the foundation in order to

make the retrofit design effective. Therefore, any retrofit options that do not consider this fact should be removed from the possible options. By looking back to the selected and reserved retrofit positions for the first story and upper stories, it can be seen that retrofits can be located at Positions 1, 2, 5, 7, 8, 9 and at Positions 1, 2, 6, 7, 9, 10 in the first story and upper stories, respectively. By knowing these constraints and total lateral stiffness of retrofit at each story, the distribution of retrofit elements can be optimized by using Equations 3-15 and 3-16. The final retrofit design along with the location of retrofit elements in the x - and y -directions are presented in Table 5-4 and Table 5-5, respectively. The eccentricity ratios (i.e., e_x/L_x and e_y/L_y) at the target inter-story drift ratio (i.e., θ_{Target}) are also presented in the tables. It can be seen that the maximum eccentricity ratio in all stories is 3% which is less than the accidental eccentricity ratio used in ASCE 7-10 (2010) for seismic design.

Table 5-4: Eccentricity and distribution of stiffness at each story in x – direction

Story	Pos. 1 – All stories (WSP – A)		Pos. 6 – Upper stories (WSP – D)		Pos. 5 – 1 st story (SMF in x -direction)		Eccentricity ratio at θ_{Target} (%)	
	$K_{Ret.}$	y	$K_{Ret.}$	y	$K_{Ret.}$	y	Before retrofit	After retrofit
	kN/mm (kip/in)	mm (in.)	kN/mm (kip/in)	mm (in.)	kN/mm (kip/in)	mm (in.)	e_x/L_x	e_x/L_x
4 th	0.27 (1.55)		1.77 (10.1)		-		10.6	3.00
3 rd	0.74 (4.25)	7315 (288)	2.89 (16.5)	1981 (78)	-	1981 (78)	10.6	2.45
2 nd	1.41 (8.04)		4.13 (23.6)		-		10.6	1.53
1 st	1.94 (11.1)		-		5.39 (30.8)		12.9	0.82

Table 5-5: Eccentricity and distribution of stiffness at each story in y – direction

Story	Pos. 7 – 1 st story (WSP – 1)		Pos. 9 – Upper stories (WSP – 3)		Pos. 10 – Upper stories (WSP – 3R)		Pos. 9 – 1 st story (SMF in y -direction)		Eccentricity ratio at θ_{Target} (%)	
	$K_{Ret.}$	x	$K_{Ret.}$	x	$K_{Ret.}$	x	$K_{Ret.}$	x	Before retrofit	After retrofit
	kN/mm (kip/in)	mm (in.)	kN/mm (kip/in)	mm (in.)	kN/mm (kip/in)	mm (in.)	kN/mm (kip/in)	mm (in.)	e_y / L_y	e_y / L_y
4 th	-		0.20 (1.12)		1.17 (6.66)		-		15.6	2.22
3 rd	-	89 (3.5)	2.36 (13.5)	5842 (230)	1.11 (6.36)	6782 (267)	-	11100 (437)	15.6	1.14
2 nd	-		3.45 (19.7)		1.62 (9.27)		-		15.6	0.56
1 st	3.24 (18.50)		-		-		3.85 (22.0)		29.7	1.07

5.3 Practical Consideration for Experimental Validation

Several options are available to retrofit soft-story buildings in which the majority of them are stiffness/strength-based retrofits. In the previous section it was shown that in order to meet the PBSR design specification, retrofit elements should be selected and positioned in the building such that they can provide the required stiffness and strength (i.e., $K_{Ret.}$) to the building. However, the PBSR procedure does not specify the types of the retrofit elements that can provide the required secant stiffness at the pre-defined target inter-story drift. In other words, it is up to the structural engineer to choose the best retrofit techniques that can satisfy the PBSR design specifications and, at the same time, address the architectural constraints, installation challenges, and economic considerations.

As mentioned in Chapter 3, one of the challenges in retrofitting existing buildings is architectural or use constraints such as garage parking spaces and openings at the first floor as well as

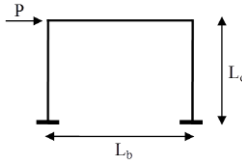
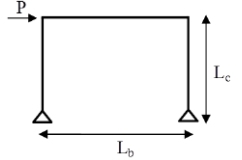
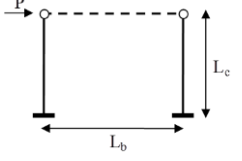
windows and living space in the upper stories. Furthermore, the retrofit technique should be known to the engineering community such that they can reasonably predict its performance. It also should be easily implemented in the building to keep the construction duration to a minimum. To address these challenges, steel moment frames (SMF) and wood structural panels (WSP) with different connector spacings (i.e., nail pattern) are selected as lateral load resisting elements of the retrofit system for retrofitting the four-story wood-frame building. Furthermore, Anchor Tie-down System (ATS) rods and wood stud packs were selected as the vertical load resisting elements of the retrofit system. These retrofit techniques are quite practical and can be implemented for a large number of wood-frame buildings. SMF's can be added over the garage door opening of the building and WSP's can be added where there are non-structural walls or nail patterns can be altered to provide stronger and stiffer walls. The ATS rods and wood stud pack can be added close to the end post of the walls retrofitted with WSP to transfer the vertical upward or downward forces to the foundation.

5.3.1 Steel Moment Frame (SMF)

As mentioned earlier, steel frames can be used at the first story (i.e., soft story) since the steel columns can be installed such that they do not interfere with parking space. Three major categories of steel frames that can be used as a retrofit option for the soft story buildings are shown in Table 5-6 (Bahmani and van de Lindt, 2011). These are: (1) SMF with fixed support; (2) SMF with pinned support; and (3) cantilever column. The lateral stiffness and displacement of each type of SMF with different end supports (i.e., boundary conditions) is presented in the table. For each type of steel frames, it was assumed that the steel frame can be modeled as a bilinear spring in which the stiffness is constant with initial stiffness of K_1 up to the yield force,

F_y , associated with the yield drift of D_y at which the stiffness reduces to K_2 . Figure 5-5 presents the numerical model of the bilinear spring for modeling steel frames.

Table 5-6: Lateral stiffness and displacement for steel frames – (after Silvia and Badie, 2008)

Steel Frame Category	Steel Frame Type	Lateral Displacement*	Lateral Stiffness*
Category 1: Fixed Support Frame: Moment resisting connections at beam-to-column and column-to-foundation connections		$\Delta = \left(\frac{6\alpha + 4\kappa}{6\alpha + \kappa} \right) \frac{P L_c^3}{24 E I_c}$	$K_1 = \left(\frac{6\alpha + \kappa}{6\alpha + 4\kappa} \right) \frac{24 E I_c}{L_c^3}$
Category 2: Pinned Support Frame: Moment resisting connections at beam-to-column; but pin connection at column-to-foundation connections		$\Delta = \left(4 + \frac{2\kappa}{\alpha} \right) \frac{P L_c^3}{24 E I_c}$	$K_1 = \left(\frac{\alpha}{4\alpha + 2\kappa} \right) \frac{24 E I_c}{L_c^3}$
Category 3: Cantilevered Column Frame: Moment resisting connections at column-to-foundation connections but free at top		$\Delta = \frac{P L_c^3}{6 E I_c}$	$K_1 = \frac{6 E I_c}{L_c^3}$

* I_c , L_c = moment of inertial and height of column; I_b , L_b = moment of inertial and length of beam;

$$\alpha = \frac{I_b}{I_c} \text{ and } \kappa = \frac{L_b}{L_c}$$

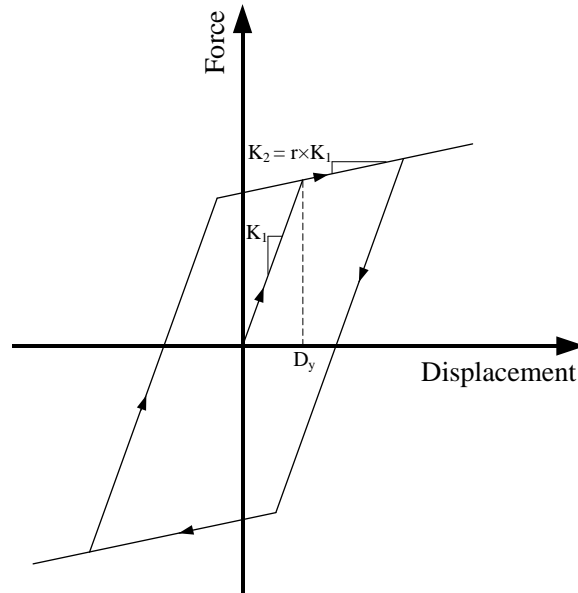


Figure 5-5: Bilinear spring model of steel frames.

From the three aforementioned possible options for a steel frame, the steel moment frame with pinned support (i.e., Category 2 in Table 5-6) has several advantages that make this frame a very suitable option for retrofitting the first story of soft-story wood-frame buildings. Some of the main advantages of the pinned-supported SMF are: (1) this retrofit technique has minimal interference with the garage openings and other architectural details of the building at the first story; (2) the SMF used here has a unique yielding link between each column and beam that moves the plastic hinge out away from the column and does not require bracing for lateral torsion buckling (LTB) of the beam. This bracing is problematic for typical moment frames since the wood diaphragm is, in general, not stiff and strong enough to provide a reaction for the brace; (3) the beams can easily be connected to the floor diaphragm by means of a wood nailer to transfer shear forces of the diaphragm of the first story to the foundation; (4) no moment is produced at the column-to-foundation connection due to the nature of the pinned connections; therefore, the foundation should be retrofitted to resist only vertical and shear forces which requires less foundation retrofit; (5) the steel moment frame is easily assembled on site using bolted, not welded, connections. This eliminates the potential fire hazard associated with field-welding in an unprotected wood structure. Perhaps more importantly, the welding fumes are not considered safe for occupants and would, in general, require either temporary relocation or ventilation; (6) the field-bolted frame connections do not require special training or tools which reduces the time and cost of the retrofit.

The design specifications and parameters were then determined such that the frame satisfies the retrofit design requirements calculated using the PBSR procedure. The secant stiffness at the target inter-story drift (i.e., Δ_{Target}) was determined by the PBSR procedure and presented in Table 5-4 and Table 5-5. The initial stiffness of the steel moment frames that can satisfy the

required secant stiffness can be found using Equation 5-1 which relates K_{Secant} to K_1 , Δ_{Target} , r , and D_y of the steel moment frame with pinned support. The K_{Secant} and Δ_{Target} are known from the PBSR design specifications. The K_1 , r , and D_y should be selected from the available sections and yield links such that the frame can provide the required K_{Secant} .

$$K_{Secant} = \frac{(1-r) D_y + r \Delta_{Target}}{\Delta_{Target}} K_1 \quad (5-1)$$

By a couple of trial and error, the sections that can provide the required secant stiffness can be specified. For this particular design, the steel sections with the design parameters are presented in Table 5-7. The backbone curves of the selected SMF's in both x - and y -direction are shown in Figure 5-6. It can be seen the secant stiffness of the steel moment frames at the 2% drift ratio are 5.41 kN/mm (30.95 kip/in.) and 3.82 kN/mm (21.81 kip/in.) in the x - and y -direction, respectively. These values are very close to the values calculated based on the PBSR procedure (Table 5-4 and Table 5-5), and hence, these SMF's are selected as the final design for the steel moment frames in the first story. It should be noted that the drift ratios for the SMF's are calculated based on the effective height of the SMF's that should be measured from the face of the foundation to the centerline of the steel beams. The effective height of 2108 mm (83 in.) is used for these SMF's.

Table 5-7: Design parameters and steel sections of the steel special moment frames

Retrofit Methodology	Direction	Column/Beam sections ^(a)	K_1 , N/mm (lb/in.)	r ^(b)	D_y , mm (in)
PBSR	x – direction (longitudinal direction)	Edge Columns: W14×38 Middle Column: W16×57 Beam: W14×38	9805 (55990)	0.199	18.5 (0.73)
	y – direction (transverse direction)	Column: W10×30 Beam: W12×30	6622 (37810)	0.220	19.6 (0.77)

^(a) Steel grade is 50 ksi.

^(b) Ratio of secondary to initial stiffness ($r = K_2 / K_1$).

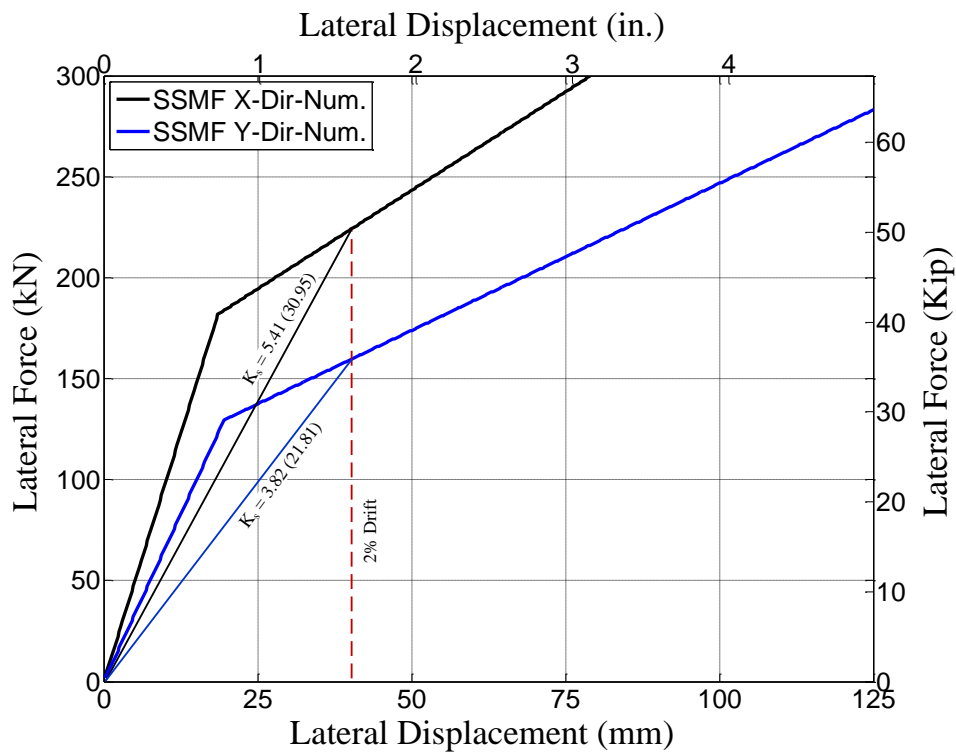


Figure 5-6: Backbones of steel special moment frames at the first story.

5.3.2 Wood Structural Panel (WSP)

Wood structural panels (WSP) can be used as a retrofit option for the upper stories and for the places that installation of steel moment frames is difficult or impossible in wood-frame buildings. This option minimizes the interference of retrofit elements with living areas and

openings since it can be installed over the existing wall frames. The WSP can also be replaced for non-structural walls. Moreover, additional fasteners can be added to walls in order to make a stiffer and stronger element (i.e., denser nail schedule in existing WSP's). The structural behavior of WSP's can be modelled using a well-known ten-parameter hysteretic model developed by Folz and Filiatrault, 2001. As mentioned earlier, the walls of the un-retrofitted four-story building are sheathed with horizontal wood sidings (HWS) and gypsum wallboards (GWB). The behaviour of these sheathings can also be modelled using the ten-parameter spring. Figure 5-7 presents the ten-parameter hysteretic spring for wood shear walls that can be used in numerical modelling of wood-frame buildings

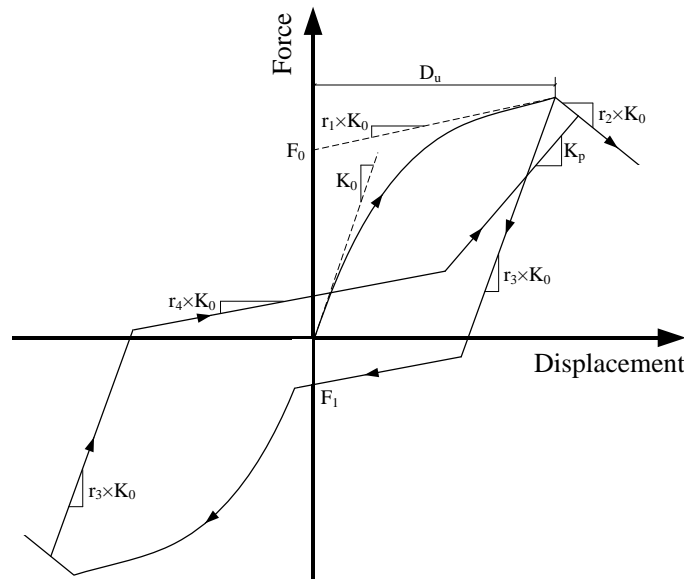


Figure 5-7: The ten-parameter hysteretic spring element used in numerical model of WSP and existing wall sheathings

The ten hysteretic parameters for the existing walls (i.e. HWS and GWB) as well as the WSP's with different nail schedule are presented in Table 5-8. It should be noted that the required secant stiffness at the target drift can be determined from the wood shear wall backbone. The backbone

curve can be obtained by the following relationship between the wall parameters, lateral force, and lateral displacement of the wall:

$$F_{bk} = \begin{cases} \left(1 - e^{-\frac{K_0 \Delta}{F_0}}\right) (r_1 K_0 \Delta + F_0) & , \Delta < D_u \\ F_u + r_2 K_0 (\Delta - \Delta_u) & , \Delta > D_u \end{cases} \quad (5-2)$$

where, F_{bk} is the backbone force corresponding to lateral displacement of Δ . The D_u is the displacement corresponding to the maximum lateral force (i.e., F_u). The rest of the ten-parameter hysteretic spring model is described in Chapter 4 of this dissertation. The backbone curves of HWS, GWB and WSP with different nail schedules are presented in Figure 5-8 and Figure 5-9. The secant stiffness corresponding to the 2% inter-story drift ratio are shown in the figures for each type of sheathing. It should be noted that the value of 2438 mm (96 in.) is used as the effective height for the walls sheathed with HWS, GWB, and WSP in order to obtain the secant stiffness.

Table 5-8: Hysteretic parameters *

Type of lateral force resisting element		Fastener spacing, mm (in.)	K ₀ , N/mm/m (lb/in./ft)	F ₀ , N/m (lb/ft)	F ₁ , N/m (lb/ft)	r ₁	r ₂	r ₃	r ₄	D _u , mm (in)	α	β
Existing SFRS	HWS ^(a)	406 (16)	85.0 (148)	657 (45)	248 (17)	0.095	-0.95	1.01	0.035	206 (8.1)	0.45	1.06
	GWB ^(b)	406 (16)	259 (450)	1459 (100)	95 (6.5)	0.023	-0.040	1.01	0.010	28 (1.1)	0.80	1.10
Retrofit SFRS	Wood Shear wall ^(c) Wood Structural Panel	51/305 (2/12)	2431 (4232)	29026 (1989)	3605 (247)	0.030	-0.073	1.01	0.033	50 (1.97)	0.76	1.24
		76/305 (3/12)	2176 (3787)	18635 (1277)	2481 (170)	0.032	-0.060	1.01	0.023	48 (1.90)	0.71	1.29
		102/305 (4/12)	1740 (3028)	14680 (1006)	2131 (146)	0.026	-0.056	1.01	0.022	47 (1.85)	0.76	1.29
		153/305 (6/12)	1355 (2359)	9850 (675)	1328 (91)	0.025	-0.049	1.01	0.019	47 (1.84)	0.71	1.29
		305/305 (12/12) ^(d)	416 (724)	3026 (207)	407 (27.9)	0.025	-0.049	1.01	0.019	47 (1.84)	0.71	1.29

* The parameters are based on 305 mm (1 ft) length of the sheathing.

^(a) 19×184 mm (0.75×7.25 in.) horizontal wood siding fastened to vertical wall stud with two 8d common nails.

^(b) 12.7 mm (0.5 in.) gypsum wall board fastened with #6 bugle head coarse threaded drywall screws.

^(c) 12 mm (15/32 in.) thick sheathing-rated plywood fastened with 10d common nail.

^(d) 9.5 mm (3/8 in.) thick sheathing-rated plywood fastened with 6d common nail.

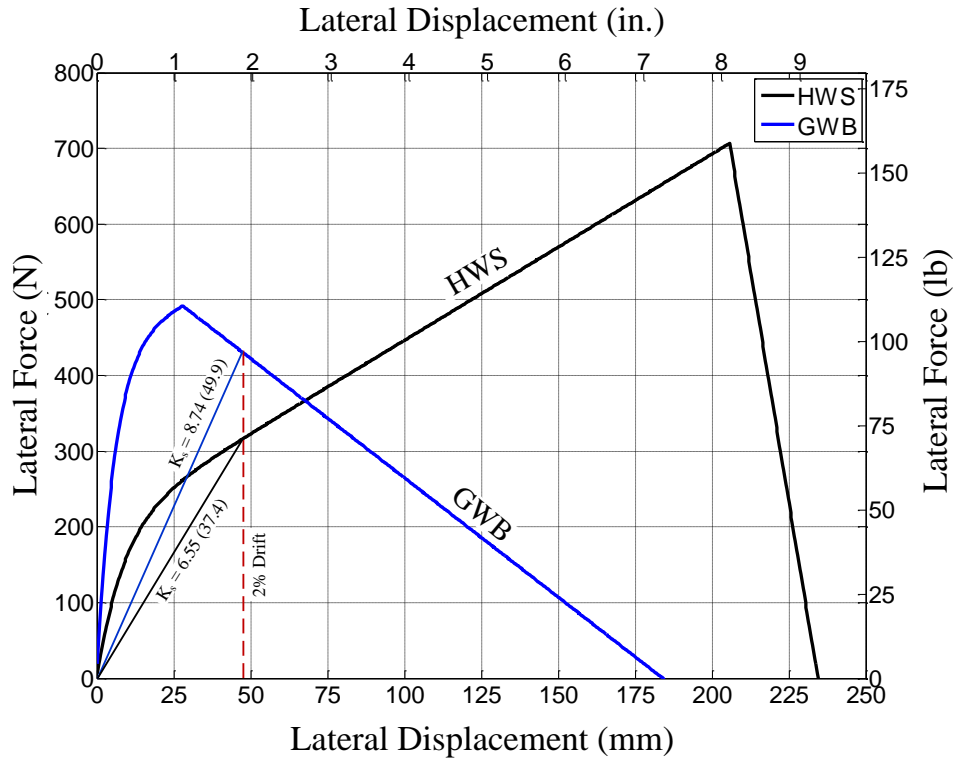


Figure 5-8: Backbones of HWS and GWB used in the PBSR procedure.

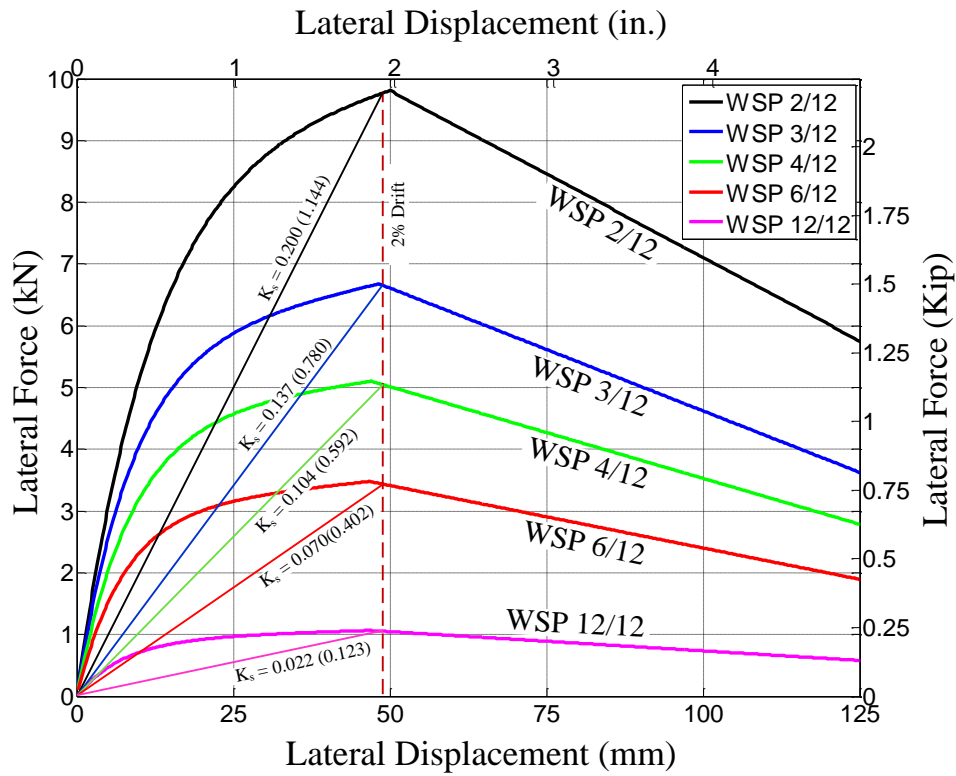


Figure 5-9: Backbones of wood structural panels with different nail schedules.

By knowing the required secant stiffness of retrofit elements and their locations from Table 5-4 and Table 5-5 and the secant stiffness per linear foot of WSP's with different nail patterns (Figure 5-8 and Figure 5-9) , the length of WSP's with the appropriate nail schedule can be selected for the design. Each ATS rod is confined with a stud pack for compression forces. The ATS rods are sized such that they would only elongate 6.4 mm (0.25 in.) at each story when the wall reaches 80% of its ultimate shear capacity, assuming a rigid body free-body diagram approach for force computation.

Table 5-9: PBSR retrofit design details and descriptions

Story	Design properties	Wood shear wall and fastener properties				
		WSP - A	WSP - D	WSP - 1	WSP - 3	WSP - 3R
4 th	Sheathing type ^(a)	Single ^(b)	Double	-	Single ^(b)	Single
	Calculated sheathing length, m (ft)	3.8 (12.6)	3.8 (12.6)	-	2.8 (9.1)	2.6 (8.5)
	Edge/Field nail spacing, mm (in)	305/305 (12/12)	153/305 (6/12)	-	305/305 (12/12)	76/305 (3/12)
3 rd	Sheathing type	Single	Double	-	Double	Single
	Calculated sheathing length, m (ft)	3.2 (10.6)	3.2 (10.6)	-	2.6 (8.6)	2.5 (8.1)
	Edge/Field nail spacing, mm (in)	153/305 (6/12)	76/305 (3/12)	-	76/305 (3/12)	76/305 (3/12)
2 nd	Sheathing type	Single	Double	-	Double	Single
	Calculated sheathing length, m (ft)	3.1 (10.3)	3.1 (10.3)	-	2.6 (8.6)	2.5 (8.1)
	Edge/Field nail spacing, mm (in)	76/305 (3/12)	51/305 (2/12)	-	51/305 (2/12)	51/305 (2/12)
1 st	Sheathing type	Single	-	Single	-	-
	Calculated sheathing length, m (ft)	3.0 (9.7)	-	7.2 (23.7)	-	-
	Edge/Field nail spacing, mm (in)	51/305 (2/12)	-	76/76 (3/12)	-	-

^(a) All sheathing is 12 mm (15/32 in.) thick sheathing-rated plywood with 10d common nail unless otherwise noted.

^(b) 9.5 mm (3/8 in.) sheathing-rated plywood with 6d common nail.

By knowing the location and type of retrofit element, the final specification for the retrofit design of the four story wood-frame building can be obtained. Figure 5-10a and Figure 5-10b present the detailed location and design of the retrofit elements in the first story and upper stories, respectively. The elevation views and details of the steel SMF installed in the x - and y -direction, are shown in Figure 5-10c and Figure 5-10d, respectively. Table 5-10 presents the final design of the wood structural panels and the ATS rods used to retrofit the four-story wood-frame building. More details for the SMF's, WSP's, ATS rods and their installation procedure are presented in Chapter 5.

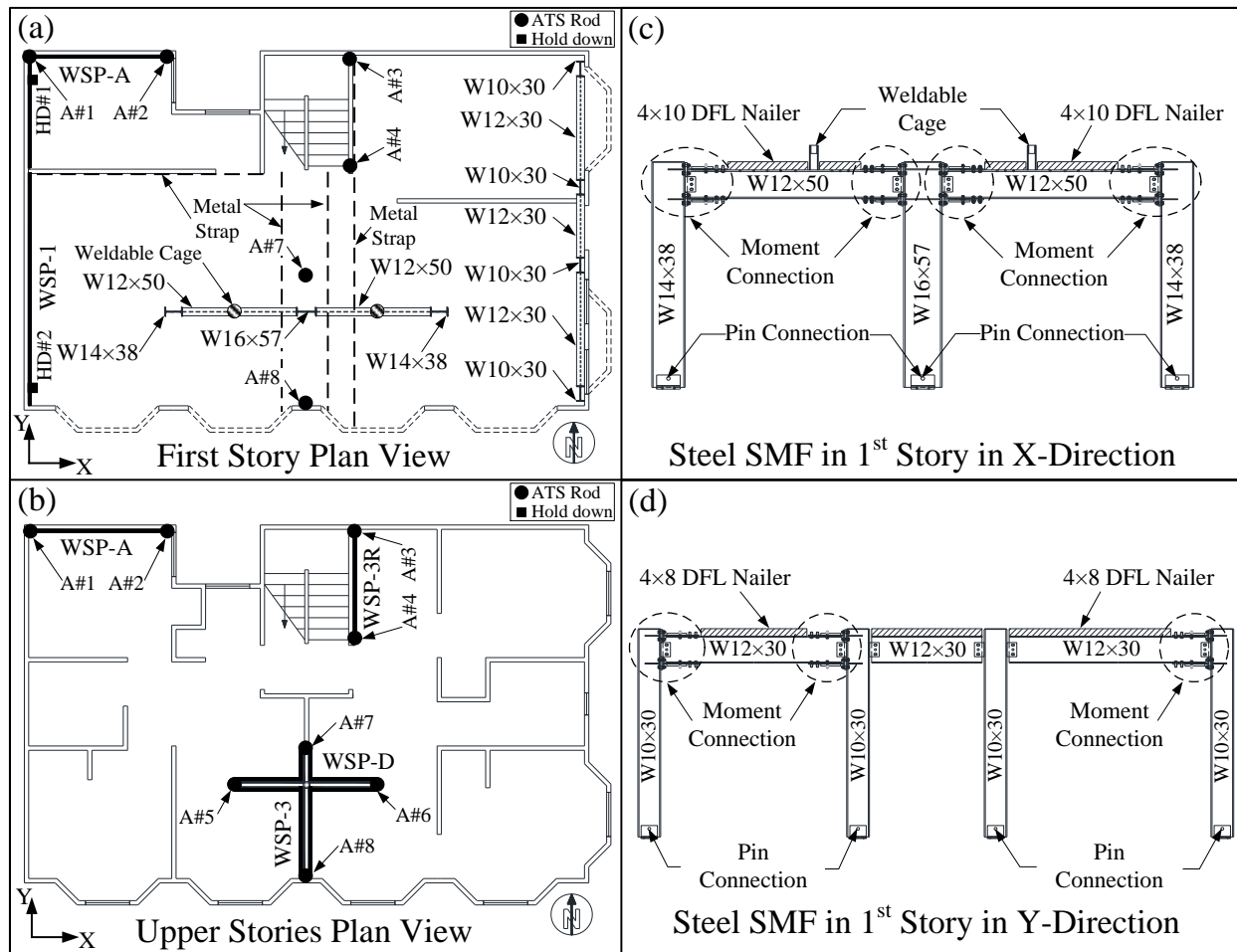


Figure 5-10: Detail of PBSR retrofit elements: (a) Plan view of first story, (b) Plan view of upper stories, (c) Steel SMF along longitudinal direction, (d) Steel SMF along transverse direction.

Table 5-10: PBSR retrofit design details and descriptions of WSP's and ATS rods

Story	Design properties	Wood shear wall and fastener properties				
		WSP - A	WSP - D	WSP - 1	WSP - 3	WSP - 3R
4 th	Sheathing type ^(a)	Single ^(b)	Double	-	Single ^(b)	Single
	Edge/Field nail spacing, mm (in)	305/305 (12/12)	153/305 (6/12)	-	305/305 (12/12)	76/305 (3/12)
	ATS Rod Diameter ^(c) , mm (in)	13 (1/2)	16 (5/8) ^(d)	-	13 (1/2)	16 (5/8) ^(d)
3 rd	Sheathing type	Single	Double	-	Double	Single
	Edge/Field nail spacing, mm (in)	153/305 (6/12)	76/305 (3/12)	-	76/305 (3/12)	76/305 (3/12)
	ATS Rod Diameter ^(c) , mm (in)	16 (5/8)	29 (1-1/8) ^(d)	-	25 (1) ^(d)	22 (7/8) ^(d)
2 nd	Sheathing type	Single	Double	-	Double	Single
	Edge/Field nail spacing, mm (in)	76/305 (3/12)	51/305 (2/12)	-	51/305 (2/12)	51/305 (2/12)
	ATS Rod Diameter ^(c) , mm (in)	22 (7/8) ^(d)	38 (1-1/2) ^(d)	-	35 (1-3/8)	29 (1-1/8) ^(d)
1 st	Sheathing type	Single	-	Single	-	-
	Edge/Field nail spacing, mm (in)	51/305 (2/12)	-	76/76 (3/12)	-	-
	ATS Rod Diameter ^(c) , mm (in)	29 (1-1/8) ^(d)	-	Hold down ^(e)	38 (1-1/2) ^(d)	32 (1-1/4) ^(d)

^(a) All sheathing is 12 mm (15/32 in.) thick sheathing-rated plywood with 10d common nail unless otherwise noted.

^(b) 9.5 mm (3/8 in.) sheathing-rated plywood with 6d common nail.

^(c) Standard steel threaded rod with min. $F_u = 400$ Mpa (58 ksi) and $F_y = 296$ Mpa (43 ksi) unless otherwise noted.

^(d) High strength steel threaded rod with min. $F_u = 827$ Mpa (120 ksi) and $F_y = 634$ Mpa (92 ksi).

^(e) Hold down with allowable tension force of $F_t = 31$ kN (6.97 kips).

5.4 Numerical Validation

The building was modeled numerically using the state-of-the-art software developed to analyze the behavior of wood-frame buildings (Pei and van de Lindt, 2008). To do this, the existing sheathings at each story were modeled using the ten-parameter hysteretic spring (Folz and Filiatrault, 2001) according to the values presented in Table 5-8 and locations shown in Figure 5-11. Then, the retrofit elements were added numerically to the unretrofitted building according to the retrofit design specifications presented in Table 5-10 and Figure 5-10.

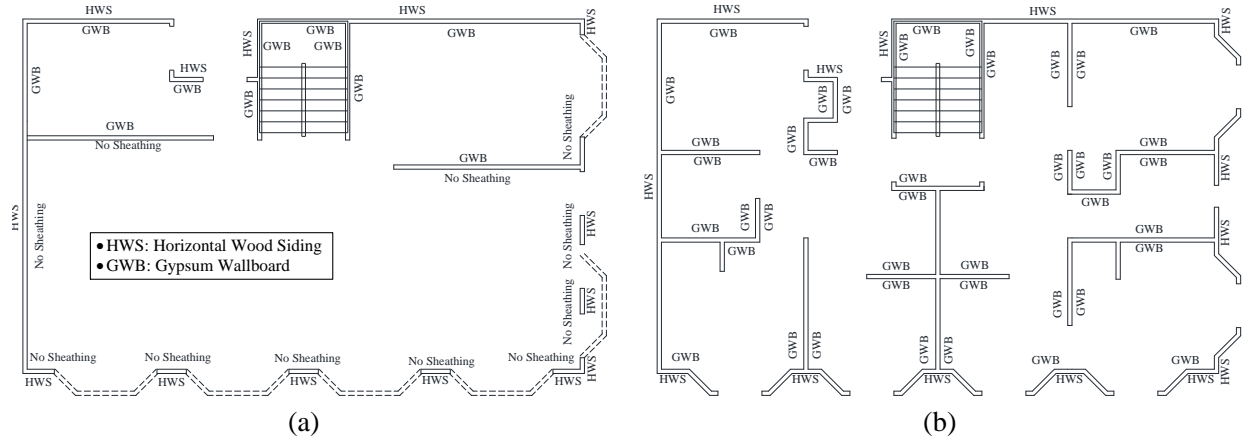


Figure 5-11: Existing wall sheathing in un-retrofitted building: (a) first story, (b) upper stories.

As mentioned earlier, the well-known ten-parameter hysteretic spring model (Folz and Filiatrault, 2001) was used to model the horizontal wood siding (HWS), gypsum wallboard (GWB), and wood structural panels (WSP). These parameters for the walls within the building (i.e., HWS and GWB) are obtained based on test data of wood-frame walls sheathed with HWS and GWB and are presented in Table 5-8. The parameters for the WSP's were obtained from the NEESWood Report NW-05 (Pang et. al, 2009). The steel SMF's in the first floor are modeled as bilinear springs in this study, but it is noted that a trilinear spring could also be used if modeling larger deformations well beyond the design range. The parameters for the bilinear springs (i.e., steel SMF) are presented in Table 5-7. The fundamental period of the building was calculated as $T_n = 0.43s$.

5.4.1 Bi-axial Analysis: Cumulative Distribution of ISD Ratios at $S_a = 1.8g$

The behavior of the retrofitted building was evaluated using non-linear time-history analysis (NLTHA) with 22 biaxial far-field ground motions (FEMA P-695, 2009) scaled to the MCE (i.e., $S_a = 1.8g$). Bi-axial analyses were utilized for the verification of the PBSR because it is a

performance-based method and not necessarily tied to either uni-axial or bi-axial analysis. Figure 5-12 presents the rank ordered peak ISD ratios in the form of probability of non-exceedance versus ISD ratios when subjected to the 22 bi-axial far-field earthquakes. A lognormal distribution was fit to the data in order to interpolate the drifts between the points and provide a general feel of the shape of the response CDF. From Figure 5-12, it can be seen that the maximum ISD ratio at the first story (i.e., governing story in X-direction) corresponding to 50% probability of non-exceedance (PNE) is 1.58%, which is less than the 2% target ISD ratio. The probability of non-exceedance corresponding to ISD ratio of 2% target ISD ratio is 70% (i.e., 20% safety margin for the retrofit design). The maximum ISD ratio corresponding to the PNE of 50% in the Y-direction at the fourth story is 1.72%, which is closer to the target ISD ratio. The probability of non-exceedance corresponding to ISD ratio of 2% target ISD ratio in Y-direction is 58% (i.e., 8% safety margin for the retrofit design). These safety margins can be reserved for uncertainties in the design and construction of the building. Some of the major uncertainties in any retrofit procedure are: (1) underestimation or overestimation of the stiffness, strength, and damping of the SFRS elements; (2) imperfection in construction and installation of the retrofit, and (3) the damages of SFRS due to previous seismic event that is not considered in the retrofit design. It should be noted that the ISD ratios in all other stories are between 1 and 2%, which numerically confirms the effectiveness of the retrofit procedure in utilizing the strength of upper stories, and more importantly eliminating the existence of soft and stiff stories in the building.

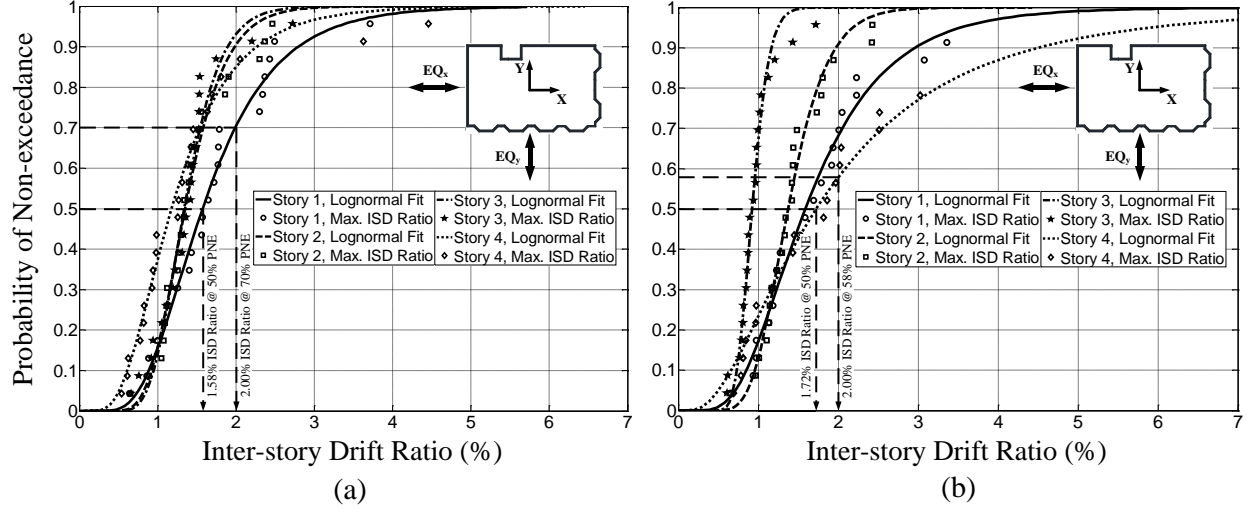


Figure 5-12: Numerical validation of the retrofitted building subjected to 22 bi-axial records:

Probability of non-exceedance vs. ISD ratio at $S_a = 1.8g$ along: (a) X-direction, (b) Y-direction.

5.4.2 Uni-axial Analysis: Cumulative Distribution of ISD Ratios at $S_a = 1.8g$

The four-story building retrofitted herein is intended to be tested experimentally at the largest shake table in the United States located at NEES at UC-San Diego laboratory. Full details of the shake table tests are presented in the next chapter (Chapter 6). It should be noted that the shake table can move only in one direction (i.e., uni-axial motion in x -direction) and thus, the building can be excited only along its x -direction. Therefore, in order to have a closer look at the inter-story drift responses of the stories when the building is subjected to uni-axial ground motions, the building is numerically subjected to the suite of 44 uni-axial earthquakes (i.e., both x and y components of the 22 bi-axial earthquake records) that are only scaled to the designed spectral acceleration (i.e., $S_a = 1.8g$). The earthquake records are scaled such that the response spectral acceleration of an elastic SDOF system with the same fundamental period as the

building (i.e., $T_n = 0.43\text{s}$) is matched the intensity that the earthquake is scaled to (i.e., $S_a = 0.01g$ to $S_a = 2.0g$). Then, for each story, the cumulative distribution of the ISD ratios is plotted and lognormal distribution is fit to the data for interpolation between the points. Figure 5-13 presents the rank ordered peak inter-story drift (ISD) ratios for all the stories of the retrofitted building in the form of probability of non-exceedance (PNE) versus the ISD ratio. At the first glance, it can be seen that the cumulative distribution of the ISD ratios for all the stories are very close to each other which shows that all the stories experience the same ISD ratios at the spectral acceleration of $S_a = 1.8g$. Furthermore, it can be seen that at a PNE of 50%, the maximum inter-story drift ratio of the building is 1.54%. This shows that all the stories meet the performance criteria, namely ISD ratios of less than 2% for 50% of the earthquakes at $S_a = 1.8g$. The maximum median ISD ratio of the building is 2.00% at the PNE of 70%. This shows that the retrofitted building exceeds the expected performance criteria with a margin of approximately 20%. Again, this safety margin can be reserved for uncertainties in the design and construction of the building, thus, the 20% safety margin is felt to be justified for this design.

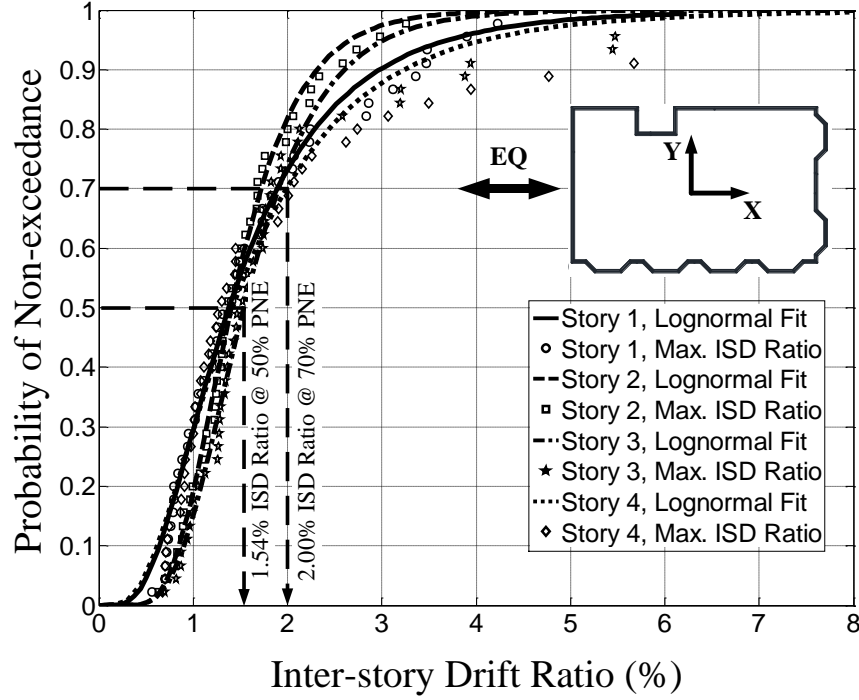


Figure 5-13: Numerical validation of the retrofitted building subjected to 44 uni-axial records:

Probability of non-exceedance vs. ISD ratio at at $S_a = 1.8g$.

5.4.3 Uni-axial Analysis: Multi-record Incremental Dynamic Analysis (MIDA)

In order to investigate the performance of the building subjected to different earthquake records scaled to different seismic intensities, a multi-record incremental dynamic analysis (IDA) is performed (Vamvatsikos and Cornell, 2002). The numerical model of the building was subjected to 44 far-field uni-axial earthquake records (FEMA P-695, 2009) scaled to intensities ranging from $S_a = 0.01g$ to $S_a = 2.0g$ along the x -direction. Since the performance of the building in this study was evaluated based on the inter-story drift (ISD) ratios of the stories, the peak ISD ratios of each story of the building are recorded when the building is subjected to each earthquake record and then the median value of the ISD ratios for the story was computed. The median value of ISD ratios is selected since it indicates that in 50% of the time the story

experiences larger (or smaller) ISD ratios than the median value. Furthermore, the design response spectrum from the hazard maps are based on the median values of spectral acceleration of a SDOF system when subjected to earthquakes associated with a specific site and hazard level. This allows the comparison between the median values of ISD ratios from the numerical analysis to the per-defined performance criteria (i.e., target ISD ratio).

Figure 5-14 presents the multi-record IDA plots of the building. Inspection of Figure 5-14 shows that all stories experience approximately the same inter-story drift ratio regardless of earthquake intensity. It can also be seen that the IDA plots are very close to straight lines. This shows that all the stories not only experience approximately the same ISD ratios at the spectral acceleration that the building is designed for (i.e., $S_a = 1.8g$), but also they go through the same ISD ratio under a range of spectral accelerations (i.e., a consistent performance for a range of ground motion intensities). Furthermore, this distributes the seismic demand over the entire height of the building which results in avoiding excessive damage in any one story. Finally, one can see that the stories have ISD ratios smaller than the target ISD ratios at MCE intensity (i.e., $S_a = 1.8g$), satisfying the performance criteria. It should be noted that the average and maximum ISD ratios at $S_a = 1.8g$ are about 1.42% and 1.52% (very close to the maximum ISD ratio at PNE of 50% from the CDF plots in Figure 5-13), respectively. The slightly conservative results are likely caused by conservative hysteretic damping in the PBSR procedure. However, the retrofit design was not modified since the uncertainties associated with this type of building are felt to be high enough to warrant this level of conservatism in design.

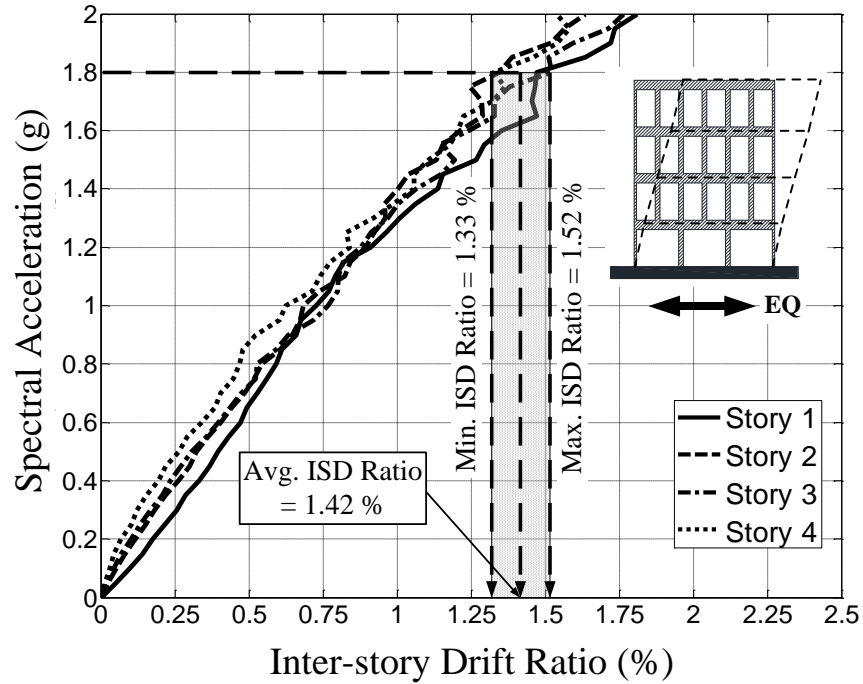


Figure 5-14: Numerical validation of the retrofitted building subjected to 44 uni-axial records:
Median multi-record incremental dynamic analysis (IDA).

As mentioned earlier, in order to validate the PBSR procedure experimentally, the four-story wood-frame building was constructed, retrofitted, and subjected to set of ground motions with different intensities including the 1.8g spectral acceleration retrofit design intensity. The next chapter presents the shake table test setup, testing plans and design details, and the test results.

Chapter 6. FULL-SCALE SHAKE TABLE VALIDATION OF THE PBSR METHODOLOGY^{7,8,9}

6.1 Background on Full-Scale Testing of Wood-Frame Buildings

Full-scale whole-building tests on wood buildings have been performed around the world only 10 to 20 times. U.S.-based projects for full-scale testing of light-frame wood buildings have increased significantly since the late 1990's as a result of the CUREE-Caltech Project (2002) and projects related to the NSF's George E. Brown Jr. Network for Earthquake Engineering Simulation (NEES). A good summary is provided in a 2009 report prepared by the National Association of Home Builders Research Center (NAHB, 2009), but significant testing has occurred in the five years since that report. For brevity, only specific projects and tests that have had a direct effect on the planning and execution of the test program presented herein are discussed.

Filiatrault et al. (2002) tested a rectangular two-story house with an integrated one-car garage. The building was full-scale but overall size was limited to the shake table dimensions, but regardless provided state-of-the-art experimental results. The building was designed in accordance with the 1988 Uniform Building Code (UBC, 1988) and performed well at code level

⁷ Bahmani, P., van de Lindt, J.W., Pryor, S.E., Mochizuki, G. L. (2014). "Performance-based Seismic Retrofit of Soft-Story Wood-frame Buildings Using Steel Special Moment Frames: Methodology and Full-Scale Experimental Validation", *Submitted to Engineering Structures*, January 2015.

⁸ Bahmani, P., van de Lindt, J.W., Gershfeld, M., Mochizuki, G.L., Pryor, S.E., Rammer, D. (2014). "Experimental Seismic Behavior of a Full-Scale Four-Story Soft-Story Wood-frame Building with Retrofits I: Building Design, Retrofit Methodology, and Numerical Validation", *ASCE J. Struct. Eng.*, DOI: 10.1061/(ASCE)ST.1943-541X.0001207.

⁹ van de Lindt, J.W., Bahmani, P., Mochizuki, G.L., Pryor, S.E., Gershfeld, M., Tian, J., Symans, M.D., Rammer, D. (2014) "Experimental Seismic Behavior of a Full-Scale Four-Story Soft-Story Wood-frame Building with Retrofits II: Shake Table Test Results", *ASCE J. Struct. Eng.*, DOI: 10.1061/(ASCE)ST.1943-541X.0001206.

(design basis earthquake, DBE) and near-fault (maximum considered earthquake, MCE) records from the 1994 Northridge earthquake. Gypsum wall board and stucco were shown to provide a very significant increase in strength and stiffness (Filiatrault et al., 2002). As part of the NEESWood Project, Filiatrault et al. (2010) conducted full-scale tri-axial tests on a two-story three-bedroom 167.2 m² (1800 ft²) townhouse with an integrated two-car garage on the twin shake tables of the State University of New York at Buffalo. This building was also designed to the 1988 UBC (UBC, 1988). The results showed that for light-frame wood buildings typical of 1980's to 1990's California, only moderate damage resulted during a design-basis earthquake (DBE), while significant and costly damage occurred during the maximum credible earthquake (MCE). This included a 12 mm (0.5 in.) wide sill plate crack around the entire building which would be very costly to repair, but did not pose a threat to the lives of would-be inhabitants. The earlier conclusion about the added strength and stiffness based on a test of a smaller floor plan resulting from the gypsum wall board and stucco was confirmed during the NEESWood townhouse test. Full building and results are available in the project report by Christovasilis et al. (2007). During the CUREE-Caltech Wood-frame project a three-story apartment building with a tuck under garage was tested by Mosalam and Mahin (2007). Their conclusions confirmed that these types of buildings are prone to torsional response and soft-story collapse.

The world's largest shake table test was conducted as part of the NEESWood Project by van de Lindt et al (2010) and was a test of a 1,300 m² (14,000 ft²) six-story apartment building at Japan's E-defense facility in Miki, Japan. The building was 12.2×18.3 m (40×60 ft) in plan and 17.1 m (56 ft) tall. Full details are available in the project task report (Pei et al., 2010). The objectives of this test program were to (1) provide a general understanding of how midrise light-frame wood buildings perform in a major earthquake; (2) provide validation for the performance-

based seismic design philosophy developed within the project which was a variation on direct displacement design (DDD) developed by Pang et al (2009). Overall performance was excellent at MCE level, but it should be kept in mind that the test structure was designed at a level expected to provide seismic performance superior to current code (van de Lindt et al., 2014). Although these test programs provided valuable information on structural behavior of light-frame wood buildings, they did not address the challenge in retrofitting existing buildings, specifically, at-risk soft-story wood-frame buildings.

In order to investigate and evaluate different retrofit approaches for soft-story wood-frame buildings, van de Lindt et al. (2014) and Bahmani et al. (2014) retrofitted and tested a four-story soft-story wood-frame building in the summer of 2013 as part of a multi-university-industry project entitled “*NEES-Soft: Seismic Risk Reduction for Soft-Story Wood-frame Buildings*” sponsored by the National Science Foundation and led by Colorado State University.

6.1.1 Brief Overview of the NEES-Soft Project

The NEES-Soft project was a five-university multi-industry effort that culminated in a series of full-scale soft-story wood-frame building tests to validate retrofit philosophies proposed by the FEMA P-807 guidelines and the performance-based seismic retrofit (PBSR) approach presented in Chapter 3 of this dissertation (Bahmani et al, 2014). There were several major test objectives: (1) to experimentally determine whether the FEMA P-807 guideline is effective and should be recommended by the NEES-Soft project team for use to the practicing earthquake engineering community; (2) to determine whether the retrofits designed based on the performance-based seismic retrofit (PBSR) methodology allowed the building to meet its performance objectives; (3) to provide a better understanding of the global behavior of full-scale soft-story wood-frame

buildings; and (4) to gain better insight into the collapse limits of soft-story wood-frame buildings with archaic building materials.

In order to examine the effectiveness of two retrofit methodologies (i.e., FEMA P-807 and PBSR) a four-story wood-frame building with a soft- and weak-story at the ground level was retrofitted and experimentally tested in the summer of 2013 at the outdoor shake table facility at Network for Earthquake Engineering Simulation (NEES) at UC-San Diego. The comprehensive test program examined each of the four retrofits experimentally, namely (1) cross laminated timber (CLT) rocking walls based on the FEMA P-807 (FEMA, 2012) guidelines and a recent City of San Francisco Soft Story Retrofit Ordinance; (2) steel special moment frames (SMF) based on the FEMA P-807 retrofit guideline; (3) steel special moment frames and wood structural panels (i.e., wood shear walls) based on the performance-based seismic retrofit (PBSR) method; and (4) supplemental damper assemblies designed based on a PBSR methodology. Table 6-1 presents the retrofit methodologies, testing phases, and specifics of the design criteria that were used in the retrofit designs for the four-story wood-frame building. This chapter focuses on experimental validation of the PBSR methodology in retrofitting a four-story soft-story wood-frame building by using steel special moment frames and wood structural panels (i.e., Phase 3 in Table 6-1). The full detail of the retrofit design and shake table test results can be found in Bahmani et al. (2014), van de Lindt et al. (2014), Tian et al. (2014). It should be noted that the un-retrofitted building was tested to collapse in order to investigate the collapse mechanism and deformation capacity of soft-story wood-frame buildings. The details of the collapse testing are presented in Chapter 7 of this dissertation.

Table 6-1: Retrofit techniques and design criteria for the four-story building

Retrofit methodology	Testing phase	Number of seismic tests	Retrofit technique	Retrofit design criteria
FEMA P-807	1	4	CLT ^(a)	PNE ^(e) =80% at $S_a = 0.9g^{(f)}$
	2	4	SMF ^(b) and WSP ^(c)	PNE=80% at $S_a = 1.1g$
PBSR	3	5	SMF and WSP	PNE=50% at $S_a = 1.8g$
	4	5	FVD ^(d) and WSP	PNE=50% at $S_a = 1.8g$

^(a) Cross-Laminated Timber

^(b) Steel Special Moment Frame

^(c) Wood Structural Panel

^(d) Fluid Viscous Damper Frame Assembly

^(e) Probability of non-exceedance

^(f) Records were scaled per ASCE7-10 (2010) scaling method.

6.2 Shake Table Test Setup and Construction of the Test Building

6.2.1 Building Details

A number of site visits were conducted to identify typical architecture that the test building should replicate with the focus placed on the San Francisco Bay Area in California. Although the exterior architecture was important for aspect ratio and determining locations and number of openings at the soft and other stories, there were several other features of this particular building era that had to be identified, such as: interior wall density at first and upper floors, typical room sizes, floor and wall construction assemblies, and nailing schedules for various components. The test building plan dimensions were dictated by the shake table size which was 7.6×12.2 m (25×40 ft) resulting in plan dimensions of 7.3×11.6 m (24×38 ft). Figure 6-1 (also Figure 5-1) shows the floor plans of the first story (soft-story) and upper stories. Each of the upper three stories had two two-bedroom apartment units as can be seen in Figure 5-1b. Figure 6-2 presents the elevation views of the building from all four sides and Figure 6-3 presents isometric views of the building from four directions.

On the first floor, there was a garage space for four cars, a large laundry room, a storage room, and a light well. The light well was included since many of these buildings are surrounded by other buildings on two sides (i.e., north and west sides in the test building) and therefore have two essentially solid sides and two open sides. The test building was designed to replicate these conditions, thus making it, in some ways, a worst case scenario but not an atypical building. It should be noted that the building was soft and weak on two adjacent sides resulting in significant torsion (see Chapter 5 for more details).

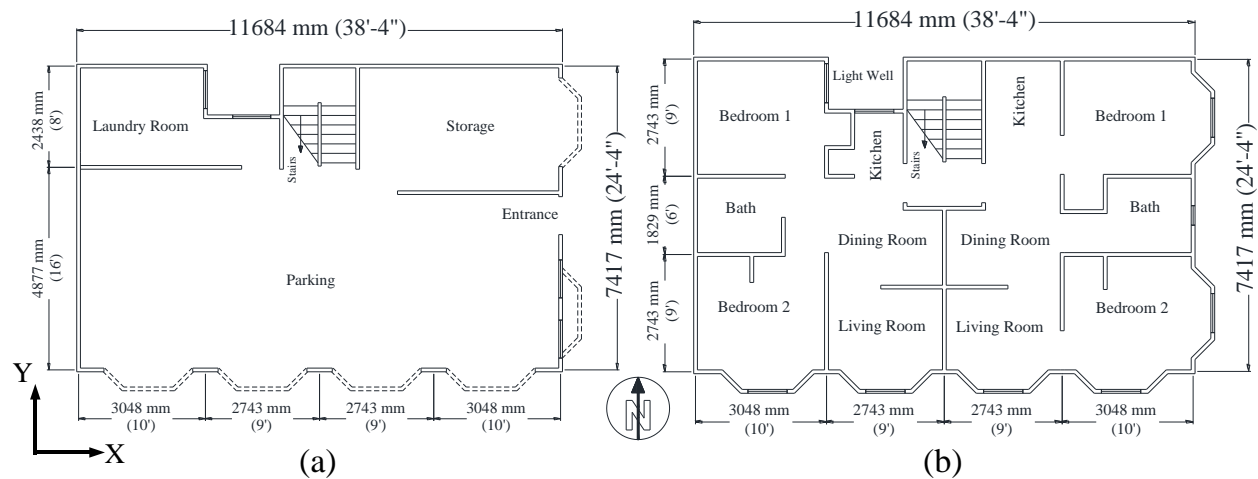


Figure 6-1: Floor plan views of the four-story test building: (a) first story, and (b) upper stories

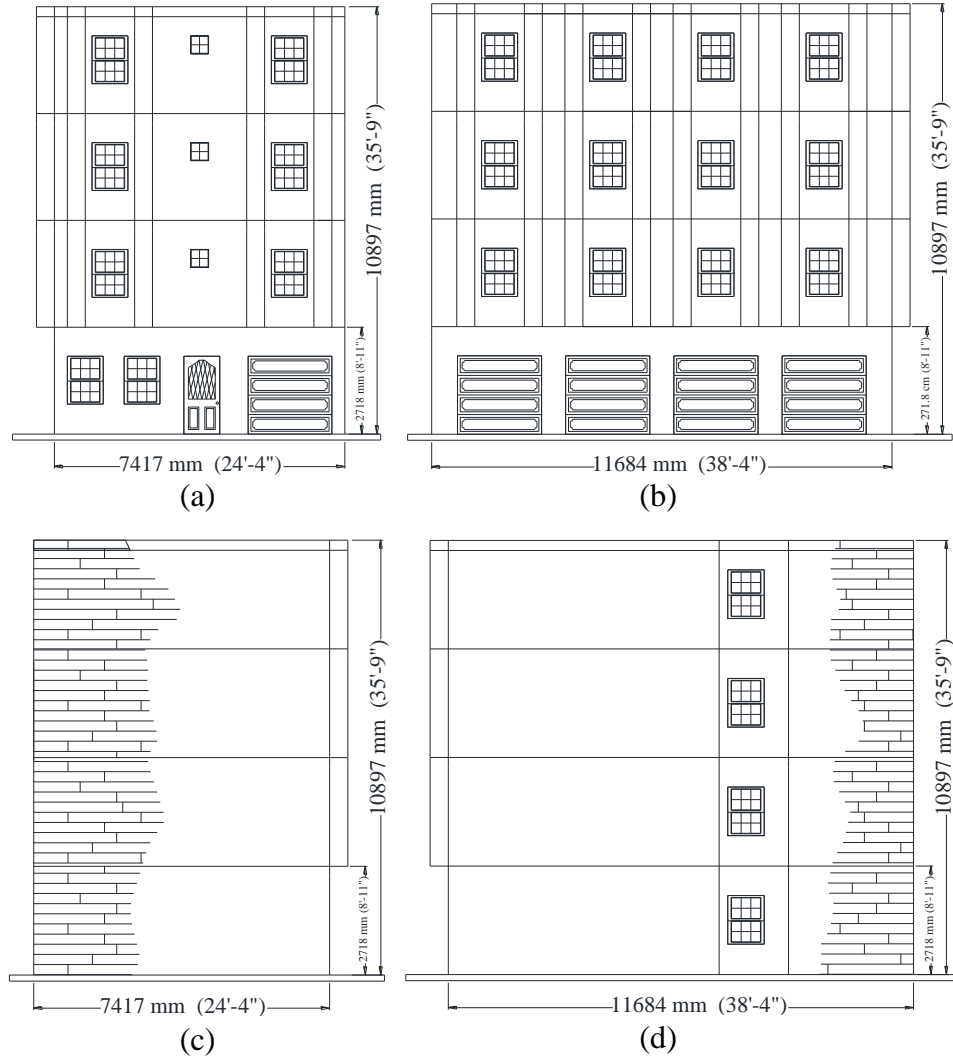


Figure 6-2: Elevation views of the test building: (a) East view, (b) South view, (c) West view, (d) North view.

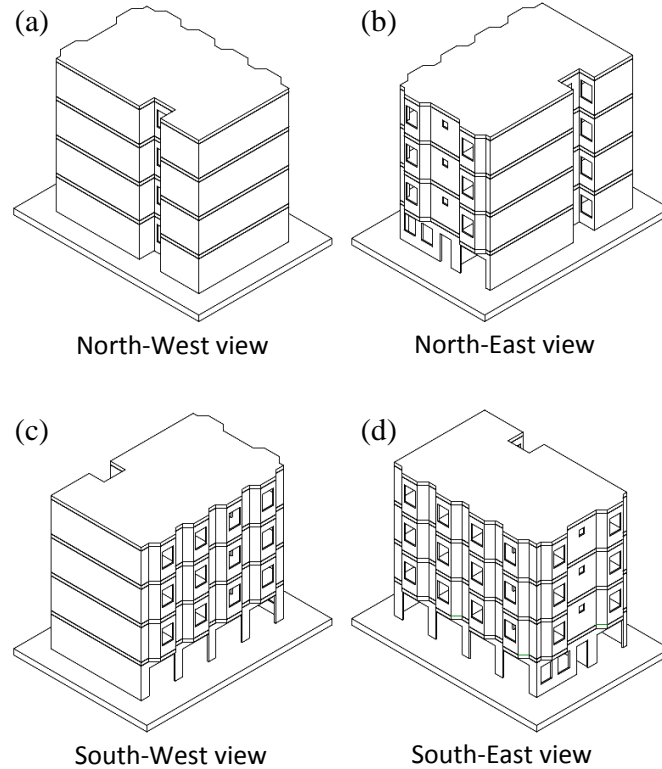


Figure 6-3: Isometric views of the test building

It should be noted that modifications to the archaic building materials were necessary to ensure that the test building could be quickly and economically repaired between tests (i.e., gypsum plaster on wooden lath repair would be cost and time prohibitive), since a number of tests were conducted at moderate to high seismic intensity and damage was expected after each test. Table 5-2 provides a comparison between the features commonly found in these types of soft-story buildings and the NEES-Soft four-story test building. The interior wall density in the upper stories was high, but this is in line with many soft-story wood-frame buildings of that era. In fact, this high difference between wall densities in the first story compared with the upper stories exacerbates the soft-story behavior at the first story for these types of buildings. The exterior was covered with 19×184 mm (0.75×7.25 in.) horizontal wood siding (HWS) attached to each stud of the wall framing with 2-8d common nails with shank diameter of 3.4 mm (0.134 in.) and length

of 63.5 mm (2.5 in.). The interior walls were covered with 12.5 mm (0.5 in.) thick gypsum wall board (GWB) and fastened to wood studs with #6 bugle head coarse threaded drywall screws. Figure 6-4a shows a photo of a typical Bay Area soft-story wood-frame building and Figure 6-4b shows a photo of the four-story test building constructed on the top of the shake table prior to the start of the test program.

Table 6-2: comparison between construction material in archaic building and the test building

Construction category	Features/items commonly observed during site visits	Features/items in the test building	
		Included	Not included
Architecture	Bay windows	✓	-
	Light well	✓	-
	Large openings (garage)	✓	-
Interior	Wall density	✓	-
	Plank flooring	✓	-
	Hardwood floors	✓	-
	Plaster (on lathe)	✓ ^(a)	-
	Tile	-	✓ ^(b)
Exterior	Wood siding	✓	-
	Trim	-	✓
	Stucco (not all buildings)	-	✓ ^(c)

^(a) 12.5 mm (0.5 in.) gypsum wall board was used in the test building.

^(b) Equivalent mass for tile added in kitchens and bathrooms.

^(c) Stucco was not used; thus, no mass was added to account for weight of stucco.



Figure 6-4: Comparison of the architecture for a soft-story wood building (a) in the San Francisco Bay Area, and (b) the test building designed as part of the NEES-Soft project.

6.2.2 Construction

The construction of the four-story wood-frame building began in May 2013 at the NEES@UCSD laboratory site. Figure 6-5 presents the construction sequence for the four-story wood-frame building built on top of the shake table at NEES@UCSD. This is the largest and only shake table in the USA capable of conducting this type of test. Interface steel framing beams for connecting the framing to the shake table were designed and fabricated at Colorado State University (Figure 6-5a-c). In order to expedite the construction time, wall and floor framing assemblies were pre-fabricated and moved to the shake table once it became available for building erection (Figure 6-5d). The interface framing was shipped to the USCD site and installed on top of the shake table to serve as a foundation for the building and allow for anchor bolt connections between the wood-frame and the shake table (Figure 6-5e and Figure 6-5f). The

prefabricated wall floor and roof framing assemblies were gradually erected on top of the interface framing until the entire building was constructed on top of shake table. Figure 6-5g through Figure 6-5j present the erection of wall and floor assemblies. The floor was covered with 1×6 (19×140 mm) dimension lumber and 19 mm (3/4 in.) unfinished red oak flooring to provide the building with the in-plane diaphragm stiffness observed in-situ. Figure 6-5k, Figure 6-5l, and Figure 6-5m present the installation of GWB, wood floor boards, and hardwood flooring, respectively. Figure 6-5n shows the typical installation of the added mass to compensate for the difference between the design mass and as-built mass of each part of the floor, e.g. tile in the kitchen and bathrooms. The steel plates used for additional mass were rigidly attached to the floor and smaller steel plates were sandwiched between wood that was bolted or screwed to the floor joists. Figure 6-5o-q show different views of the finished building prior to the start of the shake table test program. In order to prevent damaging the shake table control room in case of collapsing of the building, three safety towers were installed between the structure and the control room (i.e., south side of the building) and on the opposite side (i.e., north side of the building). Figure 6-5r presents the south-east view of the building with safety towers in place.

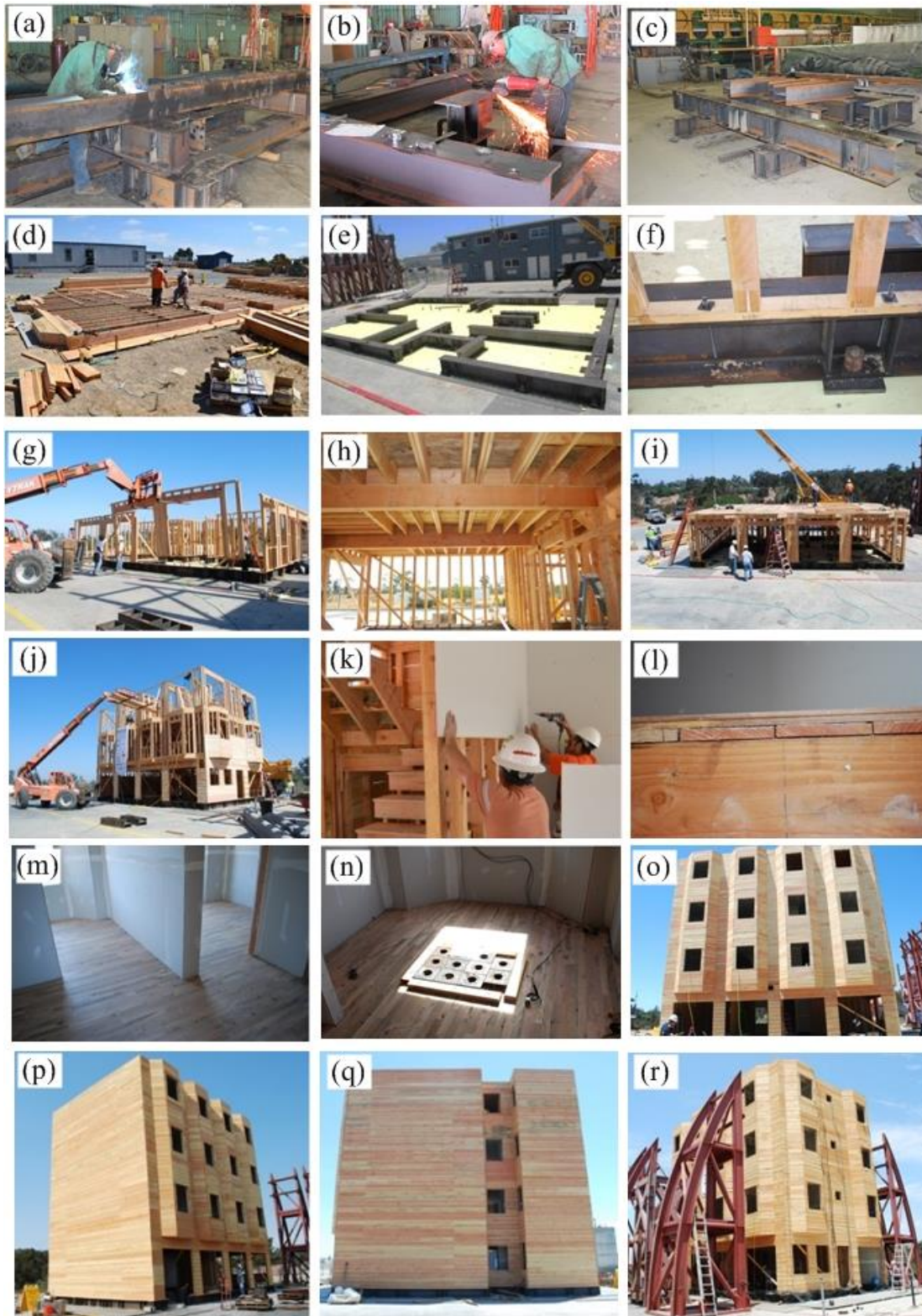


Figure 6-5: Construction sequence of the four-story wood-frame building on top of the shake table.

Figure 6-6 presents the shake table, the footprint of the building (shown in bold), and the south and west elevation views (i.e., sections A-A and B-B in Figure 6-6a). The gap between the concrete slab and the shake table which allows the shake table to move was covered by a 25.4 mm (1 in.) thick steel plate (i.e., steel platen) bolted to the top of the shake table and allowed to slide over the concrete slab. The shake table is a 7.6×12.2 m (25×40 ft) uni-axial shake table with a maximum gravity payload of 20,000 kN (4,496 kips); full details on the shake table performance and capabilities can be found in Ozcelik et al. (2008).

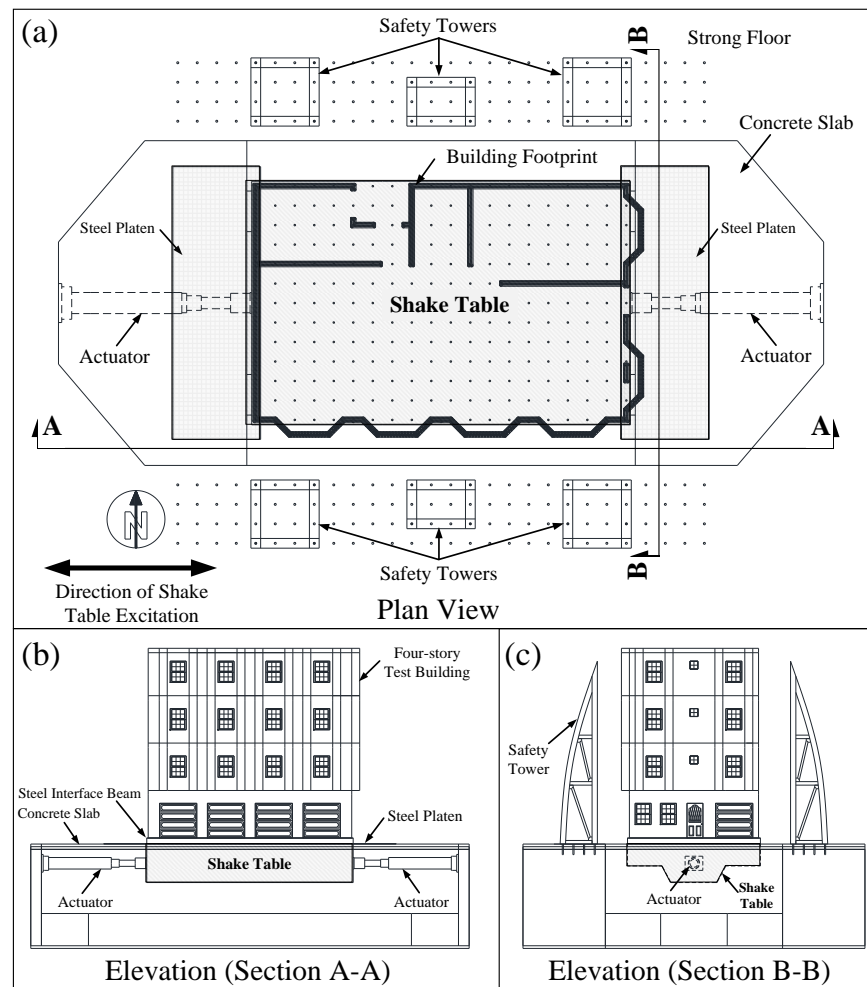


Figure 6-6: Position of the four-story building on top of the shake table: (a) plan view, (b) south elevation view (Section A-A), (c) west elevation view (Section B-B).

6.3 Installation of Retrofits

In order to validate the PBSR method and retrofit procedure, the four-story building was retrofitted with steel special moment frames at the first story and wood shear walls with continuous overturning restraint (i.e., anchor tie-down system (ATS) rods) at all stories. The structural specifications and the locations of the retrofit elements were determined in Chapter 5 (Table 5-10) based on the proposed PBSR methodology. Figure 6-7 presents the retrofit types and locations at the first story as well as the upper stories.

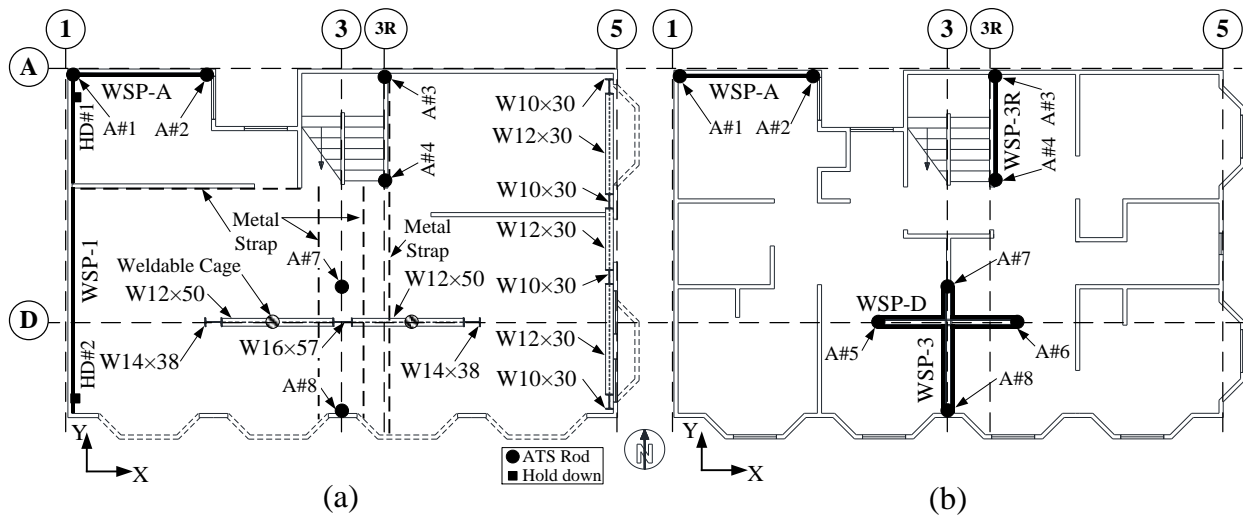


Figure 6-7: Location of retrofits: (a) first story, (b) upper stories.

One of the key factors for selecting a retrofit technique is the installation procedure and the time required for retrofit. The use of a steel pinned-base SMF combined with WSP's for retrofitting has several advantages: (1) this retrofit technique has minimal interference with the garage openings and other architectural details of the building; (2) the use of this unique SMF with yielding links between the columns and beam moves the formation of the plastic hinge out of the beam and into the links. This in turn permits the beams to be designed without the need for lateral torsion buckling bracing (Pryor and Murray, 2013). This bracing is problematic for typical

moment frames since the wood diaphragm is, in general, not stiff and strong enough to provide a reaction for the brace; (3) the use of a pinned-base simplifies the retrofit foundation design while providing more certainty as to the actual boundary conditions (fixity) at the bottom of the column as compared to a fixed-base design; (4) the frame is easily assembled on site using bolted, not welded, connections. This eliminates the potential fire hazard associated with field-welding in an unprotected wood structure; (5) the beams can easily be connected to the floor diaphragm by means of wood nailers attached to the flanges of the beams; (6) the field-bolted frame connections do not require special training or tools, hence, reducing the time and cost of the retrofit. Figure 6-8 presents the steel SMF installed at the first story (ground level). It can be seen that the parking space is still usable, which is one of the advantages of a moment frame versus adding shear walls.

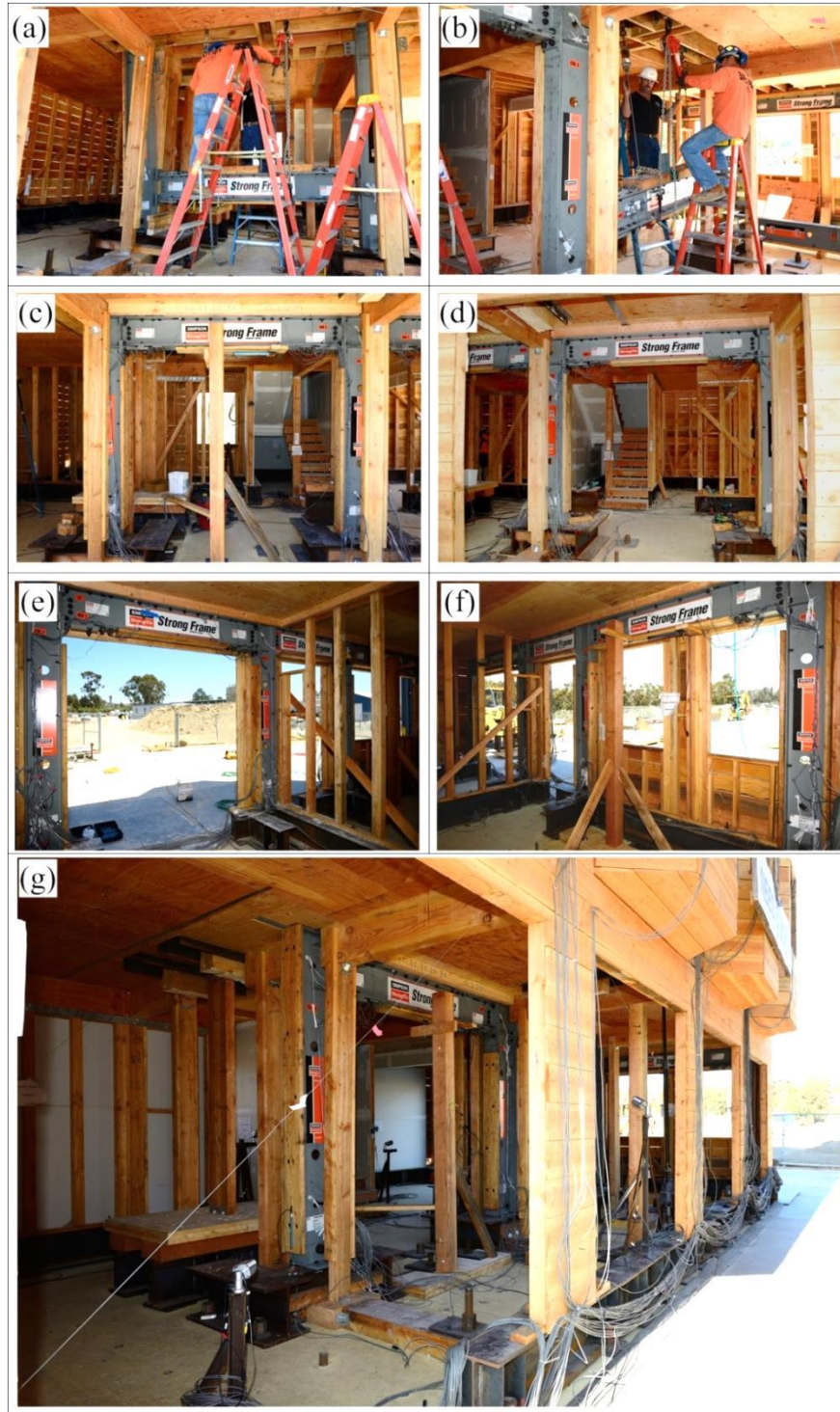


Figure 6-8: SMF retrofits at the first floor: (a) installation of west span of SMF in Line D, (b) installation of east span of SMF in Line D, (c) West span of SMF in Line D, (d) East span of SMF in Line D, (e) North span of SMF in Line 5; (f) South span of SMF in Line 5; (g) view of SMF installed in Line D from outside of the building.

Figure 6-9 presents the details of the steel SMF installed in Line D along the longitudinal direction of the building. Figure 6-9a shows the pinned-base connection of the steel frame to the base steel (i.e., foundation). As can be (partially) seen from this photo, one central pin through the column connects to back-to-back angles on either side of the column web, secured to the foundation by four bolts. Figure 6-9b shows the weldable cage connected to the top of the steel beam to support the ATS rod from the wood shear walls above (Line D in Figure 6-7). Figure 6-9c shows the connection between the SMF beam to the floor diaphragm by means of self-tapping screws that connect the 4×4 to 4×10 nailer plate and the beam in the floor diaphragm. Figure 6-9d presents the beam-to-column connection using the steel yield links installed at the top and bottom flanges of the beam.

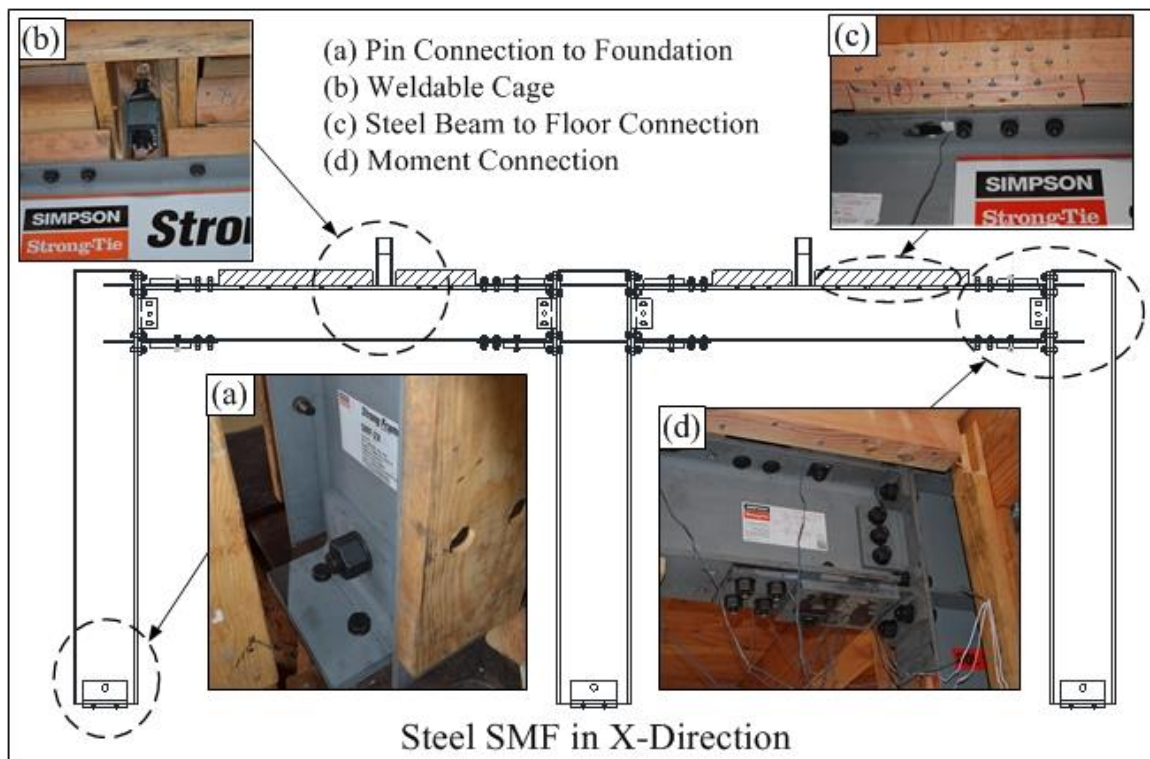


Figure 6-9: Details of steel SMF in Line D along the X-direction

Figure 6-10 shows wood structural panels (WSP's) installed on the two perpendicular walls in Line D and Line 3 at the 2nd story and Figure 6-11 presents ATS rods and stud packs installed near the end posts of the designated shear walls to transfer the uplift and downforce to the foundation.



Figure 6-10: WSP's at the 2nd story: (a) Line D, (b) Line 3, (c) intersection of Lines D and 3.

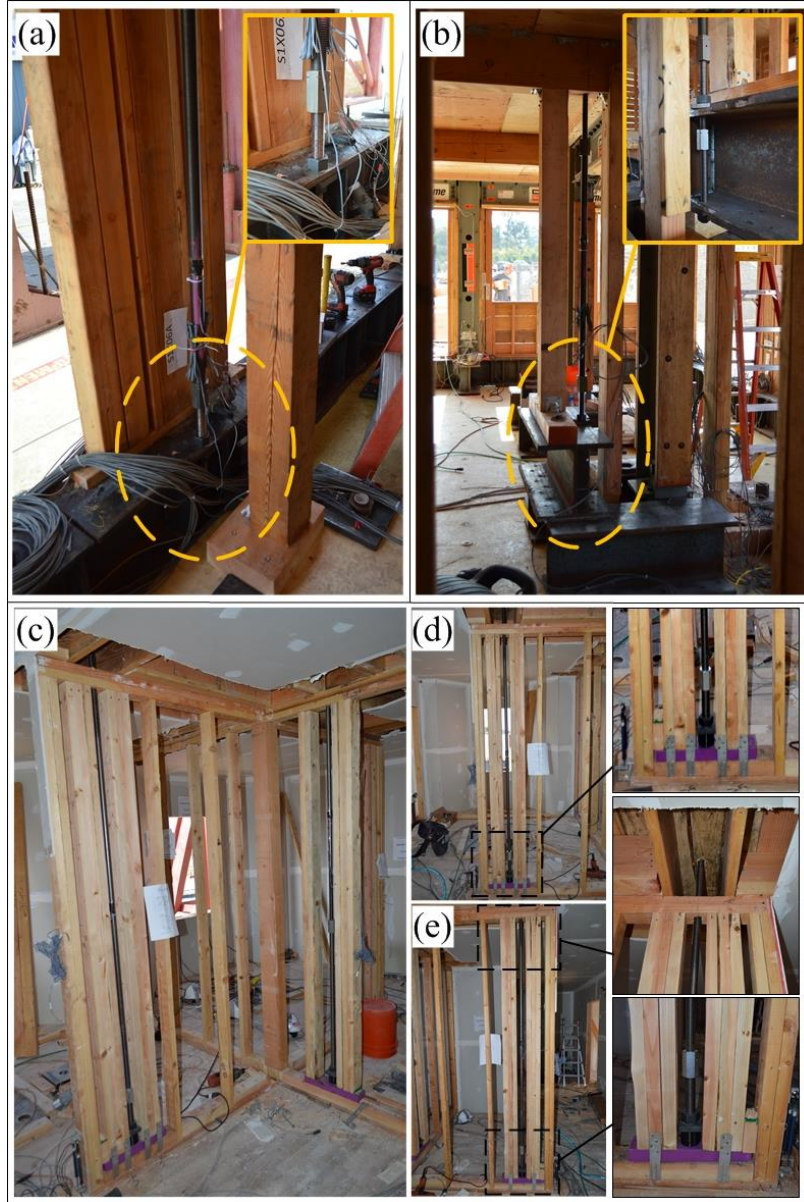


Figure 6-11: Installation of ATS rods: (a) first story A-8, (b) first story A-7, (c) third story A-6 and A-7, (d) close up view of A-6 at 3rd story, (e) close up view of A-7 at 3rd story

It should be noted that the diaphragm of the first floor was retrofitted with plywood to assure transferring the shear forces induced in the shear walls above to the resisting lines at the first story. Figure 6-12 shows the WSP (i.e., plywood) , steel connectors, and metal straps attached to the 1st floor diaphragm.

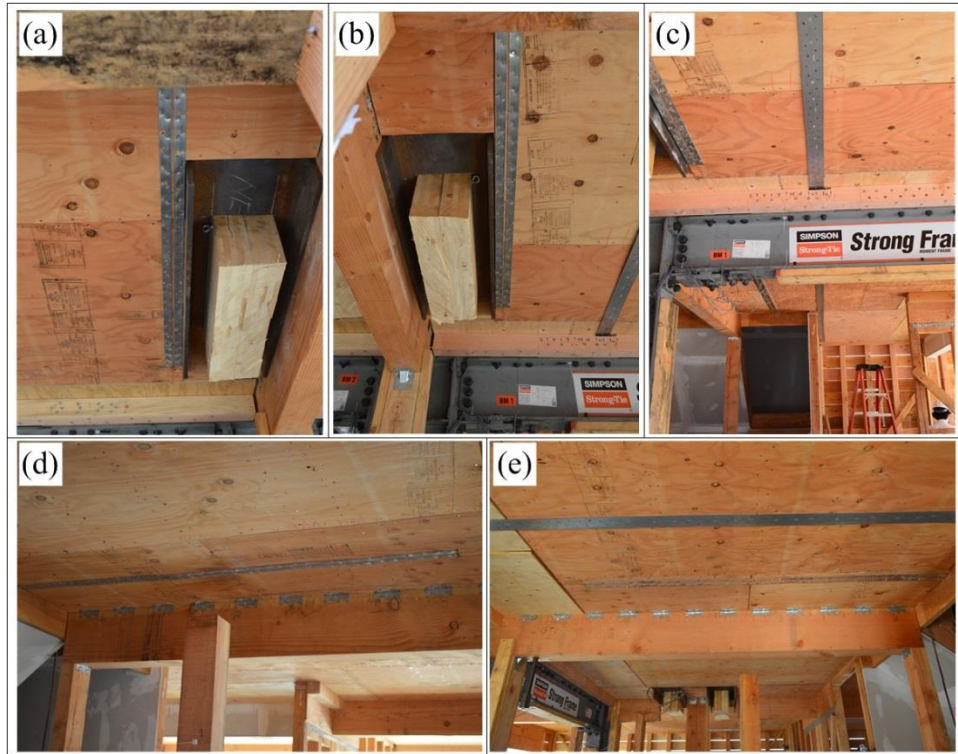


Figure 6-12: First story diaphragm retrofitted with WSP, steel connectors, and metal straps: (a) left side of Line 3, (b) right side of Line 3, (c) Line 3R, (d) steel connectors at left side of Line 3, (e) steel connectors and metal straps at Line 3R

6.4 Shake Table Test Planning and Preparation

6.4.1 Instrumentation

The responses of the building to seismic excitation were recorded by 396 sensors that were installed in different locations throughout the building. Two accelerometers were installed at every corner of each story and at the center of mass (CM) of each floor diaphragm to record the acceleration in both the X- and Y-directions. Two arrays of five accelerometers were installed at each of the two-bedroom units to record the accelerations and eventually to compute displacement (via numerical integration over time) of the diaphragm during each seismic test.

String potentiometers and linear potentiometers were installed in different locations to record the displacement of shear walls due to shear and uplift forces. Strain gauges were installed on the steel special moment frame and ATS rods to record the strains at different locations of the frames and elongation on the ATS rods. Twenty-two load cells were installed underneath the anchor bolts of the exterior and interior walls of the first story to record the uplift forces at each anchor bolt. Table 6-3 presents the type, location and quantity of each sensor used in the experimental tests. Figure 6-13 presents typical locations of accelerometers and string potentiometers within the first story and Figure 6-14 shows a figure of each of the instrument used in the test building. The instrumentation plan for the entire building is presented in Appendix B of this dissertation.

Table 6-3: Summary of instrumentation of the four-story wood-frame building

Measurement	Location	Sensor Type	Quantity
Absolute Acceleration ^(a)	Each floor	Accelerometer	91
Anchor bolt force	First floor	Load cell	22
Floor displacement ^(b)	Building exterior	String potentiometer	8
In-plane diaphragm deformation	Bedrooms	String potentiometer	12
Shear wall diagonal deformation	Selected shear wall	String potentiometer	51
Shear wall slippage/uplift	Selected shear wall	Linear potentiometer	50
SMF lateral deformation	SMF frames	Linear potentiometer	2
SMF base rotation/uplift	SMF base connection	Linear potentiometer	5
Strain on SMF	SMF column, beam, link	Strain gauge	95
ATS hold-down strain	ATS rods	Strain gauge	60
Total			396

^(a) 2D accelerometers were installed at the corners and center of mass of each floor.

^(b) Diagonal string potentiometers installed at west and north side of the building from base steel to each floor.

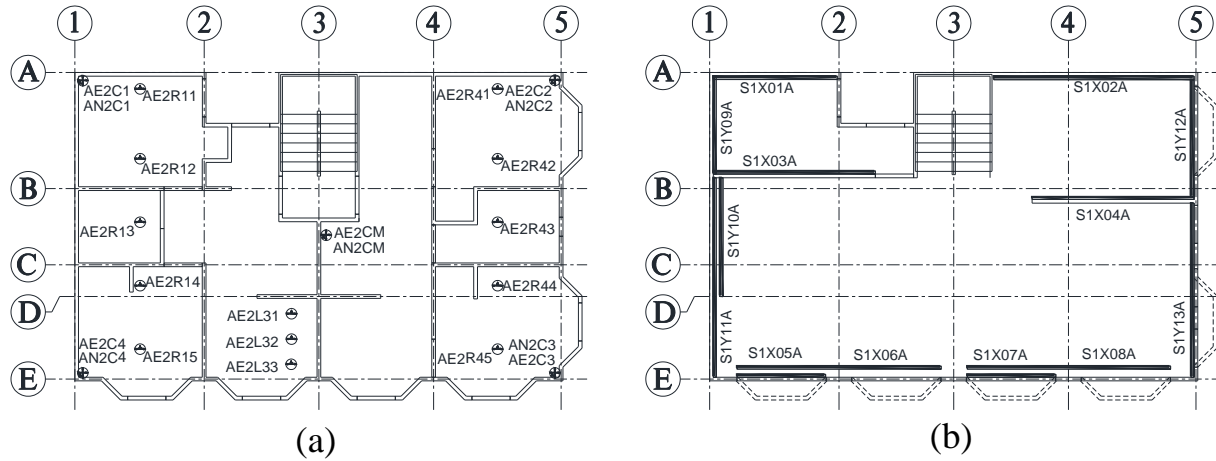


Figure 6-13: Location of sensors installed in the first story: (a) accelerometers, (b) string potentiometers.

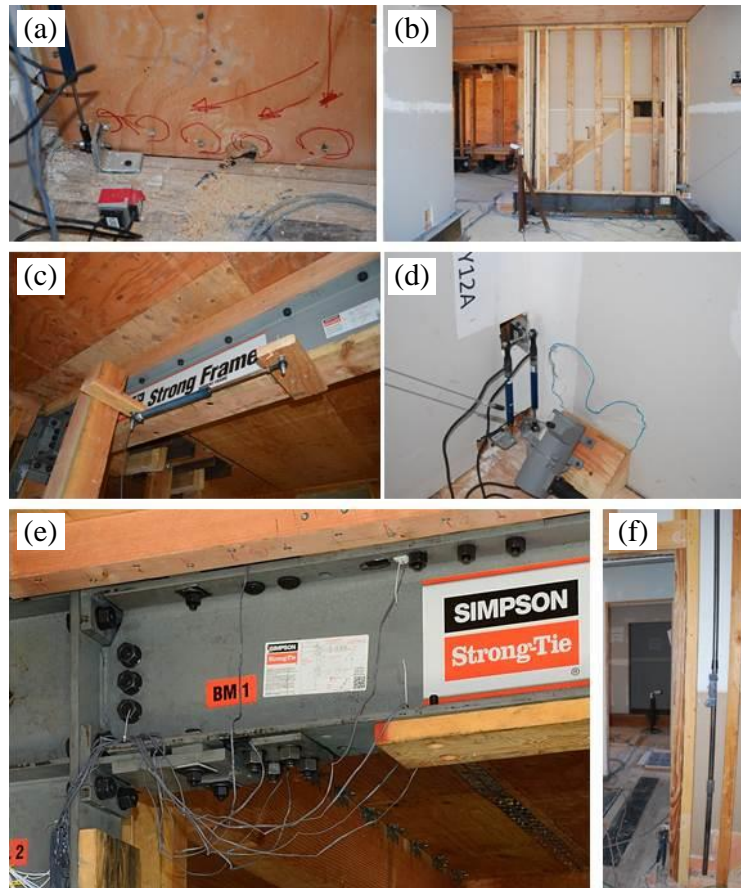


Figure 6-14: Instrumentations: (a) accelerometers in X- and Y-directions, (b) cameras, (c) linear potentiometer mounted on SMF in Line D, (d) string potentiometer and linear potentiometers at a wall corner; (e) strain gauges mounted on SMF, (f) strain gauges mounted on ATS rod.

6.4.2 Testing Plan and Ground Motion Records

In order to verify the effectiveness of the proposed retrofit method under seismic loading, the building was subjected to two different ground motions, both originally recorded in California. The 1989 Loma Prieta-Gilroy (component G03000) earthquake record and the 1992 Cape Mendocino-Rio (component RIO360) earthquake record were selected and scaled using ASCE 7-10 scaling (2010). For scaling the ground motions, 22 bi-axial far-field earthquake ground motion records of the FEMA P-695 (2009) were used. Each ground motion consisted of a pair of horizontal ground motions in X- and Y-directions. A SRSS (square root of the sum of the squares) spectrum was constructed by taking the SRSS of the 5 percent-damped response spectra of two components of each pair of the horizontal ground motion components. Each pair of ground motions was scaled such that in the period range from 0.08 sec. to 1.5 sec., the average of the SRSS spectra of all pairs of components did not fall below the site design spectrum. This period range represented 0.2 times the period of the stiffest retrofitted building to 1.5 times the period of the un-retrofitted building based on the numerically predicted periods. For generation of the design spectrum in the San Francisco Bay Area, the spectral response acceleration at short periods (S_s) and at a period of 1.0 sec. (S_1) were 1.8g and 1.2g, respectively. Recall from Chapter 5 that the building was retrofitted in both X- and Y-direction to withstand bi-axial ground motions and satisfy the performance criteria (i.e., translational and torsional responses); therefore, the bi-axial ground motion scaling procedure consistent with ASCE 7-10 (2010) was used even though the shake table was able to produce excitation in the X-direction only. Figure 6-15a and Figure 6-15b present the spectral acceleration for the two ground motions scaled to $S_a = 1.2g$ and $S_a = 1.8g$, respectively, and the acceleration time histories of the ground motions scaled to MCE level (i.e., $S_a = 1.8g$) are presented in Figure 6-15c and Figure 6-15d.

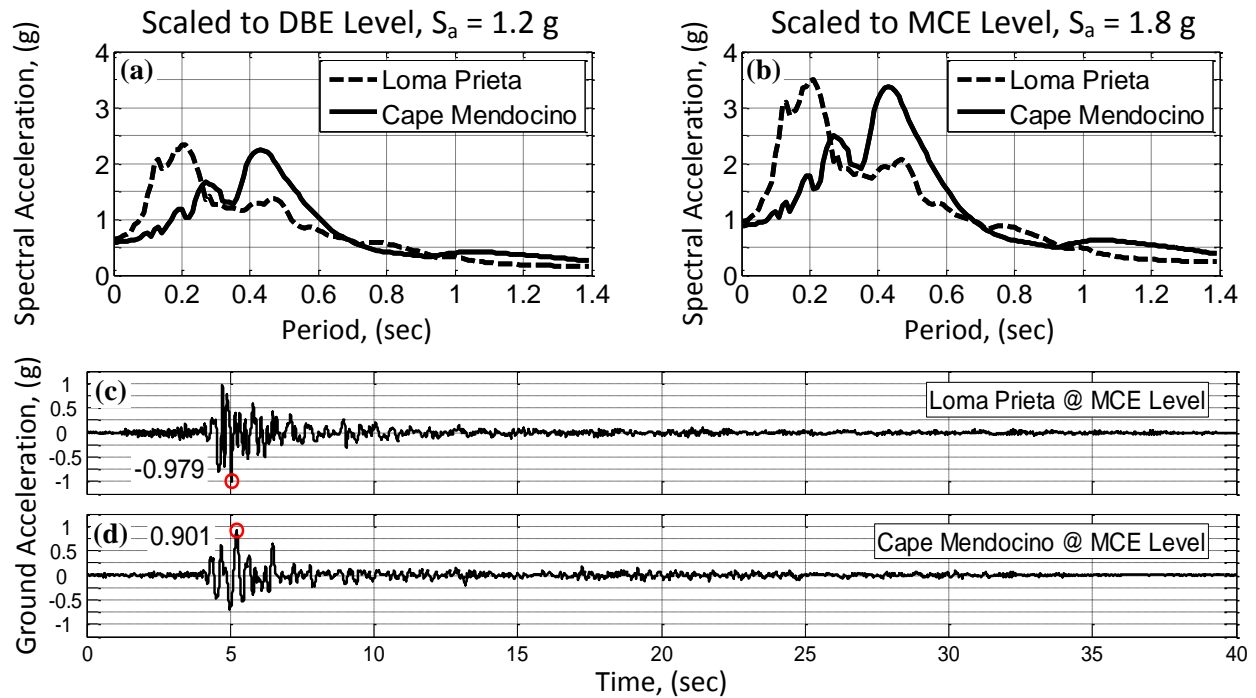


Figure 6-15: Ground motions and spectral accelerations: (a) spectral acceleration scaled to 1.2g, (b) spectral acceleration scaled to 1.8g, (c) Loma Prieta record scaled to $S_a = 1.8$ g, (d) Cape Mendocino record scaled to $S_a = 1.8$ g.

Table 6-4 presents the sequence of white noise and seismic tests with their corresponding intensity levels and peak ground accelerations (PGA). It should be noted that a small shake with spectral acceleration of 0.20g and PGA of 0.11g was conducted before the first seismic test in order to check the instrument readings. In order to obtain the natural frequencies of the test building at each stage of the test a white noise test with a root-mean-square (RMS) acceleration amplitude of 0.05g was conducted before and after each seismic test and repair. It should be noted that the building was retrofitted using the FEMA P-807 retrofit methodology by means of cross laminated timber (CLT) and steel SMF (i.e., Phase 1 and 2 in Table 6-1) prior to being retrofitted in accordance with PBSR methodology. However, in order to bring the building to its (new) original condition, a major repair was conducted before the building was retrofitted using

the PBSR method. The full testing plan of the four-story wood-frame building can be found in van de Lindt et al. (2014).

Table 6-4: Test sequences and ground motions used in shake table tests

White noise Test ^(a)	Seismic Test No.	Shake table excitation	Intensity level	S _a (g)	PGA (g)
1	-	0.05g RMS	-	-	-
-	1	Loma Prieta, 1989 - Gilroy	DBE	1.20	0.65
2	-	0.05g RMS	-	-	-
-	2	Cape Mendocino, 1992 - Rio	DBE	1.20	0.60
3	-	0.05g RMS	-	-	-
-	3	Cape Mendocino, 1992 - Rio	MCE	1.80	0.90
4	-	0.05g RMS	-	-	-
5 ^(b)	-	0.05g RMS	-	-	-
-	4	Loma Prieta, 1989 - Gilroy	MCE	1.80	0.98
6	-	0.05g RMS	-	-	-

^(a) White noise tests of 0.05g RMS were conducted between all tests and/or repairs. Also see Figure 6-17.

^(b) Repair and white noise test were performed before seismic Test No. 4.

6.5 Shake Table Test Results

6.5.1 Data Sampling and Analysis

The behavior of the building subjected to each ground excitation was recorded by means of the sensors and instruments installed inside and outside of the building. Two data acquisition systems were used in order to record the data from instruments as well as the shake table equipment. The sampling rate of the data acquisition system that collected the instruments reading was 240 samples per second and the sampling rate of the data acquisition system that recorded the shake table data was 256 samples per second. It should be noted that both data acquisition systems were synchronized. Linear interpolation between the data points of the instruments readings was used in order to increase the sampling rate to 256 samples per second.

Because of random noise in the data acquisition system, the data recorded by accelerometers was filtered using cut off frequencies of 0.30 Hz to 25 Hz and then integrated once and twice with respect to time in order to obtain velocity and displacement, respectively. A baseline correction function was applied to the processed data after obtaining the velocity in order to set the baseline to zero at the end of each seismic test (i.e. forcing zero velocity at the end of each test).

6.5.2 White Noise Analysis: Fundamental Period and Intrinsic Damping

6.5.2.1 Fundamental Period

As mentioned earlier, to obtain the natural frequencies of the test building a series of white noise tests conducted before each seismic test or major repair. Generally, after each seismic test and repair, the fundamental period of the building increased due to structural and non-structural damage. Figure 6-16 presents the responses of the building versus the input excitation frequencies that were obtained by analyzing the white noise tests using a Fast Fourier Transform (FFT). The data was filtered in order to achieve smoother plots with more defined peaks. Figure 6-17 presents the fundamental period of the building before and after each seismic test. It can be seen that the fundamental period of the building had an increasing trend except after the repair. It should be noted that damage inspection of the building was conducted between tests. During the repair, additional drywall screws were added to the drywall with loose connectors and withdrawn nails in the HWS and WSP were replaced, to the extent possible. Some drywall was also replaced when large shear cracks were present. This decreased the fundamental period of the building to approach its fundamental period after the first DBE test.

The fundamental period of the building without retrofit (i.e., the original condition) was 0.99 sec. The initial fundamental period of the building after it was retrofitted in accordance with PBSR

method was 0.37 s (i.e. close to the fundamental period of 0.43 s obtained from the numerical analysis in Chapter 5). The building was subjected to MCE level with spectral acceleration of 1.8g in the third seismic test that ultimately increased the overall fundamental period of the building even after repairing the building.

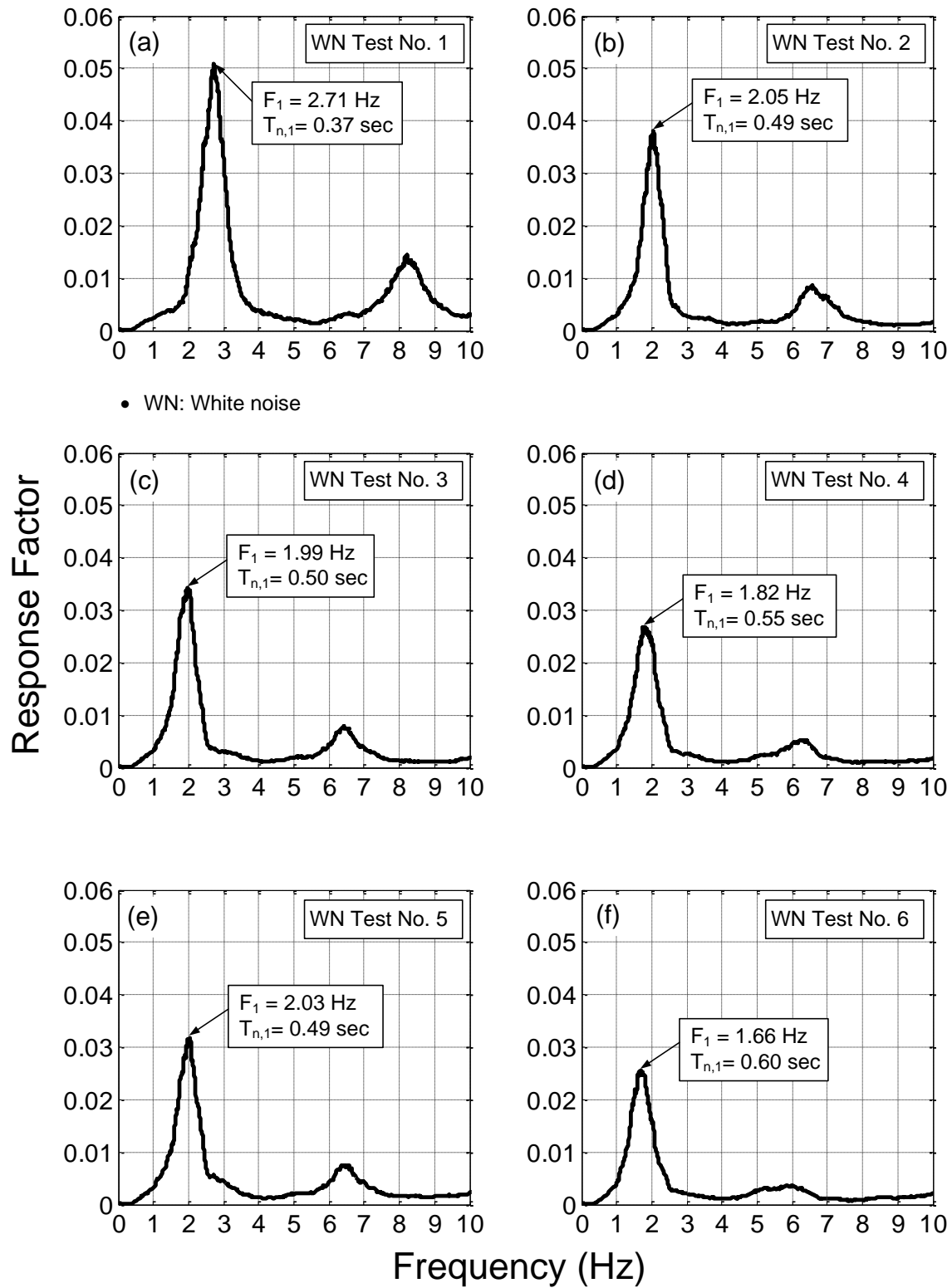


Figure 6-16: Fundamental period of the building and effect of repair

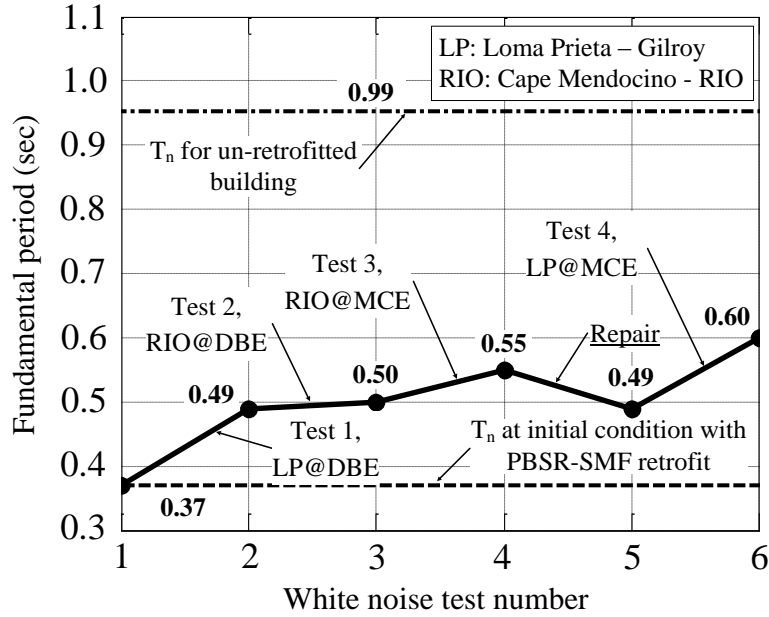


Figure 6-17: Fundamental period of the building and effect of repair

6.5.2.2 Intrinsic Damping

The intrinsic damping of the building right before the first test was evaluated using the half-power bandwidth method (Chopra, 2005). In order to obtain the intrinsic damping of the system the frequencies (periods) corresponding to the peak (i.e., h in Figure 6-18) and $1/\sqrt{2}$ of the peak value should be measured accurately. The intrinsic damping then can be calculated using the following equation:

$$\xi = \frac{F_b - F_a}{2F_n} \quad (6-1)$$

where, F_n is the fundamental frequency and F_a and F_b are the frequencies corresponding to the $1/\sqrt{2}$ of the peak point. Figure 6-18 presents the FFT of the first white noise test. The intrinsic damping of the building retrofitted in accordance with PBSR method can be calculated using Equation 6-1 and Figure 6-18:

$$\xi = \frac{F_b - F_a}{2F_n} = \frac{2.47 - 2.41}{2 \times 2.44} = 1.2\% \quad (6-2)$$

It can be seen that the 1.2% intrinsic damping obtained from the experimental test is very close to the assumed value of 1% during the design of the building (Chapter 5).

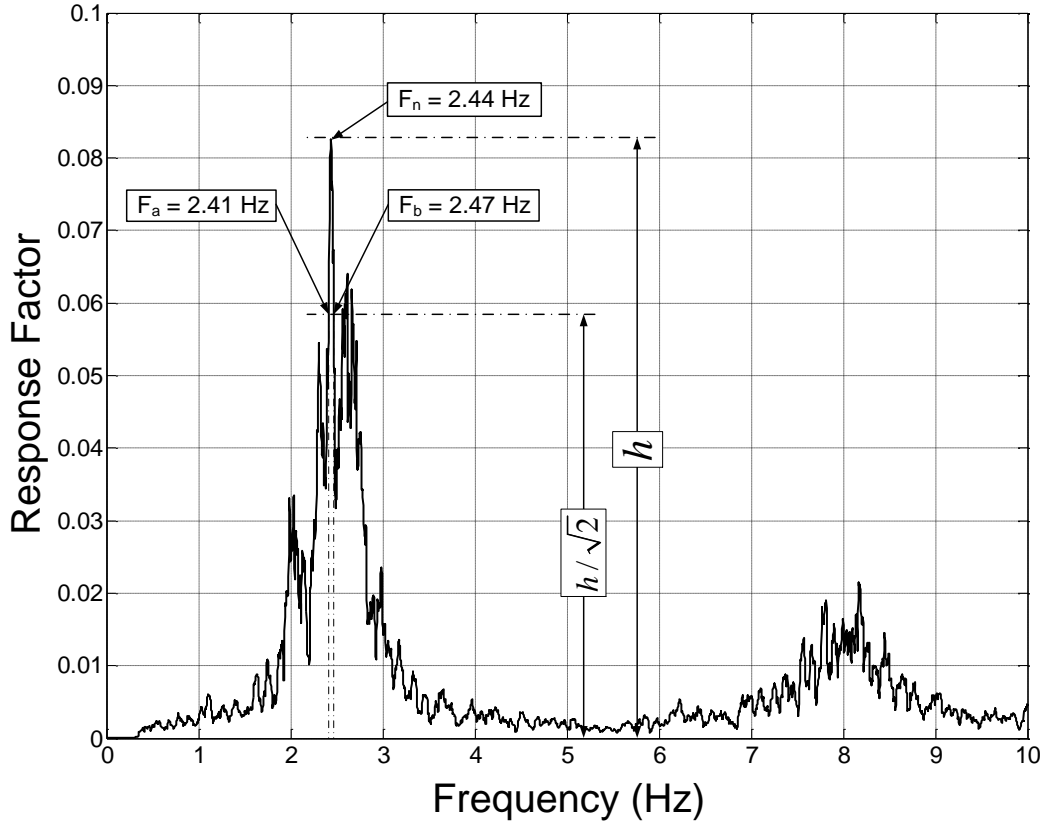


Figure 6-18: Intrinsic Damping – White noise test No. 1

It should be noted that according to Equation 6-1, the intrinsic damping is very sensitive to the values of the response factors (i.e., y-axis in Figure 6-18) the data should be filtered in a smaller window (i.e., higher bandwidth) in order to capture the response factors corresponding to $1/\sqrt{2}$ of the peak value. However, this has a very small effect on the fundamental frequency (or period) of the building since filtering has very small effect on the frequencies corresponding to the

peaks. This can be seen from the small difference between the fundamental period of the building obtained from the FFT of the first white noise filtered with smaller bandwidth (Figure 6-16a) and the fundamental period of the building obtained from FFT of the same white noise with higher bandwidth (Figure 6-18). The difference in fundamental periods is about 0.04s.

6.5.3 Global Responses

6.5.3.1 Peak Inter-story Drifts

In order to investigate the global behavior of the building, the accelerations of the corners of each story were recorded and then integrated twice with respect to time to obtain the absolute displacements with a stationary reference point. The maximum absolute displacement of each story was obtained by taking the average of the displacements at the four corners of each story. The inter-story drifts parallel and perpendicular to the direction of shake table motion (i.e., X- and Y-directions) were obtained by calculating the difference between the average absolute displacements of successive stories. The average peak inter-story drift ratios along the X-direction for each of the four seismic tests are presented in Table 6-5. It can be seen from Table 6-5 that the peak inter-story drift ratios for all stories was less than the 2% target ISD ratio when the building was subjected to ground motions with MCE intensity (i.e., Seismic Test 3 and 4), with the exception of the third story; approximately validating the retrofit design procedure in a global sense. The ISD ratio at the third story which exceeded the target performance criteria (i.e., 2.26% instead of 2%), was approximately 13 percent high. However, this error is in the acceptable range of error from the structural engineering design standpoint.

Table 6-5: Global response of retrofitted four-story building subjected to ground motion excitations

Seismic Test	Normalized dissipated energy (E_i / E_{Total}) ^(a) (%)				Average peak inter-story drift ratio ^{(b), (c)} (%)				Normalized maximum story shear (V_i / W) ^(d) (%)			
	Sty 1	Sty 2	Sty 3	Sty 4	Sty 1	Sty 2	Sty 3	Sty 4	Sty 1	Sty 2	Sty 3	Sty 4
1	26	43	27	3	1.05	0.99	1.07	0.25	54	52	44	22
2	19	45	32	3	0.97	1.38	1.48	0.25	54	56	47	24
3	12	45	39	3	1.05	1.83	2.26	0.43	54	63	54	29
4	13	39	42	5	1.35	1.55	1.94	0.40	60	54	48	27

^(a) Less than 1% of the total input energy (E_{Total}) dissipated due to intrinsic damping.

^(b) Average of drifts recorded at four corners of the building at each story.

^(c) Effective height of 2438 mm (96 in.) was used in calculating inter-story drift ratios.

^(d) Total weight of the building above the base steel, $W = 467$ kN (105 kips). V_i is the story shear force at i^{th} story.

6.5.3.2 Building Displacement Profile

Figure 6-19 presents the displacement profile of the test building when the maximum displacement relative to the ground occurs at the roof level (i.e., fourth story). It should be noted that peak inter-story drift of single stories do not necessarily occur when the roof is at its peak displacement, i.e this would only occur in a first mode response. This was particularly noticeable when higher mode response was observed during MCE shakes. It can be seen that all stories (except the fourth story) experienced inter-story drifts such that the profile of the building is closer to a straight line (i.e., one of the basic assumptions in the PBSR methodology is that the stories are designed to achieve approximately the same peak drifts. This will be validated later in Section 6.6.1 of this chapter). However, note that the fourth story experienced lower ISD's since the stiffness of the existing building at the fourth story was very close to the stiffness required per PBSR method. Namely the 4th story was strengthened with WSPs that were needed to reduce the eccentricity in this story and thus, were slightly overdesigned when practical considerations in applying retrofits were considered). The maximum displacement of the roof occurred during

Seismic Test 3 (i.e., when the building was subjected to the Cape Mendocino ground motion scaled to $S_a=1.8g$). The maximum roof displacement relative to the ground (i.e., shake table) was 129 mm (5.08 in.).

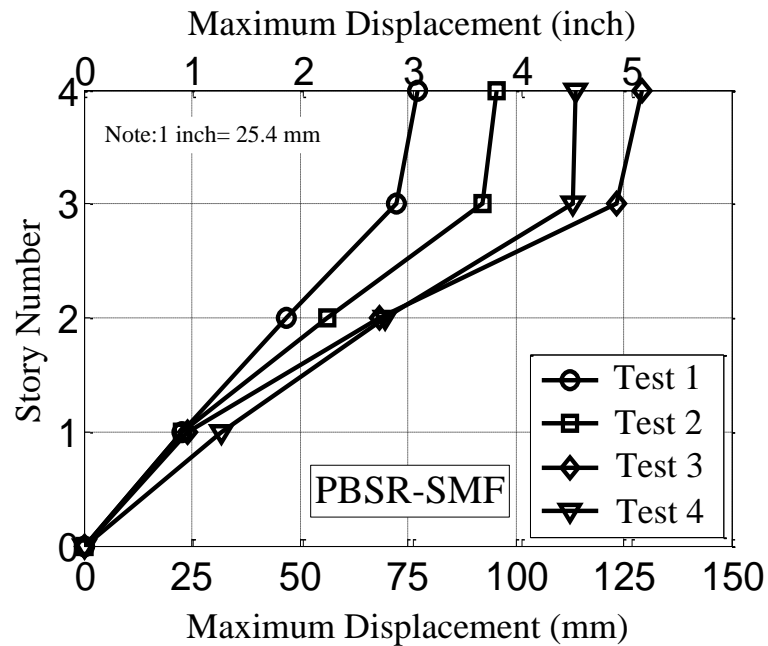


Figure 6-19: Maximum building displacement profile in X-direction.

6.5.3.3 Story Shear Force and Global Hysteresis

The performance of the retrofitted building was also investigated with regard to the distribution of story shear forces and global response of the building. To do this, the inertial force at each story was calculated by applying Newton's second law by multiplying the spatial average of the acceleration time histories recorded at each corner of each story and the mass associated with each story. The shear force at each story was then calculated for each of the seismic tests. Table 6-5 presents the maximum story shear force normalized by the weight of the building for all seismic tests and Figure 6-20 shows its variation along the height of the building. It should be

noted that the maximum story shear forces do not necessarily occur at the same time since higher modes occurred.

It can be seen that the maximum base shear coefficient, ($C_{\text{Story}} = V_{\text{Story}}/W_{\text{Total}}$), was 0.60 which occurred during the Loma Prieta ground motion at MCE (i.e., Seismic Test 4). By taking a closer look at the variation of the coefficient C along the height of the building it can be seen that its value decreases from the first story to the fourth story, when the building was subjected to Loma Prieta ground motion (i.e., seismic tests 1 and 4); whereas, its value increased from the first to the second story and then decreases to the fourth story when the building is subjected to the Cape Mendocino ground motion (i.e., seismic tests 2 and 3). This behavior is expected since the Cape Mendocino ground motion excites the higher mode shapes of the building which can result in a smaller displacement at the first story than the first mode shape. Therefore, the contribution of higher modes changes the distribution of story forces and consequently story shear forces, as is known from basic structural dynamics.

In order to obtain the global hysteresis curve of the building for each test, the roof displacement with respect to the shake table (i.e., ground) was plotted against the base shear (i.e., story shear at the 1st story). Figure 6-21 presents the global hysteresis curves for all four seismic tests. The maximum values of the roof displacements with their corresponding base shear are marked in the plots. It can be seen that the maximum roof displacement occurs in seismic Test 3 at 129 mm (5.08 in.) and the maximum base shear occurred in seismic Test 4 at 280 kN (62.9 kip corresponding to $C=0.6$ in Table 6-5 and Figure 6-20).

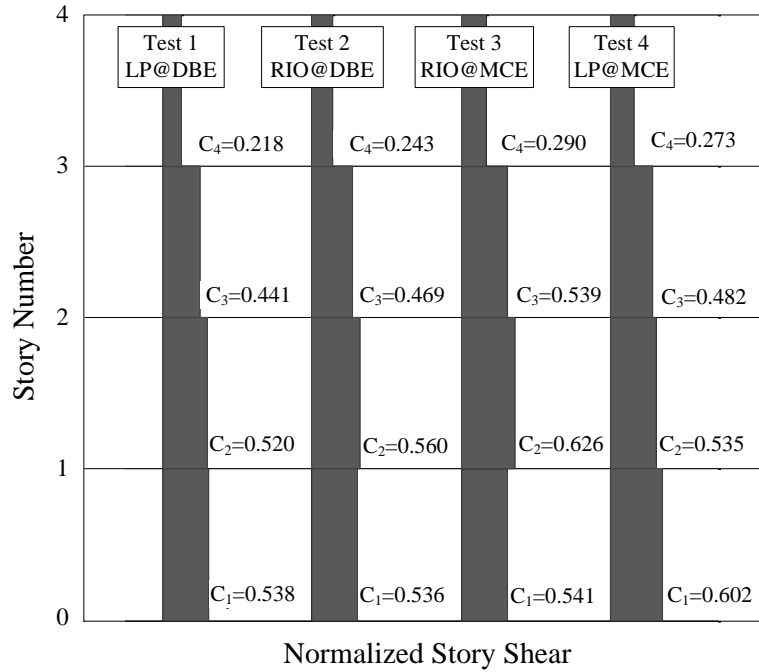


Figure 6-20: Normalized story shear ($V_{\text{story}}/W_{\text{Total}}$) for the building retrofitted in accordance with PBSR method ($C_{\text{Story}} = V_{\text{Story}}/W_{\text{Total}}$).

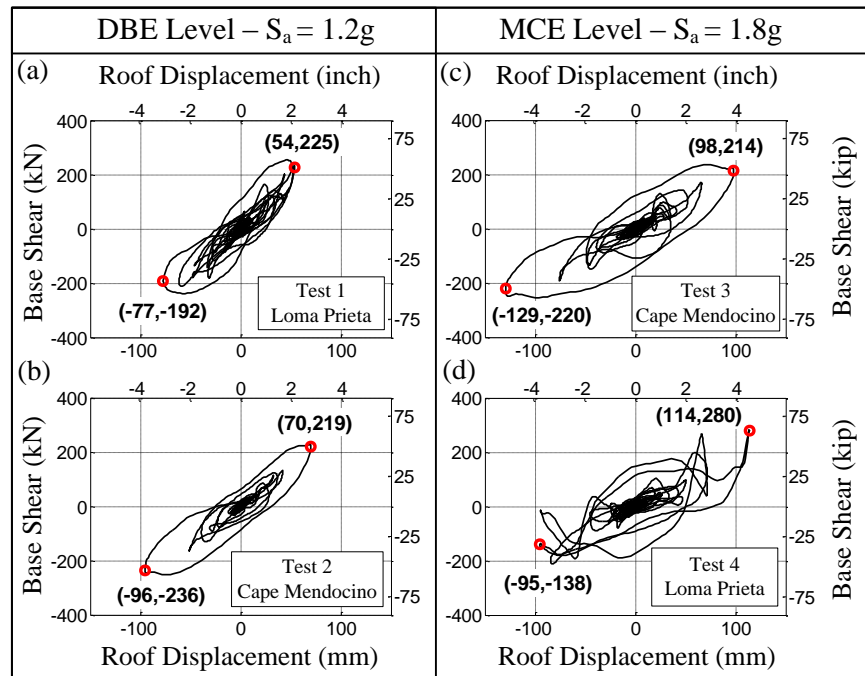


Figure 6-21: Base shear v.s. roof displacement subjected to: (a) Loma Prieta at DBE, (b) Cape Mendocino-Rio at DBE, (c) Cape Mendocino-Rio at MCE, (d) Loma Prieta at MCE.

6.5.3.4 Time-History Response

In order to take a closer look at the behavior of the building during ground motions at MCE intensity, translational and rotational time history responses of the building at each story were obtained by processing the accelerometers' readings at the four corners of each floor.

6.5.3.4.1 Translational Response

The time-history translational response of each story was calculated by averaging the displacements at the four corners of each story. This averaged story displacement was then plotted against time in order to produce the time history response of each story (Figure 6-22 and Figure 6-23). Figure 6-22a and Figure 6-23a present the average translational responses in the X-direction during the Cape Mendocino-Rio and Loma Prieta ground motions at MCE intensity, respectively. It can be seen that the inter-story drifts recorded at the first story (i.e., retrofitted soft-story) are approximately 26 mm (1 in.) and 33 mm (1.3 in.) for Cape Mendocino and Loma Prieta ground motions, respectively. The peak inter-story drifts of 55 mm (2.17 in.) and 47 mm (1.85 in.) occurred at the third story for Cape Mendocino and Loma Prieta ground motions, respectively.

Figure 6-22b and Figure 6-23b present the average translational responses the Y-direction during the Cape Mendocino-Rio and Loma Prieta ground motions, respectively. The peak responses of the building at the 4th story perpendicular to the motion of the shake table (i.e., Y-direction) were 3.7 mm and 4.5 mm, approximately 35% and 47% of the peak response in the X-direction, when the building was subjected to Cape Mendocino and Loma Prieta ground motions, respectively. These values seem a little bit high, however, this is due to the low ISD values in X-direction in the fourth story (i.e., small denominator). It should be noted that the maximum ratio of the ISD

in Y-direction to the ISD in X-direction for the other stories was 6.5%. Since no seismic force was applied in Y-direction (i.e., uni-axial motion), it can be concluded that any displacement in Y-direction is due to the effect of in-plane torsional moments which can be caused by in-plane eccentricities at the stories in Y-direction. Therefore, very small translational responses in Y-direction can prove that in-plane eccentricities and eventually in-plane torsional moments were successfully reduced to an acceptable range by the PBSR method.

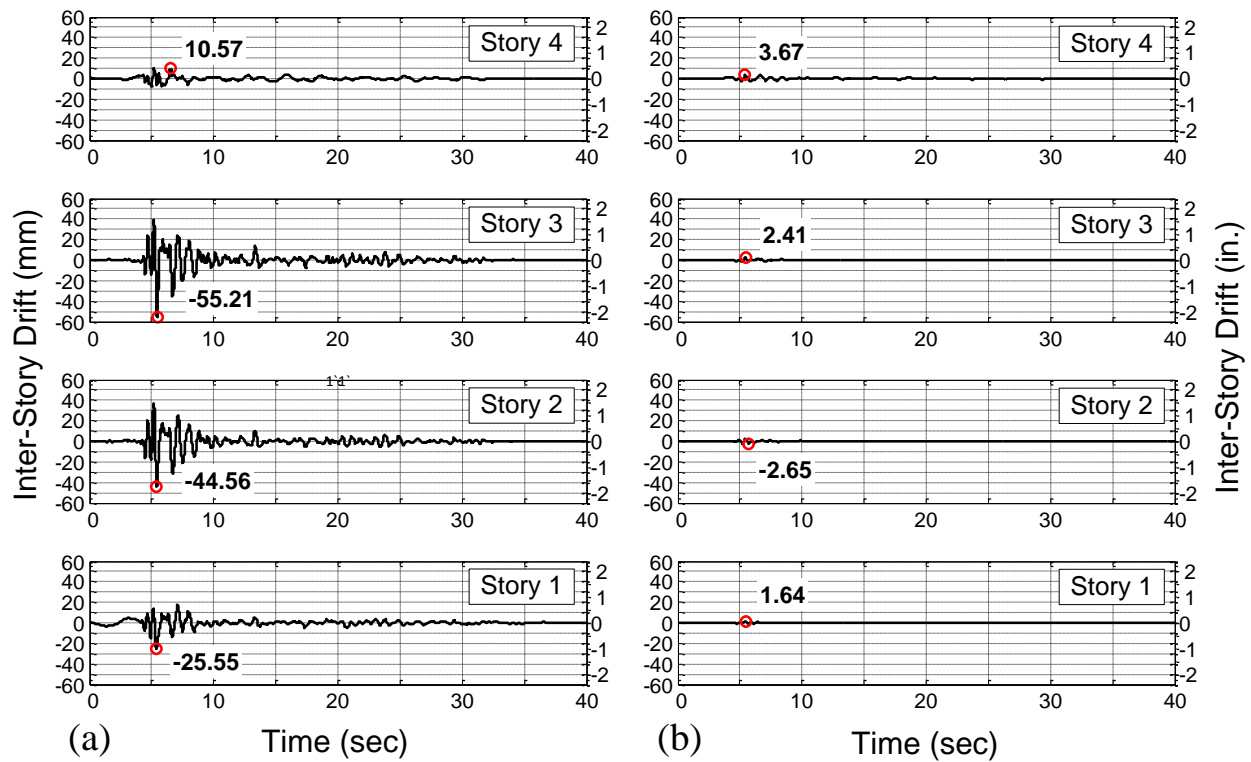


Figure 6-22: Translational response of the retrofitted building subjected to Cape Mendocino-Rio ground motion at MCE intensity (Seismic Test 3): (a) X-direction, (b) Y-Direction.

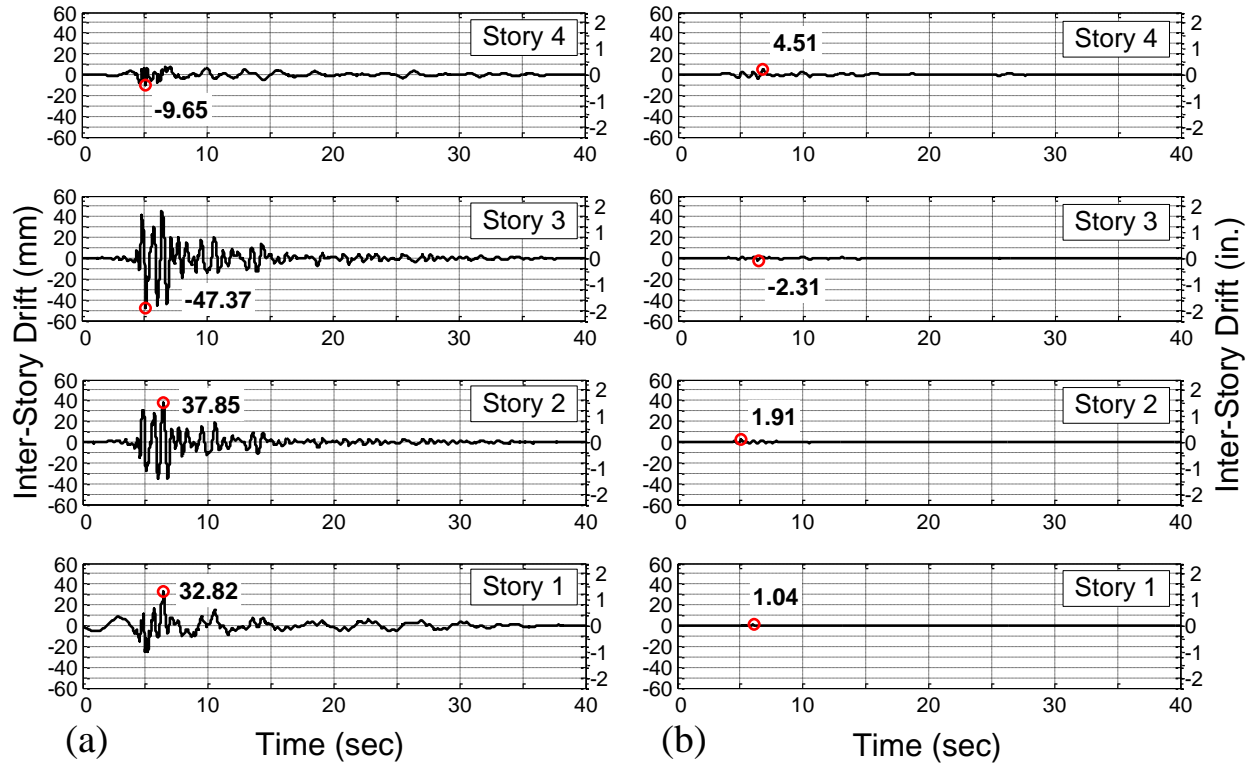


Figure 6-23: Translational response of the retrofitted building subjected to Loma Prieta-Gilroy ground motion at MCE intensity (Seismic Test 4): (a) X-direction, (b) Y-Direction.

6.5.3.5 Time-History Response: Torsional Response

As mentioned previously, soft-story buildings can be soft in both translation and torsion. The four-story test building was not only soft in both translational directions, but also had a very low torsional stiffness due to the stiffness irregularity in the first story (i.e., location of garage doors, window openings, etc.). The PBSR methodology, discussed in this dissertation is intended to eliminate torsional response of buildings by reducing, or ideally, eliminating in-plane eccentricity at all floors. In order to take a closer look at the torsional behavior of the building the time-history responses of each story was obtained and presented in this section.

Figure 6-24 presents a generic rectangular-shape floor plan that experiences both translational and rotational displacements. The rotational angles (i.e. θ_1 , θ_2 , θ_3 , and θ_4) can be obtained by dividing the difference between the displacements recorded at two adjacent corners and then dividing it by the distance between the two corners perpendicular to the direction of the displacement (Equation 6-1). The average rotational response of each story was then calculated by averaging the values of the four angles (Equation 6-2). It should be noted that in calculation of the rotational responses, the diaphragm of all stories were assumed to behave rigidly (the basic assumption in PBSR method). This assumption will be verified in Section 6.5.5 of this chapter.

$$\theta_1 = \frac{\Delta X_4 - \Delta X_1}{L_y} ; \theta_2 = \frac{\Delta Y_2 + \Delta Y_1}{L_x} ; \theta_3 = \frac{\Delta X_3 - \Delta X_2}{L_y} ; \theta_4 = \frac{\Delta Y_3 + \Delta Y_4}{L_x} \quad (6-3)$$

$$\theta_{\text{Avg}} = \frac{\theta_1 + \theta_2 + \theta_3 + \theta_4}{4} \quad (6-4)$$

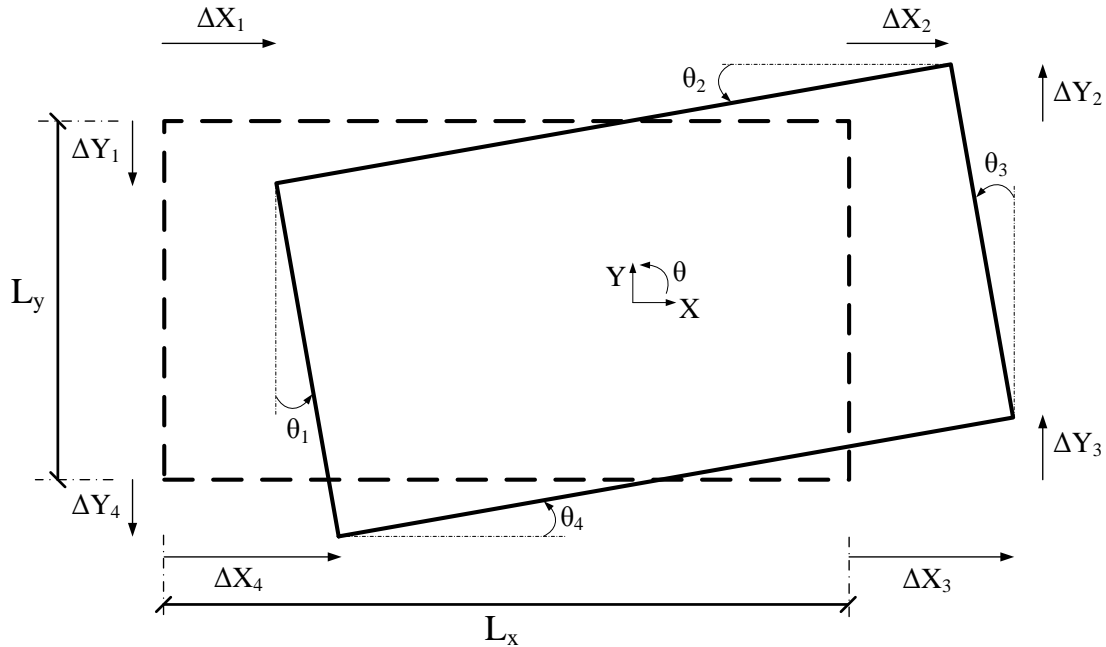


Figure 6-24: In-plane translational and torsional displacements of a rectangular-shape diaphragm

The inter-story torsional responses of the test building at all stories when subjected to the ground motions at MCE intensity are shown in Figure 6-25. It can be seen that the maximum absolute inter-story rotations were 0.0027 (0.155 degrees) and 0.0018 (0.103 degrees) for the Cape Mendocino and Loma Prieta ground motions, respectively, and occurred at the 2nd story for both ground motions. If it is assumed that the CR coincides with the CM at all floors (i.e., one of the PBSR assumptions), in the worst case scenario, the maximum displacements of the corners of the 2nd story due to torsion during the Cape Mendocino ground motion are 9.9 mm (0.39 in.) and 15.7 mm (0.62 in.) in the X- and Y-direction, respectively. These values will be very close to zero at the location of the CM of the floors due to very small distances between the CR and CM (i.e., in-plane eccentricity) at all the floors. Again, these small values of torsional response reinforce the assertion that the PBSR method was able to eliminate the torsion.

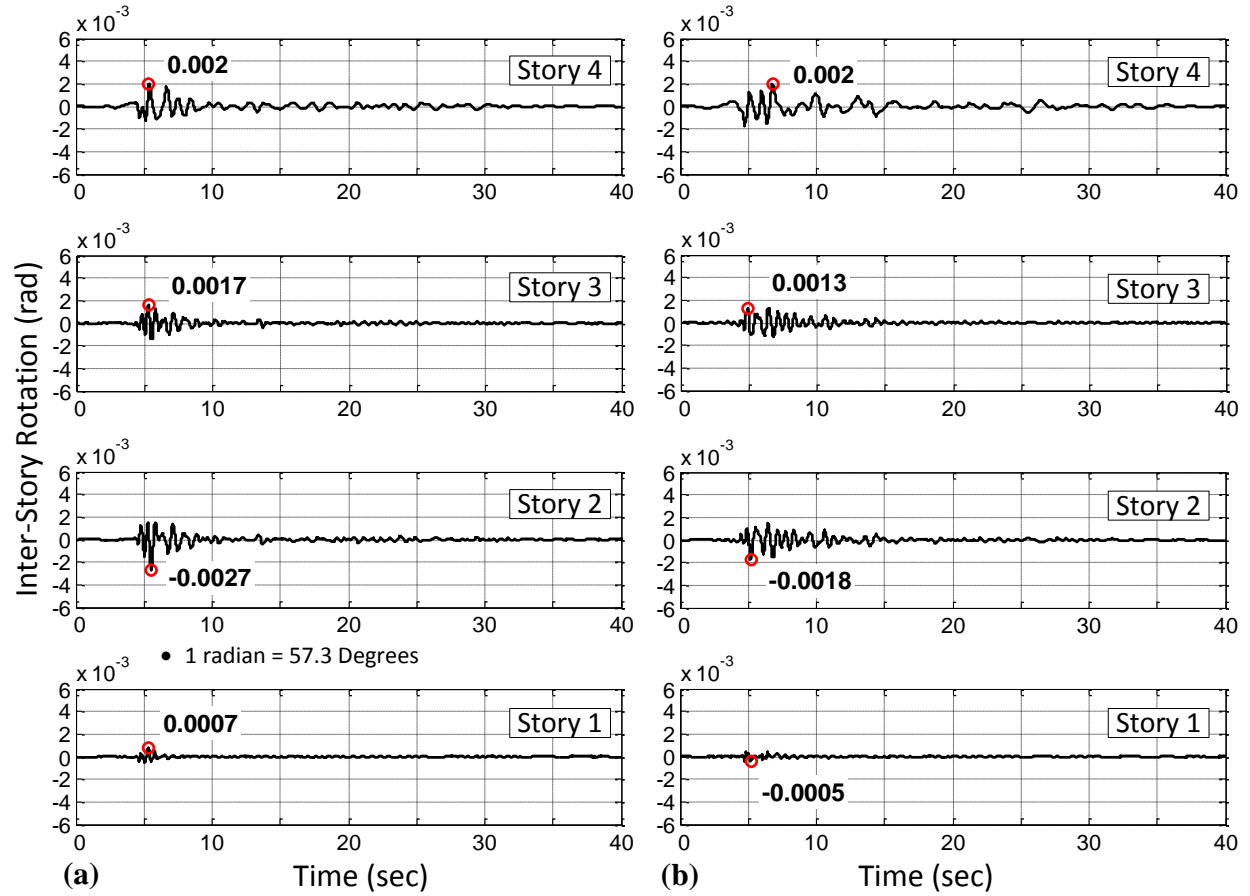


Figure 6-25: Inter-story rotational response of the building subjected to ground motions scaled to MCE intensity: (a) Cape Mendocino (Test 3), (b) Loma Prieta (Test 4).

6.5.4 Response of the Retrofit Components

Retrofit elements (e.g., SMF, WSP, and ATS rods) were instrumented during each seismic test to quantify their individual response for eventual calibration of numerical models. In this chapter, the response of the steel SMF frame installed parallel to the shake table motion (i.e., Line D in Figure 6-7) and the Anchor Tie-down System (ATS) rods located near the end posts of the WSP are presented.

6.5.4.1 *Lateral Forces in Steel SMF's*

To find the forces resisted by the steel SMF in Line D, the displacement time-history responses of the frame obtained using the accelerometers installed above the steel frame; then, the displacement was applied as input to the bi-linear spring model used in the design (Figure 5-6) to obtain the lateral resisting force developed in the frame. Figure 6-26a and Figure 6-26b present the hysteresis curve and lateral force time-history responses of the steel SMF, respectively, when the building was subjected to the Cape Mendocino ground motion at MCE intensity. The hysteresis curve and time history response of the frame during the Loma Prieta ground motion at MCE intensity are presented in Figure 6-26c and Figure 6-26d, respectively. By comparing the maximum values in Figure 6-20 and Table 6-5, it can be seen that the maximum force in the steel SMF in Line D in some cases is very close to the total base shear. For example, the maximum base shear of the building was 252.6 kN (from the data in Table 6-5) and the maximum lateral force in the steel SMF frame was determined as 252.2 kN (Figure 6-26a-b) when the building was subjected the Cape Mendocino-Rio ground motion. At first glance, one can conclude that the lateral forces were not calculated correctly since the steel SMF in Line D was not the only SFRS element at the first floor; however, this conclusion is true only if the building was symmetric (i.e., torsionally balanced). As mentioned earlier, the four-story building was highly asymmetric; therefore, torsional moments were resisted by individual retrofit elements (i.e., steel SMF and WSP) in addition to lateral forces. In order to resist torsion at the first story, a portion of the forces in WSP and steel SMF should make a couple which requires two equal and opposite forces. Therefore, the steel SMF at its maximum displacement has to resist both lateral force induced by pure seismic lateral force and additional torsional moment.

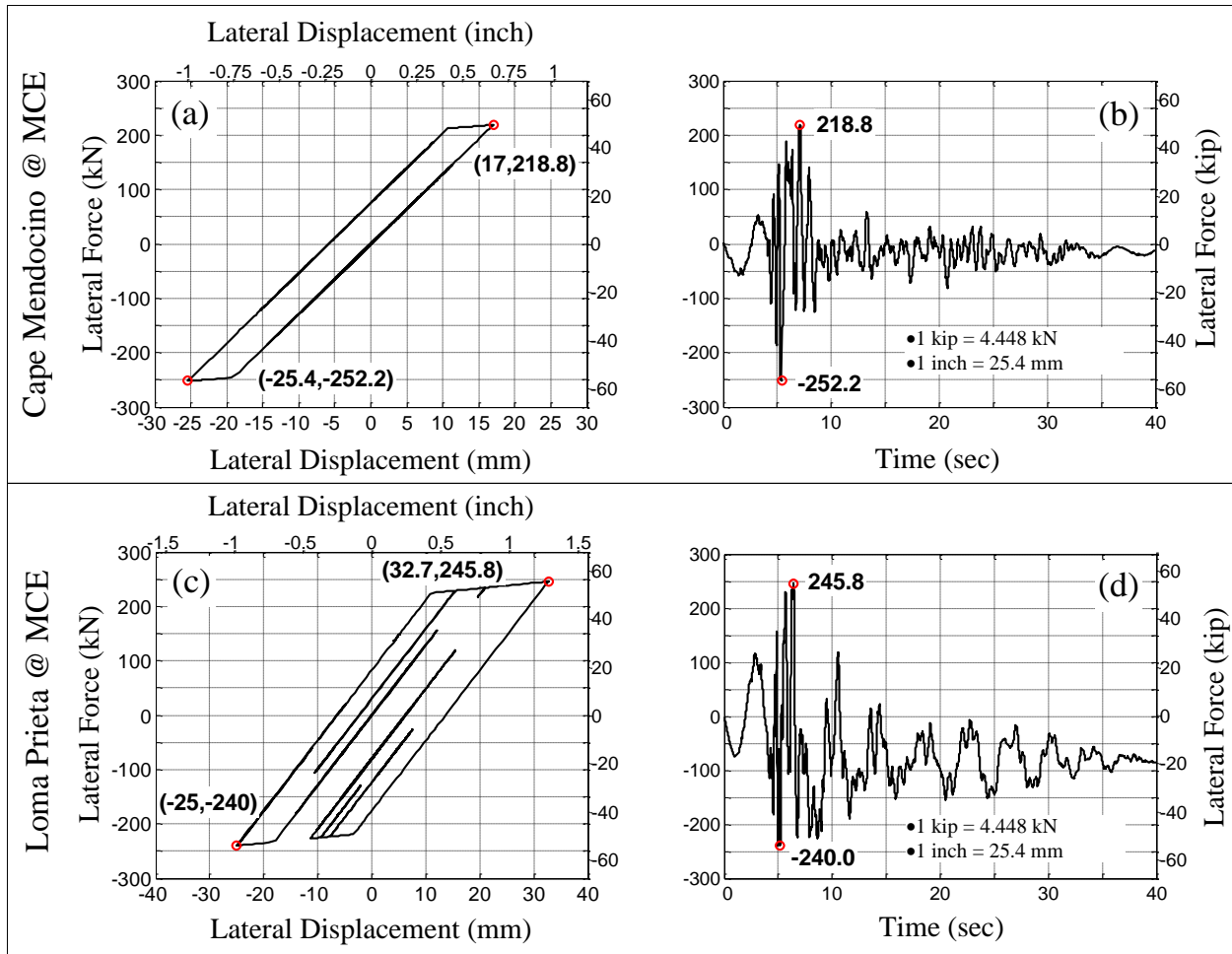


Figure 6-26: Hysteresis time-history response of the steel SMF along X-direction subjected to the ground motion records at MCE intensity: (a) Cape Mendocino, (b) Loma Prieta.

6.5.4.2 Uplift Force in Anchor Tie-down System (ATS) Rods

The distribution of uplift forces in the ATS rods was also investigated, since controlling overturning is critical for good shear performance for wood-frame buildings. Without these rods, full design shear forces cannot be developed in the shear walls. In retrofitting the four-story building, the ATS rods were installed adjacent to the end posts of each WSP panel (see Figure 6-11). A total of eight continuous ATS rods (vertical multi-story runs) were installed in the test building. Each shear wall had a stud pack for compression forces with the ATS rod located

appropriately between an equal numbers of studs. The required cross-sectional area of the rods was determined based on the maximum allowable uplift displacement in the rods and shear forces at each story. The design process and criteria were presented in detail in Chapter 5 of this dissertation.

Table 6-6 presents the maximum uplift forces in all the ATS rods when the building was subjected to the Cape Mendocino and Loma Prieta ground motions at MCE intensity. The maximum uplift force experienced by each ATS rod is also presented in Figure 6-27. It can be seen that ATS rods that were located at the north-west side of the building (i.e., A-1 and A-2 in Figure 6-7) experienced the highest uplift forces since these WSP's were parallel to the motion of the shake table and also had to resist additional lateral forces to help remove the torsional response of the building. The ATS rods installed at the end posts of WSP-D (i.e., A-5 and A-6) experienced the second largest uplift force since the WSP located at line D was also parallel to the motion of the shake table. It should be noted that the forces in ATS rods were measured by multiplying the strain by the cross section area and modulus of elasticity at each story and location.

Table 6-6: Maximum uplift forces in ATS rods during ground motions at MCE intensity

Seismic Test	Story No.	ATS ⁽¹⁾ uplift force, kN (kip)							
		WSP - A		WSP -3R		WSP - D		WSP - 3	
		A - 1	A - 2	A - 3	A - 4	A - 5	A - 6	A - 7	A - 8
Test 3 (Cape Mendocino-Rio)	4	16.1 (3.62)	14.7 (3.30)	2.4 (0.54)	4.3 (0.97)	11.5 (2.59)	9.4 (2.11)	1.8 (0.40)	1.1 (0.25)
	3	31.5 (7.08)	26.6 (5.98)	3.9 (0.88)	4.8 (1.08)	26.1 (5.87)	31.5 (7.08)	1.3 (0.29)	3.8 (0.85)
	2	52.8 (11.9)	62.6 (14.1)	7.9 (1.78)	12.1 (2.72)	53.8 (12.1)	38.1 (8.57)	7.3 (1.64)	7.8 (1.75)
	1	85.5 (19.2)	99.4 (22.4)	7.9 (1.78)	11.0 (2.47)	- ⁽²⁾	- ⁽²⁾	4.3 (0.97)	3.7 (0.83)
Test 4 (Loma Prieta-Gilroy)	4	14.2 (3.19)	25.2 (5.67)	2.5 (0.56)	2.7 (0.61)	12.6 (2.83)	12.9 (2.90)	0.7 (0.16)	0.8 (0.18)
	3	25.1 (5.64)	27.7 (6.23)	3.4 (0.76)	2.2 (0.49)	25.4 (5.71)	36.4 (8.18)	2.6 (0.58)	2.9 (0.65)
	2	37.9 (8.52)	48.9 (11.0)	5.5 (1.24)	7.0 (1.57)	35.0 (7.87)	28.1 (6.32)	10.5 (2.36)	13.9 (3.12)
	1	74.2 (16.7)	67.9 (15.3)	6.2 (1.39)	6.3 (1.42)	- ⁽²⁾	- ⁽²⁾	8.8 (1.98)	7.1 (1.60)

⁽¹⁾ ATS: Anchor Tie-down System.⁽²⁾ A-5 and A-6 were attached to the steel frame in the first story to avoid interference with the garage space.

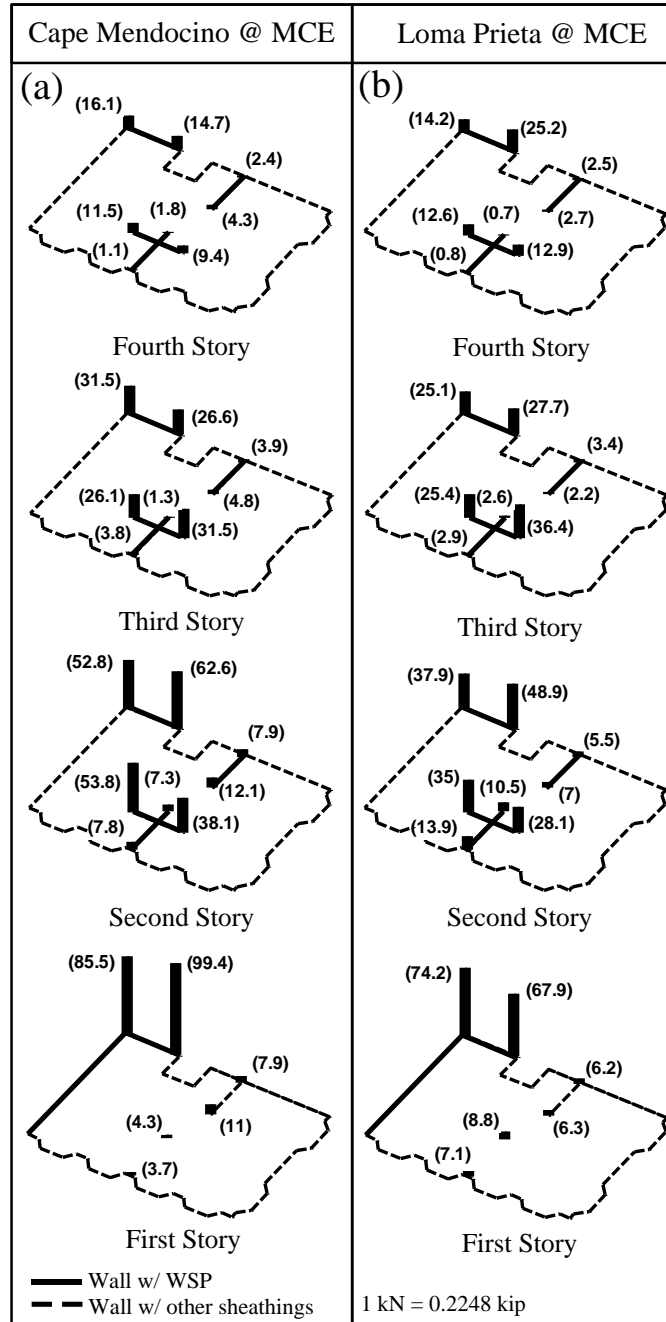


Figure 6-27: Maximum ATS tensile forces when the building is subjected to ground motions at MCE intensity: (a) Cape Mendocino, (b) Loma Prieta.

6.5.5 Rigidity Level of Diaphragm

One of the critical factors in many building design and retrofit procedures, including the PBSR method, is the level of rigidity of the diaphragms. The distribution of lateral forces in the plane of each story and eventually the design of the SFRS elements highly depends on the behavior of the diaphragm. For a rigid diaphragm, the lateral force at each story should be distributed based on the stiffness ratio of the SFRS elements; whereas, for a flexible diaphragm, the lateral force at each story should be distributed based on the tributary area (perpendicular to the lateral force) of each SFRS element. Furthermore, in the PBSR method, in order to calculate the center of rigidity (CR) and eventually eliminate torsion, it is assumed that the diaphragm behave rigidly during ground motions. In this section, the validity of this assumption is checked by using the displacement of the diaphragm at all stories during the Cape Mendocino and Loma Prieta ground motions at MCE intensity and then check it with the definition described in ASCE7-10 (2010).

Per ASCE7-10 (2010) Section 12.3 the diaphragm is flexible if the Maximum Diaphragm Deflection (MDD) is greater than twice the Average Drift of Vertical Element (ADVE) (Equation 6-3). The MDD and ADVE are shown in Figure 6-28.

$$(MDD) > 2 (ADVE) \quad (6-5)$$

In order to check this condition in the four-story building, the absolute displacement of each diaphragm was calculated by obtaining the displacements of two arrays of accelerometers mounted on the floor of each story along the lines at the right side of Line 1 and 4 in Figure 6-13. The black dashed lines in Figure 6-29 and Figure 6-30 show the footprint of the diaphragm at each story when the building is stationary. The blue solid bold lines in the figures present the absolute displacement of the two dashed lines shown inside of the building footprint. It should be

noted that the deflection of the diaphragm shown in these figures are multiplied by 50 in order to illustrate the deflections better. In order to evaluate the rigidity of the diaphragms based on Equation 6-3, the third story (i.e., the worst case scenario) was selected and evaluated for each seismic test. The values of MDD and ADVE are shown in Table 6-7. It can be seen that the ratios of MDD to ADVE for both lines at the third story are approximately 0.1 for both seismic tests at MCE intensity (recall that the ratio of MDD to ADVE should be greater than 2.0 for a flexible diaphragm). This confirms that the diaphragm was rigid and the assumption used in developing the PBSR method was valid; at least for the earthquakes used in this test program.

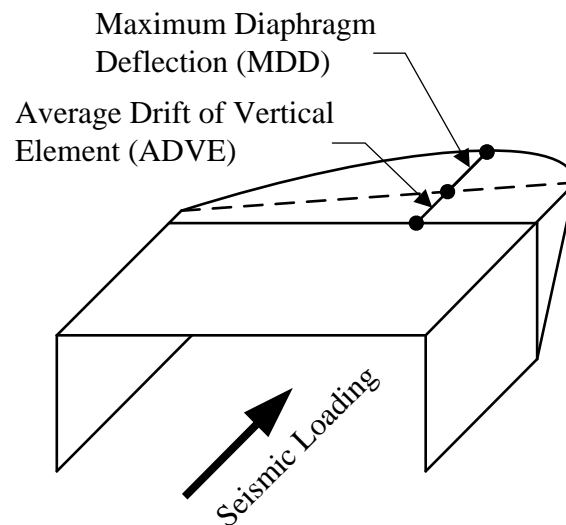


Figure 6-28: Illustration of flexible diaphragm (Figure from ASCE7-10, 2010 – Figure 12.3-1)

Table 6-7: Third story's diaphragm rigidity level for ground motions at MCE intensity

Seismic Test No.	Accel. No.	Right of Line 1				Right of Line 4			
		Deflection mm (in.)	ADVE mm (in.)	MDD mm (in.)	MDD/ADVE	Deflection mm (in.)	ADVE mm (in.)	MDD mm (in.)	MDD/ADVE
Test 3	1	44.0 (1.73)				46.1 (1.81)			
	2	41.9 (1.65)				46.3 (1.82)			
	3	46.9 (1.85)				46.2 (1.82)			
	4	46.2 (1.82)	47.2 (1.86)	3.2 (0.13)	0.07 << 2	47.1 (1.85)	51.0 (2.01)	4.9 (0.19)	0.10 << 2
	5	49.9 (1.97)				49.4 (1.95)			
	6	50.0 (1.97)				52.3 (2.06)			
	7	50.4 (1.99)				55.9 (2.20)			
Test 4	1	39.7 (1.56)				41.6 (1.62)			
	2	38.3 (1.51)				42.2 (1.66)			
	3	43.2 (1.70)				42.6 (1.68)			
	4	43.2 (1.70)	43.7 (1.72)	4.0 (0.16)	0.09 << 2	43.0 (1.69)	46.8 (1.84)	5.2 (0.21)	0.11 << 2
	5	46.7 (1.84)				46.2 (1.82)			
	6	47.5 (1.87)				48.8 (1.92)			
	7	47.7 (1.88)				52.0 (2.05)			

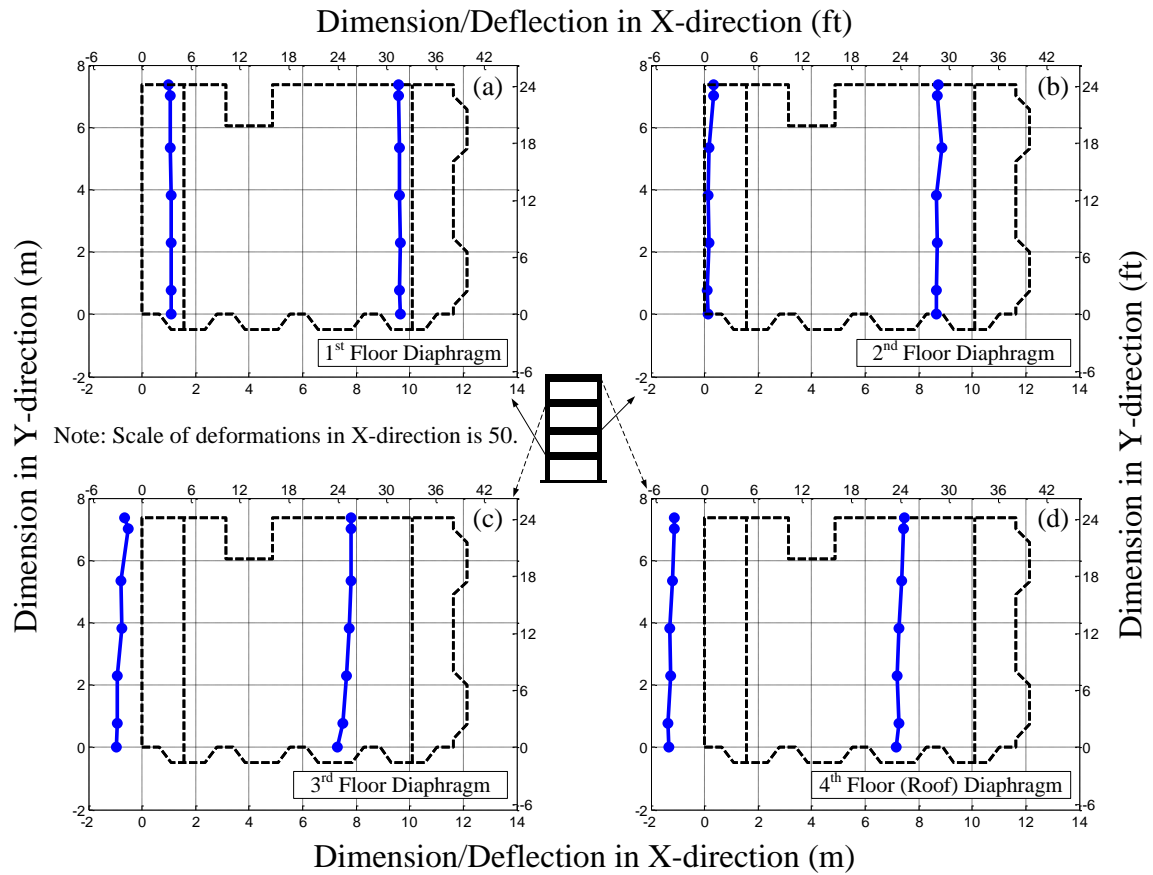


Figure 6-29: Maximum diaphragm deflection during Cape Mendocino ground motion at MCE
(Seismic Test 3)

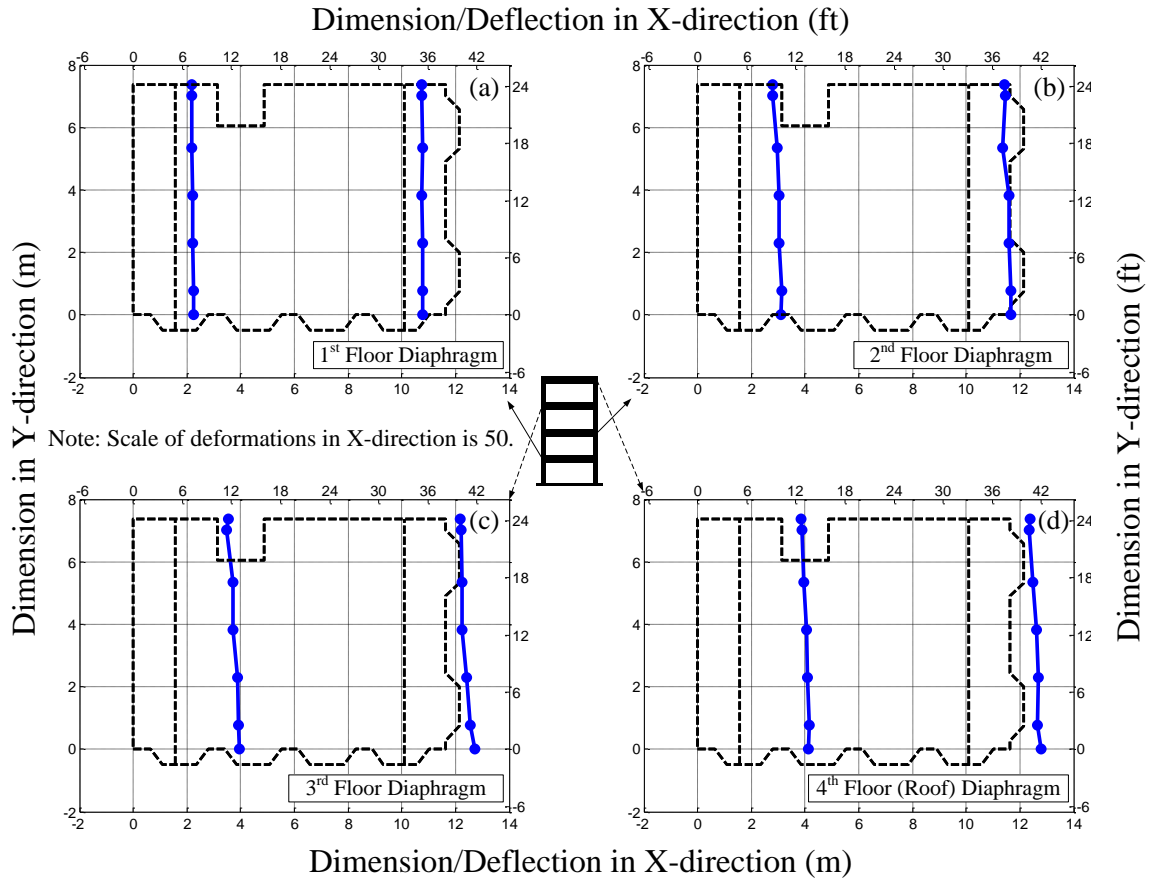


Figure 6-30: Maximum diaphragm deflection during Loma Prieta ground motion at MCE
(Seismic Test 4)

6.5.6 Energy Distribution

In this section, the distribution of energy that was dissipated at each story for the retrofitted building is presented. Generally, two methods are typically used to determine the energy distribution for a structure: (1) the absolute energy method, and (2) the relative energy method. Although both methods have been used in previous studies, the first method gives a more meaningful physical approach in calculating the energy of a system (Uang and Bertero, 1990), therefore in this section, the first method is employed to calculate the distribution of energy.

The absolute energy for an N-story building subjected to a ground motion can be obtained from Equation 6-4 (Uang and Bertero, 1990):

$$\frac{1}{2}[\dot{u}]^T [m] [\dot{u}] + \int [\dot{u}]^T [C] d[u] + \int [f_s]^T d[u] = \int \left(\sum_{j=1}^N m_j \ddot{u}_{t,j} \right) du_g \quad (6-6)$$

where, $[m]$, $[C]$, and $[u]$, are the diagonal mass matrix, diagonal damping matrix, and relative displacement vector, respectively. Also, m_j is the mass of the j^{th} story and $\ddot{u}_{t,j}$ is the absolute acceleration of the j^{th} story and u_g is the ground motion displacement. On the left side of Equation 6-4, the first term is the total kinetic energy at each story (E_k), the second term is the intrinsic damping energy dissipated at each story (E_ξ), and the third term is the absorbed energy by SFRS (E_a) that can be divided to recoverable elastic energy (E_s) and irrecoverable hysteretic energy (E_{hys}) (i.e., hysteric damping energy). Summation of all the energy terms in the left hand side of Equation 6-4 should be equal to the total input energy (E_{input}) that is expressed in the right hand side. Therefore, the absolute energy equation in its short form can be expressed as:

$$E_{input} = E_k + E_\xi + (E_s + E_{hys}) \quad (6-7)$$

In order to determine the distribution of energy dissipated at each story, Equation 6-4 was applied to the test results when the building was retrofitted with PBSR method and subjected to the Cape Mendocino and Loma Prieta ground motions at MCE intensity. Figure 6-31a and Figure 6-31c present the distribution of energy normalized by the total input energy at the end of the Cape Mendocino and Loma Prieta ground motions, respectively; and Figure 6-31b and Figure 6-31d present the cumulative energy absorbed by each story as a function of time for the

Cape Mendocino and Loma Prieta ground motions, respectively. The bold line in Figure 6-31b and Figure 6-31d represents the total input energy which can be obtained by using Equation 6-5. It can be seen that the energy absorbed by the 1st, 2nd, 3rd, and 4th stories were 12, 45, 39, and 4 percent of the total input energy of the Cape Mendocino ground motion at MCE intensity, respectively. The percentile of the dissipated energy normalized by the total input energy are 13, 39, 42, and 6 percent for the 1st, 2nd, 3rd, and 4th stories, respectively, at the end of the Loma Prieta ground motion.

It should be noted that the first story absorbs less energy than the upper stories in these two cases since the steel SMF's did not go through their full non-linear hysteresis curve (Figure 6-26), which obviously would have dissipated much more energy. It should be noted that the energy dissipation plots presented herein are only for these two selected earthquake records, which in fact are not the most intense MCE earthquake for this particular building. For a more critical, i.e. intense, MCE level earthquake much more energy would have been dissipated at the first story and perhaps be even close to approximately 30% at each of the first three stories. The distribution of the dissipated energy at each story of the retrofitted building highlights the fact that the PBSR method has an advantage of using the capacity of the entire building to dissipate the energy of the ground motion.

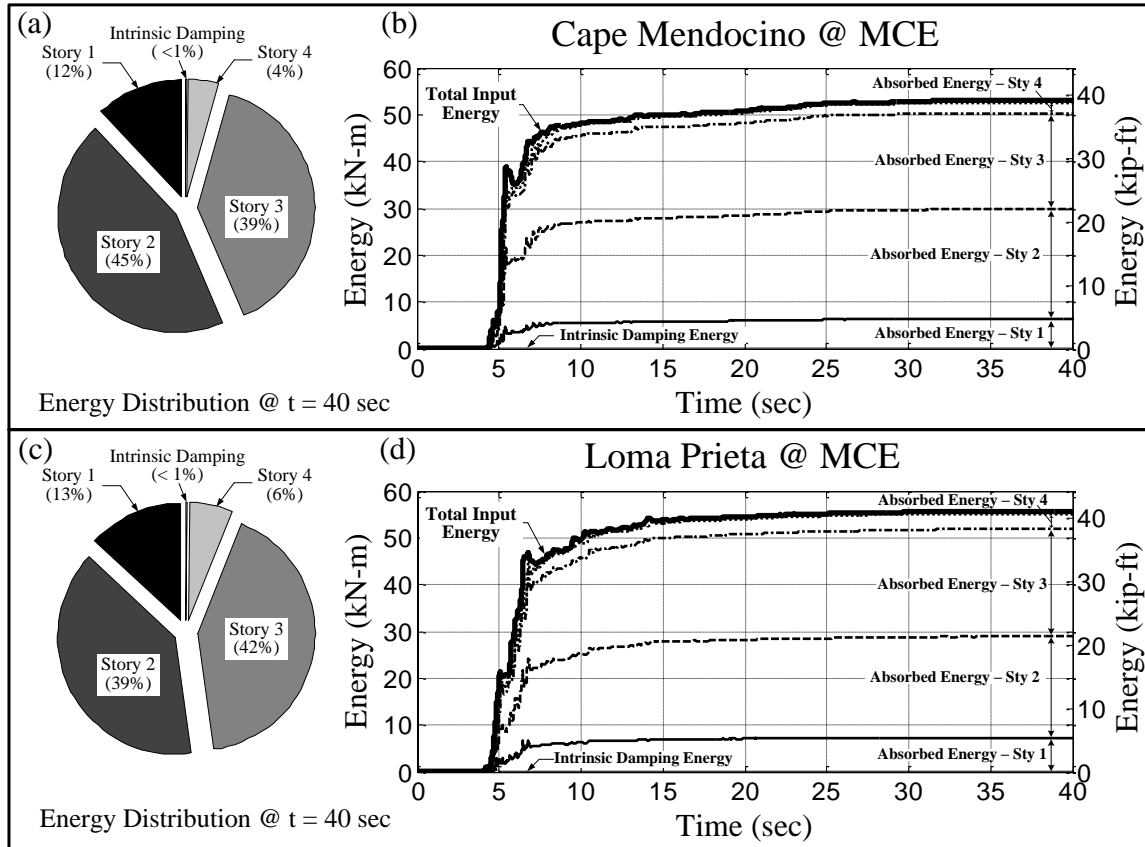


Figure 6-31: Distribution of energy dissipated at each story subjected to ground motions at MCE intensity: (a) Cape Mendocino, (b) Loma Prieta.

6.5.7 Damage Inspection

A thorough damage inspection was conducted after each seismic test to evaluate what, if any, structural and non-structural damage occurred during each test. The building was divided into four areas in order to facilitate the damage inspection process. Each area was then assigned to a team of four to five persons to conduct damage inspection. Since the tests had to be conducted in a short time, damage inspection had to be done as quickly as possible between each test. It should be noted that there was a team of three to four students that followed the damage inspection teams after each test to conduct minor repairs such as replacing fasteners, adding extra

nails to WSP, and pounding back the withdrawn nails. It should be noted that the building was tested eight times prior to the PBSR method tests and then was repaired for the PBSR tests.

As mentioned previously, for the PBSR methodology, it is expected that all stories will experience approximately similar inter-story drifts; hence the distribution of damage over all building stories was expected during the seismic tests. Diagonal cracks on the drywall at the corner of the window of the laundry room and cracks in WSP and partial nail withdrawal were observed after the building was subjected to the ground motions at DBE and MCE level; however, no major structural damage was observed even during the MCE tests. Figure 6-32 presents photos of typical damage that occurred during the four seismic tests when the building was retrofitted in according with the PBSR method.

Figure 6-32a presents diagonal cracks at the window openings at the first story during the Loma Prieta shake at DBE intensity and Cape Mendocino shake at MCE intensity. Figure 6-32b presents a typical drywall screw withdrawal during the test due to shear deformation of the wall framing behind the drywall. Figure 6-32c presents diagonal cracks at the light well window (perpendicular to the shake table motion) at the 2nd story when the building was subjected to the Cape Mendocino ground motion at MCE level (Seismic Test 3). It should be noted that there were some cracks in the walls due to the pervious testing phases (i.e., FEMA P-807 retrofit tests) which were not repaired due to time constraints. It was observed that these cracks opened up more and propagated during MCE level tests. Figure 6-32d present a large diagonal crack at the door opening located in the wall parallel to the shake table at the north-west bedroom of the 2nd floor. The large cracks initiated during the first MCE level test (i.e., Seismic Test 3) and then grew to the ceiling during the second MCE level test (i.e., Seismic Test 4). Figure 6-32e and

Figure 6-32f present nail withdrawal at the bottom edge of the WSP located in Line 3 at the 2nd story when the building was subjected to the Cape Mendocino ground motion at MCE intensity (i.e., Seismic Test 3). Figure 6-32g presents diagonal cracks at the window opening in the wall (perpendicular to the shake table motion) at the 3rd story. It can be seen that the crack was initiated during the Cape Mendocino ground motion at DBE intensity (i.e., Seismic Test 2) and then propagated in the next seismic test (at the MCE intensity). Figure 6-32h shows a vertical crack at the bottom of the WSP located at the 3rd story during Cape Mendocino ground motion at MCE intensity (i.e., Seismic Test 3). Figure 6-32i presents local diaphragm buckling perpendicular to the shake table motion (i.e., Y-direction) next to the WSP in Line 3 at the 4th story. This damage occurred during the last seismic test (i.e., Loma Prieta at MCE intensity) and was the only diaphragm damage observed during the entire test program. Finally, Figure 6-32j shows a diagonal crack at the top of the window located in the dining room of the 4th story. The crack initiated during the first seismic test and propagated during the 2nd and 3rd seismic tests.

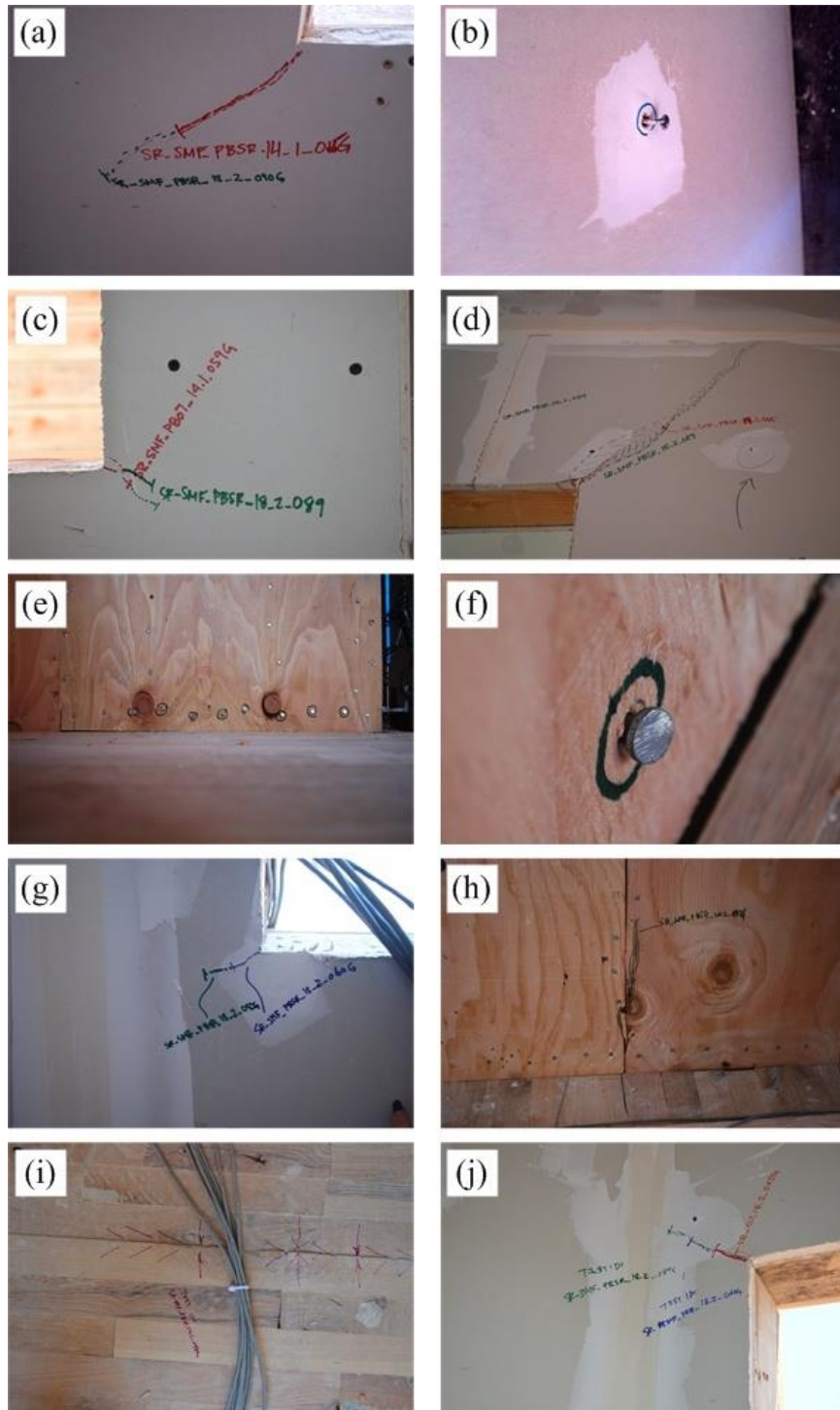


Figure 6-32: Typical damage observed in different locations of the building retrofitted with PBSR method.

6.6 Comparison of Multi-story and Single-story Retrofit Methods

6.6.1 Displacement Profile

In order to present the performance of the retrofitted building with PBSR method and compare it to a single-story retrofit (i.e., FEMA P-807 retrofit methodology), the displacement profiles of the two retrofitted buildings are plotted side-by-side and shown in Figure 6-33. Specifically, Figure 6-33a presents the building profile when it was retrofitted in accordance with FEMA P-807 retrofit methodology (recall this was the single story-only retrofit method) and Figure 6-33b shows the displacement profile for the building retrofitted with the PBSR method. It should be noted that the displacement profiles presented herein were recorded when the maximum absolute displacement (i.e., displacement relative to the ground) occurred at the roof level (i.e., 4th story).

Inspection of Figure 6-33a shows that the peak ISD occurs at the first story when only the first story was retrofitted (e.g., FEMA P-807 retrofit method). As mentioned earlier, this is typical of a soft-story building response where the upper stories behave essentially as a rigid body and thus experience little damage. In fact, no damage was observed in the upper stories of the building retrofitted with FEMA P-807 with the exception of minor hairline cracks near the door and window corners on the second level according to the damage inspection reports conducted during Phase 2 of the test program.

However, for the case where the building was retrofitted with the PBSR methodology (Figure 6-33b), all stories were expected to experience approximately the same inter-story drifts and contribute to the response of the building, i.e. better vertical distribution of the seismic demand over all stories. It can be seen from Figure 6-33b that the maximum displacement profile of the building retrofitted with the PBSR methodology is very close to a straight line for each seismic

test confirming the PBSR method assumption that all the stories should experience approximately the same inter-story drifts. The only exception is the fourth story (i.e., roof) which experienced a smaller average ISD compared to the other stories. As mentioned earlier, this is because the strength and stiffness of the existing walls at the fourth story were very close to the required lateral stiffness calculated based on PBSR, and also the upper story experienced less damaging cycles (i.e., low amplitude displacement) which led to less stiffness and strength degradation in the walls and eventually resulted in smaller ISD. It should be noted that the WSP added to the fourth floor was mostly required to reduce the in-plane eccentricity and thus resulted in a slightly oversized retrofit at this story.

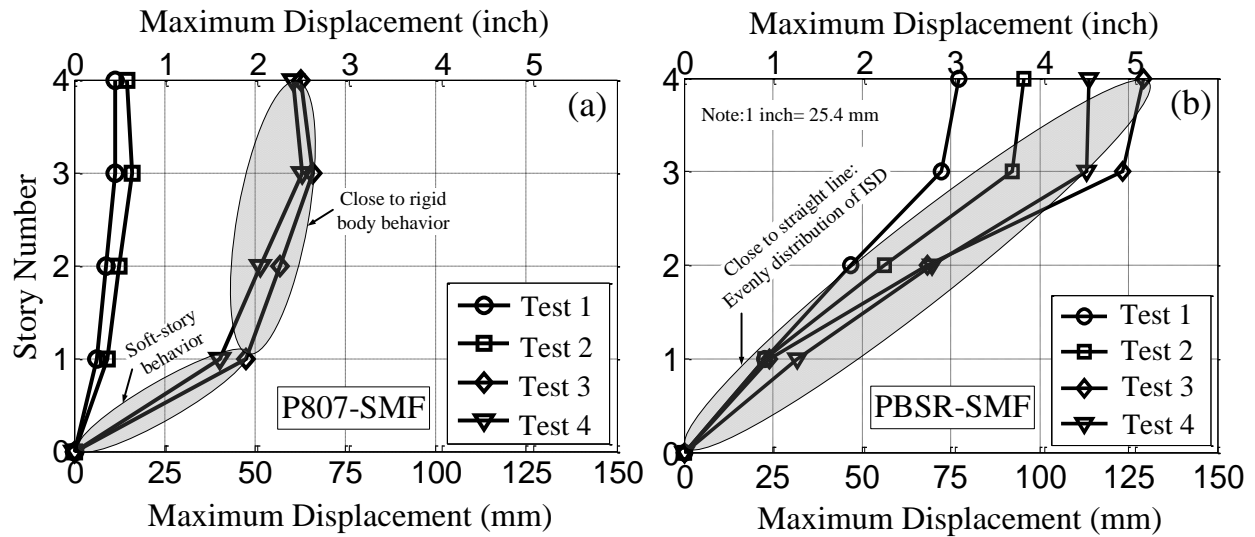


Figure 6-33: Maximum displacement profile the retrofitted building: (a) FEMA P-807 guidelines; (b) PBSR methodology.

6.6.2 Energy Distribution

One of the advantages of the multi-story retrofit methods (e.g., PBSR method) over single-story retrofits (e.g., FEMA P-807) is the distribution of seismic demand over the stories in the building, avoiding concentration of deformation and damage at any one story, and consequently, enabling a building to survive high intensity ground motions. Since the four-story building was retrofitted in accordance with both FEMA P-807 retrofit and PBSR methods, a comparison between the dissipated energy for both cases can be made using the method described in Section 6.5.6.

Figure 6-34a presents the distribution of energy over the entire building at the end of the ground motion excitation and Figure 6-34b presents the cumulative energy absorbed by each story, as a function of time, for the building subjected to the Loma Prieta ground motion scaled to $S_a=1.1g$ (Table 6-1) and retrofitted with the FEMA P-807 retrofit method. The bold line in Figure 6-34b represents the total input energy which can be obtained by adding the absorbed energy by each story and the energy dissipated from intrinsic damping. It can be seen that the first story absorbed 76% of the total input energy and the rest of the stories absorbed approximately 24%. This confirms the fact that in the building retrofitted based on the FEMA P-807 retrofit methodology, or perhaps more generally a soft-story-only retrofit, the first story absorbs most of the energy from the ground motion. This aligns with the observation that the first story experiences more structural and non-structural damage; whereas, the upper stories do not contribute significantly in absorbing ground motion energy.

Figure 6-34c and Figure 6-34d present the same types of plots as Figure 6-34a and Figure 6-34b with the difference that these figures present the distribution of energy dissipated in the building

retrofitted in accordance with PBSR method and subjected to Loma Prieta ground motion at MCE intensity (i.e., scaled to $S_a=1.8g$). It can be seen that the first story dissipated 13% of the input energy and rest of the energy was dissipated in upper stories (39% in the 2nd story, 42% in the 3rd story, and 5% in the 4th story). The first story absorbed less energy than the upper stories (except the 4th story) in this case since the steel SMF's did not go through their full non-linear hysteresis curve (Figure 6-26c). This shows that the dissipated energy was distributed more evenly to all stories in the building retrofitted with the PBSR method than the building retrofitted with FEMA P-807 retrofit.

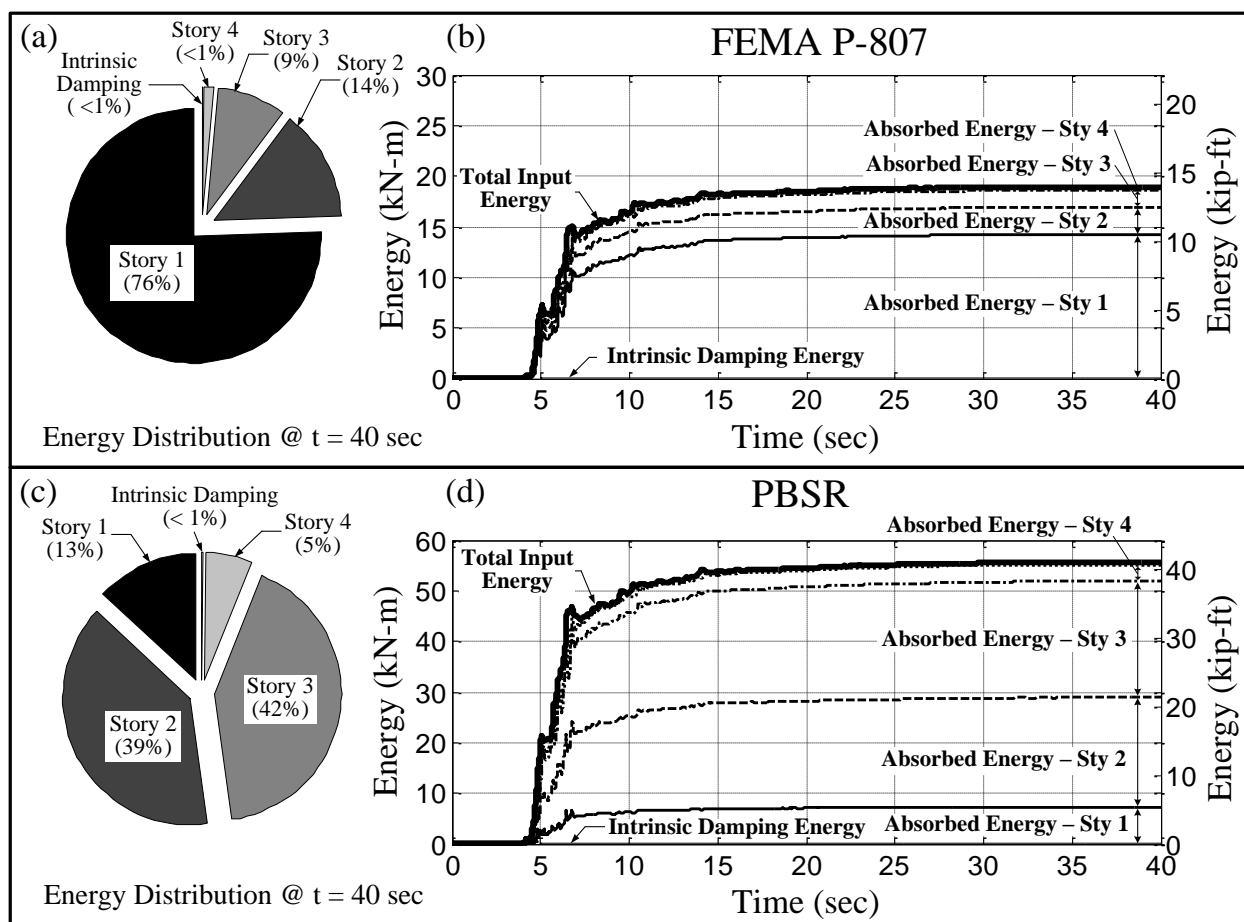


Figure 6-34: Distribution of energy dissipated at each story subjected to Loma Prieta ground motion: (a) Normalized dissipated energy for FEMA P-807 retrofit, (b) Time-history of absorbed cumulative energy for FEMA P-807 retrofit, (c) Normalized dissipated energy for PBSR method, and (d) Time-history of absorbed cumulative energy for PBSR method.

Chapter 7. COLLAPSE MECHANISM AND DEFORMATION CAPACITY¹⁰

One of the objectives of this dissertation is to investigate the collapse behavior of soft-story wood-frame buildings when subjected to earthquakes. This enables one to better understand the deformation capacity of these types of buildings and provides valuable information on the correlation of damage with near collapse and eventually the margin against collapse. In order to achieve this goal, full-scale collapse testing of soft-story buildings was felt to be necessary.

7.1 Background and Motivation for Full-Scale Collapse Test

In the previous chapter, a history of full-scale testing of wood-frame buildings was presented. Although these test programs provided valuable contribution to better understanding of the behavior of wood-frame buildings subjected to seismic load, they did not investigate the behavior at large displacements which are necessary for better quantifying the collapse margin and for improvement of the non-linear numerical models predicting the behavior of wood-frame buildings.

Full-scale collapse testing of wood-frame buildings subjected to earthquake has been conducted only a few times worldwide. The laboratory equipment requirements and safety provisions needed for these types of tests can be quite complex and costly and are available in only a few laboratories worldwide. Sakamoto et. al (2002) discussed the planning of a series of tests on a full-scale two-story town house at the E-Defense laboratory in Miki, Japan as part of Dai-Dai-Toku project. The testing then occurred several years later at the Grand Opening of the laboratory. The project had three phases including testing of a retrofitted and un-retrofitted

¹⁰ Bahmani, P., van de Lindt, J. W., Mochizuki, G. L., Gershfeld, M., Pryor, S.E. (2014). “Experimental Seismic Collapse Study of a Full-Scale Four-Story Soft-Story Wood-frame Building”, *ASCE J. Archit. Eng.*, November 2014. DOI: 10.1061/(ASCE)AE.1943-5568.0000166.

building and finally collapsing the building. In 2004, a two-story Japanese conventional wood-frame house was tested to investigate the collapse mechanism and predict the collapse margin for these types of buildings (Miyake et al., 2004 and Koshihara et al., 2004). However, none of these tests investigated the collapse behavior of western style wood-frame buildings.

The need for investigating the collapse of western style wood-frame buildings in the United States is critical for the following reasons: (1) there is no data for full-scale mid-rise residential buildings subjected to large drifts; and (2) the tests in Japan were on buildings representative of conventional post-and-beam, not light-frame wood construction. Thus, collapse testing of a full-scale building subjected to seismic loads was considered valuable to better understanding the collapse behavior of these types of buildings. This study is the first experimental test of its kind that helps to: (1) better understand the behavior of light wood-frame buildings near and at collapse; (2) quantify the collapse displacement; and (3) investigate the collapse mechanism of soft-story buildings. The collapse test was conducted on the un-retrofitted four-story wood-frame building, described in Chapter 6 of this dissertation, as the last phase of the five-phase shake table test program in San Diego, California.

7.2 Experimental Test Setup, Test Planning, and Feasibility of the Collapse Test

Prior to conducting the collapse test it was necessary to perform feasibility checks to determine if the shake table had sufficient capacity and if equipment and personnel safety might be compromised in any way. The shake table at NEES@UCSD can provide 1.2g horizontal base acceleration for a 400 ton (803.6 kips) payload. The total weight of the building including the steel interface framing was about 60.3 tons (135 kips) and the maximum ground acceleration that

would be generated by the entire set of test ground motions was approximately 1.0g thus, the shake table was capable of accommodating the proposed collapse test.

The next challenging part of the collapse test was predicting the potential landing location of the collapsing building and, if necessary, reinforcing that area to avoid damaging the equipment underneath the shake table. Figure 7-1 presents the shake table with the building footprint shown in bold. The gap between the concrete slab and the shake table which allows the shake table to move was covered by a 25.4 mm (1 in.) thick steel plate (the steel platen in Figure 7-1) bolted to the top of the shake table and was allowed to slide over the concrete slab. The concrete slab was vulnerable to impact load from a collapsing building and required either strengthening or protection. This was resolved by providing temporary shoring of the concrete slab from underneath the shake table, thus effectively reducing the span and corresponding slab maximum bending moment that might be caused by the impact of the building collapse. The shored slab and the steel plate also protected the actuators from possible damage. The building was expected to collapse entirely on its first floor and lean toward the south-east or south-west safety tower. The height of the first story was 2.7 m (9 ft); therefore, the collapse area was expected to be approximately 3.7 m (12 ft) from each side. In Figure 7-1b, the shaded area represents the moving parts of the shake table assembly which includes the shake table itself and the steel platen attached to its west and east side. Figure 7-1b shows the south elevation view of the building (section A-A) erected on top of the shake table.

Three safety towers placed at each side of the building parallel to the direction of motion of the shake table are shown in Figure 7-1a. The distance from the face of the tower to the outside edge of the building was approximately 1.7 m (5.5 ft) allowing the building to collapse freely on the potential collapse area shown in Figure 7-1a. Recall that the towers prevent excessive transverse

movement of the building to protect the control room and other laboratory facilities located to the south of the test building. The collapse test feasibility check helped to confirm test site capabilities and identify safety or damage to equipment concerns. The concerns were effectively addressed, and the collapse test of the four-story building on top of the shake table was determined by the NEES-Soft project team and NEES@UCSD site staff and management to be feasible and safe.

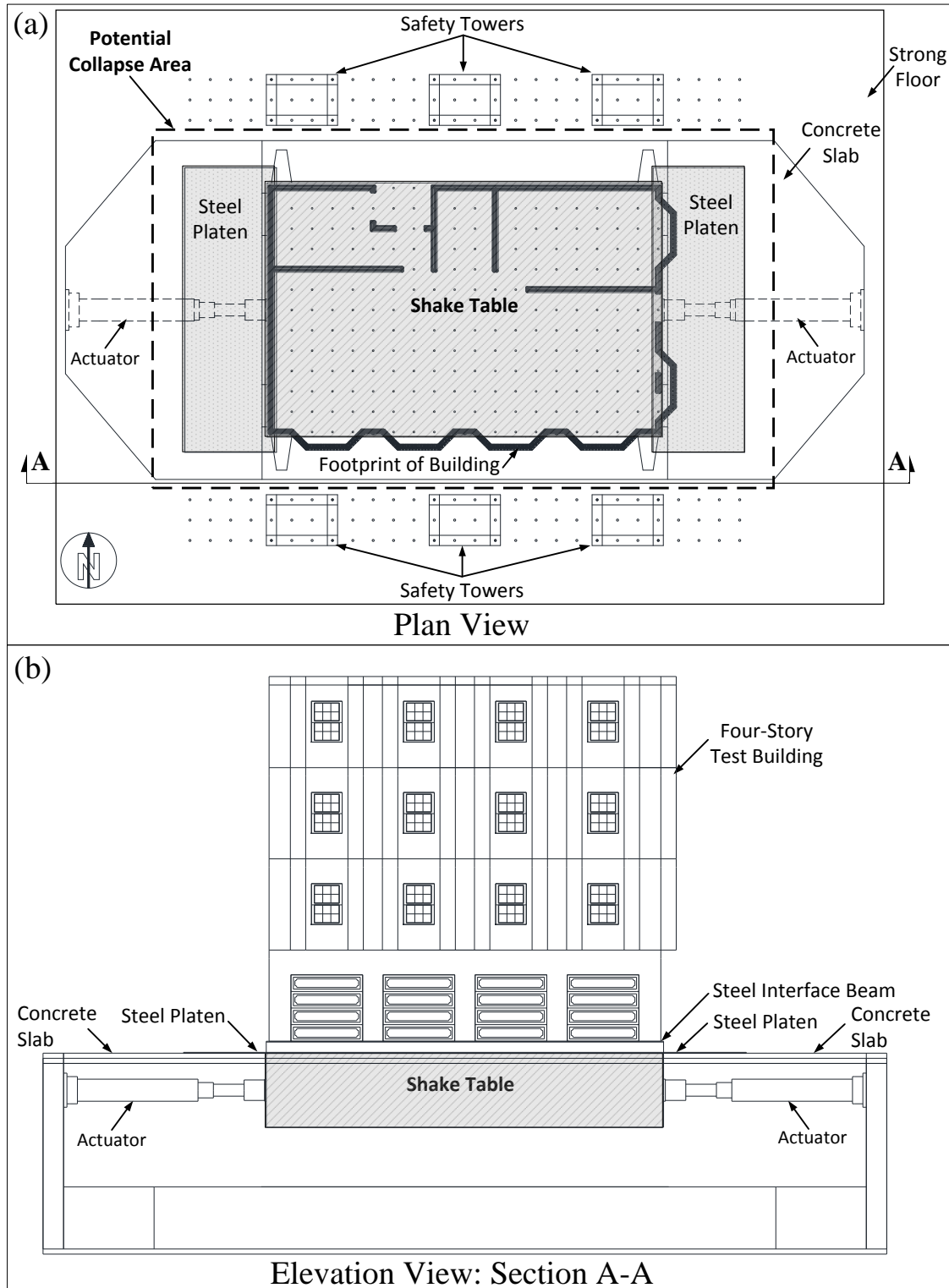


Figure 7-1: Position of the four-story building with its potential collapse area on top of the shake table: (a) plan view, and (b) elevation view (section A-A).

7.3 Instrumentation

In order to monitor the behavior of the building during testing, the building was instrumented with two string potentiometers and four accelerometers at the first floor and three accelerometers at the roof. During earlier phases of the NEES-Soft program the building was instrumented with more than 300 sensors. Most of these were removed and those left in place were expected to be damaged during the collapse test phase, i.e. only gathering data until they were destroyed. Moreover, the movement of the building was monitored with six video cameras. One camera was installed inside the south-east bedroom at the fourth floor which was furnished with a bookshelf, dining table, chairs, and photo frames to observe the non-structural damage during each shake. Figure 7-2 presents the location and details of the instrumentation used in the series of tests leading to the collapse of the test building.

String potentiometers were installed at the first floor parallel to the direction of the motion of the shake table to measure the primary displacement of the soft-story (i.e., first story). The readings of the string potentiometers were not zeroed between tests in order to track the residual displacement of the first story after each shake. Accelerometers were used to record the acceleration of the first story and roof. The accelerometers generated very good recordings of accelerations until the building period increase following the fourth shake. This is believed to be caused by an increase in the natural period of the building and the resulting very low frequency movement of the building which the accelerometer readings were not able to capture.

It should be noted that most of the instruments used in this phase of the testing were destroyed due to the collapse of the building and could not be recovered. The efficient and careful

placement of the instrumentation allowed good quality monitoring of the building behavior during the test while minimizing the cost of “sacrificial instrumentation”.

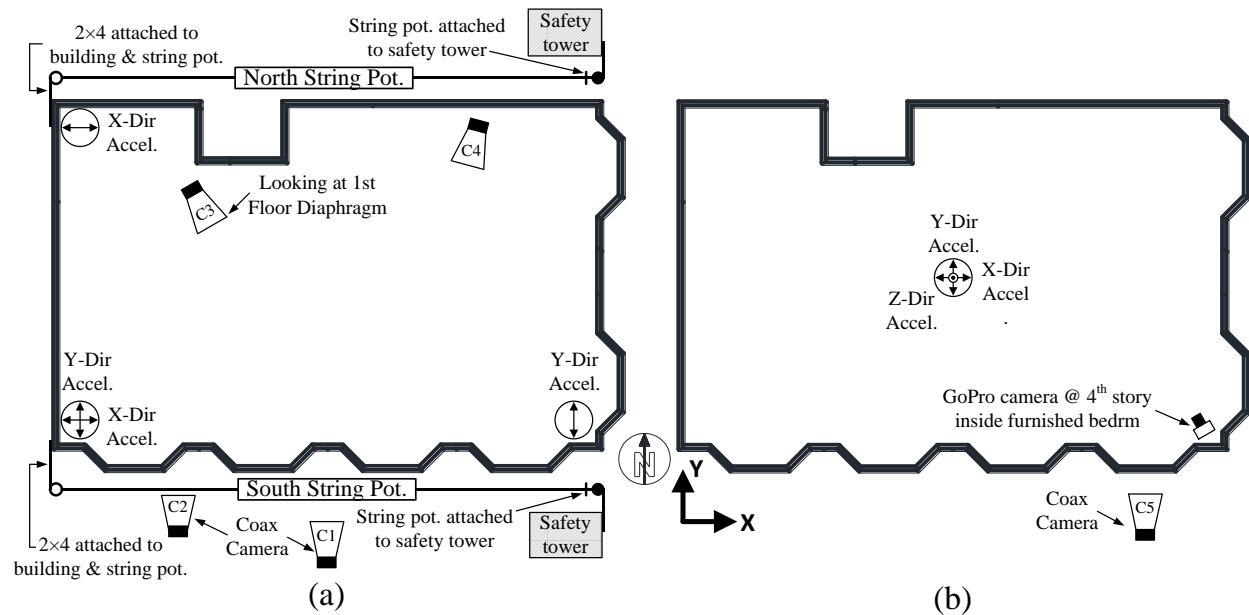


Figure 7-2: Instrumentation plan: (a) first story, and (b) fourth story.

7.4 Ground motions

To study the collapse mechanism and behavior of this type of at-risk soft-story building the building was subjected to range of ground motions with different scaling. Three different ground motions with different intensities were used. The selections were such that they would provide a range of earthquake records based on differences in ground displacement, even if the seismic intensity as determined through spectral acceleration was similar. The ground motions were then scaled to spectral accelerations ranging from $S_a = 0.4g$ (33% of the design-based earthquake (DBE) level) to $S_a = 1.8g$ (maximum credible earthquake (MCE) level). Table 7-1 presents the ground motions and test sequences with the corresponding peak ground acceleration (PGA) and peak ground displacement (PGD) for each test. The testing started with the Cape Mendocino-Rio

station record with a PGA of 0.21g and ended with the Superstition Hills record with a PGA of 0.86g.

Table 7-1: Ground motions used in collapse test

Seismic Test No. ^a	Earthquake record	S_a (g)	PGA (g)	PGD, mm (in.)
1	Cape Medocino - Rio	0.40	0.21	13.1 (0.52)
2	Cape Medocino - Rio	0.90	0.44	29.4 (1.16)
3	Cape Medocino - Rio	1.20	0.56	39.2 (1.54)
4	Cape Medocino - Rio	1.80	0.90	58.8 (2.31)
5	Loma Prieta - Gilroy	1.80	0.98	72.1 (2.84)
6	Superstition Hills	1.80	0.86	277 (10.9)
7	Superstition Hills	0.90	0.42	138 (5.43)
8	Superstition Hills	1.80	0.86	277 (10.9)

^(a) Only seismic test numbers are shown. White noise tests of 0.05g root mean square (RMS) was conducted before the first test.

Figure 7-3 presents the response spectral acceleration and time history record of the ground motions used in the collapse test. It can be seen that the Loma Prieta and Cape Mendocino records significantly affect buildings when the fundamental period is less than 0.6 s, whereas, the Superstition Hills ground motion has a substantial effect on the building at longer periods. Figure 7-3d presents the spectral acceleration of the three ground motions scaled to $S_a = 1.8g$. It can be seen that between the periods of $T_n = 0.4$ s and $T_n = 0.6$ s, which is the range of the periods for the retrofitted wood-frame buildings when strength and stiffness is added, the maximum and minimum spectral accelerations are from the Cape Mendocino and Superstition Hills records, respectively. However, for a building with a period of greater than about $T_n = 0.9$ s, which includes the un-retrofitted building with a soft story tested here, the maximum spectral acceleration is clearly present in the Superstition Hills record. It can be seen from Figure 7-3d

that the spectral acceleration corresponding to the Superstition Hills record was about $0.9g$ which has been shown to be enough to collapse typical soft-story buildings (i.e., fundamental period greater than $T_n = 1.0\text{ s}$).

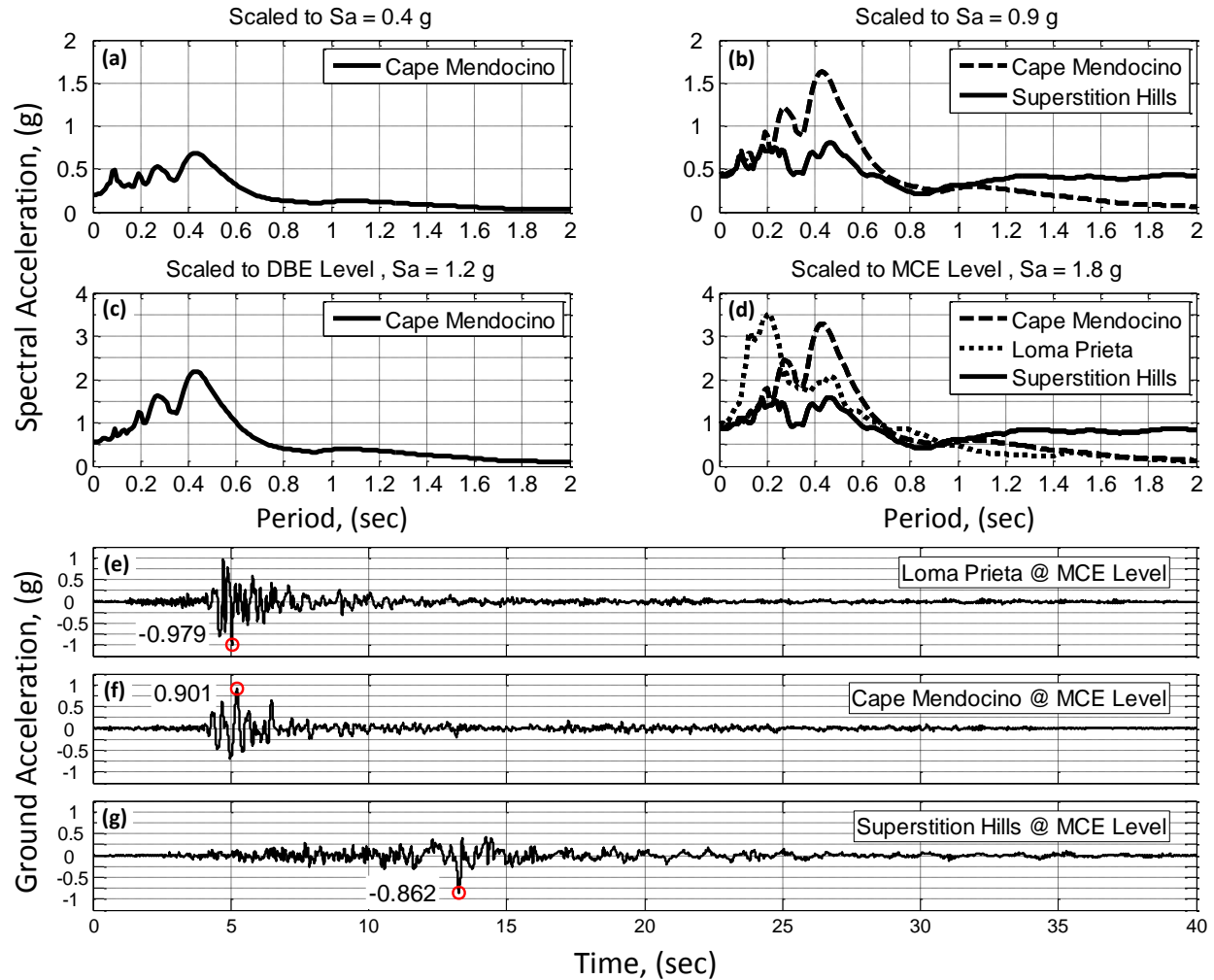


Figure 7-3: Response spectral accelerations of ground motions scaled to (a) $S_a = 0.4\text{ g}$; (b) $S_a = 0.9\text{ g}$; (c) $S_a = 1.2\text{ g}$; (d) $S_a = 1.8\text{ g}$; ground acceleration records at MCE intensity for (e) Loma Prieta; (f) Cape Mendocino; (g) Superstition Hills.

Although high ground accelerations clearly produce large inertial forces within a building it has been observed over the years that global instabilities leading to full collapse often result from

large ground displacements. This is particularly true when large reversals of the motion occur. Therefore, spectral displacements of the ground motions should also be investigated in selecting the ground motion for conducting the collapse tests. Figure 7-4 presents the spectral displacements for the ground motions used in the collapse test. As expected, the Superstition Hills record dominates the spectral displacement response for the periods higher than 1.0 s. From Figure 7-4g it can be seen that the maximum ground displacement of the Superstition Hills record scaled to $S_a = 1.8g$ is 277 mm (10.9 in.), having just displaced 170 mm in the other direction, then returning after the peak displacement to 250 mm. This type of ground motion is similar to the 1995 Kobe recording at the Takatori and Japan Meteorological Agency (JMA) recording stations which have been used repeatedly in Japanese research projects focused on studying collapse.

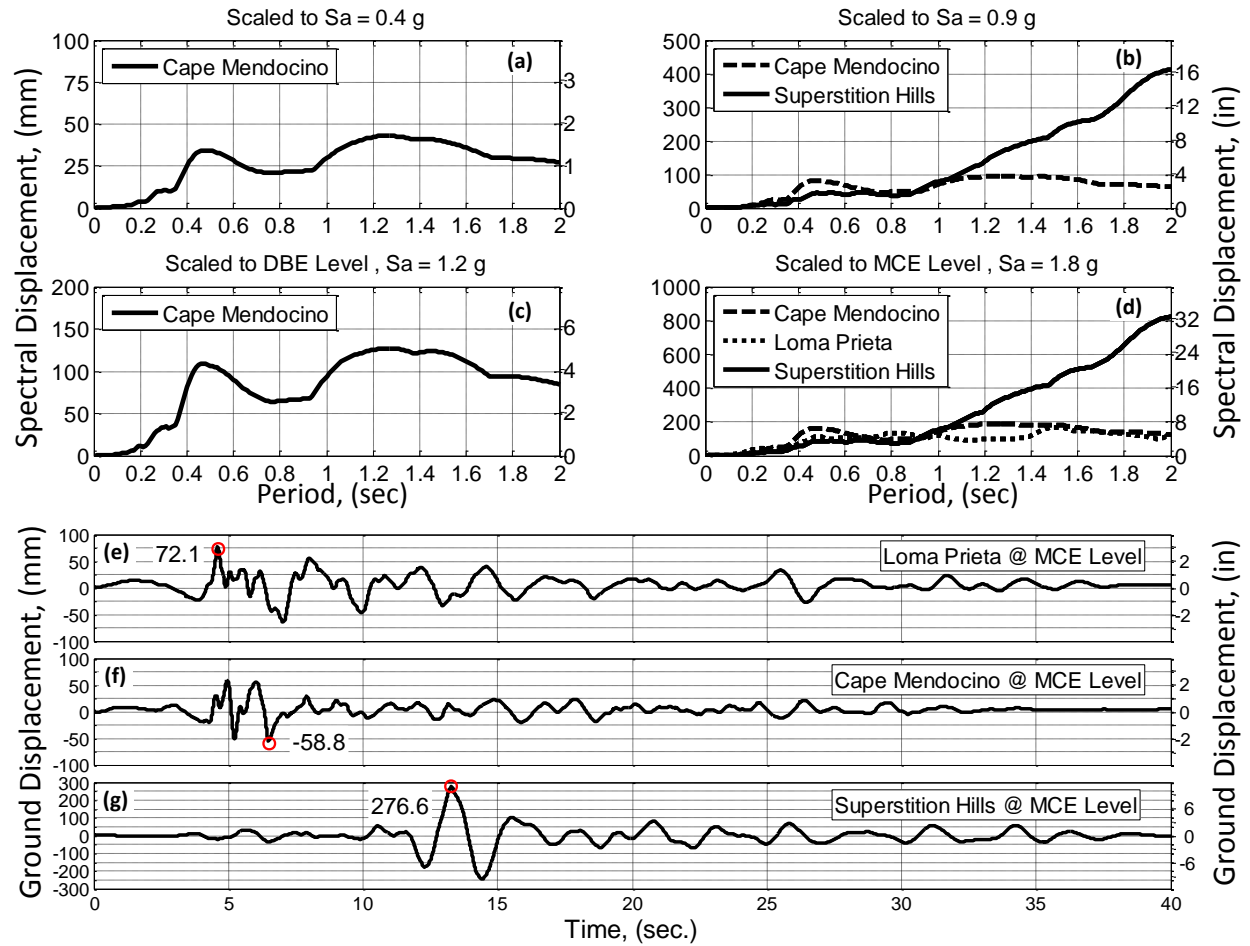


Figure 7-4: Response spectral displacements of ground motions scaled to (a) $S_a = 0.4g$; (b) $S_a = 0.9g$; (c) $S_a = 1.2g$; (d) $S_a = 1.8g$; ground acceleration records at MCE intensity for (e) Loma Prieta; (f) Cape Mendocino; (g) Superstition Hills.

7.5 Numerical Analysis

In order to investigate and predict the behavior of the test building before conducting the tests, the building was modeled numerically using a well-known analog approach that treats each shear wall as a ten-parameter hysteretic spring (Folz and Filiatrault, 2002) and analyzed using non-linear time-history (NLTH) analysis. In this model, floor systems were assumed to be rigid plates with six degrees-of-freedom which has been shown to be effective modeling approach for multi-

story wood-frame construction (Pei and van de Lindt, 2010). However, it should be noted that more advanced numerical wood-frame building models are available (Pang and Ziaei, 2013), and research in this area is clearly ongoing. The ten-parameter models for the HWS and GWB were developed based on wall testing of 38×89 mm (1.5×3.5 in.) framing sheathed with HWS and GWB tested at Colorado State University's Structures laboratory (Bahmani and van de Lindt, 2014). Then, a suite of 44 uniaxial far field earthquake records (FEMA P695, 2009) scaled to seismic intensities ranging from $S_a = 0.4g$ to $1.8g$ (depending on desired intensity) were used to statistically evaluate the behavior of the building under different ground motions.

Figure 7-5 presents the probability of non-exceedance (PNE) versus inter-story drift (ISD) ratios for four different spectral accelerations based on rank ordering the peak ISD ratios from each of the NLTH analyses. Although a state-of-the-art program is used in modeling the building numerically, the software was likely not able to model the building behavior at very large drifts (this also emphasizes the need for conducting full-scale collapse testing). Therefore, an ISD ratio of 35% was used as the maximum ISD ratio to develop the response cumulative distribution functions (CDF's), although this is far beyond what a building would experience prior to collapse; thus, all the numerical data was truncated at an ISD ratio of 35%.

From Figure 7-5, it can be seen that the upper stories experienced low inter-story drifts, as expected with the soft story at the first floor. This shows that the upper stories move essentially as a rigid body on top of the first story and do not go through significant damage even under seismic excitations that lead to building collapse. This behavior was seen and confirmed during the experimental test which will be discussed later in this chapter. Furthermore, the plots in Figure 7-5 show that the soft story (i.e., first story) experiences smaller inter-story drift when

subjected to Loma Prieta than when it is subjected to the Superstition Hills ground motion. This is in agreement with the displacement response spectra for the ground motions shown in Figure 7-4 which served as a basis for selecting ground motions for this experimental collapse study. As discussed earlier, it has been observed with full-scale building testing around the world that large ground displacement often results in collapse when combined with moderate to high ground accelerations (van de Lindt, 2014). It should be noted that the fundamental period of the building right before starting the series of tests was close to $T_n = 1.0 \text{ s}$ (using the white noise test data conducted before the test). The numerical collapse study that was conducted by Pang and Ziaei (2013) showed that this wood-frame building would be expected to collapse at ISD ratios between 11 and 16 percent; therefore, the ISD ratios between these two values are marked as *Expected collapse range* in Figure 7-5.

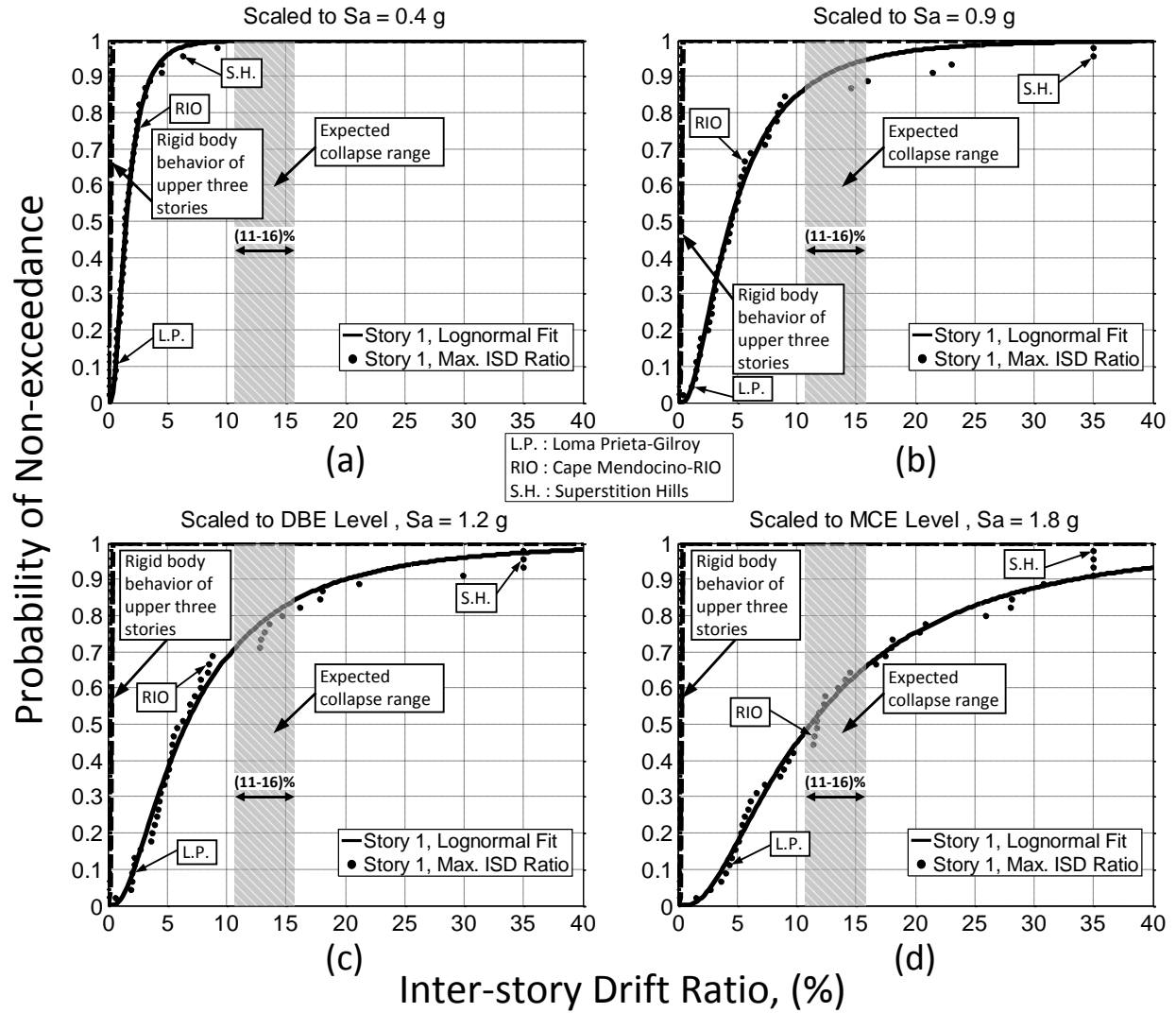


Figure 7-5: Probability of non-exceedance versus inter-story drift ratio of the four-story building subjected to ground motions scaled to different spectral accelerations: (a) $S_a = 0.4g$, (b) $S_a = 0.9g$, (c) $S_a = 1.2g$, and (d) $S_a = 1.8g$.

7.6 Experimental Test Results

The four-story wood-frame building was subjected to eight successive seismic tests with several different ground motion records scaled to spectral accelerations ranging from $S_a = 0.4g$ to $1.8g$.

The approach specified in ASCE7-10 (2010) was slightly modified for scaling ground motions

over the period of 0.08 to 1.5 seconds to ensure a fair comparison between retrofitted and un-retrofitted test building during the entire NEES-Soft test program. In order to find the building mode shapes and their corresponding periods, a white noise test with a 0.05g root mean square (RMS) was conducted before the first seismic test. White noise tests were not performed between seismic tests to be sure to avoid the possibility of accidentally collapsing the building. The initial period of the un-retrofitted building right before starting the seismic tests was $T_n = 0.99\text{ s}$ which was very close to the fundamental period calculated from the numerical analysis. Due to safety regulations, no damage inspection and repair was conducted between each consecutive test; therefore, the structural and non-structural damage accumulated during the entire collapse test phase. It was observed that the period of the building increased significantly after the fourth shake (Test No. 4) due to permanent structural damage and was likely between 1.5 and 2.0 seconds. Figure 7-6a presents the complete back-to-back seismic tests with their corresponding time-history of ground acceleration, velocity, and displacements measured directly from the shake table feedback output. Figure 7-6b shows the translational and torsional response of the first story recorded from the north- and south-string potentiometers. The rotation of the building was obtained by calculating the difference between the readings of the two string potentiometers along x -direction (i.e., $\Delta x_{South} - \Delta x_{North}$) and divided it by the dimension of the building in y -direction (i.e., L_y):

$$Rotation\ (rad) = \frac{(\Delta x_{South} - \Delta x_{North})}{L_y} \quad (7-1)$$

It should be noted that the building experienced some displacement in the y -direction due to asymmetry of the building; but the center of mass of the building did not have a significant displacement in the y -direction since the building was excited only in x -direction.

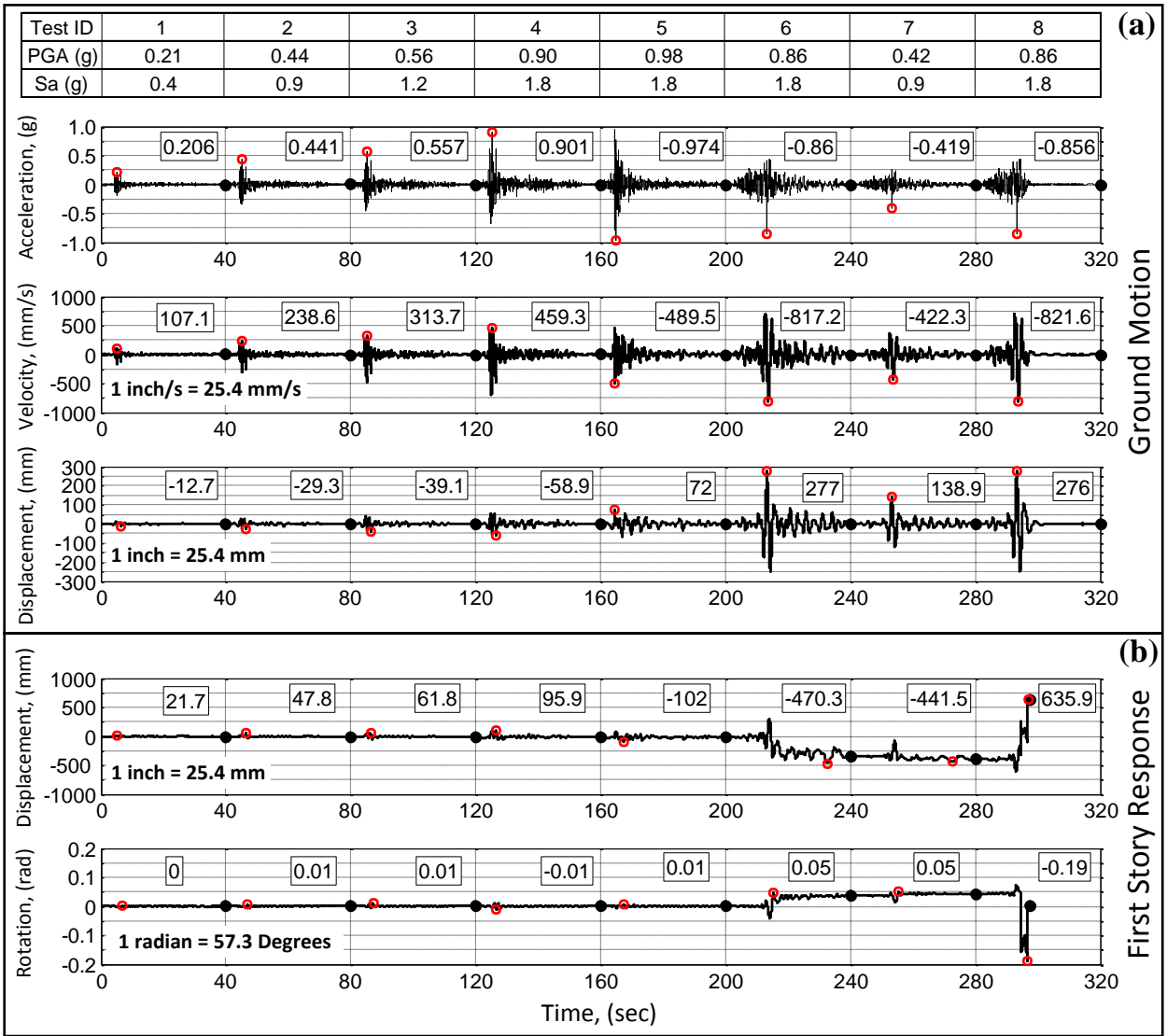


Figure 7-6: Time-history of ground motions and corresponding responses of the building during consecutive seismic tests: (a) time-histories of the ground motions, (b) time-history responses of the first story.

The series of seismic tests began with three relatively small shakes with maximum spectral acceleration of 1.2g (Tests No. 1 to 3) resulting in a maximum displacement of 61.8 mm (2.43 in.) at the first story. The Loma Prieta and Cape Mendocino ground motions have relatively small response spectral accelerations and displacements for periods greater than 1.0 s and therefore were selected to ensure that the building was subjected to ground motions with increasing spectral acceleration and displacements. The maximum ISD was about 95.9 mm (3.78 in.) and 102 mm (4.02 in.) with almost no observed residual drift for the Cape Mendocino and Loma Prieta ground motions scaled to MCE level, respectively. The last three tests (Tests No. 6 to 8) that led to collapse of the building were conducted by subjecting the building to the Superstition Hills ground motion. As shown in Figure 7-3d and Figure 7-4d, this ground motion has very high response spectral acceleration and displacement for periods larger than 1.0 s. Furthermore, from Figure 7-6a it can be seen that the ground motion velocity and displacements of the Superstition Hills record are larger than those for the two other ground motions. Therefore, the probability of collapse for the test building is significantly greater when subjected to this ground motion. The building was first subjected to the Superstition Hills ground motion scaled to $S_a = 1.8g$ which lead to large permanent damage to the building bringing it to the verge of collapse. It should be mentioned that at this level of damage the building would have been red tagged and the entry into the building would not be allowed except by emergency rescue personnel. Then, it was subjected to the same ground motion scaled to $S_a = 0.9g$ to evaluate the aftershock performance of the building; however, the building did not collapse even with about 400 mm (16 in.) residual inter-story drift and 2.3 degrees of residual rotation. From Figure 7-6b, it can be seen that the building experienced very high translational displacement and rotational movement during these two seismic tests. In fact, the building never even passed through its

original equilibrium position further underscoring the severity of the damage sustained during the first Superstition Hills shake. The building was then subjected to the same ground motion but this time with it again scaled to MCE intensity, $S_a = 1.8g$, which led to collapse of the building. The shake table was stopped after the full collapse to protect the lab equipment rather than allow the collapsed building to potentially be damaged further. It can be seen from the last column in Figure 7-6b that the building experienced about 635.9 mm (25.0 in.) of translational displacement and about 11 degrees of in-plane rotation at the onset of collapse.

Figure 7-7 presents the displacement of the first story of the building subjected to the Superstition Hills record scaled to $S_a = 1.8g$ for the first time (i.e., Test No. 6) and the second time (i.e., Test No. 8) which led to the collapse of the test building. It was observed that the building had a very low residual displacement before being subjected to the Superstition Hills earthquake. However, as expected, the building went through excessive displacements with maximum displacements of 470 mm (18.5 in.) (i.e., 19.3% ISD ratio) and residual displacements of about 350 mm (13.8 in.) (i.e., 14.4% ISD ratio) when subjected to the Superstition Hills earthquake (Test No. 6).

Figure 7-7b shows the lateral response details of the last test (Test No. 8) for the test series which led to the collapse the building. It can be seen that the building had about 400 mm (15.7 in.) of residual displacement (i.e., 16.4% ISD ratio) leaning toward the west at the start of the ground motion. Then, it moved slowly further to the west for the last time then moved toward the east and rotated about 11 degrees before hitting the safety towers. Since the maximum stroke of the string potentiometers was ± 635 mm (± 25 in.), the last recorded displacement was 635.9 mm (25.0 in.), and after reaching this displacement the string potentiometers were destroyed and no

longer recorded the displacements of the first story. It should be noted that the building was in a collapse state following the Test No. 6 which means that it was not repairable and unsafe to enter (residual displacements of approximately 350 mm and an ISD ratio of 14.4%).

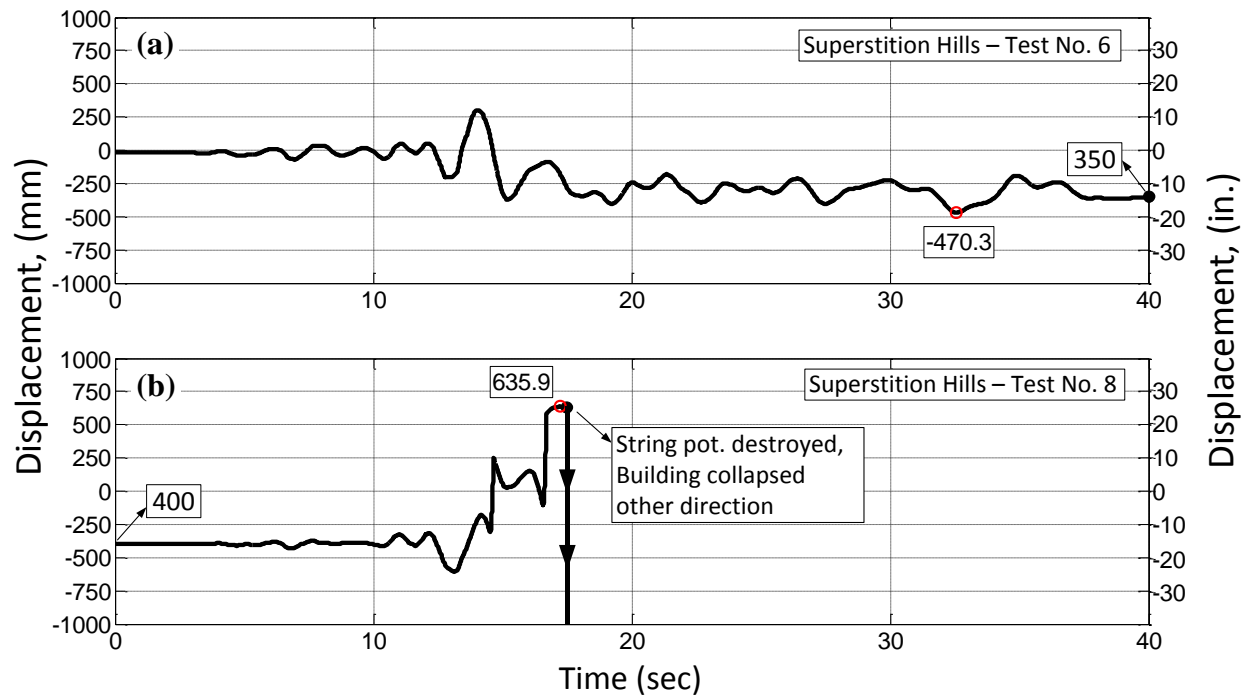


Figure 7-7: Displacement time-history record of the first story subjected to Superstition Hills earthquake record: (a) Test No. 6, and (b) Test No. 8.

Figure 7-8 presents the collapse sequence of the building subjected to Superstition Hills record scaled to MCE intensity (Test No. 8) and Figure 7-9 shows the photos of the collapsed building from different angles. It can be seen that the building rotated substantially before it collapsed and hit the safety towers at the south-east corner of the building. Also, the first story was completely destroyed as expected.

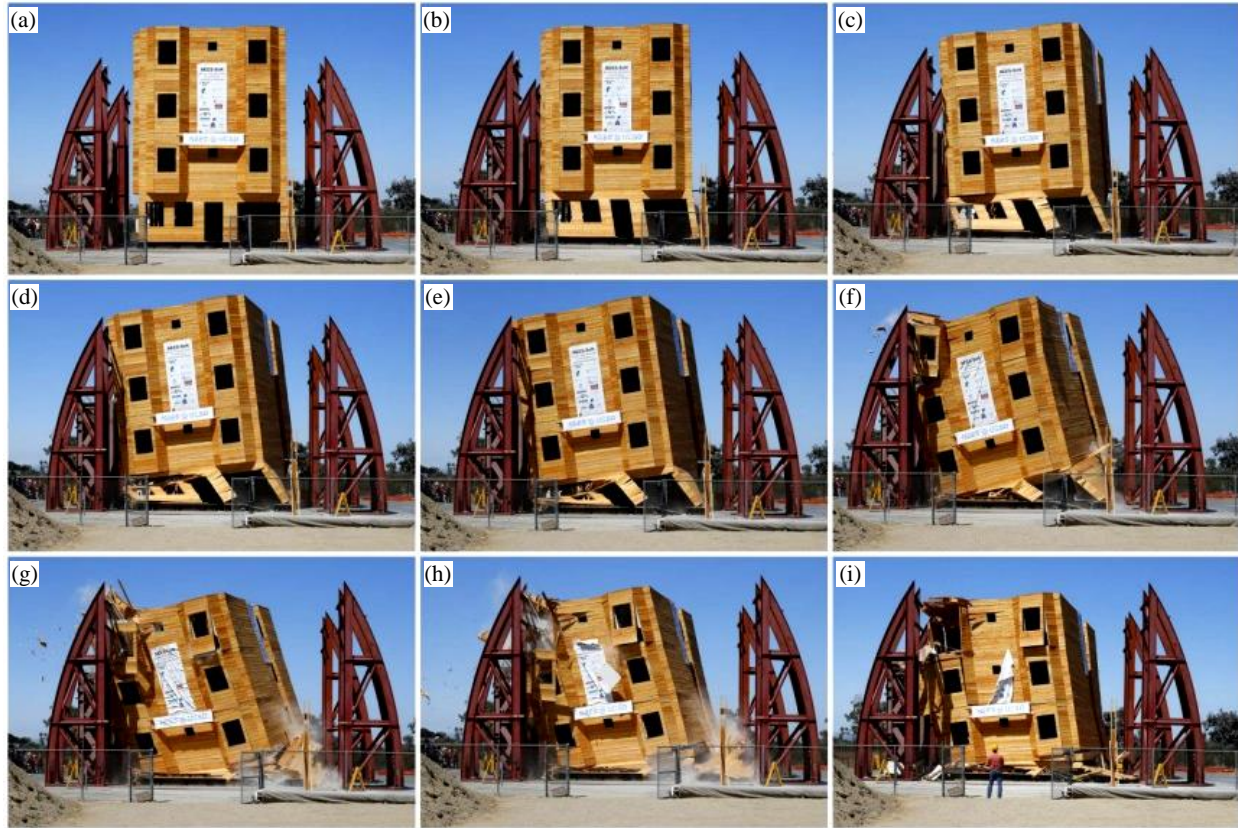


Figure 7-8: Collapse sequence of the four-story building (from its east view) subjected to Superstition Hills record at $S_a = 1.8g$ (Test No. 8) – Photo courtesy of Reuters.

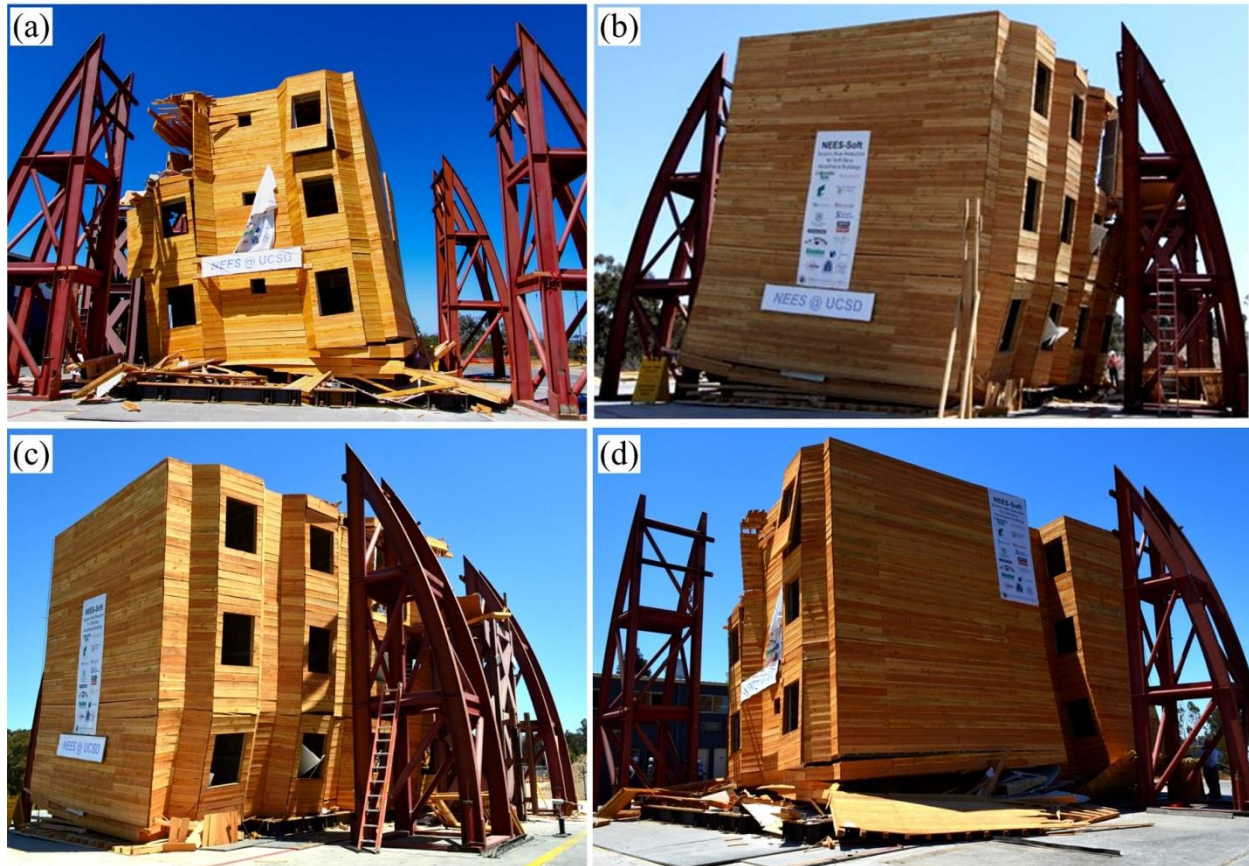


Figure 7-9: Photos of the collapsed building: (a) east view, (b) west view, (c) south-west view, and (d) north-east view.

7.7 Comparison of Retrofitted and Un-retrofitted Building

As mentioned earlier, the un-retrofitted building was subjected to series of ground motions with different intensity including the one that used to test the retrofitted building (Chapter 6). This enables one to compare the behavior of the retrofitted and un-retrofitted building subjected to the same ground motions with the same intensities. It should be noted that the behavior of the first story is investigated since (1) this story was the soft-story in the un-retrofitted building therefore, its behavior before and after applying the retrofits was felt necessary to observe, and (2) the upper stories in the un-retrofitted building was assumed to move rigidly on top of the first story;

therefore, the sacrificial string potentiometers were mounted only at the first story and their readings were compared to the response of the first story in the retrofitted building.

Figure 7-10 presents the comparison between the response of the first story (i.e., soft-story) with and without retrofits when the building is subjected to the Cape Mendocino and Loma Prieta ground motions. The displacement profiles of the first story are presented in Figure 7-10a and Figure 7-10b and the time-history responses are presented in Figure 7-10c to Figure 7-10f. It can be seen that the maximum absolute displacements of the first story from its equilibrium condition were 25.6 mm (1.01 in.) and 105.7 mm (4.16 in.) for the retrofitted and un-retrofitted buildings, respectively, when the building was subjected to the Cape Mendocino ground motion at MCE intensity. The maximum absolute displacements of the first from its equilibrium condition were 32.8 mm (1.29 in.) and 89.3 mm (3.52 in.), respectively, when the building was subjected to the Loma Prieta ground motion at MCE intensity. This shows that the displacements at the first story of the un-retrofitted building were approximately 4 and 3 times higher than the of the retrofitted building and confirms the effectiveness of the PBSR method in reducing the displacement to an acceptable design range.

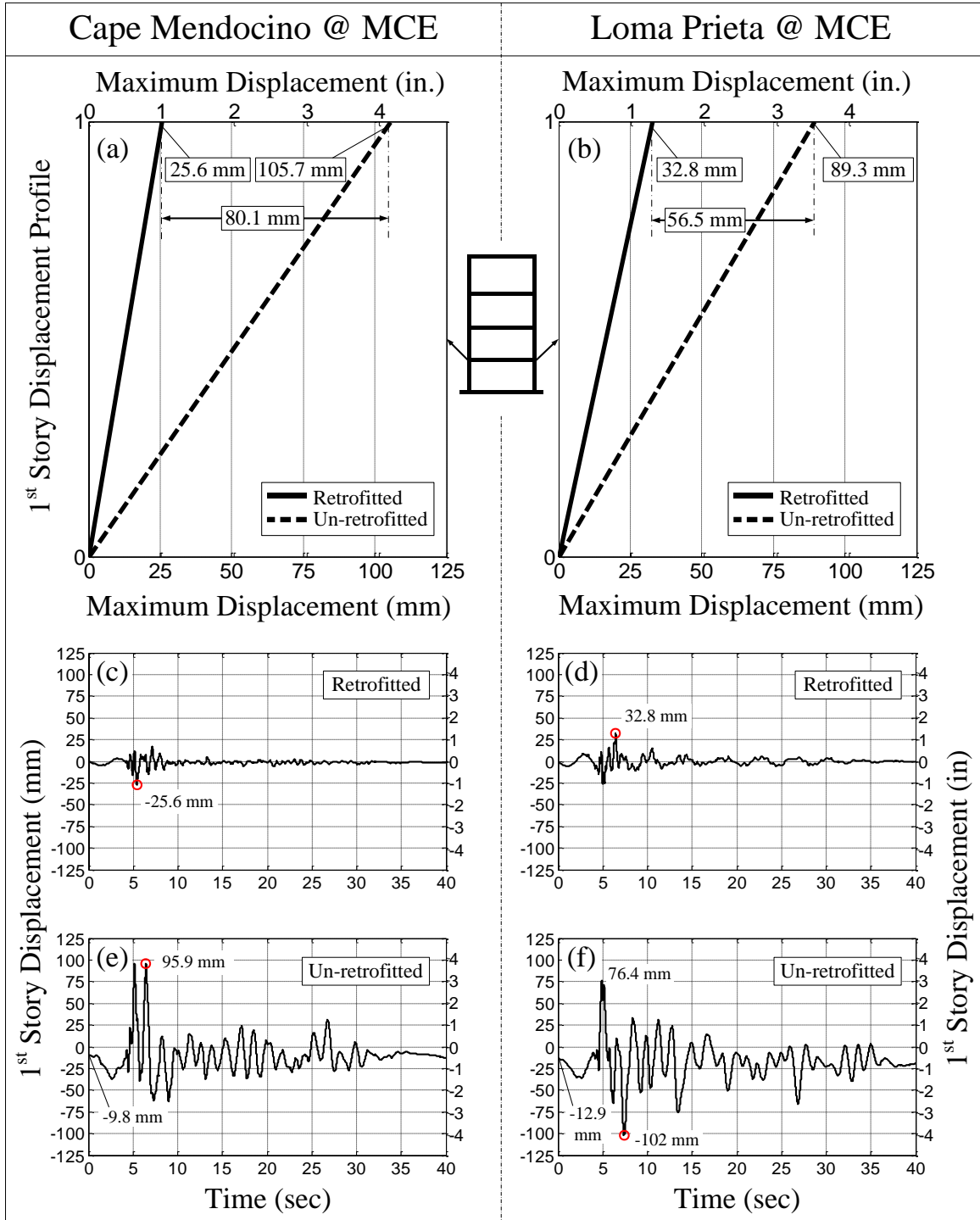


Figure 7-10: Comparison of Retrofitted and Un-retrofitted building subjected to ground motions at MCE intensity.

Chapter 8. SUMMARY, CONCLUSIONS, CONTRIBUTIONS, AND RECOMMENDATIONS

8.1 Summary

In this dissertation, a new displacement-based design method with the ability to account for torsion (DBDT) was developed by decoupling and standardizing translational and torsional mode shapes. The DBDT method was applied to a three-story linear building and a ten-story non-linear building with vertical and torsional irregularities at all stories and validated numerically through non-linear time-history analysis (NLTHA) using a suite of 22 far-field earthquake records. Furthermore, a new performance-based seismic retrofit (PBSR) method for retrofitting existing multi-story buildings with torsional (horizontal) and vertical irregularities was developed based on the proposed DBDT method. The PBSR method was validated numerically to retrofit a three-story soft-story building with torsional irregularities at all stories.

The PBSR method was then modified to eliminate the torsion in the building at the pre-defined target ISD ratio (i.e., the designated performance criteria). This enables the design to use only the dominant translational mode shape (i.e., first mode shape) for the retrofit. This also eliminates the need for modal analysis and the decoupling of translational and torsional mode shapes will make it easier for engineers to apply the method. The new simplified PBSR method for retrofitting multi-story buildings was then applied to a four-story soft-story wood-frame building with torsional irregularities at all stories and assessed numerically using NLTHA. Finally, the method developed in this dissertation was validated experimentally by conducting a series of full-scale tests on a four-story 370 m² (4,000 ft²) soft-story wood-frame building at the outdoor uni-axial shake table at the University of California - San Diego Network for Earthquake

Engineering Simulation (NEES) laboratory. The building was subjected to the Loma Prieta-Gilroy and Cape Mendocino-Rio ground motions both scaled to DBE (i.e., $S_a = 1.2g$) and MCE ($S_a = 1.8g$) intensities. Its seismic response was monitored by almost 400 sensors mounted at different locations inside and outside of the building. It was observed that the ISD ratios of the stories were less than the target ISD ratio (with reasonable safety margins) which ultimately validated the PBSR method developed as part of this dissertation work. A combination of steel special moment frames (SMF), wood structural panels, and anchor tie-down system (ATS) rods were used as practical retrofitting techniques for the four-story soft-story wood-frame building.

In order to investigate the behavior of the un-retrofitted building and its deformation capacity, the retrofits were removed from the building, repairs made, and the building was then subjected to ground motions with different intensities. It was also observed that the building collapsed over its soft story (i.e., first story), and the upper stories moved as a rigid body on top of the first story during all shakes, as expected. The building was weak and soft in both directions at the first story, which caused rotation toward the south side (i.e., the street side if it had been a real building) when it collapsed. This shows that the contribution of torsion in asymmetric buildings may accelerate the collapse of the building and lead to more significant damage to the building, nearby property, and street.

8.2 Conclusions

The main goal of this study was to develop and validate a new performance-based seismic retrofit (PBSR) methodology to retrofit vertically and horizontally irregular buildings in order to reduce the seismic risk of at-risk buildings in the United States. The numerical analysis and full-scale shake table test showed that the proposed PBSR method can be applied to retrofit existing

irregular buildings in order to satisfy specific performance criteria. Based on the body of work presented in this dissertation it can be concluded that:

- 1) The PBSR methodology can be applied to vertically and horizontally irregular buildings (i.e., a building with an extreme soft/weak story and torsional irregularity) to achieve a prescribed performance criteria for a prescribed seismic intensity by identifying the necessary addition of stiffness and strength at each story level.
- 2) The PBSR method was able to effectively eliminate torsion in the building for all earthquakes tested at all intensity levels.
- 3) The use of steel SMF's, wood structural panels, and ATS rods is an effective technique for retrofit soft-story wood-frame buildings and minimizes the interference of retrofit elements with architectural constraints for existing buildings.
- 4) The PBSR methodology leads to a more uniform distribution of seismic demand over the height of the structure than a single story retrofit thereby, allowing the building to resist very large earthquakes with a lower probability of collapse.
- 5) The PBSR methodology leads to a more even dissipation of energy over the entire building than a single story retrofit and can therefore provide a good balance of energy dissipation over a building's height. This feature enables designers to meet the design criteria not only in terms of distribution of ISD ratio (i.e, performance), but also in terms of energy distribution.
- 6) The upper limit of the collapse ISD ratio for the four-story soft-story wood-frame test building was close to 19% ISD ratio, likely between 14 and 19%; however, it was observed

that the building was unrepairable and uninhabitable when it reached approximately a 14% ISD ratio. An ISD ratio between 14% and 19% could be suggested as a collapse range for this type of building although 10% would be a more conservative estimate since only one building was tested. It was also shown that the collapse margin for these types of building is significantly higher than what is currently being assumed in building codes and research projects (i.e., ISD ratio of 3% to 7%). Furthermore, it was confirmed that ground displacement has more effect on collapse than ground acceleration, at least for this building.

- 7) The 1"×6" wood planks with ¾" hardwood flooring was able to provide the strength needed for the wood-frame diaphragms to transfer load to the vertical shear elements for the SFRS.

8.3 Contributions to Research and Practice in Structural and Earthquake Engineering

- 1) A new displacement-based design procedure with the ability to account for torsion (DBDT) was developed. A performance-based seismic retrofit (PBSR) procedure was developed based on the DBDT method in order to retrofit vertically and horizontally irregular buildings. A simplified PBSR method was developed by using the first translational mode shape (i.e., dominant mode shape), and at the same time, by eliminating the torsional responses of the building during earthquakes.
- 2) Practicality and constructability for retrofitting techniques of soft-story wood-frame buildings were investigated experimentally by considering structural, architectural, and constructional constraints in retrofitting these types of buildings.
- 3) A first-of-its-kind (landmark) dataset for use by researchers and practitioners for retrofitting wood-frame buildings was produced through the shake table testing of multi-story soft-story

wood-frame building. This dataset was made available to the public and will provide information as retrofit programs begin nationwide. The dataset includes the response of the retrofitted and un-retrofitted building in terms of accelerations and displacements at each story, deformation of floor diaphragms, shear deformation of wood shear walls, and uplift forces at each story.

- 4) The collapse mechanism and deformation limits of soft-story wood-frame buildings subjected to earthquakes were investigated by conducting the first-ever full-scale collapse test on a multi-story wood-frame residential building. Previous tests had only been conducted for traditional post-and-beam buildings in Japan.
- 5) Hysteretic parameters for wood-frame walls with an array of combinations of new and archaic materials were identified experimentally through cyclic testing of isolated wood-frame walls. The dataset is the first-of-its-kind which can be used by researchers and practitioners to conduct more accurate analysis, design, and retrofit of wood-frame buildings.

8.4 Recommendations for Future Research

8.4.1 *Recommendations for the PBSR Method*

- 1) In order to tune the PBSR method, it is recommended to obtain the equivalent damping at the system level for a structure with different seismic force resisting systems (e.g., steel moment frame and wood structural panels, etc.), or to develop a computational approach to include this more accurately in the method.

- 2) It is recommended to investigate the effect of the torsional component of ground motions (torsional ground motions) in the behavior of a building that is designed in accordance with the DBDT method or retrofitted in accordance with the PBSR procedure.

8.4.2 Recommendations for the Full-scale Shake Table Testing

- 1) It is recommended to use a tri-axial (or bi-axial) shake table in order to investigate the behavior of the retrofitted building when it is subjected to both horizontal components (i.e., along X- and Y-direction) and perhaps a vertical component (i.e., along Z-direction).
- 2) It is recommended to measure displacements at each story directly by mounting string potentiometers, or using optical tracking.
- 3) Use of stucco and plaster on wood lathe is recommended for exterior and interior walls, respectively, of the test building.

8.4.3 Recommendations for the Isolated Wall Testing

- 1) The effect of different boundary conditions (i.e., fixed-fixed, fixed-free, etc.) in the structural behavior of isolated wood-frame walls is needed.
- 2) Testing of different combinations of sheathing material with three specimens for each combination is recommended.

REFERENCES

- ASCE7-05, (2010), “Minimum Design Loads for Buildings and Other Structures, ASCE/SEI 7-10, American Society of Civil Engineers”, Reston, Virginia.
- ASCE7-10, (2005), “Minimum Design Loads for Buildings and Other Structures, ASCE/SEI 7-05, American Society of Civil Engineers”, Reston, Virginia.
- ATC-58, Applied Technology Council (2006), “Next Generation Performance-based Seismic Design Guidelines”, Report No. ATC-58, Redwood City, CA.
- Bahmani, P. and van de Lindt, J. (2014). "Experimental and Numerical Assessment of Woodframe Sheathing Layer Combinations for Use in Strength-Based and Performance-Based Design." *J. Struct. Eng.* , 10.1061/(ASCE)ST.1943-541X.0001134 , E4014001.
- Bahmani, P. and van de Lindt, J. (2013). “Direct Displacement Design of Vertically and Horizontally Irregular Woodframe Buildings”. *Proc. of Structures Congress 2013*: pp. 1217-1228.
- Bahmani, P., and van de Lindt, J. W. (2012). “Numerical modeling of soft-story woodframe retrofit techniques for design.”, *Proc. of Structures Congress 2012*, ASCE, 1755-1766.
- Bahmani, P., van de Lindt, J., and Dao, T. (2014). ”Displacement-Based Design of Buildings with Torsion: Theory and Verification.” *J. Struct. Eng.*, 140(6), 04014020. DOI 10.1061/(ASCE)ST.1943-541X.0000896 , 04014020

- Bahmani, P., van de Lindt, J.W., Gershfeld, M., Mochizuki, G.L., Pryor, S.E., Rammer, D. (2014). “Experimental Seismic Behavior of a Full-Scale Four-Story Soft-Story Woodframe Building with Retrofits I: Building Design, Retrofit Methodology, and Numerical Validation”, *ASCE J. Struct. Eng.*, DOI: 10.1061/(ASCE)ST.1943-541X.0001207.
- Bahmani, P., van de Lindt, J., Mochizuki, G., Gershfeld, M., and Pryor, S. (2014). "Experimental Seismic Collapse Study of a Full-Scale, 4-Story, Soft-Story, Wood-Frame Building." *J. Archit. Eng.* , 10.1061/(ASCE)AE.1943-5568.0000166 , B4014009.
- Bahmani, P., van de Lindt, J.W., Pryor, S.E., Mochizuki, G. L. (2014). “Performance-based Seismic Retrofit of Soft-Story Wood-frame Buildings Using Steel Special Moment Frames: Methodology and Full-Scale Experimental Validation”, *Engineering Structures*, 2015.
- Bahmani, P., van de Lindt, J.W., Pryor, S.E., Mochizuki, G., Gershfeld, M. and Park,S. (2014) “Performance-Based Seismic Retrofit Methodology of Soft-Story Woodframe Buildings with Full-Scale Shake Table Test Validation.”, *World Conference on Timber Engineering*, Quebec City, Canada, August 2014.
- Borzi, B., Calvi, G. M., Elnashai, A. S., Faccioli, E., and Bommer, J. J. (2001). “Inelastic spectra for displacement-based seismic design.” *Soil Dyn. Earthquake Eng.*, 21(1), 47–61.
- CAPSS, (2010). “A Community Action Plan for Seismic Safety”, Applied Technology Council (ATC), Redwood City, California.

- Chopra, A. K., and Goel, R. K. (1999). "Capacity-demand-diagram methods for estimating seismic deformation of inelastic structures: SDF systems." Rep. No. PEER-1999/02, Pacific Earthquake Engineering Research Center, Univ. of California, Berkeley, CA.
- Chopra, A.K. (2005) "Dynamics of Structures: Theory and Applications to Earthquake Engineering" *Prentice Hall*; 5 Edition.
- Christovasilis, I.P., Filiatrault, A., and Wanitkorkul, A. (2007). "Seismic testing of a full-scale two-story light-frame wood building: NEESWood benchmark test," NEESWood Report No. NW-01, Dept. of Civil, Structural and Environmental Engineering, University at Buffalo, State University of New York, Buffalo.
- Clough, R. W., and Penzien, J. (1975). Dynamics of structures, McGraw- Hill, New York, 239–41, 557–562.
- Dao, T. and van de Lindt, J. (2013). "Seismic Performance of an Innovative Light-Frame Cold-Formed Steel Frame for Midrise Construction." *J. Struct. Eng.* 139, *SPECIAL ISSUE: Cold-Formed Steel Structures*, 837–848.
- Ellingwood, B., Rosowsky, D. V., Li, Y., and Kim, J. H. (2004). "Fragility assessment of light-frame wood construction subjected to wind and earthquake hazards." *J. Struct. Eng.*, 130 (12), 1921–1930.
- FEMA, Federal Emergency Management Agency (2012), "Seismic Evaluation and Retrofit of Multi-Unit Wood-Frame Buildings With Weak First Stories - FEMA P-807, Washington, D.C.

FEMA, Federal Emergency Management Agency. (2009). "Quantification of Building Seismic Performance Factors, FEMA P-695". Washington, D.C.

Filiatrault, A, I. Christovasilis, A. Wanitkorkul, and J.W. van de Lindt. (2010). "Experimental Seismic Response of a Full-Scale Light-Frame Wood Building", *J. Struct. Eng.*, 136(3), 246-254.

Filiatrault, A., Fischer, D., Folz, B., and Uang C-M. (2002). "Seismic Testing of a Two-Story Woodframe House: Influence of Wall Finish Materials", *J. Struct. Eng.*, 128, No. 10, 1337-1345.

Filiatrault, A. and Folz, B. (2002). "Performance-Based Seismic Design of Wood Framed Buildings." *J. Struct. Eng.*, 128(1), 39–47.

Filiatrault, A., Fischer, D., Folz, B., and Uang, C.-M. (2002). "Seismic testing of two-story woodframe house. Influence of Wall Finish Materials." *J. Struct. Eng.*, 128-1, 1337-1345.

Folz, B. and Filiatrault, A. (2001). "Cyclic Analysis of Wood Shear Walls." *J. Struct. Eng.*, 127(4), 433–441.

Folz, B. and Filiatrault, A., (2004a). "Seismic Analysis of Woodframe Structures I: Model Formulation," *J. Struct. Eng.*, ASCE, 130(9):1353-1360.

Folz, B. and Filiatrault, A., (2004b). "Seismic Analysis of Woodframe Structures II: Model Implementation and Verification," *J. Struct. Eng.*, ASCE, 130 (9):1361-1370.

- Foschi, R. O. (2003). “Estimating reliability and implementing performance based design for shearwalls.” *Proc. of Structures Congress*, Seattle.
- Gulkan, P., and Sozen, M. A. (1974). “In-elastic responses of reinforced concrete structures to earthquake motions.” *Proc. ACI*, 71(12), 605–610.
- Hamburger R. O., (2002) “Performance Based Earthquake Engineering” *Proc. of Structures conference*, 2002.
- Hamburger, R. O., Hanson, R. D., Mahoney, M., Rojahn, C. “Performance-based design” *Modern Steel Construction*, v 42, n 6, June, 2002, p 55
- Kan, C. L., and Chopra, A. K. (1977a). “Elastic earthquake analysis of torsionally coupled multistory buildings.” *Earthquake Eng. Struct. Div.*, 5 , 395–412.9.
- Kim, J. H., and Rosowsky, D. V. (2005b). “Incorporating nonstructural finish effects and construction quality in a performance-based framework for wood shearwall design.” *Struct. Eng. Mech.*, 21(1), 83–100.
- Koshihara, M., Isoda, H., Minowa, C., and Sakamoto, I., (2004). “An Experimental Study On The Collapsing Process Of Wood Conventional Houses – Shaking Table Tests of Real-Size Models”, *Proceeding of 13Th WCEE*, Vancouver, B.C., Canada.
- Krawinkler, H., Parisi, F., Ibarra, L., Ayoub, A., and Medina, R., 2000-b. “Development of a Testing Protocol for Woodframe Structures” *CUREE Publication No. W-02*.

- Leelataviwat S., Goel S. C., and Stojadinovic B. (1999). "Toward Performance-Based Seismic Design of Structures.", *Earthquake Spectra*, August 1999, Vol. 15, No. 3, pp. 435-461.
- Mackie, K., and B. Stojadinovic (2003). Seismic Demands for Performance-Based Design of Bridges. PEER Report No. 2003/16, *Pacific Earthquake Engineering Research Center*, University of California Berkeley.
- Mosalam, K.M. and Mahin, S.A. (2007). "Seismic Evaluation and Retrofit of Asymmetric Multi-story Wood-frame Building," *Journal of Earthquake Engineering*, 11(6): 968-986.
- Mieler W. M., Stojadinovic B., Budnitz R. J., Mahin S. A., and Comerio M. C. (2013). "Toward Resilient Communities: A Performance-Based Engineering Framework for Design and Evaluation of the Built Environment", Pacific Earthquake Engineering Research Center, Report PEER 2013/19
- Miyake, T., Koshihara, M., Isoda, H., and Sakamoto, I., (2004), "An Analytical Study On Collapsing Behavior of Timber Structure House Subjected to Seismic Motion.", *Proceeding of 13Th WCEE*, Vancouver, B.C., Canada.
- NAHB (2009). Evaluation of Full-Scale House Testing Under Lateral Loading, Report #5822-03_01162009, NAHB Research Center, upper Marlboro, MD.
- Ozcelik, O., Luco, J. E., Conte, J. P., Trombetti, T. L., and Restrepo, J. I. (2008). "Experimental Characterization, Modeling and Identification of The NEES-UCSD Shake Table

- Mechanical System.” *Earthquake Engng Struct. Dyn.*; **37**:243–264 (DOI: 10.1002/eqe.754)
- Pang, W., Rosowsky, D., van de Lindt, J., and Pei, S. (2009). “Simplified Direct Displacement Design of Six-Story NEESWood Capstone Building and Pre-Test Seismic Performance Assessment.” NEESWood Report NW-05.
- Pang, W., Rosowsky, D., Pei, S., and van de Lindt, J. (2010). ”Simplified Direct Displacement Design of Six-Story Woodframe Building and Pretest Seismic Performance Assessment.” *J. Struct. Eng.*, 136(7), 813–825.
- Pang, W., and Rosowsky, D. (2008). “Performance-based seismic design of six-story woodframe structure.” *Struct. Eng. Int.*, 18(2), 179–185.
- Pang W. and Shirazi SMH., (2013). “Corotational model for cyclic analysis of light-frame wood shear walls and diaphragms,” *J. of Struct. Eng.*, 139 (8): 1303-1317.
- Pang, W. C., Rosowsky, D. V., Pei, S., and van de Lindt, J. W. (2007). “Evolutionary parameter hysteretic model for wood shearwalls.” *J. Struct. Eng.*, 10.1061/(ASCE)0733-9445(2007)133:8(1118), 1118–1129.
- Pang, W., Ziaei, E., and Filiatrault, A. (2012) “A 3D Model for Collapse Analysis of Soft-story Light-frame Wood Buildings,” *World Conference of Timber Engineering*, Auckland, New Zealand, July 2012.

Priestley, M.J.N. (1998). "Displacement-based approaches to rational limit states design of new structures." Keynote Address, *Proceedings of the 11th European Conference on Earthquake Engineering*, Paris, France.

Priestley, M. J. N. (1998). "Displacement-based approaches to rational limit states design of new structures." *Proc., 11th European Conf. on Earthquake Engineering, European Association of Earthquake Engineers*, Istanbul, Turkey.

Priestley, M. J. N. (2002). "Direct displacement-based design of precast/ prestressed concrete buildings." *PCI J.*, 47(6), 67–79.

Pei, S., J.W. van de Lindt, S.E. Pryor, H. Shimizu, H. Isoda, and D. Rammer. (2010). "Seismic Testing of a Full-Scale Mid-rise Building: The NEESWood Capstone Test.", NEESWood Project Report NW-04, 532pp. Available on-line at www.nees.org.

Pei, S., van de Lindt, J., and Popovski, M. (2013). "Approximate R-Factor for Cross-Laminated Timber Walls in Multistory Buildings." *J. Archit. Eng.*, 19(4), 245–255.

Pei, S., and van de Lindt, J.W. (2008). "SAPWood: Seismic Analysis Program for Woodframe Buildings.", Users Manual, available at www.nees.org.

Pei, S., and van de Lindt, J.W. (2009). "Coupled Shear-Bending Formulation for Seismic Analysis of Stacked Shear Wall Systems", *Earthquake Engineering and Structural Dynamics*, 38 (2009), 1631-1647.

- Pei, S. and van de Lindt, J.W. (2011). “Numerical Modeling of a Six-Story Light-Frame Wood Building: Comparison with Experiments.”, *Journal of Earthquake Engineering*, 15 (2011); 924-941.
- Popovski, M., Schneider, J., Schweinsteiger, M. (2010). “Lateral load resistance of cross laminated wood panels. “ *Proc. of the World Conference on Timber Engineering*, Riva del Garda, Italy.
- Pryor, S. E. and Murray, T. M. (2013) “Next generation partial strength steel moment frames for seismic resistance”. *Research, Development, and Practice in Structural Engineering and Construction*, pages 27–32, 2013.
- Rosowsky, D.V. (2002), “Reliability-Based Seismic Design of Wood Shearwalls,” *ASCE Journal of Structural Engineering*, 128(11):1439-1453.
- Rosowsky, D., and Ellingwood, B. (2002). “Performance-based engineering of wood frame housing: Fragility analysis methodology.” *J. Struct. Eng.*, 128 (1), 32–38.
- Sakamoto, I., Kawai, N., Tsuchimoto, T., and Minowa, C., (2002)“ Wood Building Collapse Tests Using E-Defense”. *Technical Memorandum of Public Works Research Institute*, No. 4022, pp. 87 (in Japanese), 2006.
- Shepherd, R., and Donald, R. A. H. (1967). “Seismic response of torsionally unbalanced buildings.” *J. Sound Vib.*, 6(1), 20–37.
- Silvia, P., and Badie, S. S., (2008). “Optimum Beam-to-Column Stiffness Ratio of Portal Frames under Lateral Loads.” *Structure Magazine*, March 2008.

- Tian, J., Symans, M.D., Gershfeld, M., Bahmani, P., van de Lindt, J.W. (2014). "Seismic Performance of a Full-Scale Soft-Story Woodframed Building with Energy Dissipation Retrofit," *Proc. of 10th National Conf. on Earthquake Engineering (10NCEE)*, Anchorage, AK, July 2014.
- Uang, C., Bertero, V. (1990). "Evaluation of Seismic Energy In Structures." *Earthquake Engineering and Structural Dynamics*, Vol. 19, 77-90.
- UBC, *Uniform Building Code*, International Conference of Building Officials, Whittier, CA, 1988.
- Vamvatsikos, D. and Cornell, C. A. (2002), Incremental dynamic analysis. *Earthquake Engng. Struct. Dyn.*, 31: 491–514. doi: 10.1002/eqe.141
- van de Lindt, J.W., D.V. Rosowsky, A. Filiatrault, M.D. Symans, R.A. Davidson. (2006). "The NEESWood Project: Progress on the Development of a Performance-Based Seismic Design Philosophy for Mid-Rise Woodframe Construction". *Proc of the 2006 World Conference on Timber Engineering*, Portland, OR.
- van de Lindt, J., Pei, S., and Liu, H. (2008). "Performance-Based Seismic Design of Wood Frame Buildings Using a Probabilistic System Identification Concept." *J. Struct. Eng.*, 134(2), 240–247.
- van de Lindt, J.W., Bahmani, P. , Gershfeld, M., Kandukuri, G., Rammer, D., and Pei, S. (2013), "Seismic Retrofit of Soft-Story Woodframe Buildings Using Cross Laminated Timber", *Proc. of ISEC-7*, Honolulu, June 18 –23, 2013.

- van de Lindt, J.W., Bahmani, P., Mochizuki, G.L., Pryor, S.E., Gershfeld, M., Tian, J., Symans, M.D., Rammer, D. (2014) “Experimental Seismic Behavior of a Full-Scale Four-Story Soft-Story Wood-frame Building with Retrofits II: Shake Table Test Results”, *ASCE J. Struct. Eng.*, DOI: 10.1061/(ASCE)ST.1943-541X.0001206.
- van de Lindt, J.W., Rosowsky, D.V., Filiatrault, A., Symans, M.D., Davidson, R.A. (2006). “The NEESWood Project: Progress on the Development of a Performance-Based Seismic Design Philosophy for Mid-Rise Woodframe Construction”. *Proc of the 2006 World Conference on Timber Engineering*, Portland, OR.
- van de Lindt, J., Pei, S., Liu, H., and Filiatrault, A. (2010). ”Three-Dimensional Seismic Response of a Full-Scale Light-Frame Wood Building: Numerical Study.” *J. Struct. Eng.*, 136(1), 56–65.
- van de Lindt, J.W., Pei, S., Pryor, S. E., Shimizu, H., and Isoda, H. (2010). “Experimental seismic response of a full-scale six-story light-frame wood building.” *J. Struct. Eng.*, 10.1061/(ASCE)ST.1943-541X .0000222, 1262–1272.
- van de Lindt, J.W., S.E. Pryor, and S. Pei. (2011). “Shake Table Testing of a Full-Scale Seven-Story Steel-Wood Apartment Building”, *Engineering Structures*, 33(3), 757-766.
- van de Lindt, J.W., Symans, M.D., Pang, W., Shao, X. and Gershfeld, M. (2012). “The NEES-Soft project: Seismic Risk Reduction for Soft-Story Woodframe Buildings.”, *15th World Conference on Earthquake Engineering*, September 24-28, Lisbon, Portugal.

van de Lindt, J.W., D.V. Rosowsky, W. Pang, and S. Pei (2013). "Performance-Based Seismic Design of Midrise Woodframe Buildings.", *Journal of Structural Engineering*, 139 (8), 1294-1302.

van de Lindt, "Personal Communication, 2014, Jan 15".

Wang, Y., Rosowsky, D. V., Pang W. C. (2010). "Performance-Based Procedure for Direct Displacement Design of Engineered Wood-Frame Structures." *ASCE Journal of Structural Engineering*, Vol. 136(8), 978-988.

Wilkinson, J. H. (1965). "Perturbation theory." Algebraic eigenvalue problem, Clarendon Press, Oxford, U.K., 62–71.

Whittaker, A., Constantinou, M., and Tsopelas, P. (1998). "Displacement Estimates for Performance-Based Seismic Design." *J. Struct. Eng.*, 124(8), 905–912.

APPENDICES

Appendix A

In general, the equation of motion for an undamped uncouple system can be expressed as (Kan and Chopra, 1977)

$$\begin{bmatrix} M & & \\ & M & \\ & & M \end{bmatrix} \begin{bmatrix} \ddot{U}_x \\ \ddot{\tilde{U}}_\theta \\ \ddot{U}_y \end{bmatrix} + \begin{bmatrix} K_{xx} & K_{x\theta} & 0 \\ K_{x\theta}^T & K_{\theta\theta} & K_{y\theta}^T \\ 0 & K_{y\theta} & K_{yy} \end{bmatrix} \begin{bmatrix} U_x \\ \tilde{U}_\theta \\ U_y \end{bmatrix} = \begin{bmatrix} -M \bar{1} \ddot{U}_{gx} \\ 0 \\ -M \bar{1} \ddot{U}_{gy} \end{bmatrix} \quad (\text{A- 1})$$

where, U_x , \tilde{U}_θ , and U_y are the displacement sub-vectors. \ddot{U}_{gx} and \ddot{U}_{gy} are ground acceleration sub-vectors in the X – and Y – directions, respectively. M and K are mass and stiffness sub-matrices, respectively. The sub-matrices and sub-vectors are

$$U_x = \begin{bmatrix} u_{1x} \\ u_{2x} \\ \dots \\ \dots \\ u_{nx} \end{bmatrix}; \tilde{U}_\theta = \begin{bmatrix} r_1 u_{1\theta} \\ r_2 u_{2\theta} \\ \dots \\ \dots \\ r_n u_{n\theta} \end{bmatrix}; U_y = \begin{bmatrix} u_{1y} \\ u_{2y} \\ \dots \\ \dots \\ u_{ny} \end{bmatrix} \quad (\text{A- 2})$$

where r_i is the radius of gyration of i^{th} floor about a vertical axis through the center of mass of the floor. The mass sub-matrix, M , is

$$M = \begin{bmatrix} m_1 & & & \\ & m_2 & & \\ & & \dots & \\ & & & \dots \\ & & & & m_n \end{bmatrix} \quad (\text{A- 3})$$

where m_i is the mass of the i^{th} floor; and column vector $\bar{1}$ is a unit vector to match the dimensions of the matrices. Then, the stiffness sub-matrices can be expressed as:

$$K_{xx} = \begin{bmatrix} K_{x1} + K_{x2} & -K_{x2} & & & \\ -K_{x2} & K_{x2} + K_{x3} & -K_{x3} & & \\ & -K_{x3} & K_{x3} + K_{x4} & & \\ & & & \ddots & -K_{xn} \\ & & & -K_{xn} & K_{xn} \end{bmatrix} \quad (\text{A- 4})$$

$$K_{yy} = \begin{bmatrix} K_{y1} + K_{y2} & -K_{y2} & & & \\ -K_{y2} & K_{y2} + K_{y3} & -K_{y3} & & \\ & -K_{y3} & K_{y3} + K_{y4} & & \\ & & & \ddots & -K_{yn} \\ & & & -K_{yn} & K_{yn} \end{bmatrix} \quad (\text{A- 5})$$

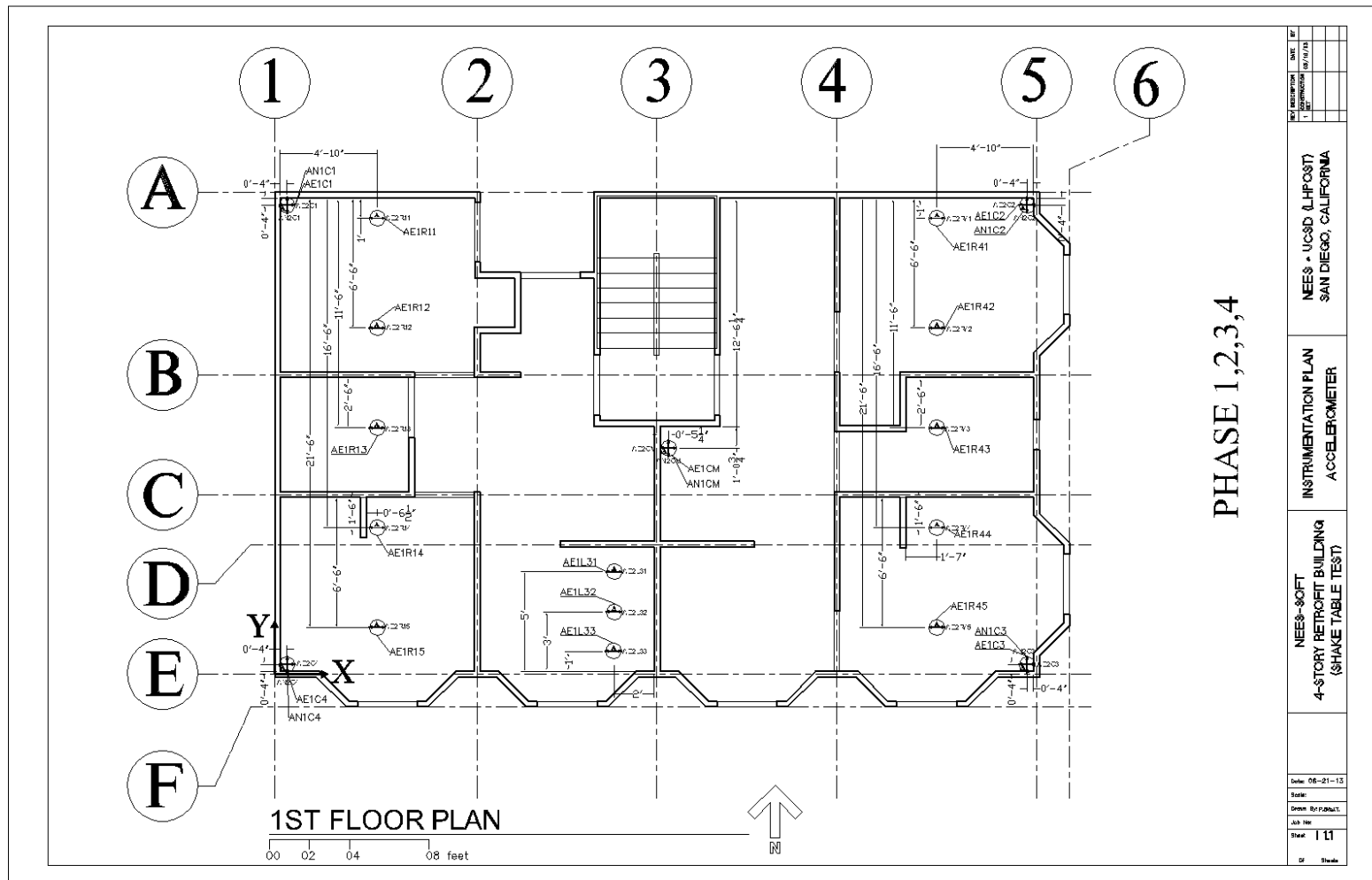
$$K_{\theta\theta} = \begin{bmatrix} \left(\frac{1}{r_1}\right)^2 (K_{\theta1} + K_{\theta2}) & -\left(\frac{1}{r_1 r_2}\right) K_{\theta2} & & & \\ -\left(\frac{1}{r_1 r_2}\right) K_{\theta2} & \left(\frac{1}{r_2}\right)^2 (K_{\theta2} + K_{\theta3}) & -\left(\frac{1}{r_2 r_3}\right) K_{\theta3} & & \\ & -\left(\frac{1}{r_2 r_3}\right) K_{\theta3} & \ddots & \ddots & \\ & & \ddots & \ddots & \\ & & & -\left(\frac{1}{r_{n-1} r_n}\right) K_{\theta n} & \left(\frac{1}{r_n}\right)^2 K_{\theta n} \end{bmatrix} \quad (\text{A- 6})$$

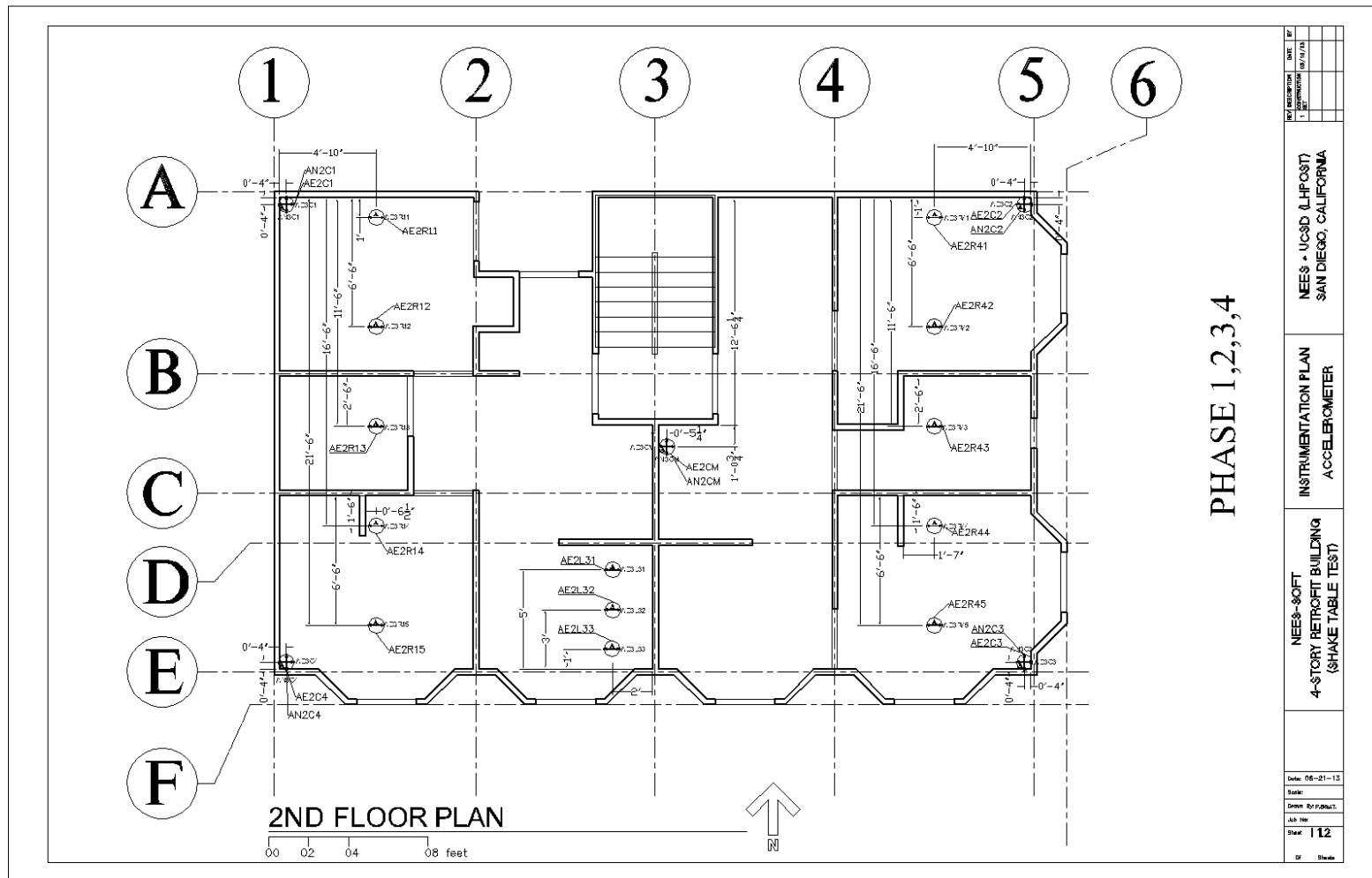
$$K_{x\theta} = - \begin{bmatrix} \left(\frac{1}{r_1}\right)(e_{y1}K_{x1} + e_{y2}K_{x2}) & -\left(\frac{1}{r_2}\right)e_{y2}K_{x2} & & & \\ -\left(\frac{1}{r_1}\right)e_{y2}K_{x2} & \left(\frac{1}{r_2}\right)(e_{y2}K_{x2} + e_{y3}K_{x3}) & \ddots & & \\ & & \ddots & \ddots & \\ & & & \ddots & \\ & & & & -\left(\frac{1}{r_{n-1}}\right)e_{yn}K_{xn} & \left(\frac{1}{r_n}\right)e_{yn}K_{xn} \end{bmatrix} \quad (\text{A- 7})$$

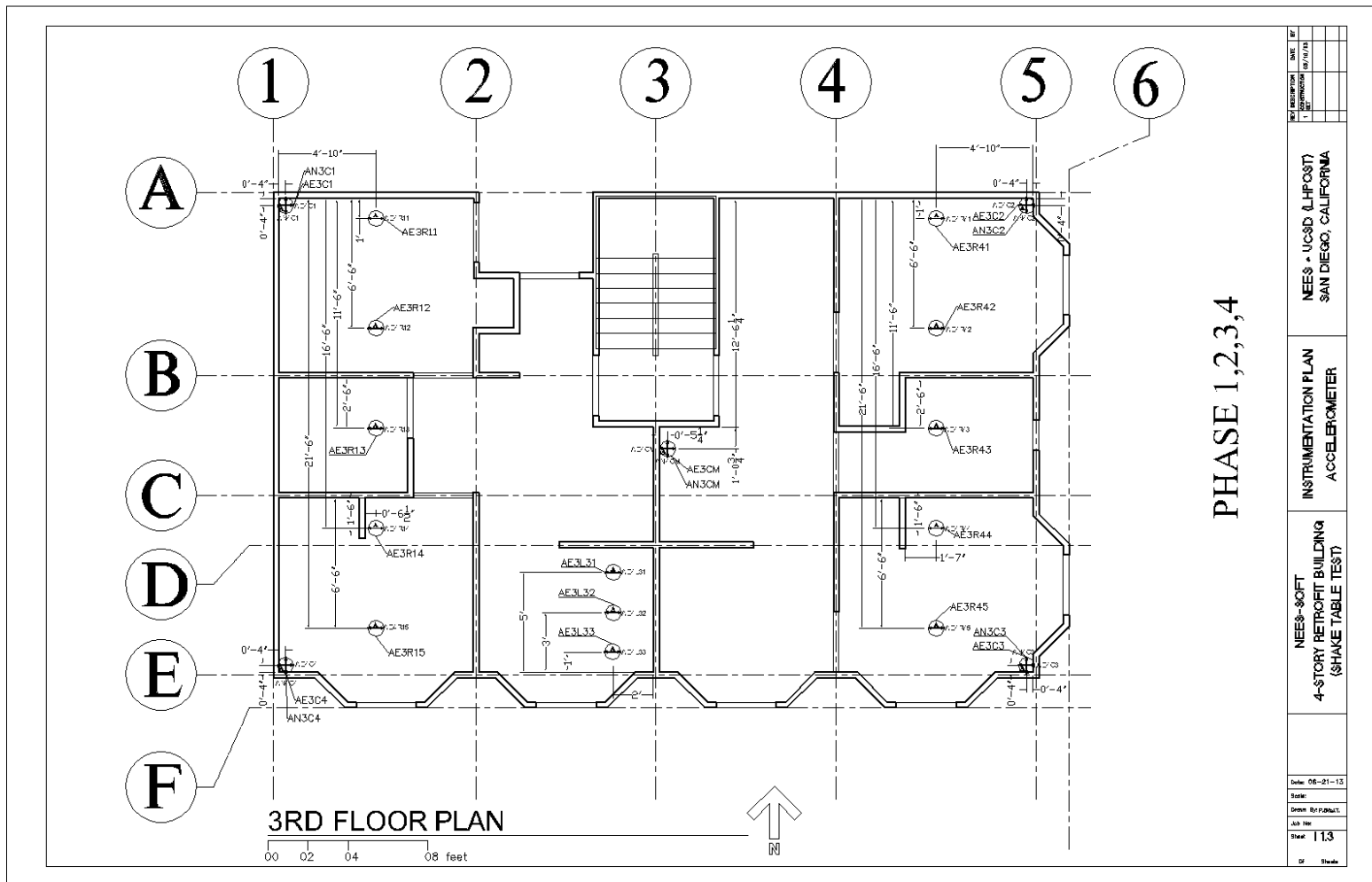
$$K_{y\theta} = \begin{bmatrix} \left(\frac{1}{r_1}\right)(e_{x1}K_{y1} + e_{x2}K_{y2}) & -\left(\frac{1}{r_2}\right)e_{x2}K_{y2} & & & \\ -\left(\frac{1}{r_1}\right)e_{x2}K_{y2} & \left(\frac{1}{r_2}\right)(e_{x2}K_{y2} + e_{x3}K_{y3}) & \ddots & & \\ & & \ddots & \ddots & \\ & & & \ddots & \\ & & & & -\left(\frac{1}{r_{n-1}}\right)e_{xn}K_{yn} & \left(\frac{1}{r_n}\right)e_{xn}K_{yn} \end{bmatrix} \quad (\text{A- 8})$$

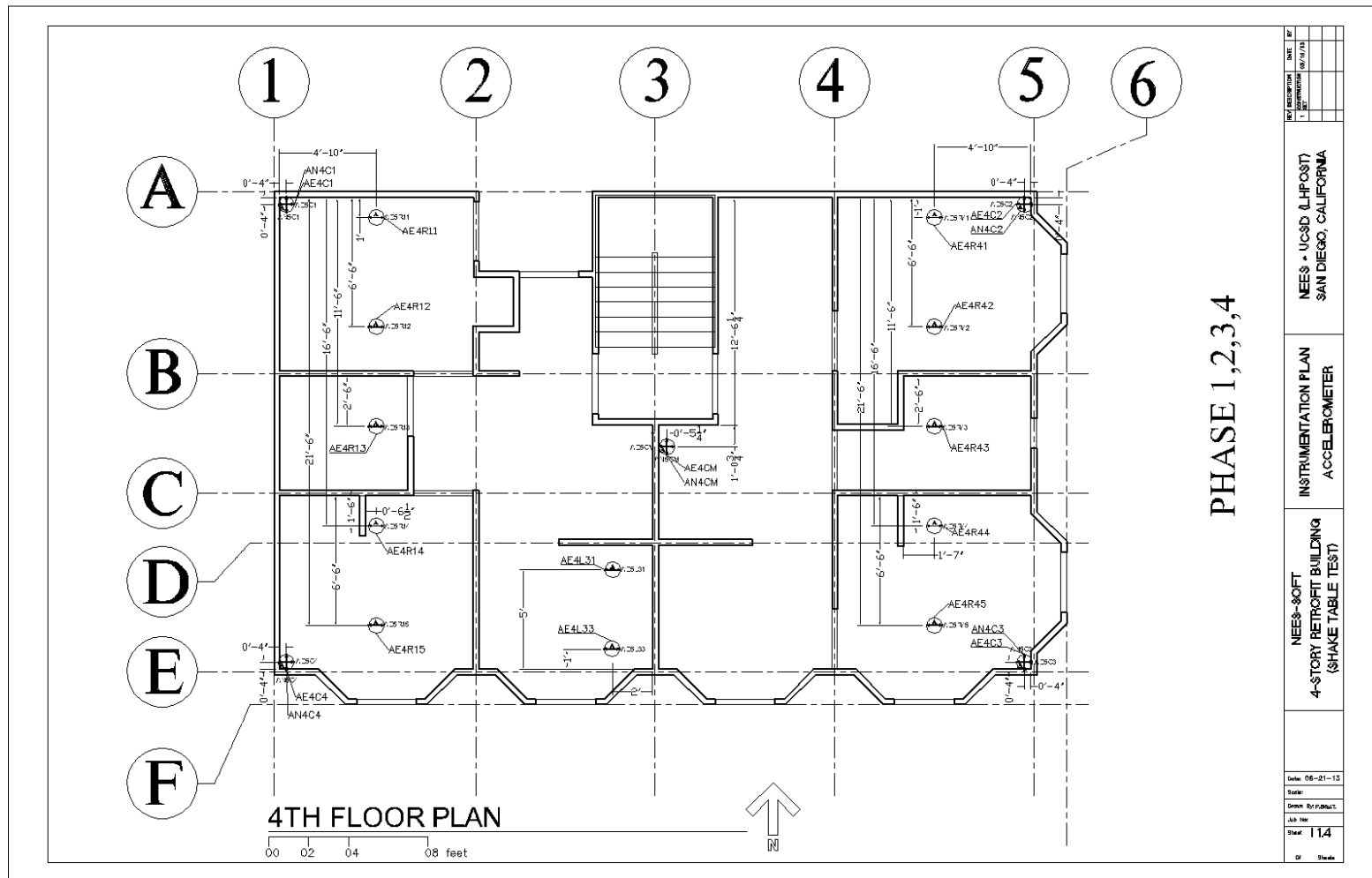
Appendix B: Instrumentation Plan for the Four-Story Wood-Frame Building

Accelerometers

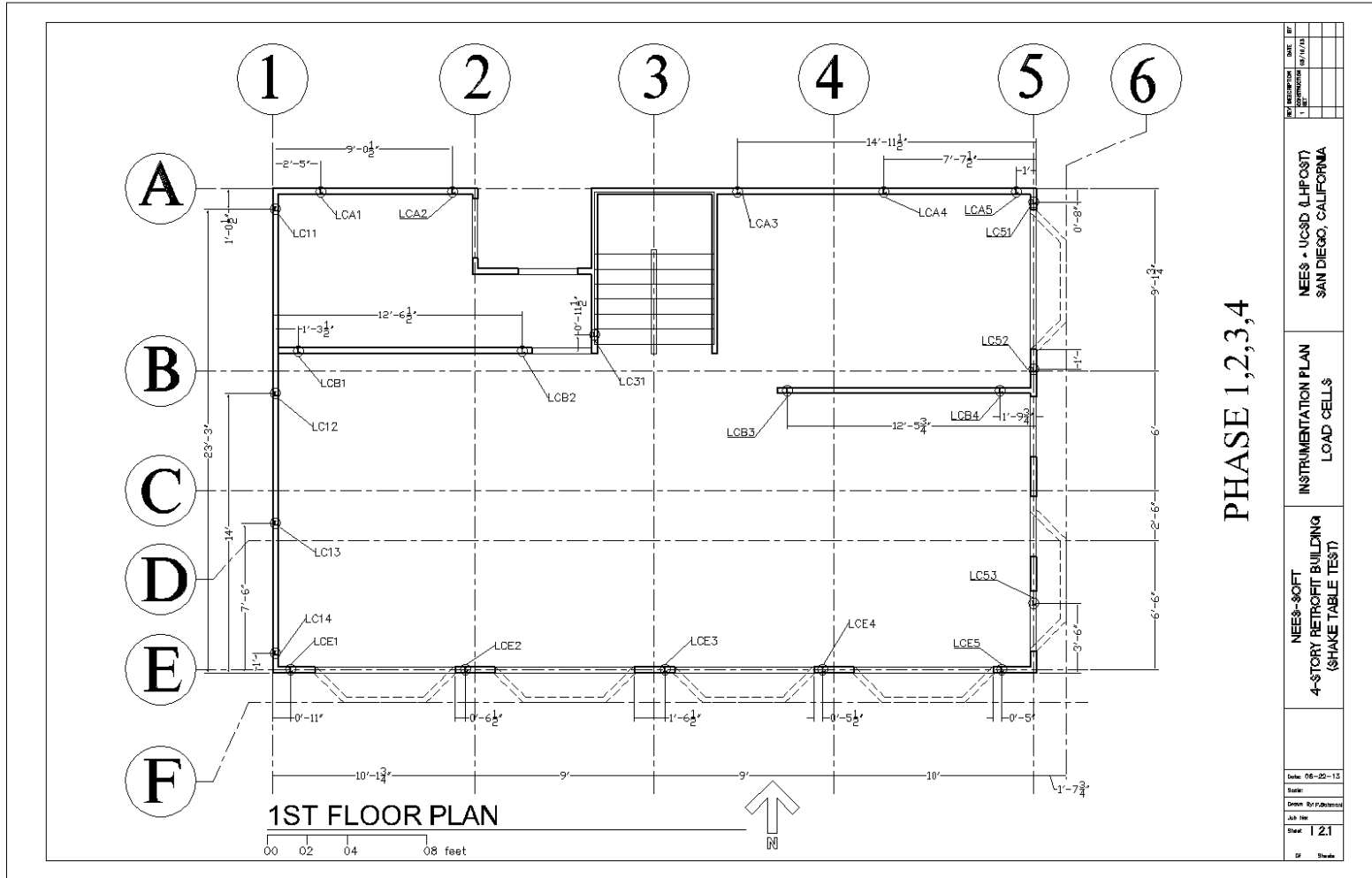




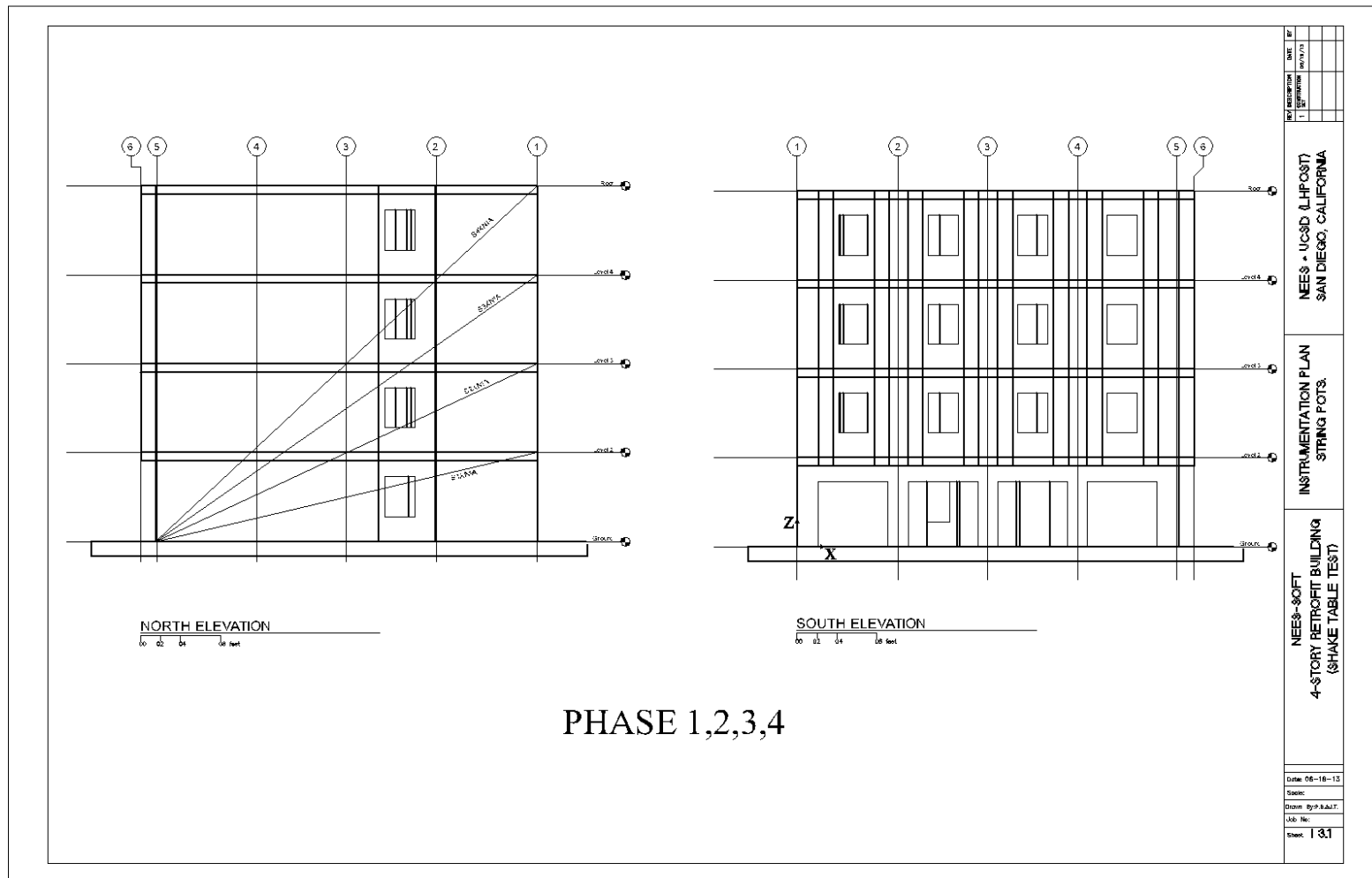


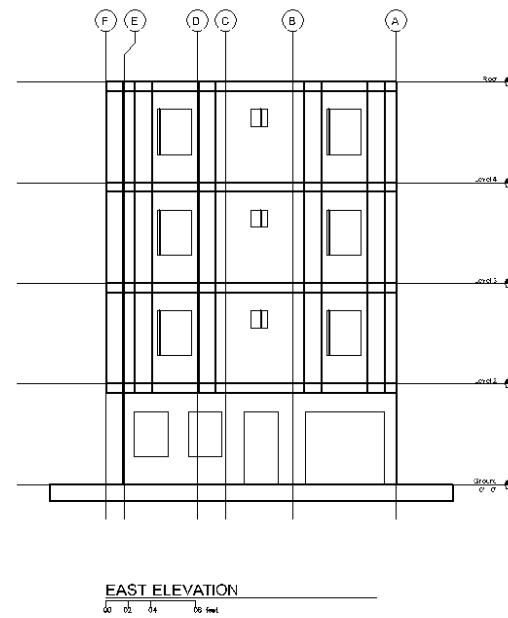
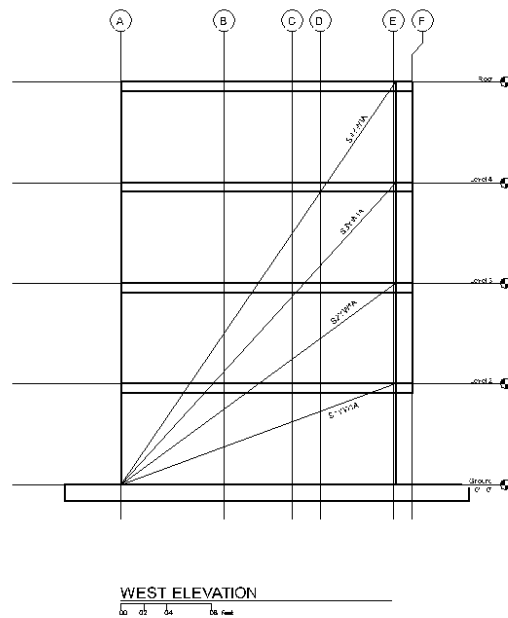


Load Cells



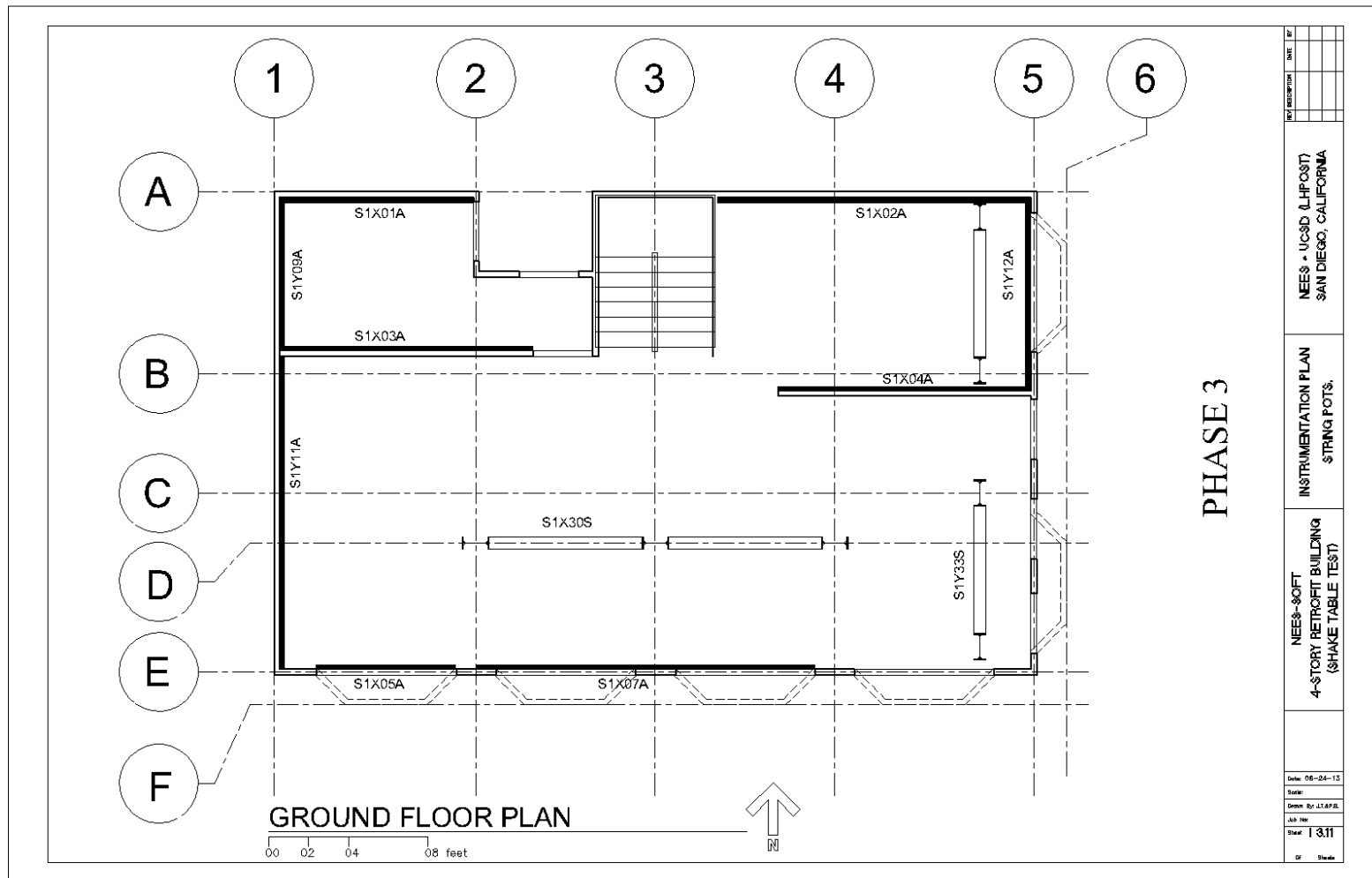
String Potentiometers

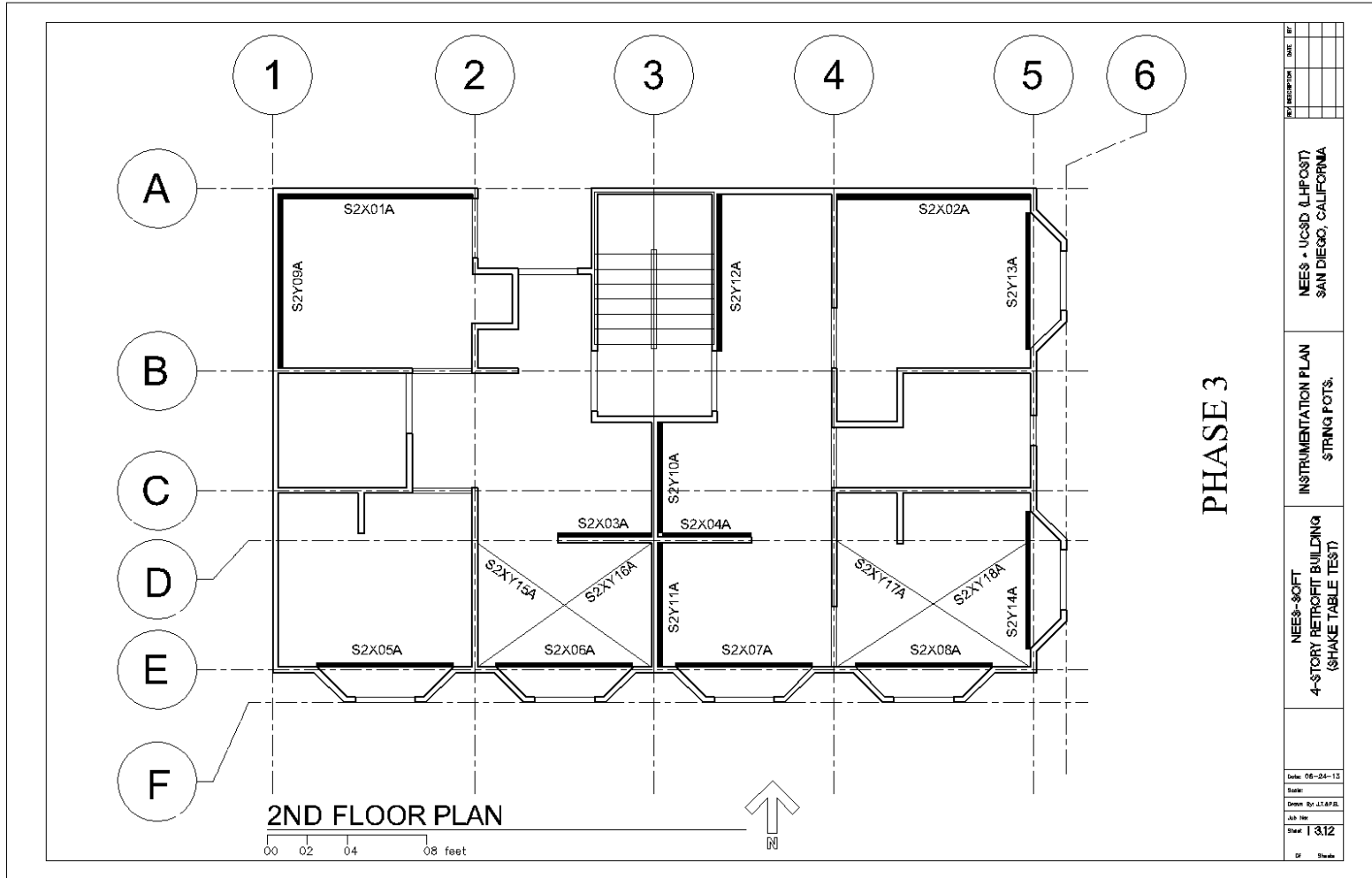


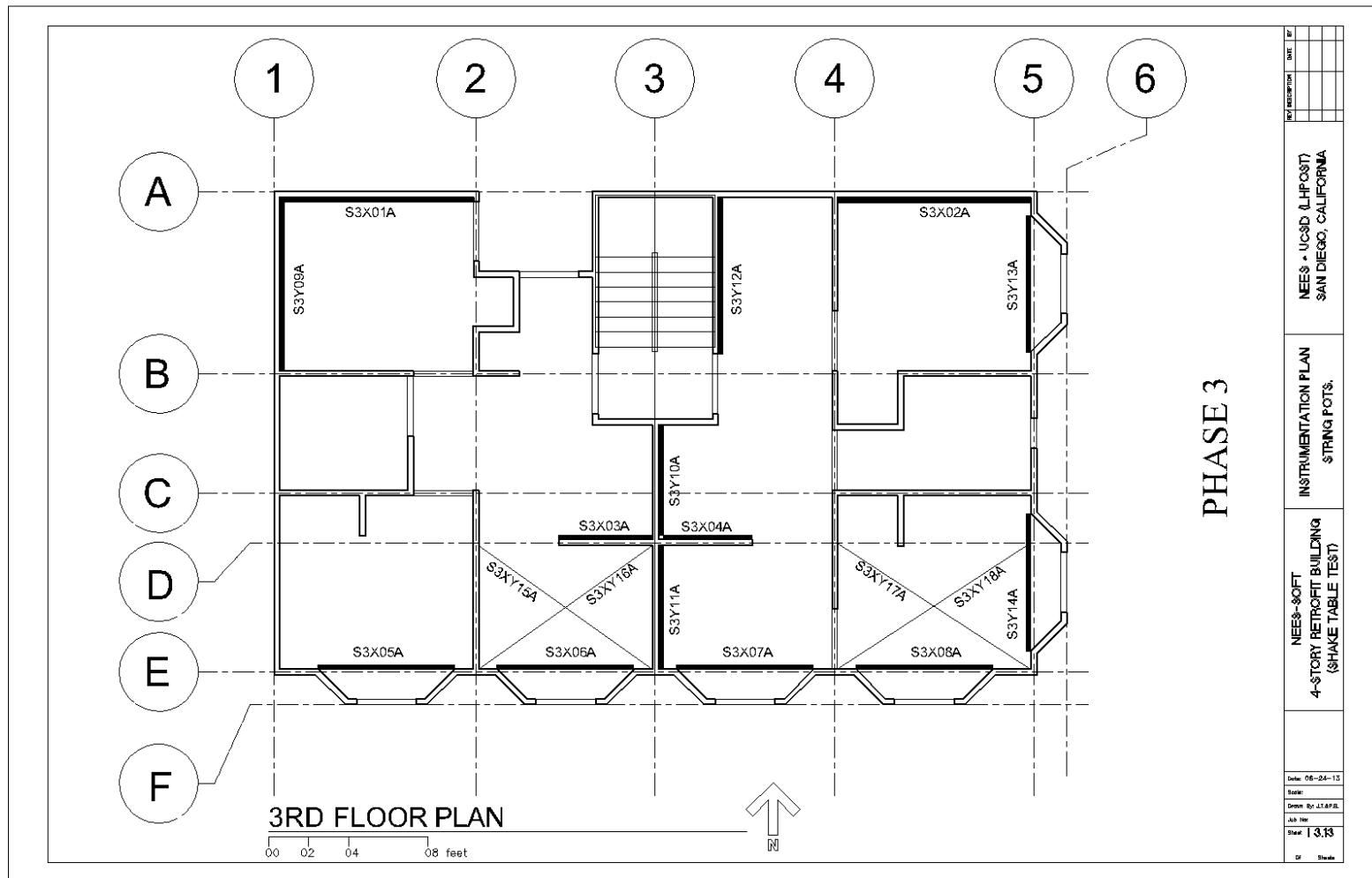


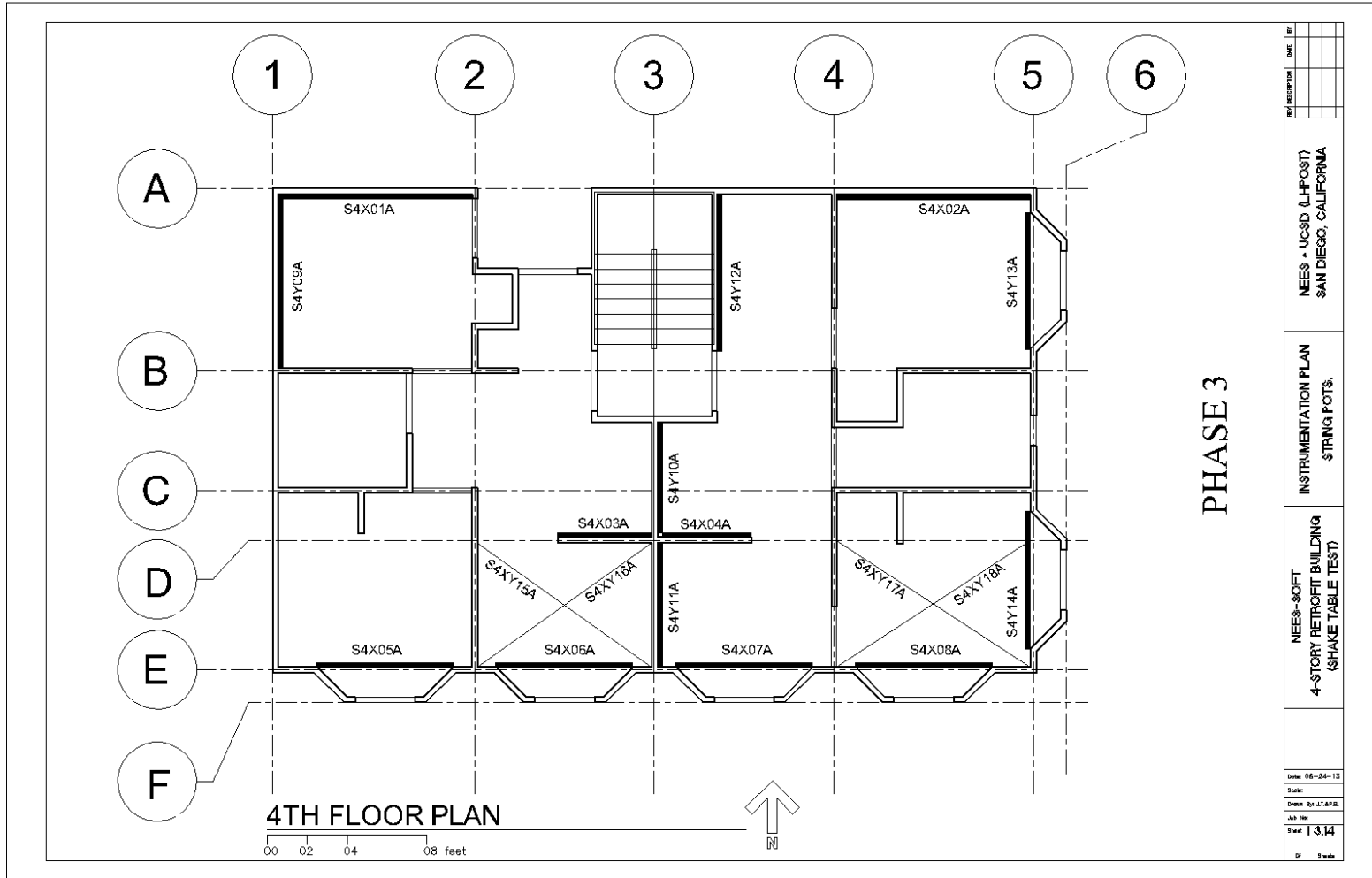
PHASE 1,2,3,4

Rev	Description	Date	By
1	Issued for construction	10/1/13	WJH
NEES - UCSB (LHPOST)			
SAN DIEGO, CALIFORNIA			
INSTRUMENTATION PLAN			
STRING POTS			
NEES-SOFT			
4-STORY RETROFIT BUILDING			
(SHAKE TABLE TEST)			
Cutset 06-16-13			
Scale:			
Drawn By: P. B. J. T.			
Job No:			
Sheet 13.2			

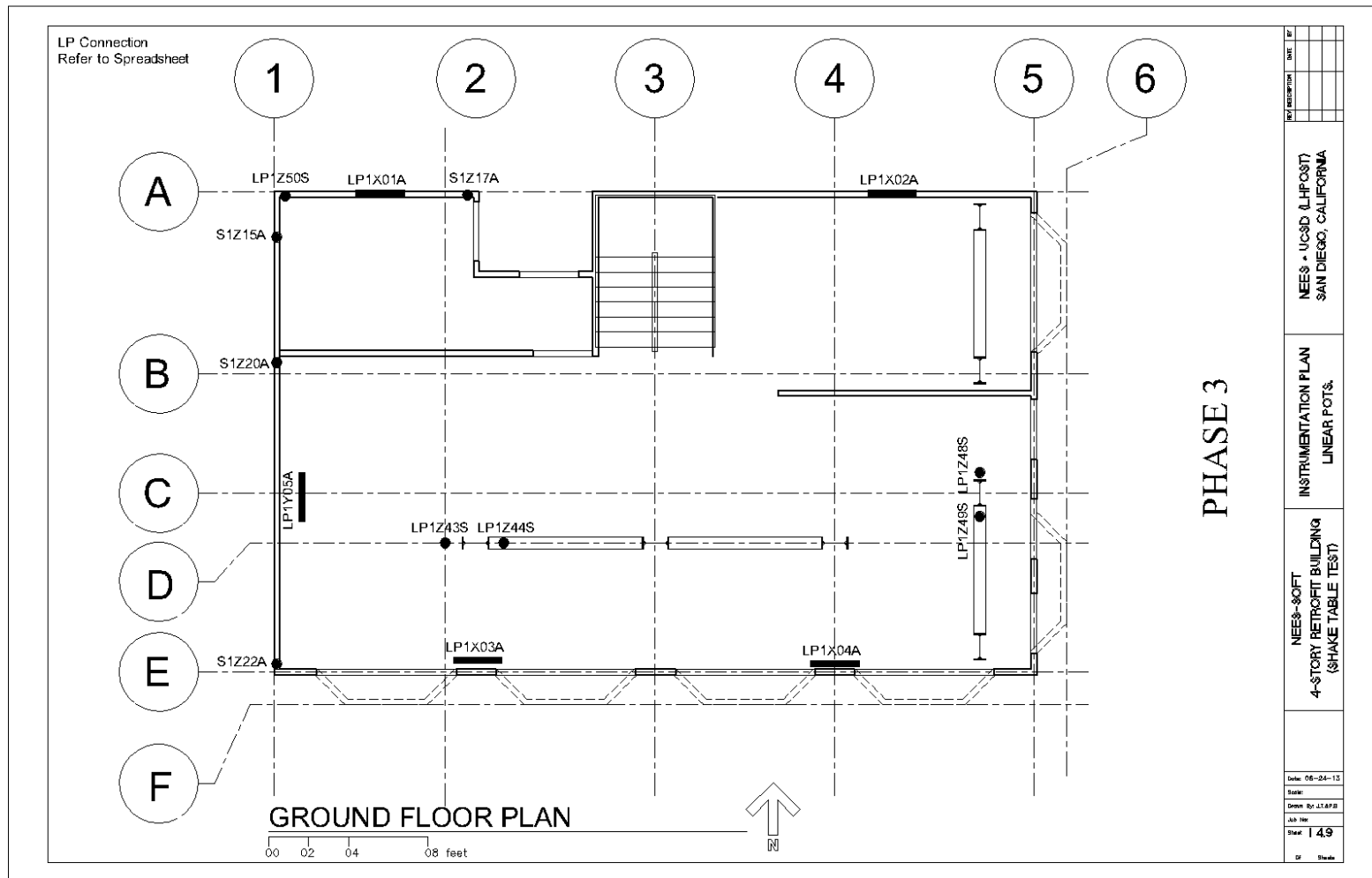


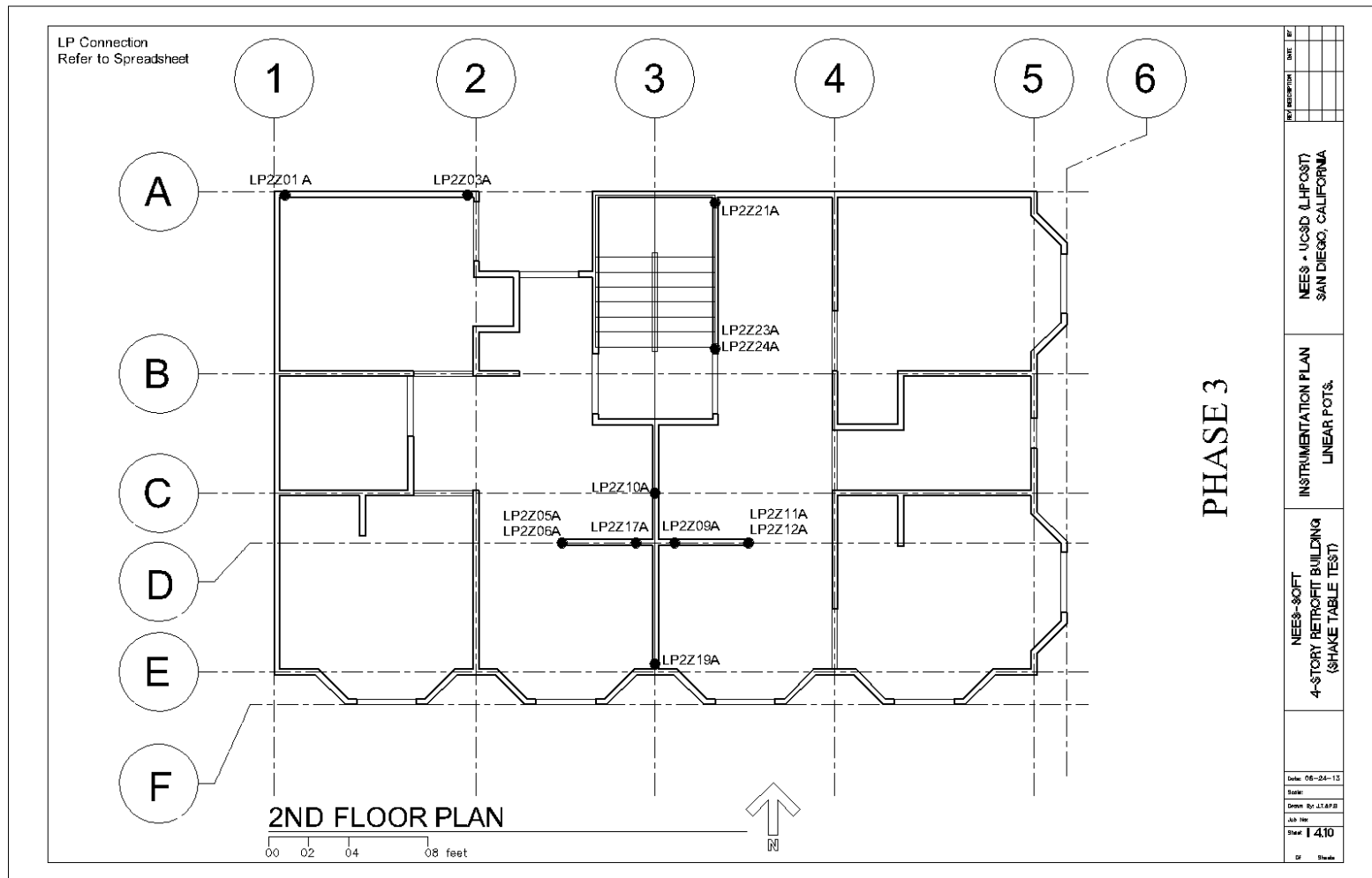


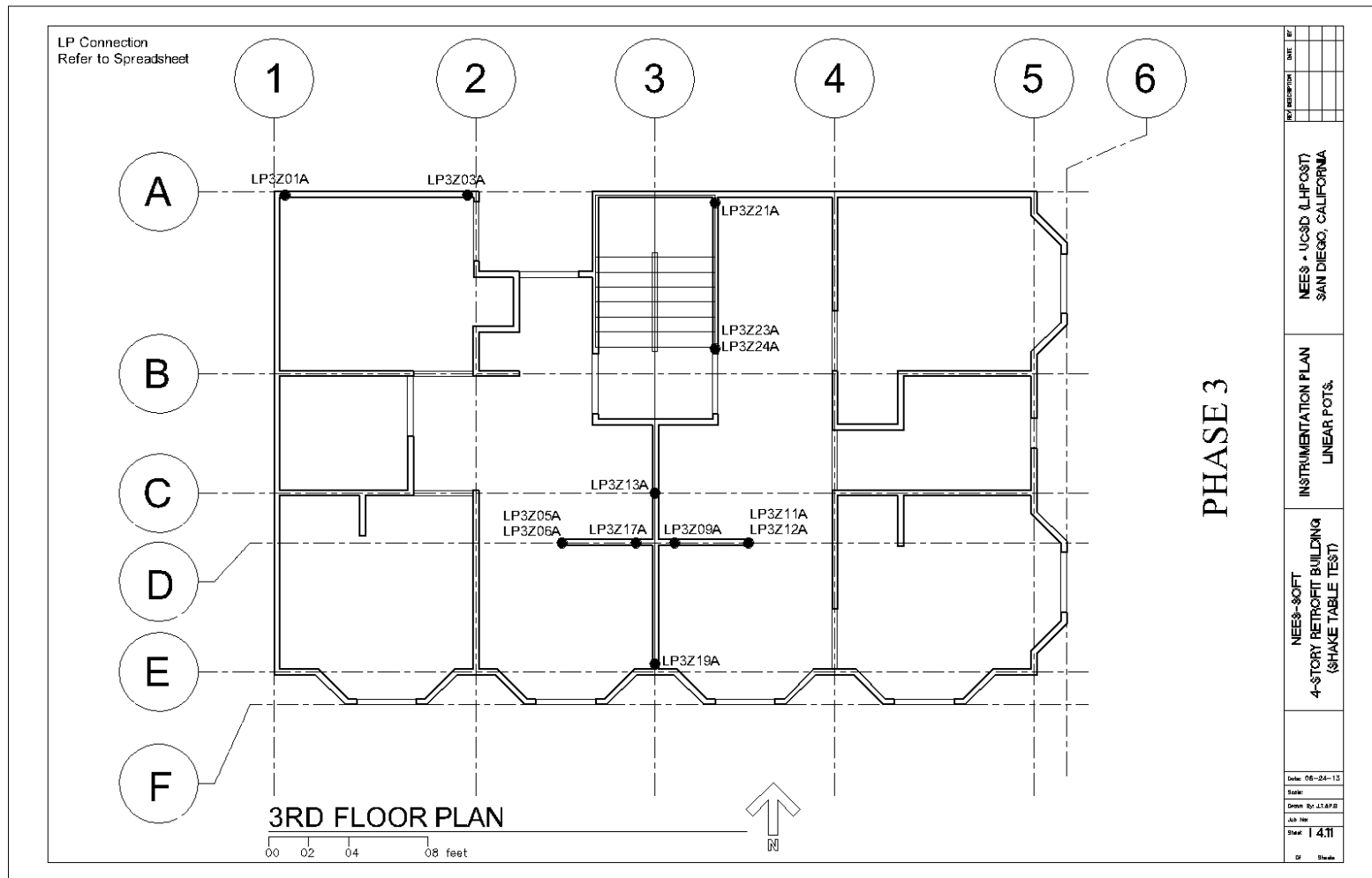


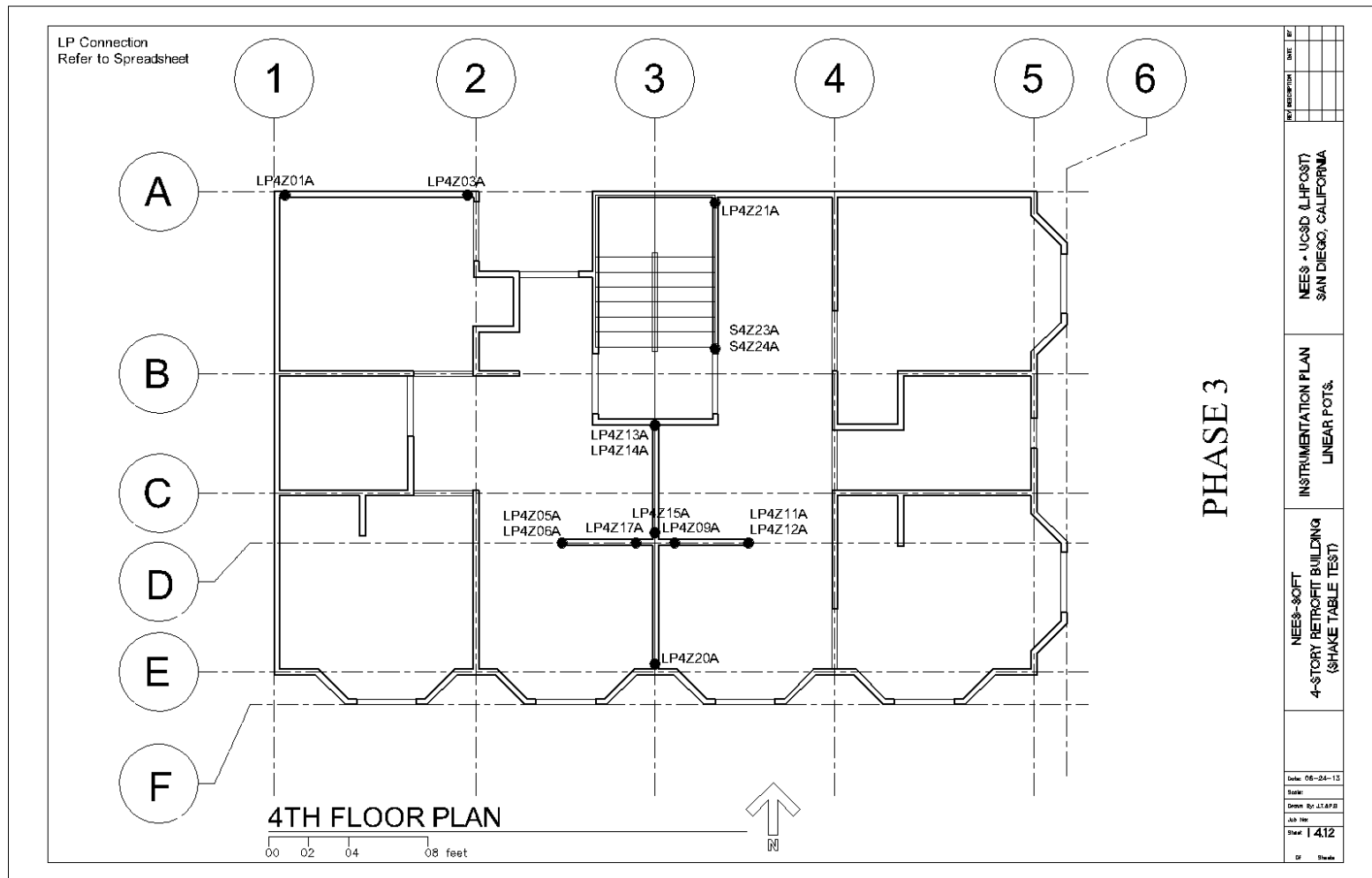


Linear potentiometers

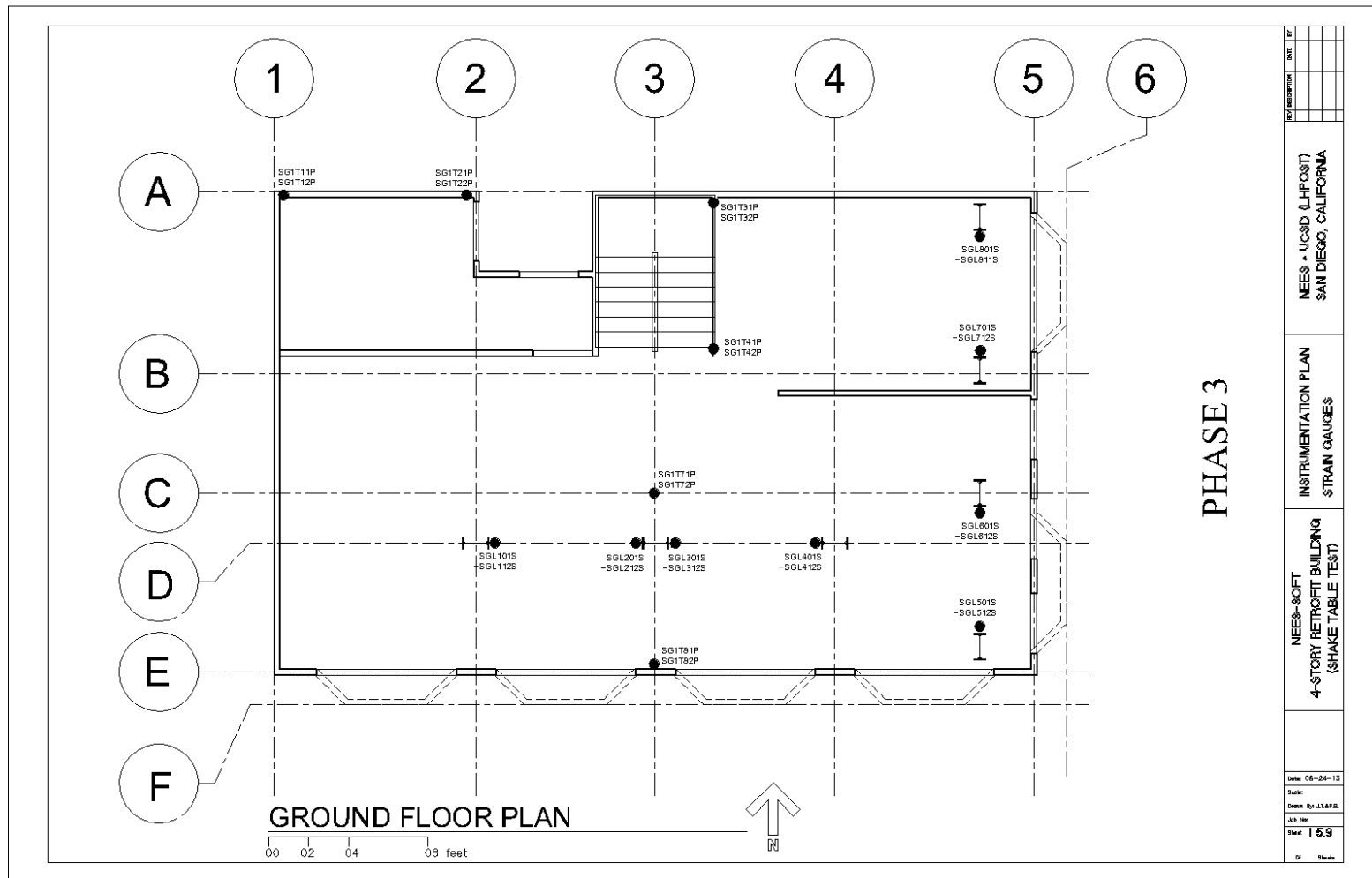


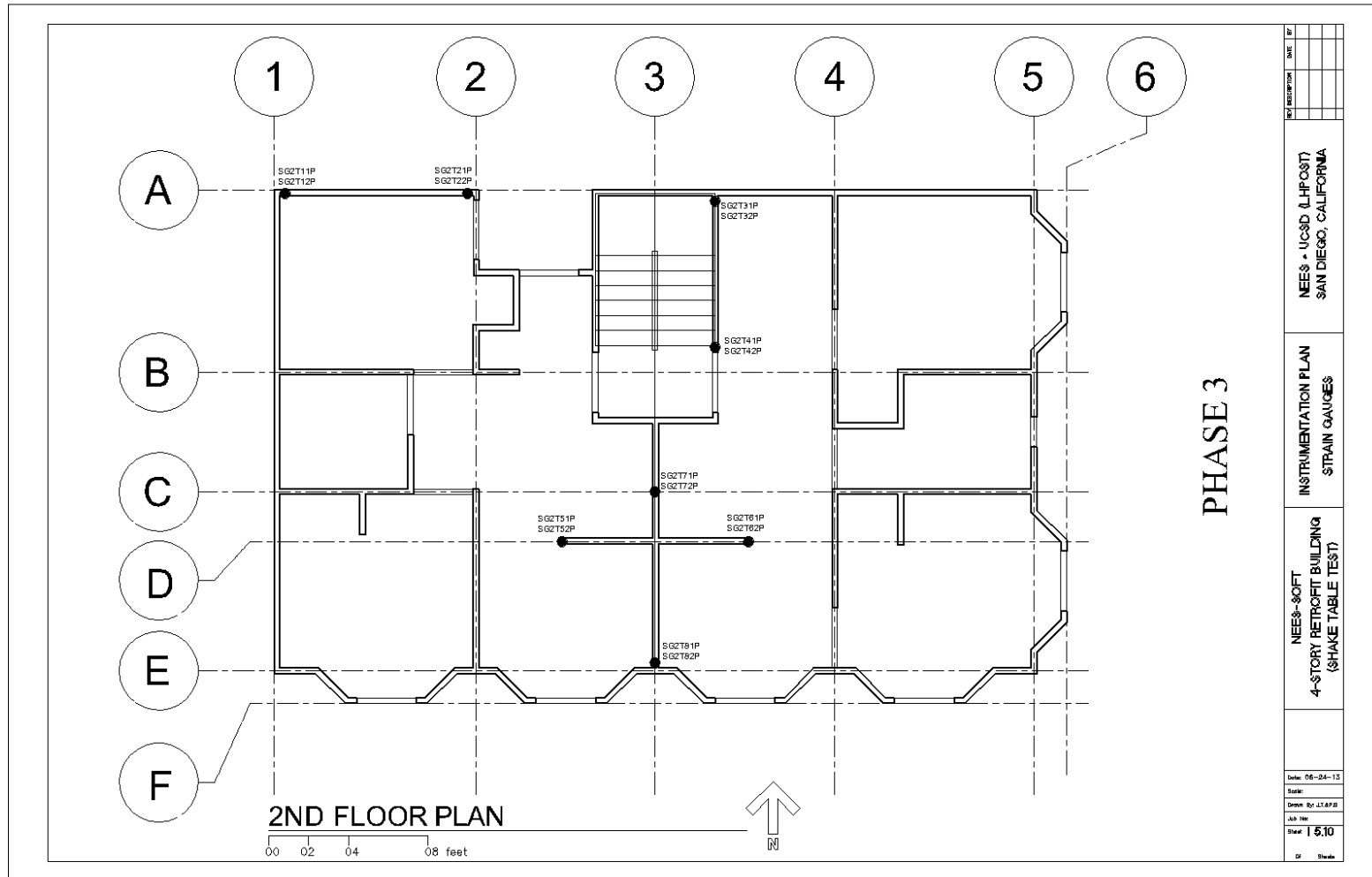


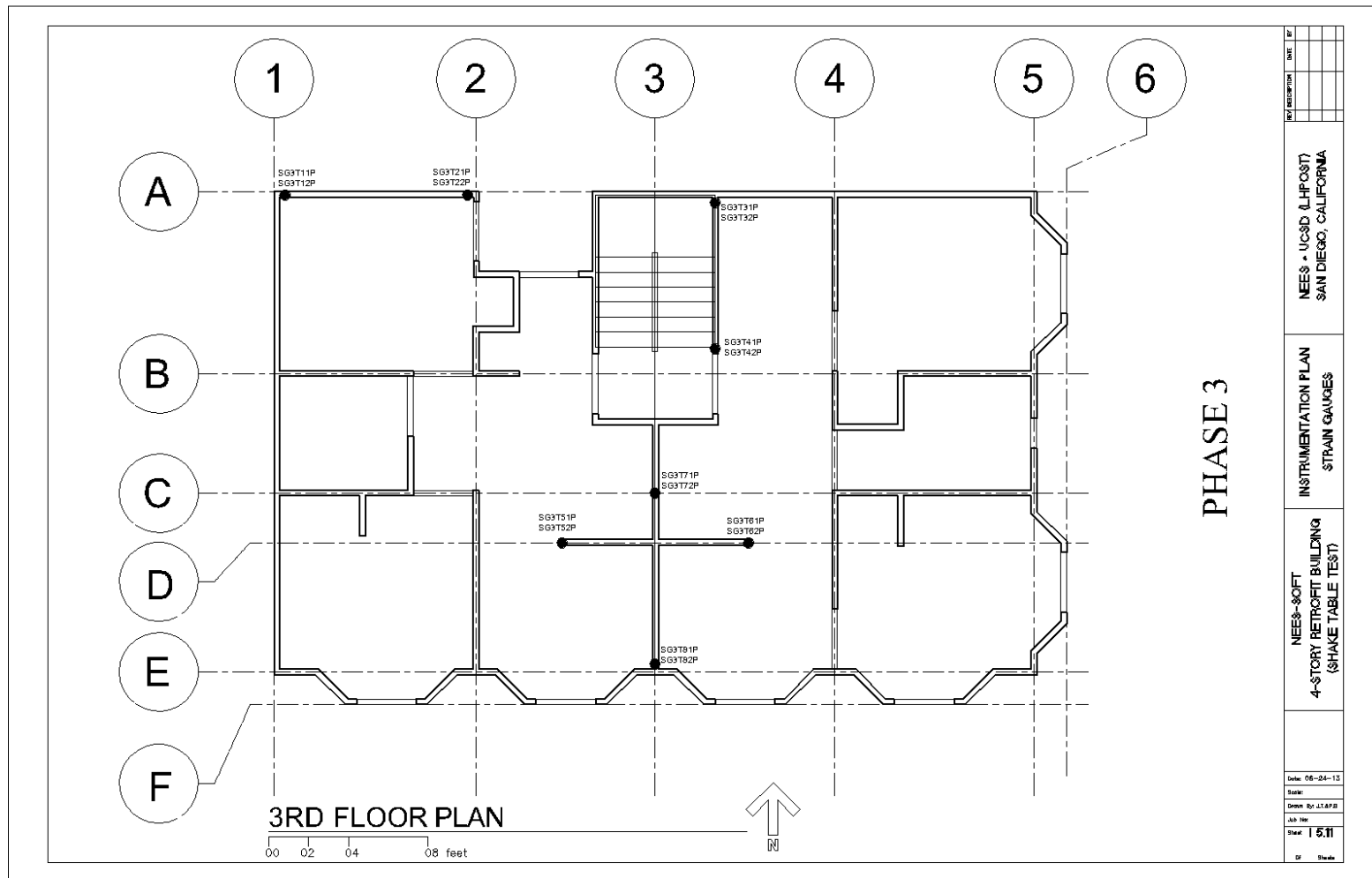


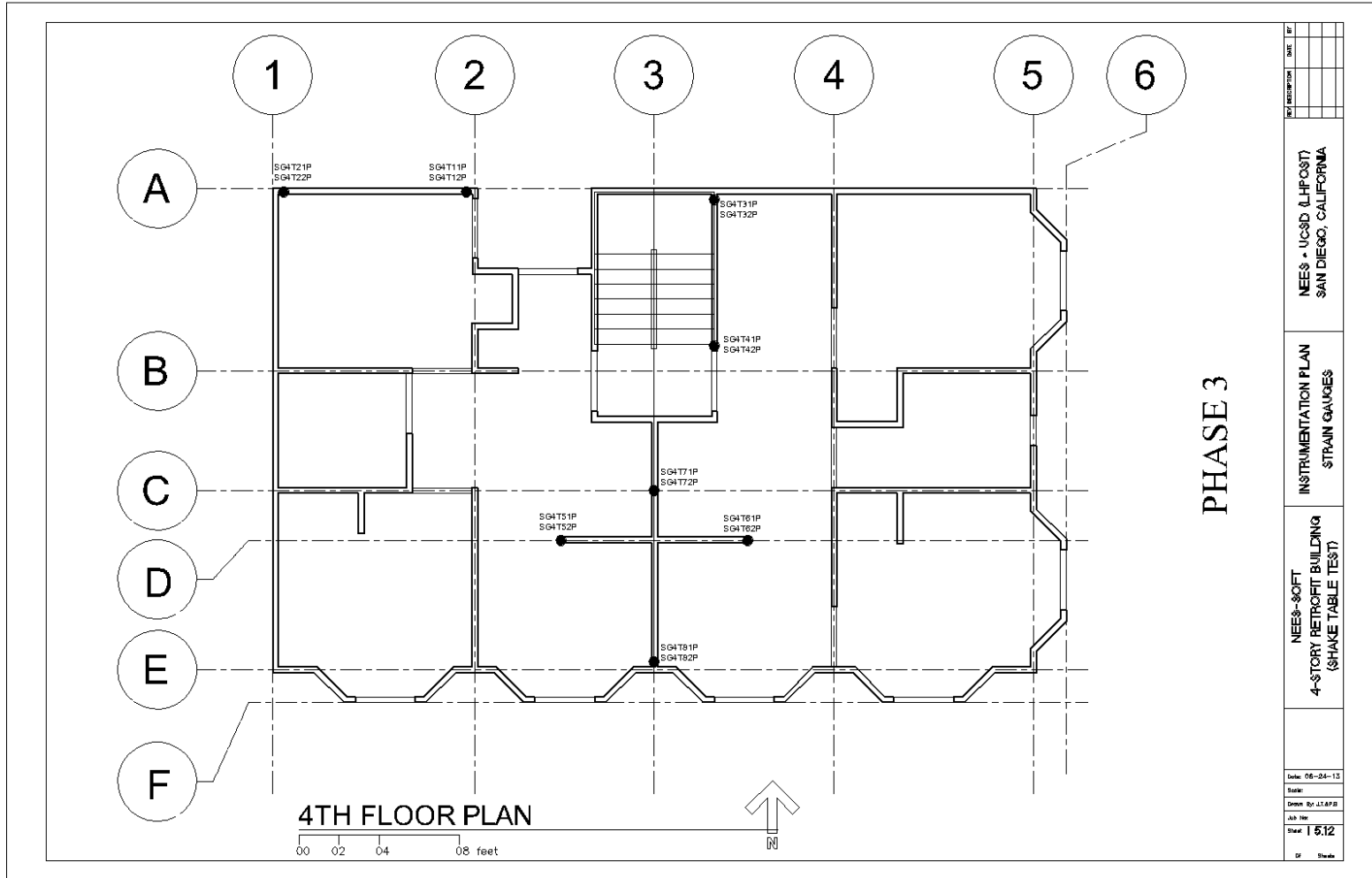


Strain Gauges

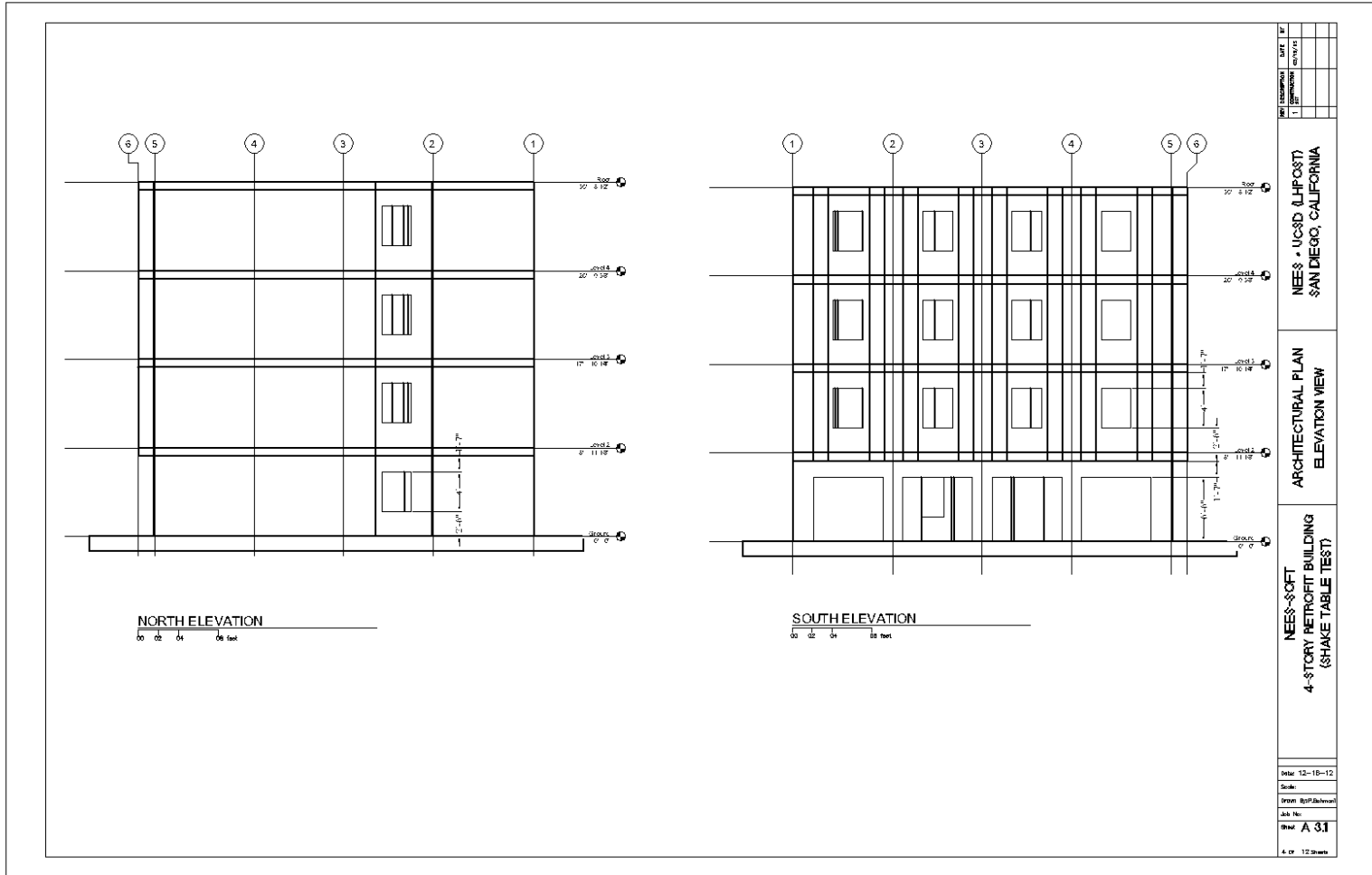


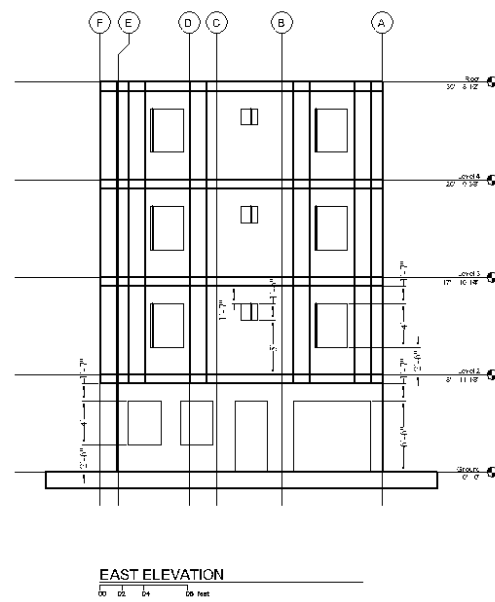
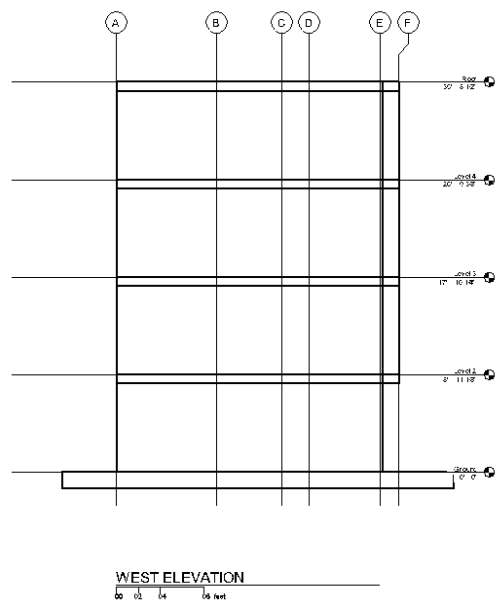




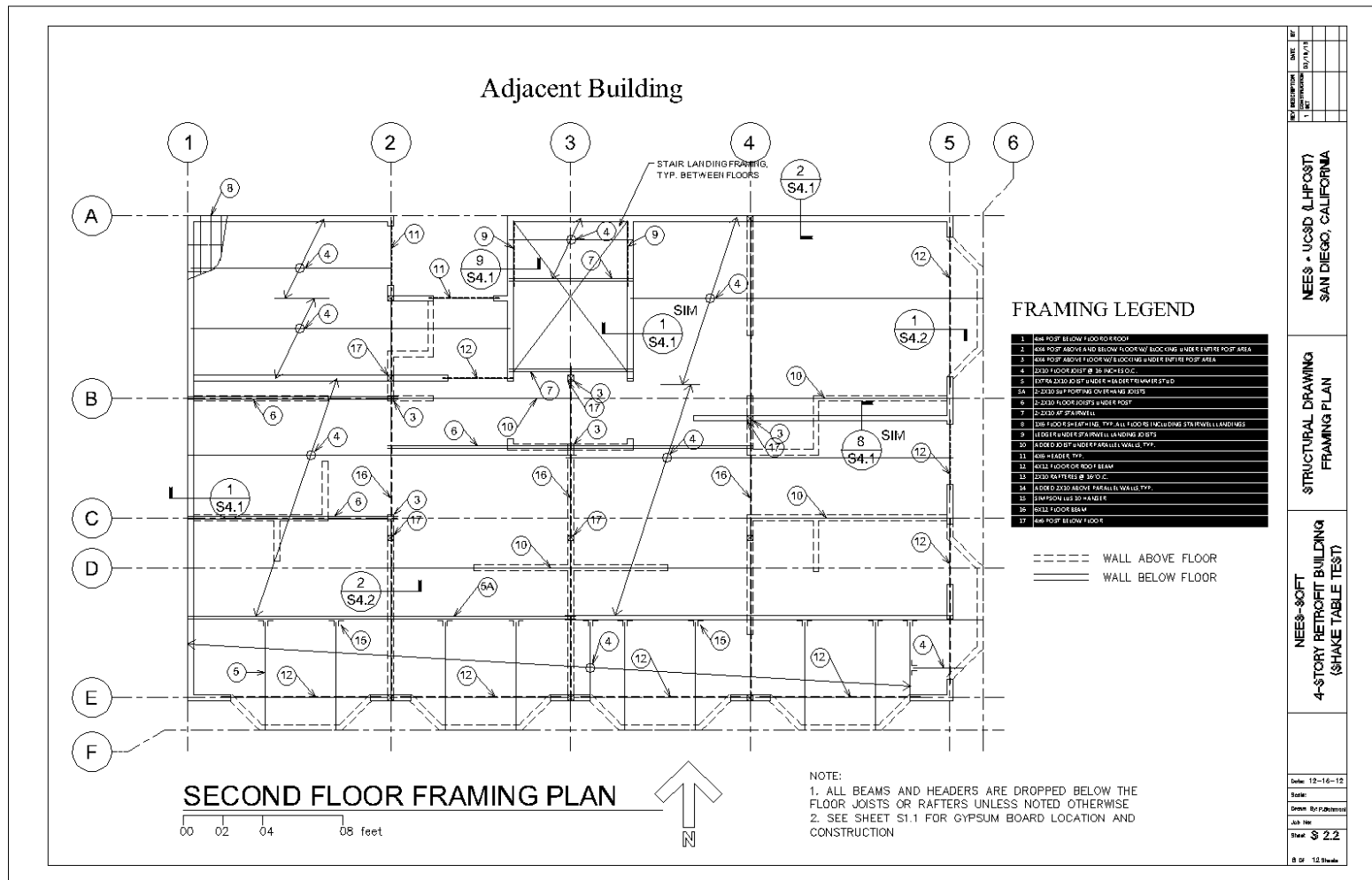


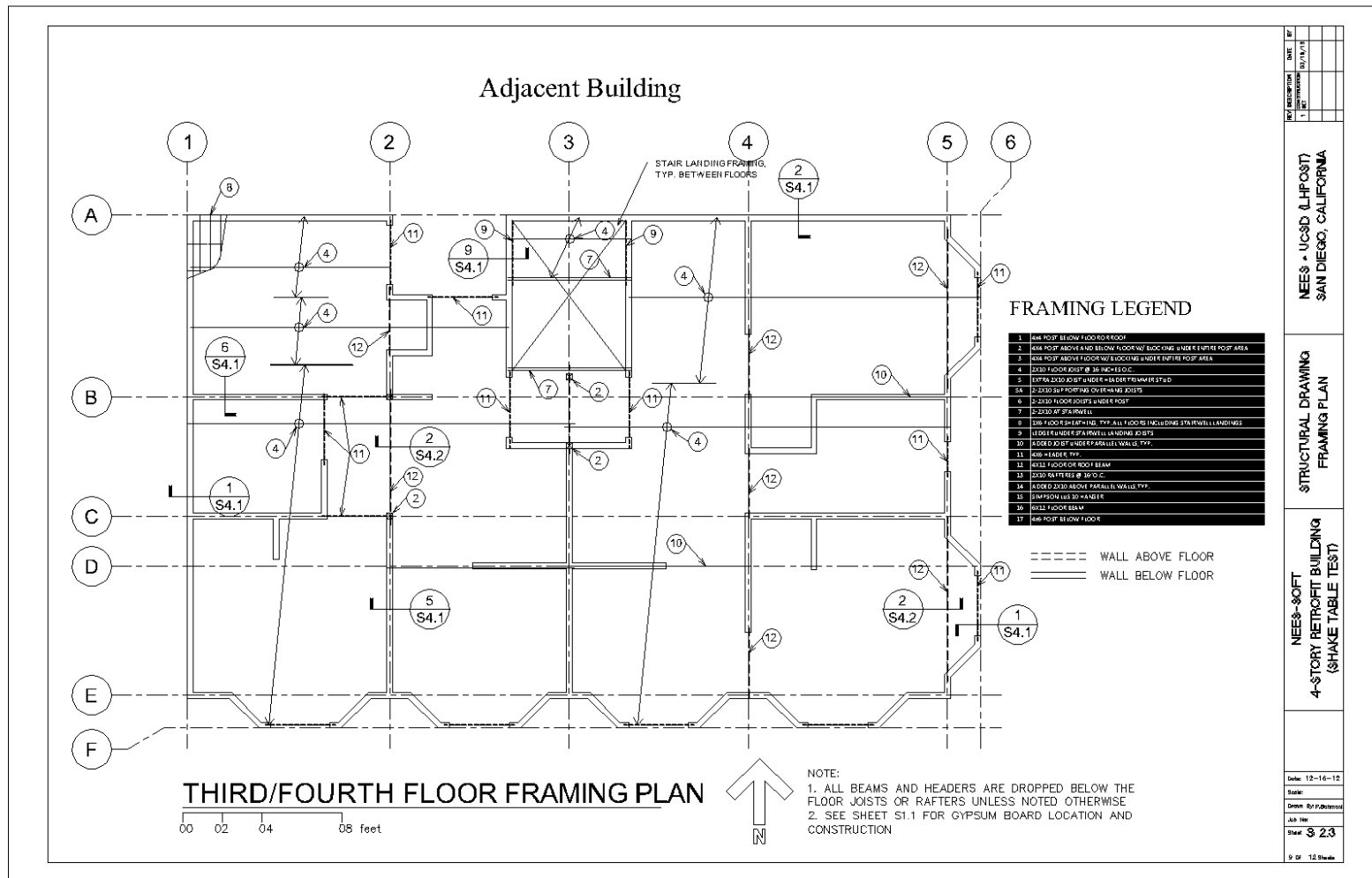
Appendix C: Structural and Architectural Drawings of the Four-Story Wood-Frame Building

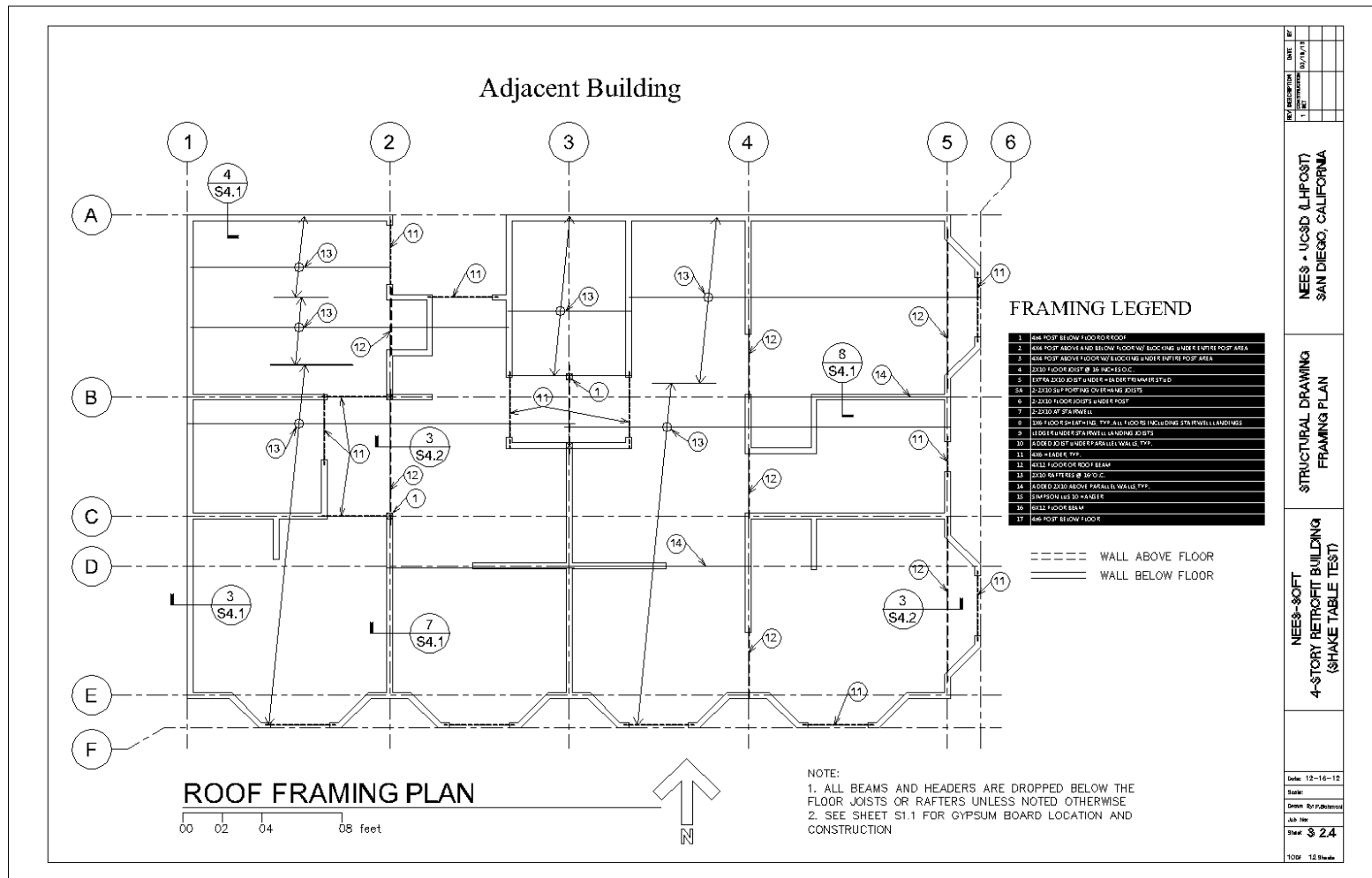




NEES-30FT 4-STORY RETROFIT BUILDING (SHAKE TABLE TEST)	ARCHITECTURAL PLAN ELEVATION VIEW	NEES • UCSD (LHPOST) SAN DIEGO, CALIFORNIA	REV. DESCRIPTION DATE 1 10/1/92	BY
Date 12-10-12	By: <u> </u>			
Drawn By: <u> </u>				
Job No. <u> </u>				
Sheet <u> </u> of <u> </u>				







LIST OF ABBREVIATIONS AND ACRONYMS

ATC	Applied Technology Council
ATS	Anchor tiedown system
ASCE	American Society of Civil Engineers
CAPSS	Community Action Plan for Seismic Safety
CDF	Cumulative distribution function
CLT	Cross laminated timber
CM	Center of mass
CQC	Complete quadratic combination
CR	Center of rigidity
CUREE	Consortium of Universities for Research in Earthquake Engineering
C_v	Distribution factors
DBD	Displacement-based design
DBE	Design basis earthquake
DDD	Direct displacement design
D_y	Yield displacement
EPHM	Evolutionary parameter hysteretic model
EPP	Elastic-perfectly plastic
F_a	Short-period site coefficient (at 0.2s-period)
FEMA	Federal Emergency Management Agency
FVD	Fluid viscous dampers
GWB	Gypsum wallboard
h_{Eff}	Effective height
HWS	Horizontal wood siding
ISD	Inter-story drift
K_I	Initial stiffness

MCE	Maximum considered earthquake
MDOF	Multi-degree of freedom
NAHB	National Association of Home Builders
NEES	Network for Earthquake Engineering Simulation
NLTHA	Non-linear time history analysis
PBSD	Performance-based seismic design
PBSR	Performance-based seismic retrofit
PNE	Probability of non-exceedance
POE	Probability of exceedance
S_a	Spectral acceleration
SDOF	Single-degree of freedom
SMF	Special moment frame
S_{MS}	5 percent damped, spectral response acceleration
SRSS	Square root of sum of squares
UBC	Uniform Building Code
W_{Eff}	Effective weight
WSP	Wood structural panel